



HAL
open science

High-pressure pathways towards new functional Si-based materials with tailored optoelectronic properties and their characterization

Silvia Pandolfi

► **To cite this version:**

Silvia Pandolfi. High-pressure pathways towards new functional Si-based materials with tailored optoelectronic properties and their characterization. Materials Science [cond-mat.mtrl-sci]. Sorbonne Université, 2019. English. NNT : 2019SORUS459 . tel-03480902

HAL Id: tel-03480902

<https://theses.hal.science/tel-03480902>

Submitted on 15 Dec 2021

HAL is a multi-disciplinary open access archive for the deposit and dissemination of scientific research documents, whether they are published or not. The documents may come from teaching and research institutions in France or abroad, or from public or private research centers.

L'archive ouverte pluridisciplinaire **HAL**, est destinée au dépôt et à la diffusion de documents scientifiques de niveau recherche, publiés ou non, émanant des établissements d'enseignement et de recherche français ou étrangers, des laboratoires publics ou privés.

Sorbonne Université

École doctorale

Physique et Chimie des Matériaux

ED397

Laboratoire - Equipe de recherche

Institut de Minéralogie de Physique des Matériaux et de Cosmochimie (IMPMC)

Design et étude de nouveaux matériaux à propriétés remarquables

High-pressure pathways towards new functional Si-based materials with tailored optoelectronic properties and their characterization

Par Silvia Pandolfi

Thèse de doctorat de science des matériaux

Dirigée par Yann LE GODEC et Alexandre COURAC

Présentée et soutenue publiquement le 13 Décembre 2019

Devant un jury composé de :

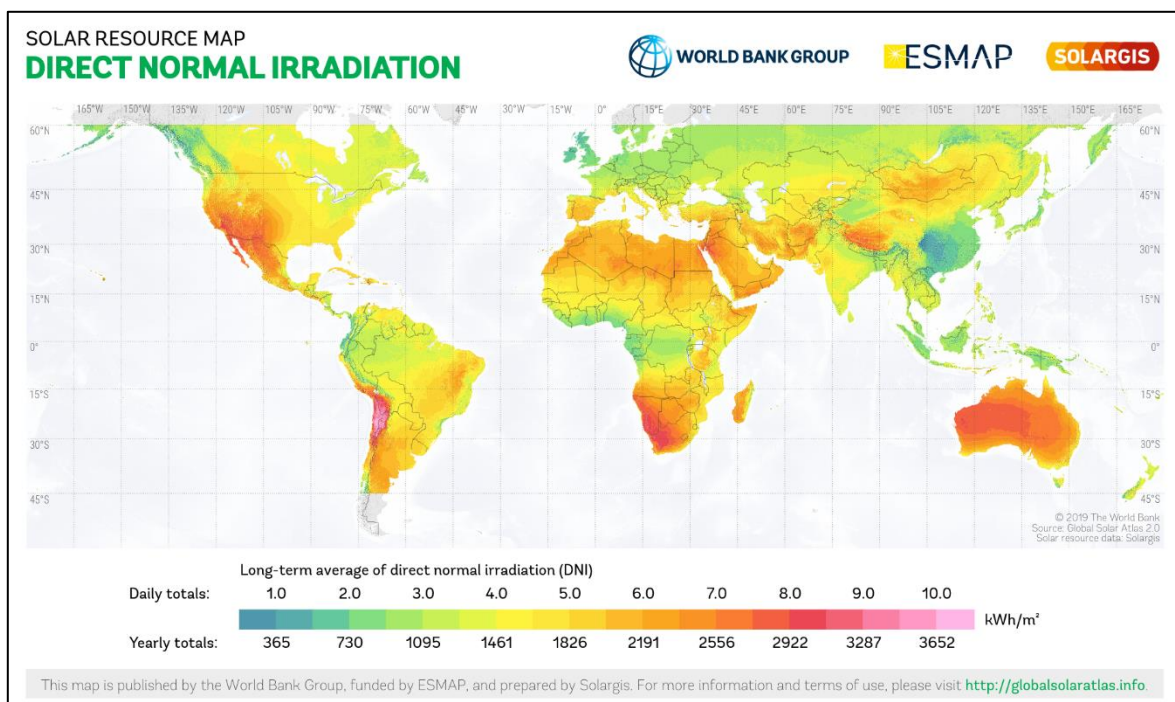
M. Fernando RODRIGUEZ	Professor – Universidad de Cantabria	Rapporteur
M. Romain VIENNOIS	Chargé de Recherche – Université de Montpellier	Rapporteur
Mme Chrystèle SANLOUP	Professeur – Sorbonne Université	Président du jury
Mme Pascale ROY	Chef de Ligne Synchrotron – SOLEIL Synchrotron	Examinatrice
Mle Leora E. DRESSELHAUS-COOPER	Lawrence Fellow – Lawrence Livermore National Laboratory	Invitée
M. Alexandre COURAC	Maître de Conférences – Sorbonne Université	Co-directeur de thèse
M. Yann LE GODEC	Directeur de Recherche CNRS – Sorbonne Université	Directeur de thèse

To my family(ies)

Introduction

With the new technological advances, modern economies depend on the reliable and affordable delivery of electricity. The net world electricity consumption has grown by 68% since the beginning of the century^a, and the production is still dominated by coal. With the limited fossil fuels available and the need to address climate change, there is an urge to develop efficient technologies to produce energy from renewable sources.

The Sun is an incredibly powerful source of energy, that arrives on the Earth in the form of electromagnetic radiation. Even accounting for the losses due to absorption and scattering from the atmosphere, the quantity of energy that arrives at the Earth's surface is enormous. Measurements from satellites have estimated that, on average, the solar irradiance above Earth's atmosphere is 1.36 kW/m², depositing ~174 PW across the entire surface of our planet. The figure below^b shows the average energy supplied by the Sun across the Earth's surface. To shift the current trend and achieve a sustainable development, it is essential to employ this clean energy.



^a World total final electricity consumption in 2017 (21372 TWh) was 68.27% higher than the correspondent consumption in 2000 (12701 TWh). Data from IEA, International Energy Agency (<https://www.iea.org/statistics/electricity/>).

^b From <http://globalsolaratlas.info>

As of 2017, solar energy accounted for only 1.8% of the global electricity production. Solar cells to convert solar light into electrical energy have been developed since the 1940s, and their efficiency has grown enormously since then. Further developments are still needed to achieve a large-scale distribution of these devices. Full market use of solar requires an increase in the efficiency and the reduction of the costs. To make solar energy sustainable and easy to bring to the consumers, one possibility could be the synthesis of new silicon material with enhanced properties. High-pressure allows to synthesize new silicon-based materials with enhanced properties for applications. At an industrial level, high-pressure has been mainly used for the synthesis of diamonds and super-hard materials, but recent studies have proved it also efficient in the synthesis of such silicon forms.

In this work, I develop high-pressure pathways to synthesize new enhanced silicon-based materials for solar applications. I begin with the study of the phase transition mechanisms at high-pressure, then describe the synthesis and characterization of a new silicon material. The work is organized as follows:

- *Chapter 1* presents the scope and the methodology of this work. The requirements for efficient photovoltaics materials, and the possibilities for material design at high-pressure are described.
- *Chapter 2* presents a brief summary of previous studies investigating silicon's behaviour at high-pressure. Previous results, as well as the open questions, are discussed briefly.
- *Chapter 3* introduces high-pressure techniques and *in-situ* structural characterization using x-ray diffraction. The design of our high-pressure cells for synchrotron-based studies is presented.
- *Chapter 4* shows our results from *in-situ* characterization of silicon phase transitions at pressures up to 14 GPa. With our results, we clarify some of the aspects that had remained unclear of silicon phase diagram, and we provide new insights on its transition mechanisms.
- *Chapter 5* presents our results on the first synthesis of pure bulk hexagonal silicon. Our high-pressure synthesis procedure, as well as some preliminary characterizations, are here reported.

- *Chapter 6* provides a detailed structural characterization of the newly synthesized hexagonal Si-4H. Our multi-scale approach reveals a complex and hierarchical structure that could enhance the potentiality of this new material.

Chapter 4-6, i.e. the chapters presenting our experimental results, are written in the form of papers, either letter or article. This choice has been motivated by the timing, but also by the will of describing our experimental results in the format of current scientific communications. Every experimental chapter has thus a brief additional introduction, more focused on the specific objectives of the project there presented, and its conclusions. Chapter 3 is focused on *in-situ* high-pressure synthesis. Even though characterization techniques other than x-ray diffraction have been used, the chapter is focused only on the latter, for which original contribution has been given with the design of adapted high-pressure cells for *in-situ* experiments.

Contents

Introduction	5
Contents.....	9
Chapter 1: High-pressure pathways to new silicon-based materials with tailored electronic properties	11
1.1 Metastable phases of silicon recoverable from high pressure treatment	14
1.1.1 Dense Si allotropes from high-pressure treatment	16
1.1.2 Stabilization of negative-pressure allotropes through high-pressure synthesis	18
1.1.3 Unconventional high-pressure synthesis methods	20
1.2 Scope of the PhD work.....	21
References Chapter 1	23
Chapter 2: Silicon under static high-pressure: state of the art	29
2.1 Overview of high-pressure phases of Si.....	30
2.2 Silicon phase diagram: <i>in-situ</i> studies.....	31
2.2.1 Phase transformations up to 20 GPa	32
2.2.2 Combining high-pressure and high temperature: phase diagram and melting curve	35
2.2.3 Comparison of experimental and theoretical studies	39
2.2.4 Conclusions	40
References Chapter 2	43
Appendix Chapter 2	47
Appendix 2.1: High-pressure phase transition at ambient temperature up to 20 GPa	47
Chapter 3: Experimental techniques: <i>in-situ</i> High-Pressure Synthesis.....	49
3.1 High-Pressure experiments with multi-anvil press	50
3.2 <i>In-situ</i> X-Ray Diffraction at extreme conditions.....	52
3.2.1 X-Ray Diffraction (XRD)	53
3.2.2 Synchrotron Radiation and <i>in-situ</i> experiments	54
3.3 Experimental setup and beamlines for <i>in-situ</i> multi-anvil experiments.....	56
3.1.1 ID06-LVP beamline at the European Synchrotron Radiation Facility (ESRF), Grenoble (France)	56
3.1.2 PSICHÉ beamline at the SOLEIL Synchrotron, Saint-Aubin (France)	58
References Chapter 3	61
Chapter 4: Topology of Si phase diagram: new insights by <i>in-situ</i> x-ray diffraction and direct observation of I-II-L triple point	63
References Chapter 4	75
Appendix Chapter 4	79
Appendix 4.1: Pressure, atomic volumes and pressure evolution for each experimental run.....	79
Appendix 4.2: x-ray radiography on PSICHE beamline.....	82
Appendix 4.3: Qualitative evaluation of hydrostaticity during Run3	82
Appendix 4.4: Run4, K:Si(1:6)	83

Chapter 5: Nature of hexagonal Si forming via high-pressure synthesis: nanostructured hexagonal 4H polytype.	85
References Chapter 5	97
Appendix Chapter 5	103
Appendix 5.1: Temperature profile during HP-HT synthesis	103
Appendix 5.2: Electron Diffraction Patterns and FFT-TEM proof of Si-4H stacking faults	104
.....	106
Appendix 5.3: DFT Calculations Results.....	106
Appendix 5.4: Experimental and Calculation Procedures	110
Appendixes References:	114
Chapter 6: Multi-scale Structure of Hexagonal Si-4H from high-pressure	115
6.1 Introduction	115
6.2 Experimental Results.....	117
6.3 Discussion	123
6.4 Conclusion.....	128
References Chapter 6	129
Appendix Chapter 6	133
Appendix 6.1: Detailed Experimental Procedure.....	133
Conclusions and Perspectives.....	135
Acknowledgements.....	139
Appendix A: High-pressure clathrate(s) in the K-Si system.....	141
References Appendix A	145
List of Figures	147
List of Tables.....	153

Chapter 1:

High-pressure pathways to new silicon-based materials with tailored electronic properties

Technology is a ubiquitous aspect of modern life. The market's demand for faster, lighter and less expensive devices motivates research for new materials with advanced properties able to meet the industry's needs. Functional materials with diverse properties have been predicted theoretically, such as room-temperature superconductors¹ or new super-hard materials². The realization of these materials with exceptional properties is not trivial and requires new synthetic approaches. This chapter introduces the scope and methodology of this PhD research. The work has been focused on the synthesis of new silicon-based material for optoelectronic applications, in particular solar energy conversion. I used static high-pressure synthesis in large-volume press. A brief overview of previous results obtained with this synthetic approach and other and less conventional high-pressure techniques are presented.

Electrical energy can be produced from absorption of solar light by exploiting the so-called *photovoltaic* effect. The simplest solar cell consists of a *p-n* junction under short-circuit conditions. The absorption of solar light generates couples of electrons and holes that exit the device as photo-generated current. Shockley and Queisser in the 1960s estimated the maximum efficiency for a *p-n* junction solar cell to be around 33% for a material with direct bandgap of 1.1 eV³ (see Figure 1.1). In photovoltaic devices, the conversion is lower than the Shockley-Queisser limit as the computation doesn't account for non-radiative recombination.

Materials for photovoltaic devices should be thus selected based on their optoelectronic properties, as illustrated in Figure 1.1. Some simple criteria are:

- i. Bandgap value close to the Shockley-Queisser limit, i.e. 1.1-1.3 eV.
- ii. Direct or quasi-direct bandgap.
- iii. Good optical absorption in the visible region of the solar spectrum, i.e. optically-allowed transitions.

The bandgap of silicon (Si) is 1.12 eV at ambient conditions⁴, close to the theoretical optimal value. The transition at 1.12 eV between the Γ and the X points of the reciprocal space is indirect. Indeed, the transition requires a transfer of momentum that cannot happen via simple

photon absorption and needs to be mediated by phonons. The direct bandgap, the lowest-energy optical transition, is around 3 eV (see Figure 1.2). Si absorption efficiency⁵ is thus limited, and the need for thick ($\sim 100 \mu\text{m}$) and high-purity⁸ Si wafers in solar cells increases the cost of photovoltaic modules. Different materials have been tested for the production of photovoltaic devices⁶⁻⁹, but they also present some disadvantages. For example, GaAs¹⁰ is a direct-bandgap semiconductor with higher efficiency than Si, but it is a toxic and expensive compound. Despite its limited performance, crystalline Si is currently the most common absorber material in the photovoltaic industry, comprising more than 80% of the global market¹¹. Commercial Si solar cells reach 20% efficiency¹², and have shown a simultaneous increase of the efficiency while decreasing the price¹³.

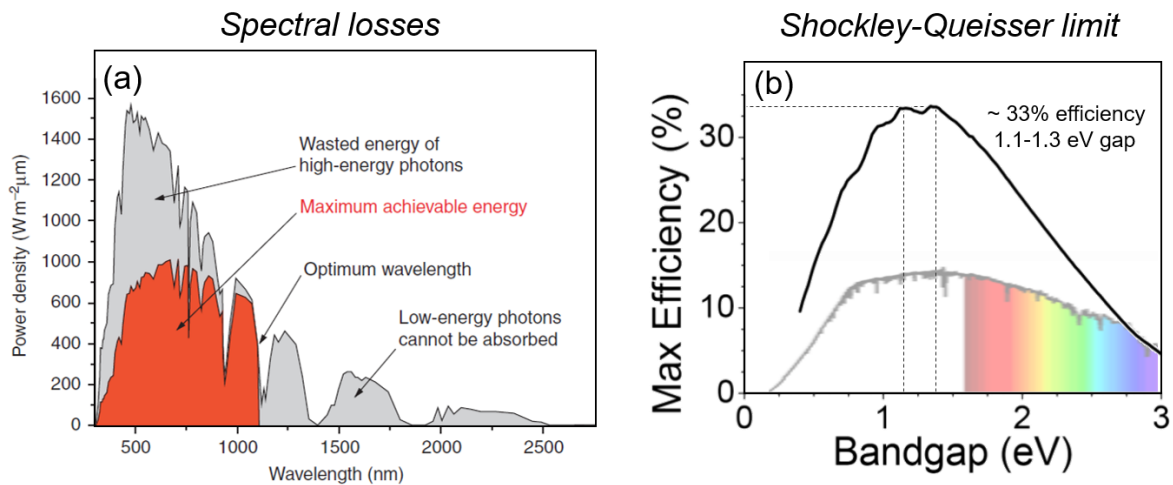


Figure 1.1 : Maximum achievable absorption and efficiency of photovoltaic materials. (a) for an ideal material with the optimal bandgap, the orange portion shows the maximum energy that can be absorbed, while the grey areas are the portion of the solar spectrum that cannot be absorbed. Figure adapted from Glunz et al¹¹. (b) absorption efficiency as a function of the bandgap energy, as calculated by Shockley and Queisser, showing that the maximum conversion efficiency is obtained for energy gaps around 1.1-1.3 eV. The solar spectrum irradiance is also shown in the lower part of the figure.

Si is and remains the material of choice for applications because, regardless of its indirect bandgap, it presents multiple advantages from a practical point of view. Si is the second most abundant element in the Earth's crust, which makes it widely available and inexpensive. It is the main component of current technologies, meaning that its properties are well understood, and it is already routinely processed on industrial scale. The ideal solution to overcome its limitations would be to engineer and optimize Si properties and its absorption in the visible region of the solar spectrum. This would open the way for high efficiency thin solar cells able to maintain all the advantages of Si manufacturing.

There are several approaches to modify Si's optoelectronic properties, and current synthesis and manipulation capabilities enable to engineer materials at unprecedented levels. Calculations and simulations explore the possible structures and morphologies of new Si materials and predict their properties. These results guide the design of synthetic pathways towards new targeted functional materials. In the following the most common methodologies are briefly presented.

- *Nanostructure, low dimensionality*

When matter is organized on the nanometric scale, new physical phenomena occur because at the nanoscale quantum confinement can modify the material's properties (e.g. hardness, optical emission, etc.). For example, in Si nanoparticles, size effects manifest as a blueshift of the bandgap energy with decreasing particle size¹⁴⁻¹⁶. Furthermore, synthesized Si nanoparticles can assume crystalline structures different than their bulk counterpart. This is observed for porous Si^{16,17}, the hexagonal inclusions in Si nanowires (NWs)¹⁸ or the epitaxially grown hexagonal Si¹⁹ and Si/Ge²⁰ shells on GaP NWs. These new structures are expected to have improved properties for photovoltaic applications²¹⁻²³.

- *Strain*

Theoretical calculations have predicted that strain can modify Si's optoelectronic properties. For bulk diamond-Si²⁴ and hexagonal-Si²⁵, strain-induced modulation of the bandstructure is expected to result in a transition from indirect to direct bandgap. The opposite transformation (i.e. direct to indirect) has been predicted in Si nanowires. Experimentally, strained structures can be obtained using indentation instruments; this technique will be discussed more in detail in Section 1.1.3.

- *Bulk synthesis of new crystal structures*

It is also possible to manipulate Si optical properties by stabilizing Si phases with different crystal symmetries. Theoretical calculations have explored the complex free-energy landscape of Si searching local energy minima²⁶⁻²⁸. Low formation energy and mechanical stability (i.e. non-negative phonon frequencies) are fundamental conditions for the feasibility of these materials. Furthermore, calculations can be oriented to search for direct bandgap materials, ideal candidates for Si-based photovoltaics. The prediction of several allotropes with desirable properties and possibly metastable²⁹⁻³¹ has motivated the research of new pathways

to stabilize exotic forms of Si. Figure 1.2 shows how the crystal symmetry influences the optoelectronic properties.

In the search for new photovoltaic Si-based materials, high-pressure (HP) synthesis is the method of choice. HP offers the possibility to synthesize metastable materials, recoverable after a series of direct phase transformations. This method allows one to obtain samples with the same purity as the starting material and does not require preparation procedures involving toxic chemicals like hydrofluoric acid (HF, widely used in the preparation of high-purity d-Si wafers). Furthermore, materials recovered from HP can go from well-crystallized to strained and/or nanostructured samples. Thus, HP synthesis can tune both the crystal structure and the grain size, offering a wide spectrum of possible outcomes in terms of properties engineering.

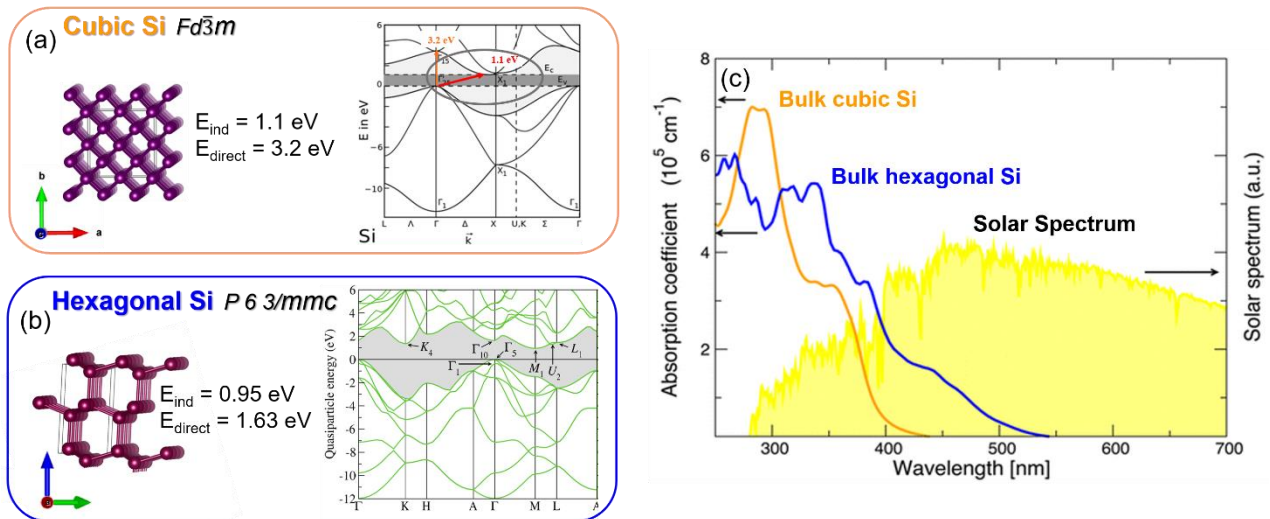


Figure 1.2 : Optoelectronic properties are determined by the crystal structure. (a) diamond Si-I and its bandstructure; (b) hexagonal Si-IV (i.e. 2H-Si polytype) and its bandstructure as calculated by Rodl et al²⁵. (c) comparison of Si-I (cubic) and Si-IV (hexagonal) absorption in the region of interest (the yellow area represents the solar spectrum). Figure adapted from Amato et al²³.

1.1 Metastable phases of silicon recoverable from high pressure treatment

In this section, the possibilities for material engineering through HP are briefly presented. After introducing the concept of HP phase transitions and metastability, the possibilities for synthesis of both dense and low-density Si allotropes via HP are illustrated. Finally, alternative *unconventional* HP methods are briefly described.

When compressed, at first crystals tend to shrink and the density increases. At high enough pressures, a rearrangement of the atoms can occur, resulting in a phase transition. In these cases, the tendency is to adopt denser structures with higher coordination number, as to reduce the nuclear repulsion energy. HP can thus stabilize energetically favourable phases with increasing densities. More details on Si HP phases and the state-of-the-art Si phase diagram are given in next chapter.

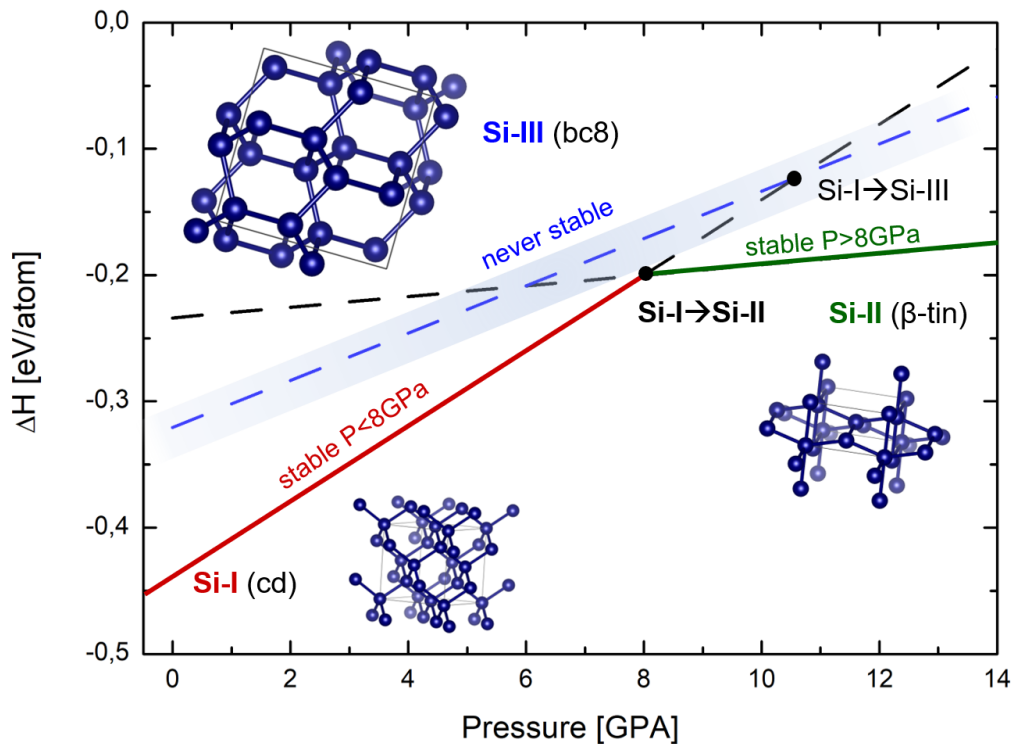


Figure 1.3 : Calculated enthalpy at $T=0$ K for Si-I, Si-II and Si-III. The figure shows that, by tuning the pressure, the enthalpy changes may induce a phase transition. At pressures higher than 8 GPa, Si-II becomes the lowest-enthalpy phase, while Si-III is not the energetically favourable phase at any P. Data are taken from ³² and ΔH are calculated with respect to the one of the cubic (bcc) high-pressure phase.

At any given pressure-temperature (P-T) condition, the stable phase corresponds to the global minimum of the Gibbs free energy (G or, equivalently, of the free enthalpy H). For Si, the stable allotrope with minimum G at ambient conditions is Si-I, with diamond-like structure. The changes of the free enthalpy with pressure and temperature can stabilize other crystal structures. When applying pressure, the cubic diamond structure's free enthalpy increases to a point at which, as shown in the Figure 1.3, it is not the most stable phase. In this case, a pressure-driven phase transition can occur, as the crystal tends to assume the structure corresponding to the lowest-energy configuration, i.e. the global minimum of the free enthalpy. Figure 1.3 shows that, according to the calculations performed by Needs and Mujica³², pressure is expected to cause a phase transition from Si-I to Si-II at around 8 GPa.

Besides the energetics of Si phases, the kinetics of the phase transitions should also be considered. Depending on the thermodynamic properties of the intermediate states, different synthetic pathways could be favoured, and phases different than the thermodynamically stable one may form. Typically, for covalent solids, at sufficiently low temperature (T), there may be several local minima of the free energy, meaning that there are several *metastable* configurations (i.e. local minima of the free energy that are stable under infinitesimal structural changes)²⁶. If a synthetic path leads to a metastable phase, it is possible that kinetic effects hinder further transition to the globally stable phase, especially when the energy difference between the two is small. The metastable phase is thus said to be *kinetically stable*. In the case of Si, reaching metastable states by tuning P-T conditions presents possibilities for material synthesis, as it can lead to the stabilization and eventual recover at ambient conditions of new phases.

1.1.1 Dense Si allotropes from high-pressure treatment

Most of the transitions of Si at HP have been observed to be reversible³³ at 300 K. One exception is the Si-I→Si-II transition, which has a high kinetic barrier³⁴. Allotropes different than diamond-like Si can be recovered by releasing pressure from the HP Si-II phase. A brief review of some such transformations is given below.

When the pressure is released slowly (i.e. seconds), Si-II has been reported to transform into rhombohedral Si-XII (r8)³⁵ around 8-10 GPa, then into Si-III (bc8) around 2 GPa³⁶. Si-III is metastable at ambient conditions and can be recovered³⁷⁻⁴⁰. This phase was first stabilized more than 50 years ago, and it was also reported to transform into the hexagonal Si-IV allotrope upon annealing at 200°C³⁷.

As shown in Figure 1.3, Si-III is unstable at every pressure (P) at 0 K. A direct transition from Si-I to Si-III under pressure is not possible because Si-I→Si-II transformation takes place at lower pressure⁴¹, i.e. 8 GPa instead of 10.5 GPa. Nevertheless, upon decompression the Si-II→Si-III pathway has lower energy than Si-II→Si-I because of the respective kinetic barriers⁴²⁻⁴⁴, as represented in Figure 1.4. Both transitions are reconstructive first-order transformations, but Si-II→Si-III is possibly favoured by the structural analogies of Si-II and Si-III stacking sequence⁴¹. Once Si-III is stabilized, its structure is comprised of twisted tetrahedral bonds. The differences in bonding angles from the ideal sp^3 hybridization are such that upon heating Si-III does not convert into the stable Si-I phase, but rather to the Si-IV phase

³⁷. The transition from Si-III to Si-IV implies a local rotation of the bonds, which can take place at moderate temperature (200°C). Further transition to Si-I requires bonds to break and twist, resulting in a higher kinetic barrier⁴². The experimental phase sequence Si-II→Si-XII (r8)→Si-III (bc8)³⁶ during decompression, as well as Si-III → Si-IV → Si-I upon heating, have been recently confirmed by the newly developed PALLAS⁴² method to assess favourable transformation pathways (see also Figure 1.4).

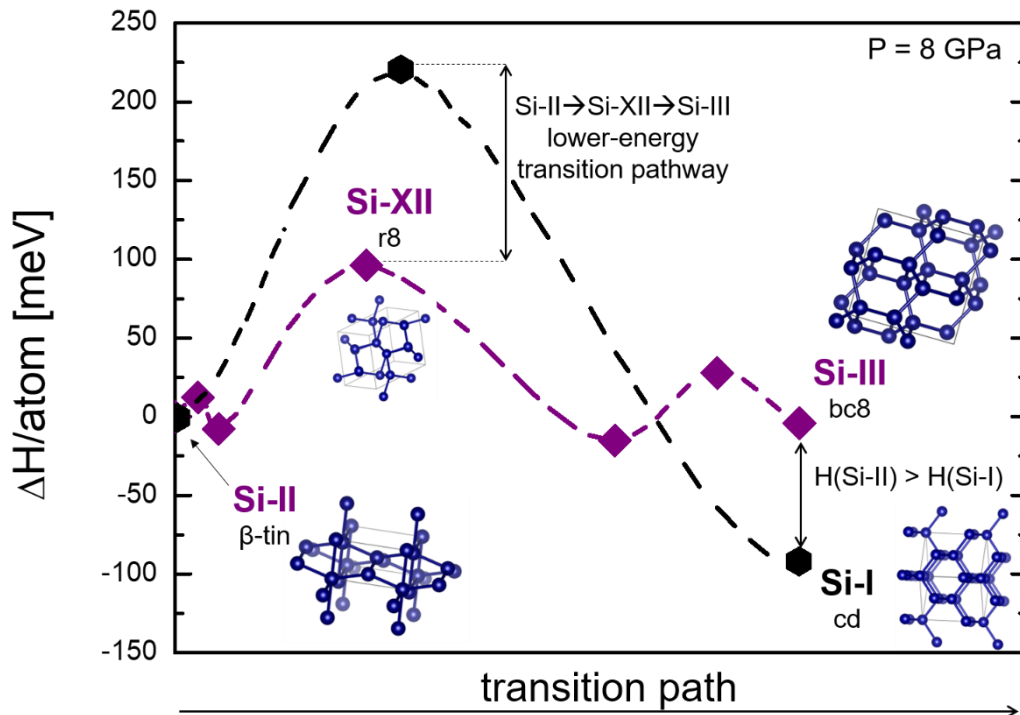


Figure 1.4 : Calculated enthalpy variations at 8 GPa along different transformation pathways starting from Si-II. In black, direct transition back to the cubic Si-I is shown to have a higher kinetic barrier than the transition Si-II (β -tin)→ Si-XII (r8)→ Si-III (bc8). This favours the formation the transition to Si-III rather than Si-I upon decompression, even though the final state (Si-III) is not the globally stable phase. Data for Si-II→Si-I pathway are taken from ⁴⁴ and have been recently reproduced by ⁴², from which the Si-II→Si-III data shown in purple have been taken.

Si-III and Si-IV have attracted attention because of their peculiar optoelectronic properties, which differ from those of Si-I. Si-III has a body-centred cubic structure (bc8) and is 9% more dense than diamond-like Si. Si-III was originally believed to be a semimetal ³⁸; recent studies, however, have demonstrated that it is a narrow-gap (20 meV) semiconductor ³⁹.

Si-IV was reported to have a wurtzite-like hexagonal diamond structure, and it is expected to play a key role in future technological applications. Computational studies predict that the change from a cubic symmetry to an hexagonal one modifies the band-structure and the value of the band-gap, increasing the absorption of visible light ^{25,45}. If these calculations are

confirmed experimentally, hexagonal Si allotropes may be used to improve the efficiency of Si-based photovoltaic absorbers.

Fast decompression (<100 ms) led to different outcomes. Upon unloading from 14.8 GPa and 12 GPa, the tetragonal Si-VIII and Si-IX have been respectively suggested⁴⁶. The structures of these phases have not been refined, and to our knowledge this is the only report of these allotropes.

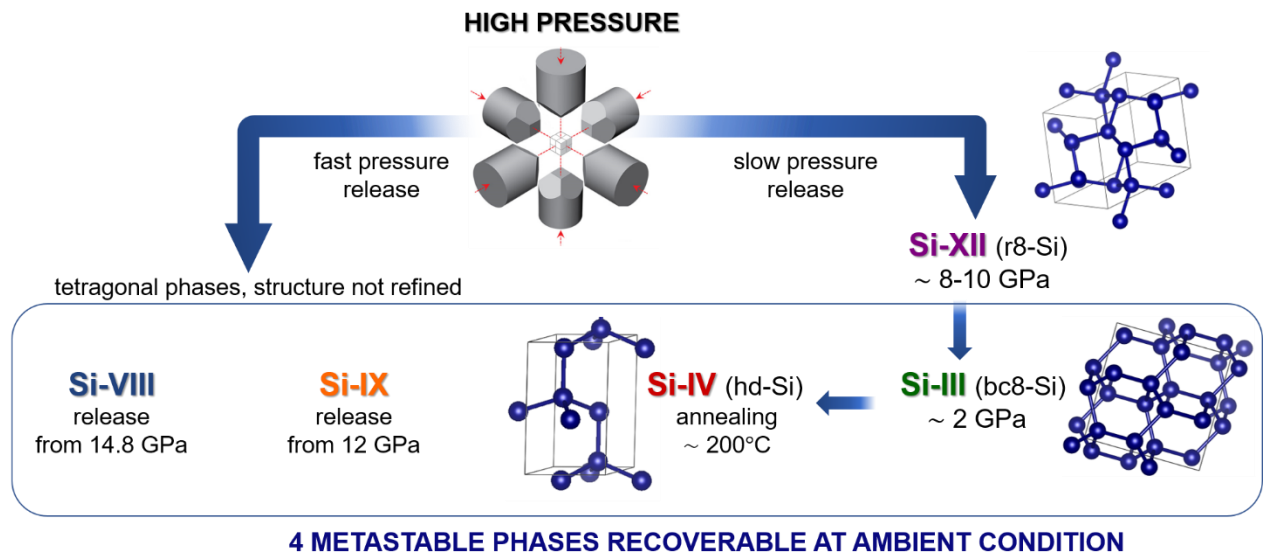


Figure 1.5 : Schematic view of the recoverable metastable phases that have been reported from HP-HT treatment of cubic Si-I. On the left, Si-VIII and Si-IX are reported; these phases can be obtained by fast (~10 GPa/ms) decompression, their structures have not been refined. On the right, the phase transformations upon slow decompression at ambient temperature (Si-II→Si-XII→Si-III) and subsequent annealing (Si-III→Si-IV) are shown.

In summary, by releasing pressure four metastable phases of Si have been reported: Si-III, Si-VIII, Si-IX and Si-IV (after annealing). These phases are represented also in Figure 1.5. High-pressure synthesis is thus an efficient method to synthesize new Si-based material. Despite a limited number of recoverable phases, the diversity of their optoelectronic properties is very promising for expanding and/or optimizing Si technological applications.

1.1.2 Stabilization of negative-pressure allotropes through high-pressure synthesis

Most of the direct-bandgap Si phases that have been predicted so far are open frameworks, thus low-density allotropes^{29,30,47}. Thermodynamically, low-density phases are stable only at negative pressures^{48–50}. The phases recoverable from HP treatment of Si-I are usually denser than the starting material. Despite that, HP synthetic routes can be still designed to stabilize low-density Si phases.

Si clathrates are guest-host cage-like intermetallic compounds^{51,52} in which the polyhedral Si cages are stabilized by the presence of the guest atom. Adams et al. were the first in 1994 to simulate a low-density Si structure analogous to emptied Si clathrates⁵³. They calculated a bandgap of 2 eV and a small (0.07 eV/atom) energy difference with respect to diamond Si. Further studies⁵⁴⁻⁵⁷ have investigated clathrate frameworks, finding interesting optoelectronic properties for application.

Si-Na clathrates were first synthesized in 1965⁵⁸ via thermal decomposition of thermodynamically stable Na_4Si_4 . Thus, the synthesis of low-density allotropes as emptied Si clathrates' cages seemed viable. The use of a metastable precursor like the clathrates allows us to explore broader regions of the possible phases of Si. This approach can reach local energy minima unattainable when starting from the globally stable phase. Recently it was shown that Na-Si clathrates are HP phases⁵⁹, thus HP can stabilize these compounds from elemental solution. Si clathrates were recovered from HP treatment and are metastable at ambient conditions.

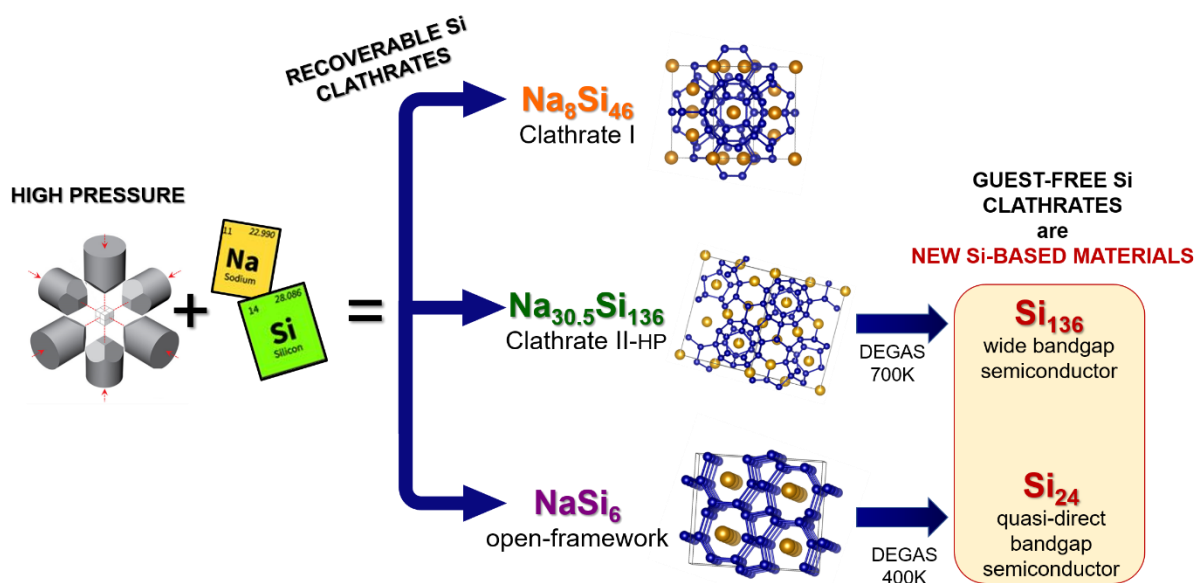


Figure 1.6 : Summary of the Na-Si clathrates synthesized via HP. Clathrate II and the open-framework NaSi_6 phases can be transformed into guest-free allotropes with bandgap energies as shown. No evidence of the guest-free clathrate I framework has been reported so far.

Figure 1.6 summarizes the results from HP synthesis. Na-Si clathrates can assume different crystal structures and stoichiometries. The most widely studied clathrates are structure I (stoichiometric formula $\text{Na}_8\text{Si}_{46}$) and structure II ($\text{Na}_{24}\text{Si}_{136}$). To obtain guest-free clathrates, the synthesis must be performed in two steps, the second being the escape of guest atoms from Si cages. This approach led to the synthesis of Si_{24} ^{60,61}, a quasi-direct bandgap material with

optimal value for photovoltaic applications. Si₂₄ is obtained by degassing the open-framework NaSi₆ clathrate⁵⁹. Guest-free clathrate II, Si₁₃₆, has also been obtained, and is a wide (2 eV) bandgap semiconductor⁵⁴. No evidence of Na-free Si framework from clathrate I has yet been provided.

The possibilities in term of material design offered by this double-step approach are countless, as changing the chemical composition of the clathrates could lead to compounds with new structures and properties. Clathrates with different chemical composition (i.e. various guest atoms or ternary clathrates with doped Si cages) have already been synthesized, including K₈Si₄₆⁶², K₂₄Si₁₃₆⁶³, Ba₈Si₄₆⁶⁴, K₇B₇Si₃₈⁶⁵ and Rb₈Ga₈Si₃₈⁶⁶. Clathrates are promising precursors to access low-energy pathways to novel functional silicon forms, and HP has been proven efficient in stabilizing these compounds.

1.1.3 Unconventional high-pressure synthesis methods

The most common static-HP devices use anvils to compress the materials, usually made of diamond or tungsten carbide. Both pressurization and heating are relatively slow, through a series of quasi-equilibrium states which allow us to access the thermodynamically stable phases. These methods for pressure generation allow us to obtain well-crystallized samples, as they avoid large shear and tensile stress, but they cannot efficiently access high-energy pathways²⁶. Alternative methods with shorter compression/heating duration can further explore the free energy landscape. By increasing the strain rate or the residual stress it is indeed possible to access new phases exploiting the kinetics of phase transitions. These HP methods, sometimes called *unconventional*²⁶, are briefly presented in the following.

Indentation applies a local pressure via uniaxial “point” pressure loading. Compression can be performed in standard indentation instruments to quantify mechanical properties. The tip is placed upon the sample’s surface and applies a pre-set force at a given rate. The pressure applied on the sample depends on the material’s hardness; the maximum pressure is determined by the yield of the material, i.e. the stress above which the material starts deforming plastically. In the case of Si, it is possible to apply pressures up to ~12 GPa, which can induce a phase transition. Formation of Si-II in the indented zone has been shown with *in-situ* electrical measurements and *ex-situ* TEM and Raman characterization^{67–72}. While indentation can be considered a “quasi-static” HP technique, the stress states in the sample have a high shear component, and the residual stress/strain remaining after pressure release is ~1-4 GPa^{73,74}.

The phases recovered from point-loading compression may be different than the ones from conventional static-HP experiments. When decompression is fast enough, amorphous Si is formed^{75,76}. Upon slow release, the sample transforms into a mixture of Si-III and Si-XII (i.e. bc8-r8)⁷⁴. Si-XII (r8), remains stable on the indented surface after pressure release⁷⁷, in contrast with quasi-hydrostatic compression of Si. Si-XII is a narrow bandgap semiconductor that can be doped at room temperature. Recently it has been possible to perform *ex-situ* diffraction to estimate the relative abundance of Si-III (bc8) and Si-XII (r8) phases in the transformed region⁷³. By annealing at 200°C the Si-III/Si-XII mixed phase, a new allotrope, Si-XIII^{74,78,79}, was detected by Raman microspectroscopy⁷⁹. Interestingly, this phase was impossible to obtain in a conventional diamond-anvil cell experiment⁷⁸, and it is thus specific to the indentation synthesis procedure.

Dynamic compression can also be used for HP synthesis, as the shock waves propagating into the material induce simultaneous HP and HT conditions. A laser can drive the shock compression via single shock or via a ramped compression. Laser-induced shock studies on Si reported phase transitions and formation of metastable phases analogous to those observed in static-HP experiments, such as Si-III, Si-VIII, Si-XII^{80–84}. Recent experiments⁸⁵ have demonstrated that laser-induced shock compression (~fs laser pulse) in a confined geometry causes microexplosions, reaching simultaneously pressures of ~1 TPa and temperatures of ~10⁵ K. These far-from equilibrium conditions enable the formation of at least two new allotropes: proposed tetragonal BT8-Si (*I4₁/a*) and ST12-Si (*P4₃2₁2*)⁸⁵.

1.2 Scope of the PhD work

High-pressure synthesis is a powerful method to synthesize new Si-based materials. HP allows the design of new materials, acting on both the structure and the morphology of the crystallites, allowing us to modify the optoelectronic properties. It is possible to recover dense metastable allotropes from HP treatment (such as Si-III and Si-IV), as well as to stabilize low-density allotropes using high-pressure precursors, like Si clathrates. Unconventional HP techniques, such as point-loading or shock compression, allow us to diversify the kinetic pathways stabilizing new phases. Indentation can be used to transform thin regions of the sample's surface to obtain thin films of new Si phases, which can be an interesting perspective for solar panel production. However, these techniques produce polycrystalline samples with very small volumes, precluding the precise characterization of these new phases.

The work presented in this PhD thesis is focused on static HP-HT synthesis of new Si phases. Our *in-situ* characterization will give significant insight on Si phase transformations, which are essential to understand and exploit HP pathways for material synthesis. We use a large-volume press to ensure large and pure samples suitable for detailed physical characterization of the newly discovered phases. Once the new phases have been characterized and their properties have been understood, samples recovered from HP can also be used as seed for soft chemical method or epitaxial deposition to ensure scalability of the production for future industrial applications.

References Chapter 1

- (1) Ashcroft, N. W. Metallic Hydrogen: A High-Temperature Superconductor? *Phys. Rev. Lett.* **1968**, *21* (26), 1748–1749. <https://doi.org/10.1103/PhysRevLett.21.1748>.
- (2) Dong, H.; Oganov, A. R.; Wang, Q.; Wang, S.-N.; Wang, Z.; Zhang, J.; Esfahani, M. M. D.; Zhou, X.-F.; Wu, F.; Zhu, Q. Prediction of a New Ground State of Superhard Compound B6O at Ambient Conditions. *Sci. Rep.* **2016**, *6*, 31288.
- (3) Shockley, W.; Queisser, H. J. Detailed Balance Limit of Efficiency of *P-n* Junction Solar Cells. *J. Appl. Phys.* **1961**, *32* (3), 510–519. <https://doi.org/10.1063/1.1736034>.
- (4) *Properties of Crystalline Silicon*; Hull, R., Institution of Electrical Engineers, Eds.; EMIS datareviews series; INSPEC: London, 1999.
- (5) Little, R. G.; Nowlan, M. J. Crystalline Silicon Photovoltaics: The Hurdle for Thin Films. *Prog. Photovolt. Res. Appl.* **1997**, *5* (5), 309–315. [https://doi.org/10.1002/\(SICI\)1099-159X\(199709/10\)5:5<309::AID-PIP180>3.0.CO;2-X](https://doi.org/10.1002/(SICI)1099-159X(199709/10)5:5<309::AID-PIP180>3.0.CO;2-X).
- (6) Repins, I.; Contreras, M. A.; Egaas, B.; DeHart, C.; Scharf, J.; Perkins, C. L.; To, B.; Noufi, R. 19.9%-Efficient ZnO/CdS/CuInGaSe² Solar Cell with 81.2% Fill Factor. *Prog. Photovolt. Res. Appl.* **2008**, *16* (3), 235–239. <https://doi.org/10.1002/pip.822>.
- (7) Rau, U.; Schock, H. W. Electronic Properties of Cu(In,Ga)Se₂ Heterojunction Solar Cells-Recent Achievements, Current Understanding, and Future Challenges. *Appl. Phys. Mater. Sci. Process.* **1999**, *69* (2), 131–147. <https://doi.org/10.1007/s003390050984>.
- (8) Todorov, T. K.; Reuter, K. B.; Mitzi, D. B. High-Efficiency Solar Cell with Earth-Abundant Liquid-Processed Absorber. *Adv. Mater.* **2010**, *22* (20), E156–E159. <https://doi.org/10.1002/adma.200904155>.
- (9) Redinger, A.; Berg, D. M.; Dale, P. J.; Siebentritt, S. The Consequences of Kesterite Equilibria for Efficient Solar Cells. *J. Am. Chem. Soc.* **2011**, *133* (10), 3320–3323. <https://doi.org/10.1021/ja111713g>.
- (10) Green, M. A.; Emery, K.; Hishikawa, Y.; Warta, W.; Dunlop, E. D. Solar Cell Efficiency Tables (Version 45): Solar Cell Efficiency Tables. *Prog. Photovolt. Res. Appl.* **2015**, *23* (1), 1–9. <https://doi.org/10.1002/pip.2573>.
- (11) Glunz, S. W.; Preu, R.; Biro, D. Crystalline Silicon Solar Cells. In *Comprehensive Renewable Energy*; Elsevier, 2012; pp 353–387. <https://doi.org/10.1016/B978-0-08-087872-0.00117-7>.
- (12) Mulligan, William P. et al. Manufacture of Solar Cells with 21% Efficiency. *Proceedings of the 19th European Photovoltaic Solar Energy Conference. Vol. 387 WIP Renewable Energies Paris, France.* 2004.
- (13) van Sark, W. G. J. H. M.; Alsema, E. A.; Junginger, H. M.; de Moor, H. H. C.; Schaeffer, G. J. Accuracy of Progress Ratios Determined from Experience Curves: The Case of Crystalline Silicon Photovoltaic Module Technology Development. *Prog. Photovolt. Res. Appl.* **2008**, *16* (5), 441–453. <https://doi.org/10.1002/pip.806>.
- (14) Kovalev, D.; Heckler, H.; Polisski, G.; Koch, F. Optical Properties of Si Nanocrystals. *Phys. Status Solidi B* **1999**, *215* (2), 871–932. [https://doi.org/10.1002/\(SICI\)1521-3951\(199910\)215:2<871::AID-PSSB871>3.0.CO;2-9](https://doi.org/10.1002/(SICI)1521-3951(199910)215:2<871::AID-PSSB871>3.0.CO;2-9).
- (15) Hannah, D. C.; Yang, J.; Podsiadlo, P.; Chan, M. K. Y.; Demortière, A.; Gosztola, D. J.; Prakapenka, V. B.; Schatz, G. C.; Kortshagen, U.; Schaller, R. D. On the Origin of Photoluminescence in Silicon Nanocrystals: Pressure-Dependent Structural and Optical Studies. *Nano Lett.* **2012**, *12* (8), 4200–4205. <https://doi.org/10.1021/nl301787g>.

- (16) Lockwood, D. J.; Wang, A. G. Quantum Confinement Induced Photoluminescence in Porous Silicon. *Solid State Commun.* **1995**, *94* (11), 905–909. [https://doi.org/10.1016/0038-1098\(95\)00186-7](https://doi.org/10.1016/0038-1098(95)00186-7).
- (17) Lockwood, D. J. Optical Properties of Porous Silicon. *Solid State Commun.* **1994**, *92* (1–2), 101–112. [https://doi.org/10.1016/0038-1098\(94\)90863-X](https://doi.org/10.1016/0038-1098(94)90863-X).
- (18) Li, Y.; Liu, Z.; Lu, X.; Su, Z.; Wang, Y.; Liu, R.; Wang, D.; Jian, J.; Lee, J. H.; Wang, H.; Yu, Q.; Bao, J. Broadband Infrared Photoluminescence in Silicon Nanowires with High Density Stacking Faults. *Nanoscale* **2015**, *7* (5), 1601–1605. <https://doi.org/10.1039/C4NR05410E>.
- (19) Hauge, H. I. T.; Verheijen, M. A.; Conesa-Boj, S.; Etzelstorfer, T.; Watzinger, M.; Kriegner, D.; Zardo, I.; Fasolato, C.; Capitani, F.; Postorino, P.; Koelling, S.; Li, A.; Assali, S.; Stangl, J.; Bakkers, E. P. A. M. Hexagonal Silicon Realized. *Nano Lett.* **2015**, *15* (9), 5855–5860. <https://doi.org/10.1021/acs.nanolett.5b01939>.
- (20) Hauge, H. I. T.; Conesa-Boj, S.; Verheijen, M. A.; Koelling, S.; Bakkers, E. P. A. M. Single-Crystalline Hexagonal Silicon–Germanium. *Nano Lett.* **2017**, *17* (1), 85–90. <https://doi.org/10.1021/acs.nanolett.6b03488>.
- (21) Cartoixà, X.; Palummo, M.; Hauge, H. I. T.; Bakkers, E. P. A. M.; Ruruli, R. Optical Emission in Hexagonal SiGe Nanowires. *Nano Lett.* **2017**, *17* (8), 4753–4758. <https://doi.org/10.1021/acs.nanolett.7b01441>.
- (22) De, A.; Pryor, C. E. Electronic Structure and Optical Properties of Si, Ge and Diamond in the Lonsdaleite Phase. *J. Phys. Condens. Matter* **2014**, *26* (4), 045801. <https://doi.org/10.1088/0953-8984/26/4/045801>.
- (23) Amato, M.; Kaewmaraya, T.; Zobelli, A.; Palummo, M.; Ruruli, R. Crystal Phase Effects in Si Nanowire Polytypes and Their Homojunctions. *Nano Lett.* **2016**, *16* (9), 5694–5700. <https://doi.org/10.1021/acs.nanolett.6b02362>.
- (24) Karazhanov, S. Zh.; Davletova, A.; Ulyashin, A. Strain-Induced Modulation of Band Structure of Silicon. *J. Appl. Phys.* **2008**, *104* (2), 024501. <https://doi.org/10.1063/1.2940135>.
- (25) Rödl, C.; Sander, T.; Bechstedt, F.; Vidal, J.; Olsson, P.; Laribi, S.; Guillemoles, J.-F. Wurtzite Silicon as a Potential Absorber in Photovoltaics: Tailoring the Optical Absorption by Applying Strain. *Phys. Rev. B* **2015**, *92* (4), 045207. <https://doi.org/10.1103/PhysRevB.92.045207>.
- (26) Haberl, B.; Strobel, T. A.; Bradby, J. E. Pathways to Exotic Metastable Silicon Allotropes. *Appl. Phys. Rev.* **2016**, *3* (4), 040808. <https://doi.org/10.1063/1.4962984>.
- (27) Mujica, A.; Pickard, C. J.; Needs, R. J. Low-Energy Tetrahedral Polymorphs of Carbon, Silicon, and Germanium. *Phys. Rev. B* **2015**, *91* (21). <https://doi.org/10.1103/PhysRevB.91.214104>.
- (28) Zhu, Q.; Oganov, A. R.; Lyakhov, A. O.; Yu, X. Generalized Evolutionary Metadynamics for Sampling the Energy Landscapes and Its Applications. *Phys. Rev. B* **2015**, *92* (2). <https://doi.org/10.1103/PhysRevB.92.024106>.
- (29) Amsler, M.; Botti, S.; Marques, M. A. L.; Lenosky, T. J.; Goedecker, S. Low-Density Silicon Allotropes for Photovoltaic Applications. *Phys. Rev. B* **2015**, *92* (1). <https://doi.org/10.1103/PhysRevB.92.014101>.
- (30) Botti, S.; Flores-Livas, J. A.; Amsler, M.; Goedecker, S.; Marques, M. A. L. Low-Energy Silicon Allotropes with Strong Absorption in the Visible for Photovoltaic Applications. *Phys. Rev. B* **2012**, *86* (12), 121204. <https://doi.org/10.1103/PhysRevB.86.121204>.
- (31) Zhang, P.; Crespi, V. H.; Chang, E.; Louie, S. G.; Cohen, M. L. Computational Design of Direct-Bandgap Semiconductors That Lattice-Match Silicon. *Nature* **2001**, *409* (6816), 69–71. <https://doi.org/10.1038/35051054>.

- (32) Needs, R. J.; Mujica, A. First-Principles Pseudopotential Study of the Structural Phases of Silicon. *Phys. Rev. B* **1995**, *51* (15), 9652–9660. <https://doi.org/10.1103/PhysRevB.51.9652>.
- (33) Mujica, A.; Rubio, A.; Muñoz, A.; Needs, R. J. High-Pressure Phases of Group-IV, III–V, and II–VI Compounds. *Rev. Mod. Phys.* **2003**, *75* (3), 863–912. <https://doi.org/10.1103/RevModPhys.75.863>.
- (34) Gaál-Nagy, K.; Strauch, D. Transition Pressures and Enthalpy Barriers for the Cubic Diamond \rightarrow β -Tin Transition in Si and Ge under Nonhydrostatic Conditions. *Phys. Rev. B* **2006**, *73* (13). <https://doi.org/10.1103/PhysRevB.73.134101>.
- (35) Piltz, R. O.; Maclean, J. R.; Clark, S. J.; Ackland, G. J.; Hatton, P. D.; Crain, J. Structure and Properties of Silicon XII: A Complex Tetrahedrally Bonded Phase. *Phys. Rev. B* **1995**, *52* (6), 4072–4085. <https://doi.org/10.1103/PhysRevB.52.4072>.
- (36) Crain, J.; Ackland, G. J.; Maclean, J. R.; Piltz, R. O.; Hatton, P. D.; Pawley, G. S. Reversible Pressure-Induced Structural Transitions between Metastable Phases of Silicon. *Phys. Rev. B* **1994**, *50* (17), 13043–13046. <https://doi.org/10.1103/PhysRevB.50.13043>.
- (37) Wentorf, R. H.; Kasper, J. S. Two New Forms of Silicon. *Science* **1963**, *139* (3552), 338–339. <https://doi.org/10.1126/science.139.3552.338-a>.
- (38) Besson, J. M.; Mokhtari, E. H.; Gonzalez, J.; Weill, G. Electrical Properties of Semimetallic Silicon III and Semiconductive Silicon IV at Ambient Pressure. *Phys. Rev. Lett.* **1987**, *59* (4), 473–476. <https://doi.org/10.1103/PhysRevLett.59.473>.
- (39) Zhang, H.; Liu, H.; Wei, K.; Kurakevych, O. O.; Le Godec, Y.; Liu, Z.; Martin, J.; Guerrette, M.; Nolas, G. S.; Strobel, T. A. BC8 Silicon (Si-III) Is a Narrow-Gap Semiconductor. *Phys. Rev. Lett.* **2017**, *118* (14), 146601. <https://doi.org/10.1103/PhysRevLett.118.146601>.
- (40) Kurakevych, O. O.; Le Godec, Y.; Crichton, W. A.; Guignard, J.; Strobel, T. A.; Zhang, H.; Liu, H.; Coelho Diogo, C.; Polian, A.; Menguy, N.; Juhl, S. J.; Gervais, C. Synthesis of Bulk BC8 Silicon Allotrope by Direct Transformation and Reduced-Pressure Chemical Pathways. *Inorg. Chem.* **2016**, *55* (17), 8943–8950. <https://doi.org/10.1021/acs.inorgchem.6b01443>.
- (41) Yin, M. T. Si-III (BC-8) Crystal Phase of Si and C: Structural Properties, Phase Stabilities, and Phase Transitions. *Phys. Rev. B* **1984**, *30* (4), 1773–1776. <https://doi.org/10.1103/PhysRevB.30.1773>.
- (42) Zhu, L.; Cohen, R. E.; Strobel, T. A. Phase Transition Pathway Sampling via Swarm Intelligence and Graph Theory. *J. Phys. Chem. Lett.* **2019**, *10* (17), 5019–5026. <https://doi.org/10.1021/acs.jpcclett.9b01715>.
- (43) Biswas, R.; Martin, R. M.; Needs, R. J.; Nielsen, O. H. Complex Tetrahedral Structures of Silicon and Carbon under Pressure. *Phys. Rev. B* **1984**, *30* (6), 3210–3213. <https://doi.org/10.1103/PhysRevB.30.3210>.
- (44) Wang, J.-T.; Chen, C.; Mizuseki, H.; Kawazoe, Y. Kinetic Origin of Divergent Decompression Pathways in Silicon and Germanium. *Phys. Rev. Lett.* **2013**, *110* (16). <https://doi.org/10.1103/PhysRevLett.110.165503>.
- (45) Raffy, C.; Furthmüller, J.; Bechstedt, F. Properties of Hexagonal Polytypes of Group-IV Elements from First-Principles Calculations. *Phys. Rev. B* **2002**, *66* (7), 075201. <https://doi.org/10.1103/PhysRevB.66.075201>.
- (46) Zhao, Y.-X.; Buehler, F.; Sites, J. R.; Spain, I. L. New Metastable Phases of Silicon. *Solid State Commun.* **1986**, *59* (10), 679–682. [https://doi.org/10.1016/0038-1098\(86\)90372-8](https://doi.org/10.1016/0038-1098(86)90372-8).

- (47) Beekman, M.; Wei, K.; Nolas, G. S. Clathrates and beyond: Low-Density Allotropy in Crystalline Silicon. *Appl. Phys. Rev.* **2016**, *3* (4), 040804. <https://doi.org/10.1063/1.4953165>.
- (48) McMillan, P. F. New Materials from High-Pressure Experiments. *Nat. Mater.* **2002**, *1* (1), 19–25. <https://doi.org/10.1038/nmat716>.
- (49) Wilson, M.; McMillan, P. F. Crystal-Liquid Phase Relations in Silicon at Negative Pressure. *Phys. Rev. Lett.* **2003**, *90* (13). <https://doi.org/10.1103/PhysRevLett.90.135703>.
- (50) Daisenberger, D.; McMillan, P. F.; Wilson, M. Crystal-Liquid Interfaces and Phase Relations in Stable and Metastable Silicon at Positive and Negative Pressure. *Phys. Rev. B* **2010**, *82* (21). <https://doi.org/10.1103/PhysRevB.82.214101>.
- (51) Karttunen, A. J.; Fässler, T. F.; Linnolahti, M.; Pakkanen, T. A. Structural Principles of Semiconducting Group 14 Clathrate Frameworks. *Inorg. Chem.* **2011**, *50* (5), 1733–1742. <https://doi.org/10.1021/ic102178d>.
- (52) Krishna, L.; Martinez, A. D.; Baranowski, L. L.; Brawand, N. P.; Koh, C. A.; Stevanovic, V.; Lusk, M. T.; Toberer, E. S.; Tamboli, A. C. Group IV Clathrates: Synthesis, Optoelectronic Properties, and Photovoltaic Applications; Freundlich, A., Guillemoles, J.-F., Eds.; 2014; p 898108. <https://doi.org/10.1117/12.2040056>.
- (53) Adams, G. B.; O’Keeffe, M.; Demkov, A. A.; Sankey, O. F.; Huang, Y.-M. Wide-Band-Gap Si in Open Fourfold-Coordinated Clathrate Structures. *Phys. Rev. B* **1994**, *49* (12), 8048–8053. <https://doi.org/10.1103/PhysRevB.49.8048>.
- (54) Gryko, J.; McMillan, P. F.; Marzke, R. F.; Ramachandran, G. K.; Patton, D.; Deb, S. K.; Sankey, O. F. Low-Density Framework Form of Crystalline Silicon with a Wide Optical Band Gap. *Phys. Rev. B* **2000**, *62* (12), R7707–R7710. <https://doi.org/10.1103/PhysRevB.62.R7707>.
- (55) Blase, X. Quasiparticle Band Structure and Screening in Silicon and Carbon Clathrates. *Phys. Rev. B* **2003**, *67* (3). <https://doi.org/10.1103/PhysRevB.67.035211>.
- (56) Moriguchi, K.; Munetoh, S.; Shintani, A. First-Principles Study of Si_{34-x}Ge_x Clathrates: Direct Wide-Gap Semiconductors in Si-Ge Alloys. *Phys. Rev. B* **2000**, *62* (11), 7138–7143. <https://doi.org/10.1103/PhysRevB.62.7138>.
- (57) Mahammedi, N. A.; Ferhat, M.; Tsumuraya, T.; Chikyow, T. Prediction of Optically-Active Transitions in Type-VIII Guest-Free Silicon Clathrate Si₄₆: A Comparative Study of Its Physical Properties with Type-I Counterpart through First-Principles. *J. Appl. Phys.* **2017**, *122* (20), 205103. <https://doi.org/10.1063/1.4999985>.
- (58) Kasper, J. S.; Hagemuller, P.; Pouchard, M.; Cros, C. Clathrate Structure of Silicon Na₈Si₄₆ and Na_xSi₁₃₆ (x < 11). *Science* **1965**, *150* (3704), 1713–1714. <https://doi.org/10.1126/science.150.3704.1713>.
- (59) Kurakevych, O. O.; Strobel, T. A.; Kim, D. Y.; Muramatsu, T.; Struzhkin, V. V. Na-Si Clathrates Are High-Pressure Phases: A Melt-Based Route to Control Stoichiometry and Properties. *Cryst. Growth Des.* **2013**, *13* (1), 303–307. <https://doi.org/10.1021/cg3017084>.
- (60) Kim, D. Y.; Stefanoski, S.; Kurakevych, O. O.; Strobel, T. A. Synthesis of an Open-Framework Allotrope of Silicon. *Nat. Mater.* **2014**, *14* (2), 169–173. <https://doi.org/10.1038/nmat4140>.
- (61) Guerette, M.; Ward, M. D.; Lokshin, K. A.; Wong, A. T.; Zhang, H.; Stefanoski, S.; Kurakevych, O.; Le Godec, Y.; Juhl, S. J.; Alem, N.; Fei, Y.; Strobel, T. A. Synthesis and Properties of Single-Crystalline Na₄Si₂₄. *Cryst. Growth Des.* **2018**, *18* (12), 7410–7418. <https://doi.org/10.1021/acs.cgd.8b01099>.

- (62) Ramachandran, G. K.; McMillan, P. F.; Dong, J.; Sankey, O. F. K_{7.62}(1)Si₄₆ and Rb_{6.15}(2)Si₄₆: Two Structure I Clathrates with Fully Occupied Framework Sites. *J. Solid State Chem.* **2000**, *154* (2), 626–634. <https://doi.org/10.1006/jssc.2000.8906>.
- (63) Stefanoski, S.; Nolas, G. S. Synthesis and Structural Characterization of Single-Crystal K_{7.5}Si₄₆ and K_{17.8}Si₁₃₆ Clathrates. *Cryst. Growth Des.* **2011**, *11* (10), 4533–4537. <https://doi.org/10.1021/cg200756r>.
- (64) Yamanaka, S.; Enishi, E.; Fukuoka, H.; Yasukawa, M. High-Pressure Synthesis of a New Silicon Clathrate Superconductor, Ba₈Si₄₆. *Inorg. Chem.* **2000**, *39* (1), 56–58. <https://doi.org/10.1021/ic990778p>.
- (65) Jung, W.; Löhrincz, J.; Ramlau, R.; Borrmann, H.; Prots, Y.; Haarmann, F.; Schnelle, W.; Burkhardt, U.; Baitinger, M.; Grin, Y. K₇B₇Si₃₉, a Borosilicide with the Clathrate I Structure. *Angew. Chem. Int. Ed.* **2007**, *46* (35), 6725–6728. <https://doi.org/10.1002/anie.200701028>.
- (66) Kröner, R.; Peters, K.; Schnering, H. G. von; Nesper, R. Crystal Structure of the Clathrates K₈Ga₈S₃₈ and K₈Ga₈Sn₃₈. *Z. Für Krist. - New Cryst. Struct.* **1998**, *213* (1–4). <https://doi.org/10.1524/ncrs.1998.213.14.707>.
- (67) Bradby, J. E.; Williams, J. S.; Wong-Leung, J.; Swain, M. V.; Munroe, P. Transmission Electron Microscopy Observation of Deformation Microstructure under Spherical Indentation in Silicon. *Appl. Phys. Lett.* **2000**, *77* (23), 3749–3751. <https://doi.org/10.1063/1.1332110>.
- (68) Gerk, A. P.; Tabor, D. Indentation Hardness and Semiconductor–Metal Transition of Germanium and Silicon. *Nature* **1978**, *271* (5647), 732–733. <https://doi.org/10.1038/271732a0>.
- (69) Kailer, A.; Nickel, K. G.; Gogotsi, Y. G. Raman Microspectroscopy of Nanocrystalline and Amorphous Phases in Hardness Indentations. *J. Raman Spectrosc.* **1999**, *30* (10), 939–946. [https://doi.org/10.1002/\(SICI\)1097-4555\(199910\)30:10<939::AID-JRS460>3.0.CO;2-C](https://doi.org/10.1002/(SICI)1097-4555(199910)30:10<939::AID-JRS460>3.0.CO;2-C).
- (70) Pharr, G. M.; Oliver, W. C.; Harding, D. S. New Evidence for a Pressure-Induced Phase Transformation during the Indentation of Silicon. *J. Mater. Res.* **1991**, *6* (6), 1129–1130. <https://doi.org/10.1557/JMR.1991.1129>.
- (71) Weppelmann, E. R.; Field, J. S.; Swain, M. V. Observation, Analysis, and Simulation of the Hysteresis of Silicon Using Ultra-Micro-Indentation with Spherical Indenters. *J. Mater. Res.* **1993**, *8* (4), 830–840. <https://doi.org/10.1557/JMR.1993.0830>.
- (72) Jiapeng, S.; Cheng, L.; Han, J.; Ma, A.; Fang, L. Nanoindentation Induced Deformation and Pop-in Events in a Silicon Crystal: Molecular Dynamics Simulation and Experiment. *Sci. Rep.* **2017**, *7* (1). <https://doi.org/10.1038/s41598-017-11130-2>.
- (73) Wong, S.; Haberl, B.; Johnson, B. C.; Mujica, A.; Guthrie, M.; McCallum, J. C.; Williams, J. S.; Bradby, J. E. Formation of an R8-Dominant Si Material. *Phys. Rev. Lett.* **2019**, *122* (10). <https://doi.org/10.1103/PhysRevLett.122.105701>.
- (74) Ruffell, S.; Haberl, B.; Koenig, S.; Bradby, J. E.; Williams, J. S. Annealing of Nanoindentation-Induced High Pressure Crystalline Phases Created in Crystalline and Amorphous Silicon. *J. Appl. Phys.* **2009**, *105* (9), 093513. <https://doi.org/10.1063/1.3124366>.
- (75) Bradby, J. E.; Williams, J. S.; Swain, M. V. *In Situ* Electrical Characterization of Phase Transformations in Si during Indentation. *Phys. Rev. B* **2003**, *67* (8). <https://doi.org/10.1103/PhysRevB.67.085205>.
- (76) Clarke, D. R.; Kroll, M. C.; Kirchner, P. D.; Cook, R. F.; Hockey, B. J. Amorphization and Conductivity of Silicon and Germanium Induced by Indentation. *Phys. Rev. Lett.* **1988**, *60* (21), 2156–2159. <https://doi.org/10.1103/PhysRevLett.60.2156>.

- (77) Ruffell, S.; Sears, K.; Knights, A. P.; Bradby, J. E.; Williams, J. S. Experimental Evidence for Semiconducting Behavior of Si-XII. *Phys. Rev. B* **2011**, *83* (7). <https://doi.org/10.1103/PhysRevB.83.075316>.
- (78) Haberl, B.; Guthrie, M.; Sinogeikin, S. V.; Shen, G.; Williams, J. S.; Bradby, J. E. Thermal Evolution of the Metastable R8 and Bc8 Polymorphs of Silicon. *High Press. Res.* **2015**, *35* (2), 99–116. <https://doi.org/10.1080/08957959.2014.1003555>.
- (79) Ge, D.; Domnich, V.; Gogotsi, Y. Thermal Stability of Metastable Silicon Phases Produced by Nanoindentation. *J. Appl. Phys.* **2004**, *95* (5), 2725–2731. <https://doi.org/10.1063/1.1642739>.
- (80) McBride, E. E.; Krygier, A.; Ehnes, A.; Galtier, E.; Harmand, M.; Konôpková, Z.; Lee, H. J.; Liermann, H.-P.; Nagler, B.; Pelka, A.; Rödel, M.; Schropp, A.; Smith, R. F.; Spindloe, C.; Swift, D.; Tavella, F.; Toleikis, S.; Tschentscher, T.; Wark, J. S.; Higginbotham, A. Phase Transition Lowering in Dynamically Compressed Silicon. *Nat. Phys.* **2019**, *15* (1), 89–94. <https://doi.org/10.1038/s41567-018-0290-x>.
- (81) Smith, R. F.; Bolme, C. A.; Erskine, D. J.; Celliers, P. M.; Ali, S.; Eggert, J. H.; Brygoo, S. L.; Hammel, B. D.; Wang, J.; Collins, G. W. Heterogeneous Flow and Brittle Failure in Shock-Compressed Silicon. *J. Appl. Phys.* **2013**, *114* (13), 133504. <https://doi.org/10.1063/1.4820927>.
- (82) Tsujino, Masashi; Sano, T.; Sakata, O.; Ozaki, N.; Kimura, S.; Takeda, S.; Okoshi, M.; Inoue, N.; Kodama, R.; Kobayashi, K. F.; Hirose, A. Synthesis of Submicron Metastable Phase of Silicon Using Femtosecond Laser-Driven Shock Wave. *J. Appl. Phys.* **2011**, *110* (12), 126103. <https://doi.org/10.1063/1.3673591>.
- (83) Turneure, S. J.; Sinclair, N.; Gupta, Y. M. Real-Time Examination of Atomistic Mechanisms during Shock-Induced Structural Transformation in Silicon. *Phys. Rev. Lett.* **2016**, *117* (4). <https://doi.org/10.1103/PhysRevLett.117.045502>.
- (84) Verburg, P. C.; Smillie, L. A.; Römer, G. R. B. E.; Haberl, B.; Bradby, J. E.; Williams, J. S.; Huis in 't Veld, A. J. Crystal Structure of Laser-Induced Subsurface Modifications in Si. *Appl. Phys. A* **2015**, *120* (2), 683–691. <https://doi.org/10.1007/s00339-015-9238-5>.
- (85) Rapp, L.; Haberl, B.; Pickard, C. J.; Bradby, J. E.; Gamaly, E. G.; Williams, J. S.; Rode, A. V. Experimental Evidence of New Tetragonal Polymorphs of Silicon Formed through Ultrafast Laser-Induced Confined Microexplosion. *Nat. Commun.* **2015**, *6*, 7555. <https://doi.org/10.1038/ncomms8555>.

Chapter 2:

Silicon under static high-pressure: state of the art

Silicon has been studied for decades, and its behaviour under high-pressure has attracted much attention because of the rich phase diagram and the numerous new allotropes that have been discovered. This chapter will present a brief summary of the main studies of Si phase diagram and their outcomes. After an overview of Si high-pressure phases, past experiments up to 15-20 GPa are presented in detail. This pressure range (i.e. 0-20 GPa) is suitable for large-volume synthesis, and is thus of interest for applied material research because it enables large-scale synthesis for industrial use. Our attention is focused on the stability of Si-II because this phase plays a key role in the recovery of metastable Si-III, Si-IV or Si-XII, as mentioned in the previous Chapter 1. Si-II is difficult to stabilize at ambient temperature, and analysis of previous results arises some questions on the topology of the phase diagram. After discussing the experiments at ambient temperature and high-temperature conditions separately, theoretical results are briefly presented and compared with experimental ones.

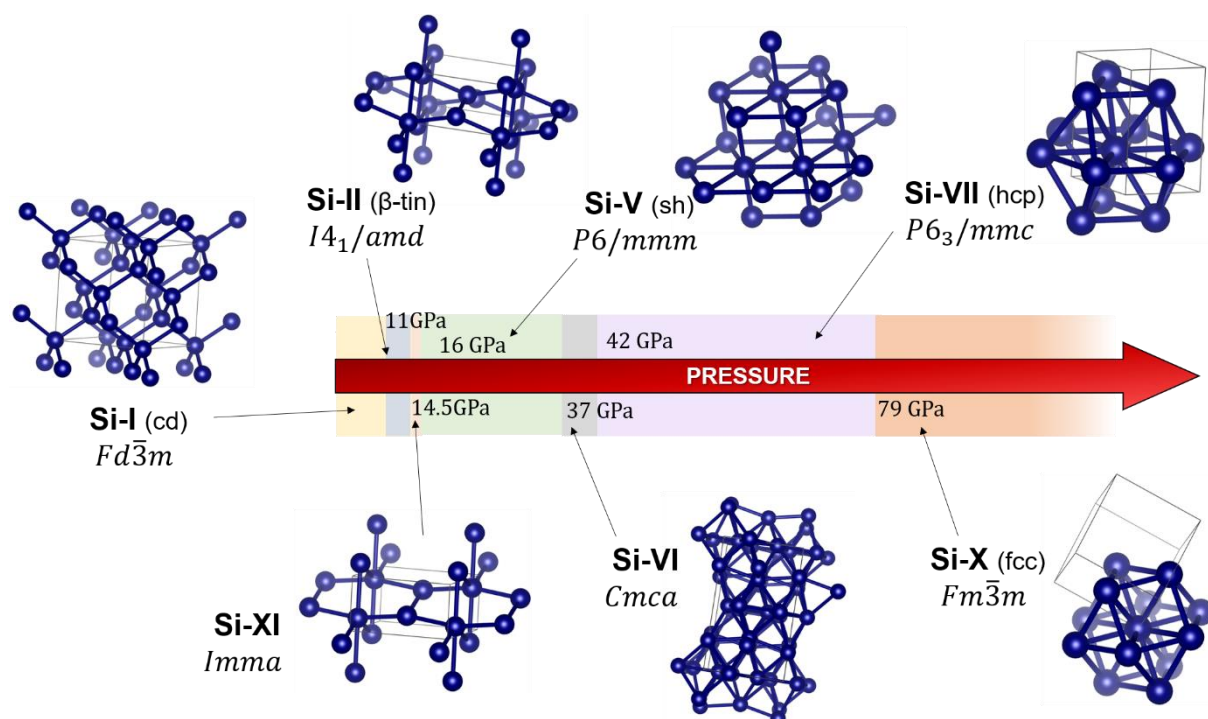


Figure 2.1 : High-pressure phases of Si. For each phase name, space group and pressure formation at ambient temperature (as determined by experiments) are reported.

2.1 Overview of high-pressure phases of Si

Silicon under high pressure undergoes a number of phase transitions. Researchers have identified several high-pressure allotropes and resolved their structures^{1,2}. Figure 2.1 shows the phases encountered upon increasing pressure. For each allotrope, the name, space group and formation pressure at ambient temperature are given.

The structures assumed by Si under pressures up to 100 GPa (Figure 2.1) are:

1. Si-I

At ambient conditions, Si assumes its globally stable phase with a cubic diamond (cd) structure and is an indirect band-gap semiconductor³. The atoms are hybridized in the sp^3 configuration and covalently bonded, resulting in fourfold coordinated atoms.

2. Si-II

Upon compression of Si-I, the first phase that forms is tetragonal Si-II, with β -tin structure and metallic behaviour. Coordination is increased to approximately 6 (4 nearest neighbours and two atoms at slightly longer distance). The Si-I \rightarrow Si-II is a so-called *reconstructive transition*¹, which means that it involves major changes in the structure, with the breaking and rearrangement of atomic bonds. The intermediate state, in which the covalent bonds are broken, is a high-energy state; this, together with the large drop of volume ($\geq 20\%$, strongly pronounced first-order phase transition) causes a large kinetic barrier (~ 0.2 eV/atom^{4,5}) between the two phases. The Si-I \rightarrow Si-II transition pressures reported in the literature are contradictory both in theoretical studies⁶⁻¹³ and in experiments¹⁴⁻¹⁸. Such inconsistencies were attributed to the large kinetic barrier associated with the Si-I \rightarrow Si-II transition. More details on the transitions from Si-I to Si-II can be found in Section 2.2.

3. Si-XI

The existence of an orthorhombic *Imma* phase obtained by compression of β -tin Si has been first reported in 1994^{16,19}. This phase appears around 13.5 GPa and remains stable up to 16 GPa. Si-XI's *Imma* structure defines a deformation path from the tetragonal β -tin (\sim sixfold coordination) and the simple hexagonal (\sim eightfold coordination) allotropes. Both the tetragonal and the hexagonal phases can be

described in the orthorhombic cell, and they can transition to the *Imma* phase via continuous distortion of their cell parameters.

4. **Si-V**

In the range 16-37 GPa, the simple hexagonal (sh) Si-V allotrope is stable. It has a primitive lattice and ~8-fold coordination; after its first observation¹⁵, the existence of this phase was confirmed by later experiments¹⁷⁻²¹.

5. **Si-VI**

Olijnyk et al.¹⁵ reported the existence of an intermediate phase between the simple hexagonal and the close-packed one around 37 GPa, Si-VI; the structure of this phase was successively refined by Hanfland et al.²². Si-VI has a based-centered orthorhombic structure with space group *Cmca* and is 10-fold coordinated; it remains stable up to ~42 GPa.

6. **Si-VII**

The hexagonal-close-packed (hcp) phase of Si has been observed in the range ~ 42-79 GPa²¹ and can be seen as an ABAB stacking of hexagonal planes with 12-fold coordination.

7. **Si-X**

Si-X has a face-centred cubic (fcc) structure, and has been reported to be stable up to 243 GPa^{21,23}. The fcc structure can be described as a hexagonal-packed structure, with ABC stacking. Recent calculations have predicted further transitions to bulk-centred cubic (bcc) and simple cubic (sc) at 2.87 and 3.89 TPa²⁴ respectively, but up to now such pressures have not been attained experimentally.

2.2 Silicon phase diagram: *in-situ* studies

The first pioneering study on Si at high-pressure was conducted by Minomura and Drickamer in 1962²⁵. Previous experiments had already investigated the influence of pressure on the electronic band-structure. They reported a redshift of the bandgap of Si²⁶ with increasing pressure and, following the trend, metallic behaviour was expected over 60 GPa. Minomura and Drickamer performed *in-situ* electrical measurements under high pressure²⁷ and detected an abrupt drop in electrical resistance at an estimated pressure of 20 GPa^c. Such a drop in

^c The pressure scale used by Minomura and Drickamer is no longer in use, and overestimates the pressure compared to the current commonly accepted one. Correction of the reported pressure values is beyond the scope of this summary.

resistance was in contrast with the predicted smooth decrease of the bandgap energy and was thus interpreted as the first signature of a high-pressure transition to a metallic state.

Since this first claim, Si behaviour under high-pressure has been extensively studied using different *in-situ* experimental techniques, and several high-pressure phases have been discovered. The main results in the range up to 15-20 GPa are discussed in the following: ambient temperature and high temperature experiments are presented separately, and a brief overview of theoretical results is provided.

2.2.1 Phase transformations up to 20 GPa

In this section, previous studies on Si phase transitions up to 20 GPa are discussed. All the experiments presented here were conducted at ambient temperature, and their outcomes are summarized in Figure 2.2. The results are reported chronologically (from top to bottom) to demonstrate the progress in determining Si phase diagram at room temperature. Refinement of the phase diagram has been observed as the precision of *in-situ* techniques and the degree of hydrostaticity of the experiments increased.

Since it was first reported, the onset pressure for Si metallization proposed in 1962 (~20 GPa²⁵) has been revised. In 1963, Jamieson used Bridgman's curve²⁸ to calibrate pressure, estimating a lower transition onset, around 16 GPa²⁹. Similar results were also found by Wentorf and Kasper³⁰. The use of Diamond Anvil Cells (DACs) enabled researchers to characterize the transition by *in-situ* spectroscopy, with pressure calibration via ruby fluorescence. In these experiments the semiconductor-to-metal transition is identified by the transition to an opaque phase, i.e. a phase with an absorption threshold lower than the Si-I's one. In 1975, both Weinstein and Piermarini³¹ (which observed a sudden decay of Raman peaks' intensities with pressure) and Welber et al.³² (who measures absorption spectra in the range [0.61-4.10] eV) reported Si metallization pressures of approximately 12.5 GPa. Gupta et al.¹⁴ suggested that the transition pressure is affected also by the anisotropic response of Si, reporting a lower onset for compression along the [111] direction. The observed threshold variability in these early studies was ultimately explained by the strong sensitivity of Si to shear forces, i.e. in the presence of stress the transition pressure was lowered because of the non-hydrostatic conditions.

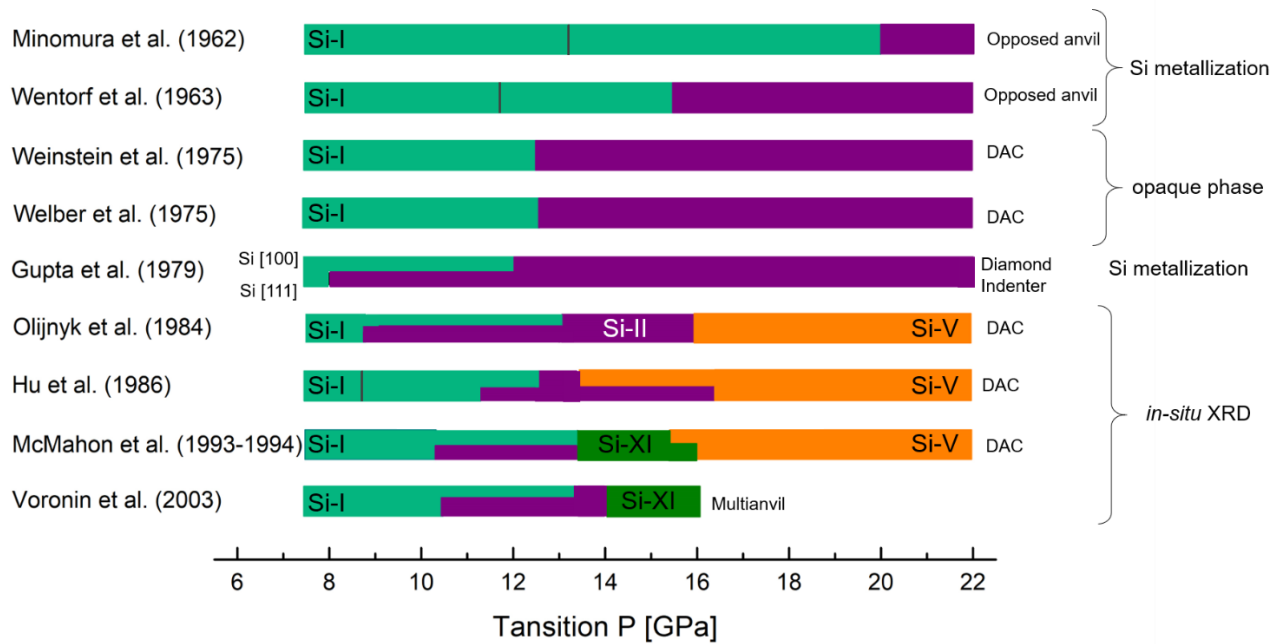


Figure 2.2 : Experimental results showing the Si phase transitions at high-pressure, presented in chronological order. Each colour corresponds to the stable phase observed for each pressure. When coexistence was observed, two colours are shown for that pressure. The only exception is the indentation study by Gupta et al.¹⁴, for which the horizontal division corresponds to the different orientation of the Si indented surfaces. The advent of high-pressure *in-situ* XRD allowed to characterize not only the structure of different high-pressure allotropes, but also the extension of coexistence domains. For each work, the high-pressure apparatus as well as the *in-situ* characterization used to detect phase transition are indicated. The vertical bars (|) indicate whether in the study Si-I→Si-II transition has been observed also at pressures lower than the reported onset.

In principle, Si metallization could happen either via a solid-to-solid phase transition or via melting. The existence of a solid-to-solid transition was proven only one year after Minomura's study. In 1963, Jamieson was the first to collect *in-situ* high-pressure XRD and reported a solid high-pressure phase, Si-II, with structure analogous to white tin, i.e. β -tin²⁹. With the advent of synchrotron sources and the spread of *in-situ* high-pressure XRD, it was possible to obtain additional information on the Si phase diagram and on the Si-I→Si-II transition dynamics. Figure 2.3 compares the results of Minomura and Drickamer²⁵ with more recent *in-situ* XRD experiments by Voronin et al¹⁷. *In-situ* structural characterization enables us, for example, to observe the coexistence of different phases during the transition. Thanks to this capability, researchers observed that Si-I→Si-II is a sluggish transition, and it takes place over a relatively large pressure interval of ~ 3 GPa^{15-17,19,20,33} at room temperature. The large coexistence interval could account for the variability of the transition pressures reported from electrical or optical characterization, for which a defined pressure threshold was reported. Observations of pure Si-II via XRD are quite rare, which may suggest that its stability region

is very narrow. The most recent studies in quasi-hydrostatic conditions (DAC with He pressure-transmitting medium¹⁸) question the possibility of observing pure Si-II at ambient temperature.

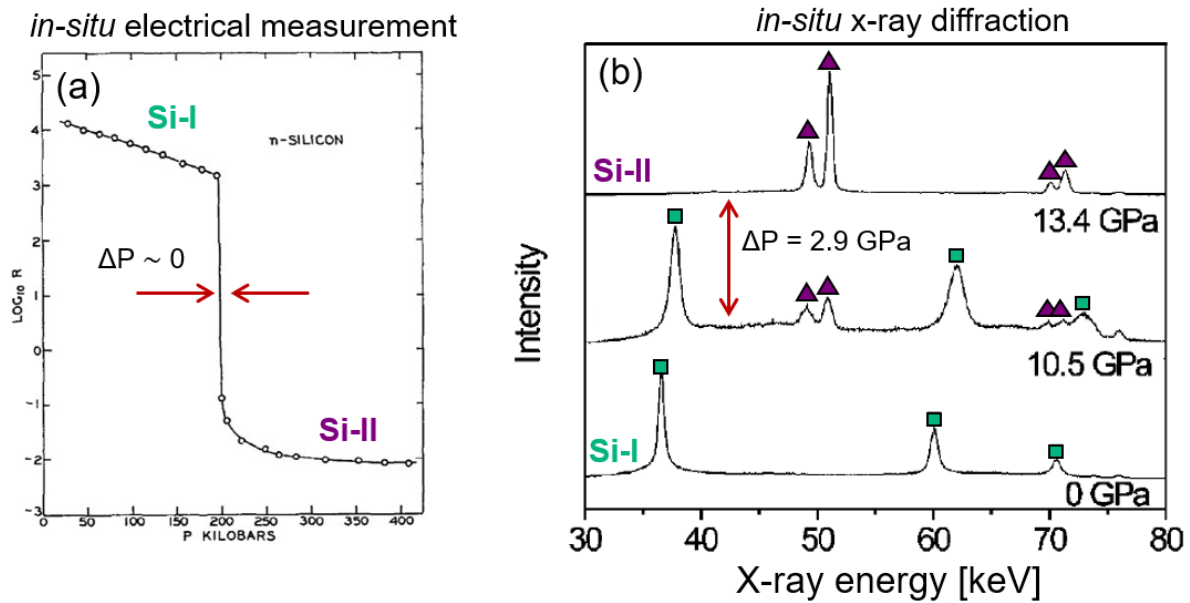


Figure 2.3 : Comparison between electrical and structural x-rays characterization under pressure. (a) Minomura's *in-situ* resistance measurements of *n*-doped Si under pressure. The transition was detected as a drop of several order of magnitude of the resistance. (b) *in-situ* XRD pattern showing the coexistence region, with Si-I peaks (\square) and Si-II ones (\triangle) present. Figures adapted from ²⁵ and ¹⁷.

The advent of *in-situ* XRD experiments allowed researchers to identify the phases appearing after Si metallization (i.e. Si-I \rightarrow Si-II). The experiments by Olijnyk et al. ¹⁵, Hu et al. ²⁰ and Duclos et al. ²¹ characterized structural transitions up to 250 GPa at ambient temperature. In the range of interest (i.e. up to \sim 20 GPa), they reported a phase transition to a simple hexagonal phase Si-V at around 16 GPa. Only with the higher resolution provided by angle-dispersive-XRD (AD-XRD) experiments, McMahon et al ¹⁹ could provide evidence of an intermediate phase between Si-II and Si-V. The intermediate phase, orthorhombic Si-XI, appears around 13.5-14 GPa, where splitting of Si-II reflections was observed. Indeed, Si-XI has an *Imma* structure that is obtained by distortion of the tetragonal cell parameters $a_{\beta-tin} = b_{\beta-tin} \rightarrow a_{Imma} \neq b_{Imma}$. The existence of an *Imma* phase had already been predicted by first-principle calculations ³⁴ but, since the energies of Si-II, Si-XI and Si-V are very close, computations fail to establish precise stability and transition pressures ^{34,35}. The phase sequence Si-I \rightarrow Si-II (β -tin) \rightarrow Si-XII (*Imma*) \rightarrow Si-V(SH) upon increasing pressure as stated by McMahon et al. was confirmed by later studies ^{17,18} (see also Appendix 2.1).

2.2.2 Combining high-pressure and high temperature: phase diagram and melting curve

In this section, we review previous high-pressure high-temperature (HP-HT) experiments to study Si pressure-temperature (P-T) phase diagram and melting curve. High temperature is an essential parameter for material synthesis as it can lower the onset of a reaction or promote the grains' growth. As discussed in Section 2.2.1, at ambient temperature there is not a consensus regarding the Si-I \rightarrow Si-II transition pressure nor on the range of coexistence of the two phases. The combination of HP-HT conditions is thus expected to facilitate the stabilization of Si-II.

Table 2.1 reports a list of representative HP-HT experiments. The first experiments determined the melting curve by *in-situ* electrical measurements^{36,37} or thermal analysis^{38,39}. Bundy et al.³⁶ and Brazhkin et al.³⁷ detected phase transitions from changes to the sample's electrical resistance. Jayaraman et al.³⁸ and Lees et al.³⁹ used thermal analysis: when energy is supplied to the sample and temperature doesn't increase, melting is taking place (i.e. the energy is converted in latent heat). More recent experiments, such as the studies by Voronin et al.¹⁷ and Kubo et al.³³, used *in-situ* XRD to characterize both the melting and the structural transitions taking place at HP-HT conditions.

Table 2.1: Selected high-pressure high-temperature experiments on Si.

Author	Apparatus	Type of Study	Maximum Pressure (GPa)	Pressure Calibration
Jayaraman ³⁸	Piston Cylinder	Thermal	5	Fixed-point Bi
Bundy ³⁶	Belt Press	Electrical	16	Fixed-points Bi,Ba,Fe,Eu,Pb
Lees ³⁹	Tetrahedral Anvil	Thermal	6	Fixed-points Bi,Tl,Ba
Brazhkin ³⁷	Toroidal Anvil	Electrical	12	Fixed-points Bi,Ba,Pb
Voronin ¹⁷	Multi-Anvil	X-Ray Diffraction	13	<i>in-situ</i> NaCl
Kubo ³³	Multi-Anvil	X-Ray Diffraction	15	<i>in-situ</i> Au+MgO

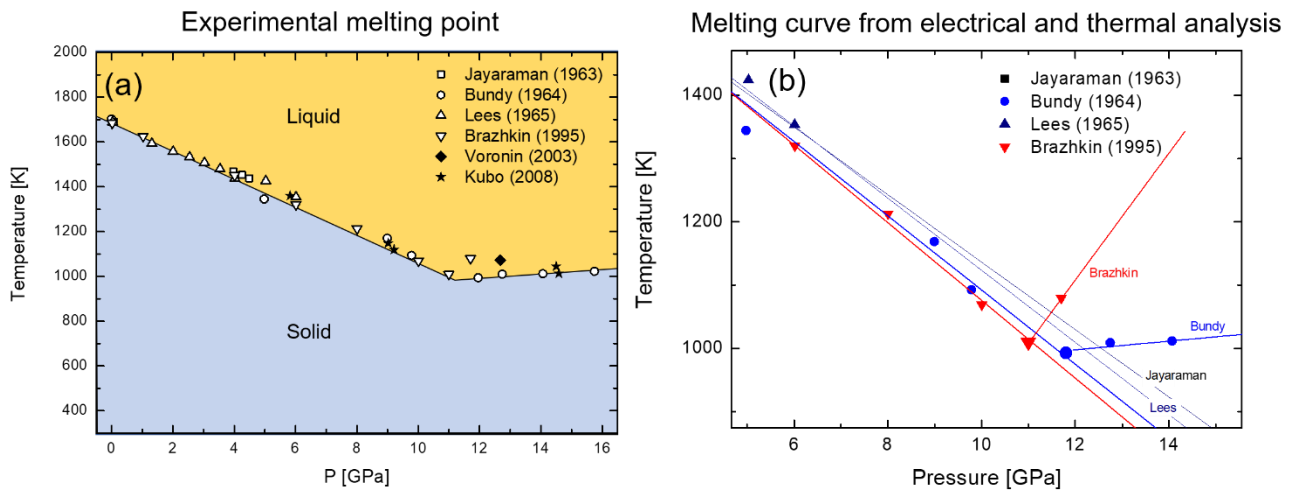


Figure 2.4 : T vs P plot showing Si melt. (a) Melting of Si with T vs P data up to 16 GPa. Black full symbols a show the experiments with *in-situ* XRD. (b) Melting points from electrical or thermal analysis only. The linear fit of the melting curve of both Si-I and high-pressure phases is shown. Crossing of the two melting lines gives the position of the extrapolated I-II-L triple points.

Figure 2.4(a) shows all the melting points from the studies in Table 2.1. A tentative melting curve is traced, and it has negative slope up to ~ 11 GPa (i.e. in the stability region of diamond-like Si-I). The slope of the melting curve depends on the relative density of the solid and the liquid phase. A negative slope implies that the liquid is denser than the solid. The change to a positive slope for $P > 11$ GPa can be thus interpreted as the onset of melting from denser phases such as Si-II or other high-pressure allotropes.

On the melting curve, the experimental points obtained via thermal or electrical measurements may have large uncertainties in the pressure determination. In these studies, pressure was calibrated using known transitions at ambient temperature and was assumed to remain constant upon increasing temperature^{36–39}. Such approximations can yield significant error above 10 GPa, where the dense allotrope Si-II is formed with a volume decrease of $\sim 22\%$. The temperatures for melting, however, were precisely determined using thermocouples^{36–39}. Figure 2.4(b) shows the melting curve of Si as determined by thermal and electrical measurements; proposed melting lines and triple points are represented (see also Table 2.2). It should be stressed that, despite the pressure uncertainty, all the melting points follow a similar trend up to 10 GPa. The slopes of Si-I melting lines vary over a range of $\pm 6\%$ ^d and are consistent with one another (Table 2.2). The uncertainty becomes more important at higher pressures, where the Si-I \rightarrow Si-II transition takes place. The melting slope at high-pressure is strongly

^d The relative dispersion range has been calculated as the standard deviation of all the low-P melting slopes reported in Table 2.2, normalized by the average slope.

affected by such uncertainties, as demonstrated by the large difference between the curves proposed by Bundy et al.³⁶ and Brazhkin et al.³⁷, which reported Si-II melting slopes of +6.8 K/GPa and +100.3 K/GPa respectively.

Figure 2.5 shows *in-situ* XRD data and a tentative phase diagram. For completeness, the room temperature experiments described in section 2.2.1 are also included. Performing *in-situ* XRD allows us to characterize the structural changes at HP-HT, determining phase boundaries in the P-T space. Pressure may also be measured in real time using a calibrant with known equation of state, assuring higher precision on the melting pressure value. In recent *in-situ* experiments Voronin et al.¹⁷ reported melting of Si-XI at 12.7 GPa, while Kubo et al.³³ reported melting of Si-XI and Si-V at very close conditions around 14.5 GPa. With so limited data points, the melting lines can still be estimated, with uncertainty from the lack of *in-situ* melting studies between 10 and 12 GPa. This range is important for the determination of the melting slope of the high-pressure phases, and for the location of the I-II-L triple point. The I-II-L triple point is the intersection of the Si-I, Si-II and liquid stability domains, i.e. the P-T condition for which both Si-I and Si-II phases melt.

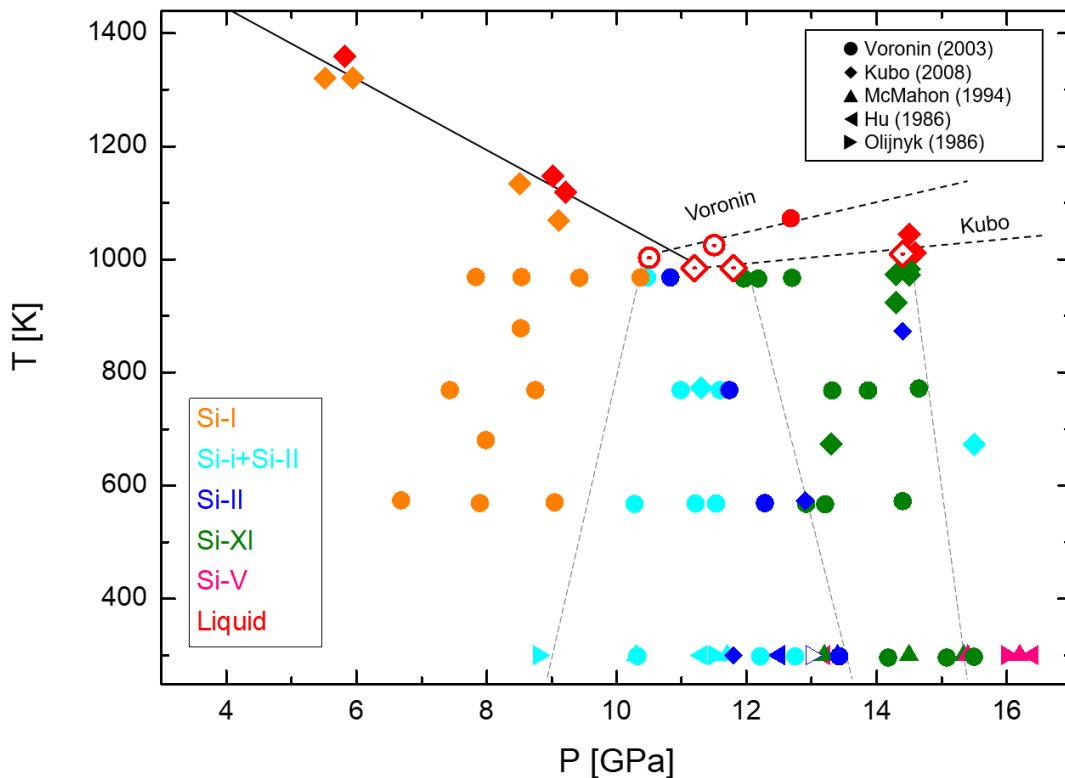


Figure 2.5 : Si P-T phase diagram from *in-situ* XRD studies. Each phase and each study are represented by a colour and a symbol respectively. Fit of the Si-I and Si-II melting curves from¹⁷ and³³ are also included. The extrapolated triple points are annotated with unfilled markers, while filled red markers indicate experimental observation of melting.

The location of the I-II-L triple point can only be extrapolated, as no direct observation has been reported. Kubo et al.³³ located the I-II-L triple point at the intersection between Si-I melting line and the I-II boundary extrapolated by their data. They used the observation of Si-II at 11.7 GPa after quench, but after quenching the conditions are not hydrostatic, and thus observation of a pure phase should not be taken as a proof of thermodynamic equilibrium. Voronin et al.¹⁷ reported series of isothermal compression and decompression ramps, from which they extrapolated I-II phase boundary. Like in previous reports, a large coexistence region ($\Delta P \sim 3$ GPa) was observed at room temperature. The effect of high-temperature is to decrease the coexistence range to $\Delta P \sim 0.3$ GPa at 973K, which constrained the I-II phase boundary with a good confidence. The I-II-L point was located at the intersection between the I-II phase boundary and the Si-I melting line.

Table 2.2 Experimental results on the melting curve of Si at high pressures and proposed triple points for I-II-L, II-XI-L and XI-V-L.

Author	Slope I-L (K/GPa)	Slope II-L (K/GPa)	Triple points	Method
Jayaraman ³⁸	-57.0			Thermal analysis up to 5 GPa
Bundy ³⁶	-58.7	+6.8	12 GPa ; 993 K (I-II-L)	Electrical measurement: slope change in melting curve
Lees ³⁹	-53.3			
Brazhkin ³⁷	-61.4	+100.3	11 GPa ; 1010 K (I-II-L)	Electrical measurement: slope change in melting curve
Voronin ¹⁷		+23	10.5 GPa; 1003 K (I-II-L)	<i>in-situ</i> XRD to constrain I-II coexistence P; T > 973 K
			11.5 GPa ; 1025 K (II-XI-L)	<i>in-situ</i> XRD to extrapolate II-XI boundary; intersection with fitted melting line
Kubo ³³	-62.3	+7.8	11.2 GPa ; 985 K (I-II-L)	Intersection of extrapolated I-II boundary and Si-I melting line
			11.8 GPa; 985 K (II-XI-L)	Intersection of extrapolated II-XI boundary and melting line
			14.4 GPa ; 1010 K (XI-V-L)	<i>in-situ</i> XRD to constrain XI-V P transition near melting

Experiments at HP-HT conditions conducted over the past years have primarily investigated the Si melting curve at high-pressure. While there is general agreement about the Si-I melting curve and its slope, results at higher pressures are contradictory and caution should be used when these data are included in the P-T phase diagram. Observations with reliable *in-situ* pressure estimation are very limited in number, thus the state-of-art phase diagram relies mostly on extrapolations. Direct observation of Si-II melting or of I-II-L triple point has not yet been attained, leaving open some questions on the topology of Si phase diagram.

2.2.3 Comparison of experimental and theoretical studies

Alongside the experimental efforts, theoretical studies have proposed several pressure-temperature phase diagrams^{24,40-44}, using different approaches. The general trends are well reproduced by calculations, but the transition pressures and temperatures are often different from the experimental values. Yang et al.⁴⁰ found through Clayperon equation results which are consistent with Bundy's dataset³⁶ (whose uncertainties in pressure determination were discussed in Section 2.2.2). Kaczmariski et al.⁴¹ used atomistic simulations, and their results are quite distant from the experimental values (i.e. Si-I→Si-II transition around 17 GPa, or I-II-L triple point 300 K higher than the one proposed by Voronin¹⁷). More recently, combined approaches have been proposed, such as Density Functional Theory (DFT)-based metadynamics by Yao et al.⁴⁴, machine-learning derived algorithms from Bartók et al.⁴³ or the combination of DFT, evolutionary algorithms and lattice dynamics used recently by Paul et al., whose results are shown in Figure 2.6²⁴. In the last study, authors have reported at 300 K the phase sequence: *cd* (Si-I) → β -tin (Si-II~12 GPa) → *Imma* (Si-XI ~14 GPa) → *sh* (Si-V~16 GPa) → *Cmca* (Si-VI~33 GPa). These calculated values are overall in good agreement with experimental data.

Nevertheless, it should be stressed that calculations are unlikely the most suited tool to resolve the controversies emerging from high-pressure studies, such as the existence and extension of Si-II thermodynamic stability region. Indeed, Si-I→Si-II is a first-order transition that implies a large volume change (>20%), thus it is difficult to define thermodynamic equilibrium between the two phases. There is also a drastic change in the electronic structure (i.e. semiconductor-to-metal) that can lead to large errors in calculating the transition pressure⁶. Over the years, various studies have been reported, and the transition pressures are often far from the experimental values and in disagreement with each other. DFT calculations have given different results depending whether they used the local density approximation (7.8 GPa⁷; 8

GPa⁸; 7.2 GPa⁴⁵; 8.2 GPa¹⁰) or the generalized gradient approximation (12.2 GPa⁹; 13.5 GPa⁴⁵; 10.2 GPa¹⁰). Quantum Monte Carlo methods have also been tested, giving results ranging between 12.6 GPa¹¹, and 16.5 GPa¹². Looking at the transitions at higher pressures, it has already been mentioned that Si-II, Si-XI (*Imma*) and Si-V (sh) have very close energy and it is thus difficult to derive the phase sequence and the transition pressures from calculations. For this reason, Si phase diagram has become a benchmark to test the validity of *ab initio* methods, rather than calculations becoming a tool to refine, validate and eventually predict Si transitions.

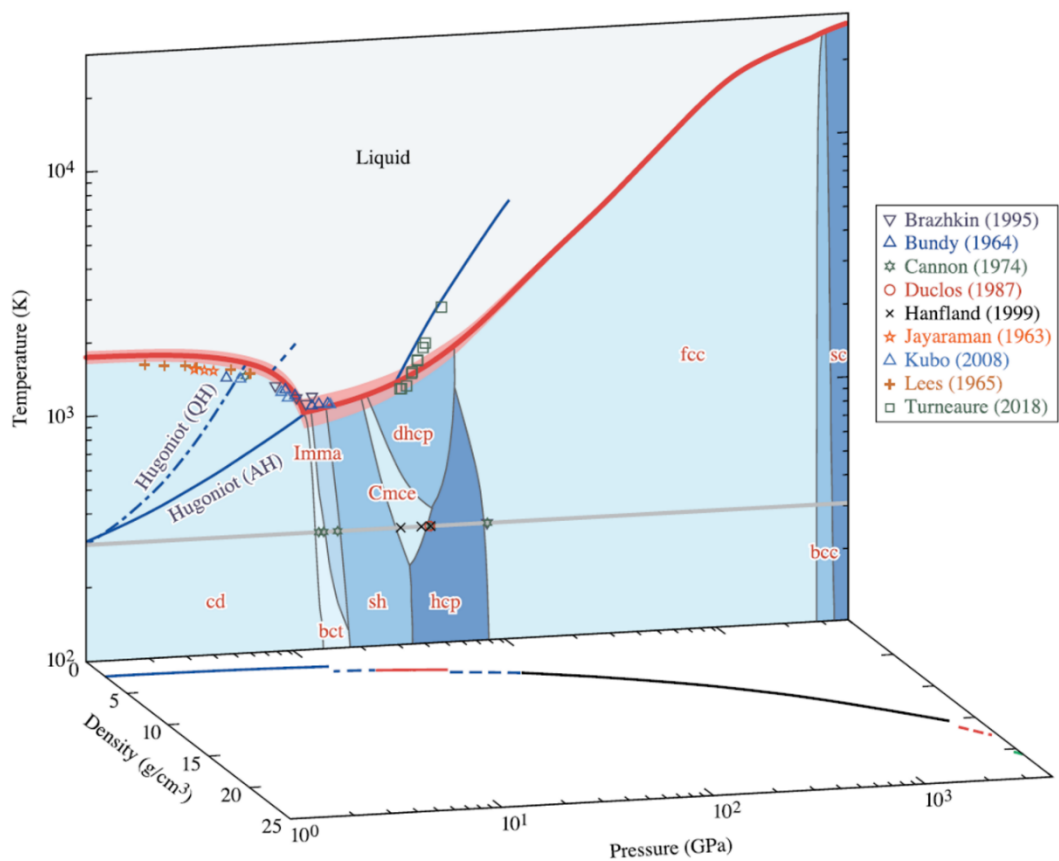


Figure 2.6: Pressure-temperature phase diagram of Si, as determined by combination of DFT, evolutionary algorithms and lattice dynamics. This new approach gives results coherent with available experimental data at ambient temperature and at melting, and it predicts two transitions above 250 GPa (fcc→bcc→sc). Figure adapted from ²⁴.

2.2.4 Conclusions

Despite decades of studies, some aspects of Si phase diagram remain unclear. The reports of Si-I→Si-II transition pressure span over 3 GPa at 300K^{14–18,20}, and Si-II has been often observed as coexisting with other phases. The melting curve at high pressures ($P > 10$

GPa) relies mostly on data with large pressure uncertainties, with a number of incoherent melting curves reported in the literature.

In such context, my thesis provides new insights and clarifies some of the critical points of Si phase diagram. Understanding of Si behaviour under extreme conditions has important implications for fundamental physics and geology, but it is also expected to have important applications in future technology. A reliable phase diagram is essential for the synthesis of new functional materials from recovery of metastable high-pressure phases. My goal is to optimize the procedure to obtain the pure phase of Si-II, which is an essential step in the synthesis of hexagonal Si allotropes for photovoltaic applications.

References Chapter 2

- (1) Mujica, A.; Rubio, A.; Muñoz, A.; Needs, R. J. High-Pressure Phases of Group-IV, III–V, and II–VI Compounds. *Rev. Mod. Phys.* **2003**, *75* (3), 863–912. <https://doi.org/10.1103/RevModPhys.75.863>.
- (2) Ackland, G. J. High-Pressure Phases of Group IV and III-V Semiconductors. *Rep. Prog. Phys.* **2001**, *64* (4), 483–516. <https://doi.org/10.1088/0034-4885/64/4/202>.
- (3) *Properties of Crystalline Silicon*; Hull, R., Institution of Electrical Engineers, Eds.; EMIS datareviews series; INSPEC: London, 1999.
- (4) Wang, J.-T.; Chen, C.; Mizuseki, H.; Kawazoe, Y. Kinetic Origin of Divergent Decompression Pathways in Silicon and Germanium. *Phys. Rev. Lett.* **2013**, *110* (16). <https://doi.org/10.1103/PhysRevLett.110.165503>.
- (5) Zhang, H.; Liu, H.; Wei, K.; Kurakevych, O. O.; Le Godec, Y.; Liu, Z.; Martin, J.; Guerrette, M.; Nolas, G. S.; Strobel, T. A. BC8 Silicon (Si-III) Is a Narrow-Gap Semiconductor. *Phys. Rev. Lett.* **2017**, *118* (14), 146601. <https://doi.org/10.1103/PhysRevLett.118.146601>.
- (6) Sorella, S.; Casula, M.; Spanu, L.; Dal Corso, A. *Ab Initio* Calculations for the β -Tin Diamond Transition in Silicon: Comparing Theories with Experiments. *Phys. Rev. B* **2011**, *83* (7). <https://doi.org/10.1103/PhysRevB.83.075119>.
- (7) Needs, R. J.; Mujica, A. First-Principles Pseudopotential Study of the Structural Phases of Silicon. *Phys. Rev. B* **1995**, *51* (15), 9652–9660. <https://doi.org/10.1103/PhysRevB.51.9652>.
- (8) Gaál-Nagy, K.; Strauch, D. Transition Pressures and Enthalpy Barriers for the Cubic Diamond \rightarrow β -Tin Transition in Si and Ge under Nonhydrostatic Conditions. *Phys. Rev. B* **2006**, *73* (13). <https://doi.org/10.1103/PhysRevB.73.134101>.
- (9) Moll, N.; Bockstedte, M.; Fuchs, M.; Pehlke, E.; Scheffler, M. Application of Generalized Gradient Approximations: The Diamond– β -Tin Phase Transition in Si and Ge. *Phys. Rev. B* **1995**, *52* (4), 2550–2556. <https://doi.org/10.1103/PhysRevB.52.2550>.
- (10) Lee, I.-H.; Martin, R. M. Applications of the Generalized-Gradient Approximation to Atoms, Clusters, and Solids. *Phys. Rev. B* **1997**, *56* (12), 7197–7205. <https://doi.org/10.1103/PhysRevB.56.7197>.
- (11) Purwanto, W.; Krakauer, H.; Zhang, S. Pressure-Induced Diamond to β -Tin Transition in Bulk Silicon: A Quantum Monte Carlo Study. *Phys. Rev. B* **2009**, *80* (21). <https://doi.org/10.1103/PhysRevB.80.214116>.
- (12) Alfè, D.; Gillan, M. J.; Towler, M. D.; Needs, R. J. Diamond and β -Tin Structures of Si Studied with Quantum Monte Carlo Calculations. *Phys. Rev. B* **2004**, *70* (21). <https://doi.org/10.1103/PhysRevB.70.214102>.
- (13) Biswas, R.; Kertesz, M. Electronic Structure and Metallization of Silicon. *Phys. Rev. B* **1984**, *29* (4), 1791–1797. <https://doi.org/10.1103/PhysRevB.29.1791>.
- (14) Gupta, M. C.; Ruoff, A. L. Static Compression of Silicon in the [100] and in the [111] Directions. *J. Appl. Phys.* **1980**, *51* (2), 1072–1075. <https://doi.org/10.1063/1.327714>.
- (15) Olijnyk, H.; Sikka, S. K.; Holzapfel, W. B. Structural Phase Transitions in Si and Ge under Pressures up to 50 GPa. *Phys. Lett. A* **1984**, *103* (3), 137–140. [https://doi.org/10.1016/0375-9601\(84\)90219-6](https://doi.org/10.1016/0375-9601(84)90219-6).
- (16) McMahon, M. I.; Nelmès, R. J. New High-Pressure Phase of Si. *Phys. Rev. B* **1993**, *47* (13), 8337–8340. <https://doi.org/10.1103/PhysRevB.47.8337>.
- (17) Voronin, G. A.; Pantea, C.; Zerda, T. W.; Wang, L.; Zhao, Y. *In Situ* x-Ray Diffraction Study of Silicon at Pressures up to 15.5 GPa and Temperatures up to 1073 K. *Phys. Rev. B* **2003**, *68* (2). <https://doi.org/10.1103/PhysRevB.68.020102>.

- (18) Anzellini, S.; Wharmby, M. T.; Miozzi, F.; Kleppe, A.; Daisenberger, D.; Wilhelm, H. Quasi-Hydrostatic Equation of State of Silicon up to 1 Megabar at Ambient Temperature. *Sci. Rep.* **2019**, *9* (1), 15537. <https://doi.org/10.1038/s41598-019-51931-1>.
- (19) McMahon, M. I.; Nelmes, R. J.; Wright, N. G.; Allan, D. R. Pressure Dependence of the *Imma* Phase of Silicon. *Phys. Rev. B* **1994**, *50* (2), 739–743. <https://doi.org/10.1103/PhysRevB.50.739>.
- (20) Hu, J. Z.; Merkle, L. D.; Menoni, C. S.; Spain, I. L. Crystal Data for High-Pressure Phases of Silicon. *Phys. Rev. B* **1986**, *34* (7), 4679–4684. <https://doi.org/10.1103/PhysRevB.34.4679>.
- (21) Duclos, S. J.; Vohra, Y. K.; Ruoff, A. L. Experimental Study of the Crystal Stability and Equation of State of Si to 248 GPa. *Phys. Rev. B* **1990**, *41* (17), 12021–12028. <https://doi.org/10.1103/PhysRevB.41.12021>.
- (22) Hanfland, M.; Schwarz, U.; Syassen, K.; Takemura, K. Crystal Structure of the High-Pressure Phase Silicon VI. *Phys. Rev. Lett.* **1999**, *82* (6), 1197–1200. <https://doi.org/10.1103/PhysRevLett.82.1197>.
- (23) Duclos, S. J.; Vohra, Y. K.; Ruoff, A. L. Hcp to Fcc Transition in Silicon at 78 GPa and Studies to 100 GPa. *Phys. Rev. Lett.* **1987**, *58* (8), 775–777. <https://doi.org/10.1103/PhysRevLett.58.775>.
- (24) Paul, R.; Hu, S. X.; Karasiev, V. V. Anharmonic and Anomalous Trends in the High-Pressure Phase Diagram of Silicon. *Phys. Rev. Lett.* **2019**, *122* (12). <https://doi.org/10.1103/PhysRevLett.122.125701>.
- (25) Minomura, S.; Drickamer, H. G. Pressure Induced Phase Transitions in Silicon, Germanium and Some III–V Compounds. *J. Phys. Chem. Solids* **1962**, *23* (5), 451–456. [https://doi.org/10.1016/0022-3697\(62\)90085-9](https://doi.org/10.1016/0022-3697(62)90085-9).
- (26) Slykhouse, T. E.; Drickamer, H. G. The Effect of Pressure on the Optical Absorption Edge of Germanium and Silicon. *J. Phys. Chem. Solids* **1958**, *7* (2–3), 210–213. [https://doi.org/10.1016/0022-3697\(58\)90263-4](https://doi.org/10.1016/0022-3697(58)90263-4).
- (27) Balchan, A. S.; Drickamer, H. G. High Pressure Electrical Resistance Cell, and Calibration Points above 100 Kilobars. *Rev. Sci. Instrum.* **1961**, *32* (3), 308–313. <https://doi.org/10.1063/1.1717350>.
- (28) Bridgman, Percy Williams. The Compression of 39 Substances to 100,000 Kg/Cm³. *Proceedings of the American Academy of Arts and Sciences*. 1948.
- (29) Jamieson, J. C. Crystal Structures at High Pressures of Metallic Modifications of Silicon and Germanium. *Science* **1963**, *139* (3556), 762–764. <https://doi.org/10.1126/science.139.3556.762>.
- (30) Wentorf, R. H.; Kasper, J. S. Two New Forms of Silicon. *Science* **1963**, *139* (3552), 338–339. <https://doi.org/10.1126/science.139.3552.338-a>.
- (31) Weinstein, B. A.; Piermarini, G. J. Raman Scattering and Phonon Dispersion in Si and GaP at Very High Pressure. *Phys. Rev. B* **1975**, *12* (4), 1172–1186. <https://doi.org/10.1103/PhysRevB.12.1172>.
- (32) Welber, B.; Kim, C. K.; Cardona, M.; Rodriguez, S. Dependence of the Indirect Energy Gap of Silicon on Hydrostatic Pressure. *Solid State Commun.* **1975**, *17* (8), 1021–1024. [https://doi.org/10.1016/0038-1098\(75\)90245-8](https://doi.org/10.1016/0038-1098(75)90245-8).
- (33) Kubo, A.; Wang, Y.; Runge, C. E.; Uchida, T.; Kiefer, B.; Nishiyama, N.; Duffy, T. S. Melting Curve of Silicon to 15GPa Determined by Two-Dimensional Angle-Dispersive Diffraction Using a Kawai-Type Apparatus with X-Ray Transparent Sintered Diamond Anvils. *J. Phys. Chem. Solids* **2008**, *69* (9), 2255–2260. <https://doi.org/10.1016/j.jpcs.2008.04.025>.

- (34) Needs, R. J.; Martin, R. M. Transition from β -Tin to Simple Hexagonal Silicon under Pressure. *Phys. Rev. B* **1984**, *30* (9), 5390–5392. <https://doi.org/10.1103/PhysRevB.30.5390>.
- (35) Lewis, S. P.; Cohen, M. L. Theoretical Study of High-Pressure Orthorhombic Silicon. *Phys. Rev. B* **1993**, *48* (21), 16144–16147. <https://doi.org/10.1103/PhysRevB.48.16144>.
- (36) Bundy, F. P. Phase Diagrams of Silicon and Germanium to 200 Kbar, 1000°C. *J. Chem. Phys.* **1964**, *41* (12), 3809–3814. <https://doi.org/10.1063/1.1725818>.
- (37) Brazhkin, V. V.; Lyapin, A. G.; Popova, S. V.; Voloshin, R. N. Nonequilibrium Phase Transitions and Amorphization in Si, Si/GaAs, Ge, and Ge/GaSb at the Decompression of High-Pressure Phases. *Phys. Rev. B* **1995**, *51* (12), 7549–7554. <https://doi.org/10.1103/PhysRevB.51.7549>.
- (38) Jayaraman, A.; Klement, W.; Kennedy, G. C. Melting and Polymorphism at High Pressures in Some Group IV Elements and III-V Compounds with the Diamond/Zincblende Structure. *Phys. Rev.* **1963**, *130* (2), 540–547. <https://doi.org/10.1103/PhysRev.130.540>.
- (39) Lees, J.; Williams, B. H. J. Combined Very High Pressure/High Temperature Calibration of the Tetrahedral Anvil Apparatus, Fusion Curves of Zinc, Aluminium, Germanium and Silicon to 60 Kilobars. *Nature* **1965**, *208* (5007), 278–279. <https://doi.org/10.1038/208278a0>.
- (40) Yang, C. C.; Li, J. C.; Jiang, Q. Temperature–Pressure Phase Diagram of Silicon Determined by Clapeyron Equation. *Solid State Commun.* **2004**, *129* (7), 437–441. <https://doi.org/10.1016/j.ssc.2003.11.020>.
- (41) Kaczmarek, M.; Bedoya-Martínez, O. N.; Hernández, E. R. Phase Diagram of Silicon from Atomistic Simulations. *Phys. Rev. Lett.* **2005**, *94* (9). <https://doi.org/10.1103/PhysRevLett.94.095701>.
- (42) Li, C.; Wang, C.; Han, J.; Yan, L.; Deng, B.; Liu, X. A Comprehensive Study of the High-Pressure–Temperature Phase Diagram of Silicon. *J. Mater. Sci.* **2018**, *53* (10), 7475–7485. <https://doi.org/10.1007/s10853-018-2087-9>.
- (43) Bartók, A. P.; Kermode, J.; Bernstein, N.; Csányi, G. Machine Learning a General-Purpose Interatomic Potential for Silicon. *Phys. Rev. X* **2018**, *8* (4). <https://doi.org/10.1103/PhysRevX.8.041048>.
- (44) Yao, Y.; Klug, D. D. Structural Phase Transitions in Si under Hydrostatic and Uniaxial Compression. *Phys. Rev. B* **2012**, *85* (21). <https://doi.org/10.1103/PhysRevB.85.214122>.
- (45) Dal Corso, A.; Pasquarello, A.; Baldereschi, A.; Car, R. Generalized-Gradient Approximations to Density-Functional Theory: A Comparative Study for Atoms and Solids. *Phys. Rev. B* **1996**, *53* (3), 1180–1185. <https://doi.org/10.1103/PhysRevB.53.1180>.

Appendix Chapter 2

Appendix 2.1: High-pressure phase transition at ambient temperature up to 20 GPa

Table 2.3: Results of high-pressure studies on Si at room temperature. All transition pressures are expressed in GPa. Si-I→Si-II (onset) column indicates the lower bound of the transition region, or the lowest pressure at which Si-II has been detected.

Author	Apparatus	Type of Study	Si-I →Si-II (onset)	Si-I →Si-II	Si-II →Si-V ^e	Si-II →Si-XI	Si-XI →Si-V
Minomura ²⁵	Opposed Anvil	Electrical	(13)	20			
Wentorf ³⁰	Opposed Anvil	Electrical	(11-12)	15-16			
Jamieson ²⁹	Opposed Anvil	AD-XRD		16			
Weinstein ³¹	Diamond Cell	Raman Scattering		12.5			
Welber ³²	Diamond Cell	Optical	11.5	12.6			
Gupta ¹⁴	Diamond Indenter	Electrical	8 Si[111]	12 Si[100]			
Olijnyk ¹⁵	Diamond Cell	ED-XRD	8.8	13	16		
Hu ²⁰	Diamond Cell	XRD	11.3 ^f	12.5	16.4		
McMahon ¹⁶	Diamond Cell	AD-XRD	10.3				15
McMahon ¹⁹	Diamond Cell	AD-XRD	11.7	13.4		13.5	15.4
Voronin ¹⁷	Multi-Anvil	ED-XRD	10.5	13.4		14.2	
Kubo ³³	Multi-Anvil	AD-XRD		11.8 ^g			

^e Si-XI phase, intermediate phase between Si-II and Si-V, has been discovered in 1993. Studies before this date did not make the distinction between Si-II and Si-XI. The data reported in this column have thus to be interpreted *a posteriori* as Si-XI→Si-V transitions.

^f The authors reported transition pressures as low as 8.5 GPa when compression was non-hydrostatic.

^g Data obtained after quenching from high temperature

Chapter 3:

Experimental techniques: *in-situ* High-Pressure Synthesis

A huge diversity of phenomena takes place at high-pressure, from life in the depth of the oceans to the dynamics of planets' interiors. The properties of matter under pressure are thus studied in diverse fields, from alimentation to material science and planetary science. High-pressure science field relies on the ability to design experiments able to reproduce high-pressure states of matter and characterize them. In this work, high-pressure experiments have been conducted primarily using multi-anvil apparatus for both *in-situ* and *ex-situ* experiments. In this chapter, a brief summary of multi-anvil high-pressure apparatus and *in-situ* synchrotron-based diffraction experiment is given.

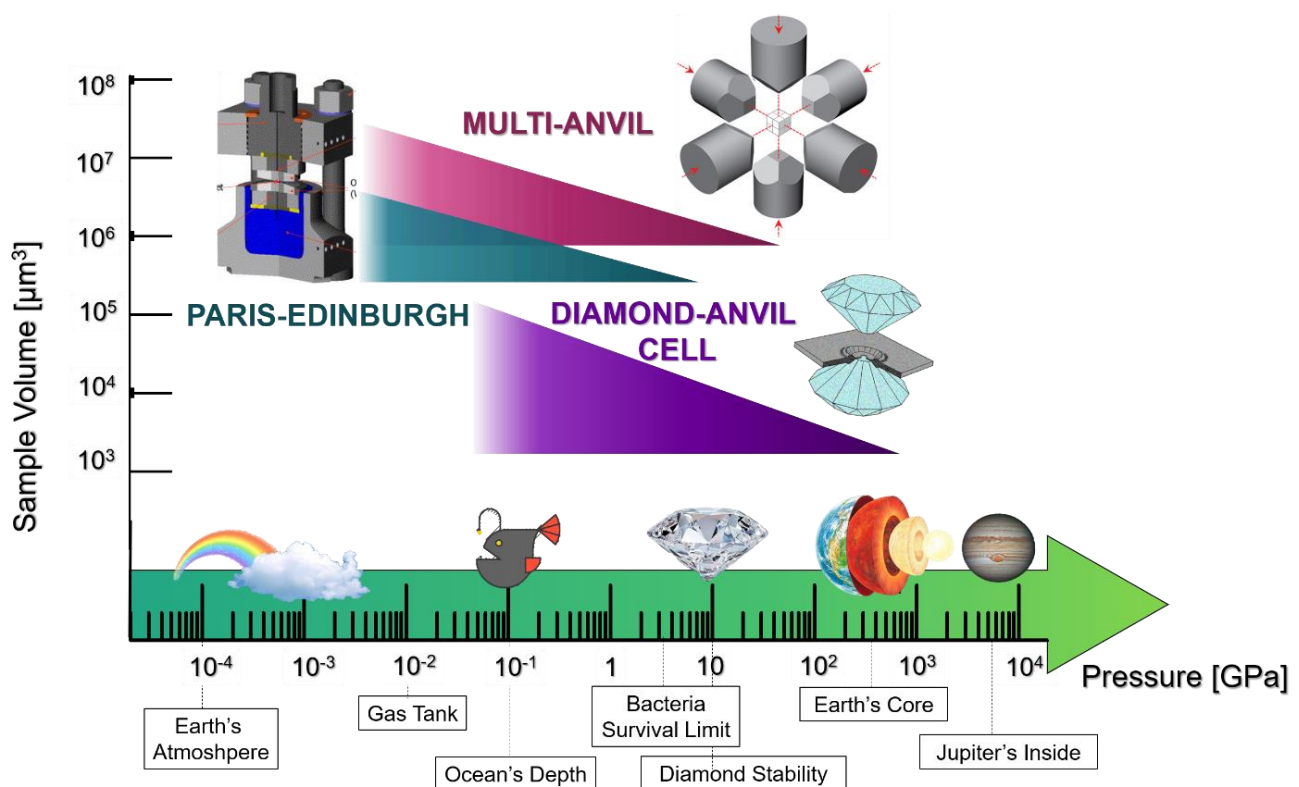


Figure 3.1 : Pressure scale, starting from the atmospheric pressure. In the lower part of the figure, natural phenomena are shown at their corresponding pressure. On the upper part of the figure, experimental capabilities for static high-pressure experiments are shown. Three different static high-pressure apparatus are represented, and the surface of the correspondent triangles shows the range of pressure attainable with each technique (along the x axis) and the sample volumes that is possible to study (along the y axis). The sample volume necessarily diminishes when we increase the pressure we want to attain.

Modern high-pressure research started at the beginning of the 20th century, with the development of the Bridgman's anvil apparatus¹, which can generate high-pressures in a laboratory-based experiment. The Bridgman anvils are made of two truncated conical pistons, with the sample compressed between the two flat surfaces. Since then, many developments have been put in place. Development of presses with increasing number of anvils and with different shapes²⁻⁴, materials⁵ has led to high-pressure techniques with various P-T capabilities as well as coupled diagnostics. Figure 3.1 shows the most-widely used static HP techniques and their range of applications, as well as the maximum volumes that can be studied⁸ in each apparatus. Diamond Anvil Cell (DAC) and Paris-Edinburgh (PE) press evolved out of the opposing anvil geometry that was developed by Bridgman, with diamond and (mainly) tungsten carbide (WC) anvils, respectively. When the number of anvils is higher, the HP apparatus is called *multi-anvil* press^{6,7}.

Despite the limited pressure range (as, for example, DACs can attain pressures higher of a factor 10), multi-anvil press is a suited apparatus for high-pressure material science. Indeed, the multi-directional compression generates more hydrostatic stress states in the sample, which facilitates the growth of crystals. The larger sample volume enables *ex-situ* physical characterization to assess the material's properties. Furthermore, high-pressure applications on industrial scale are currently limited to around 10 GPa. In the search for functional materials for large-scale production, the use of multi-anvil apparatus is not a limitation, as it covers the whole pressure range currently attainable in industries.

3.1 High-Pressure experiments with multi-anvil press

The classification of multi-anvil HP apparatus is based on the number of anvils, and thus it depends on the shape of the polyhedral space in which the pressure medium is inserted (between the anvils' truncations). Tetrahedral-, cubic- and octahedral-type presses have 4, 6 and 8 anvils respectively⁹. When the anvils are brought together, they apply a force on the pressure medium to generate high-pressure inside the assembly. Anvils can be driven either by

⁸ It has to be noted that high-pressure science is a very dynamic fields, and the attainable limits are continuously pushed forward. Furthermore, the sample volumes have to be taken only as indicative values, because they depend on the specific high-pressure cells and the P-T conditions of each experiment.

^b Experiments have been also performed using dodecahedral and icosahedral pressure media (i.e. 12 and 20 anvils respectively). Despite higher hydrostaticity, these apparatus were subject to more frequent anvils breakage, as well as more difficulties in aligning the anvils⁷.

individual ram, or by using guide blocks and applying uniaxial pressure. Alternatively, the whole system can be immersed in a fluid, and the pressure is applied by the oil or the water in the chamber. The first multi-anvil apparatuses were developed during the 1950s and 1960s: the tetrahedral apparatus by Hall in 1958⁸, with four hydraulic rams, could reach 12 GPa at room temperature. Von Platen developed a cubic apparatus with spherical anvils immersed in oil⁹, while Kawai was the first to use an octahedral apparatus¹⁰. The Kawai-type press was further developed, first by introducing an intermediate stage of compression¹¹: the octahedral pressure medium was inserted in an assembly of eight WC cubes squeezed by six spherical anvils. Subsequently, the anvils were grouped three by three and glued into a hemispherical cavity in a vessel¹². In this way, the vessels act as guide block and can be inserted into a uniaxial hydraulic press, overcoming the problems linked with the fluid chamber. The double-stage compression and octahedral Kawai-cells have been applied also in DIA apparatus, i.e. cubic press in which the force is applied by six anvils along the cubes' axis¹³.

Currently, the most commonly used multi-anvil apparatuses are the DIA and the Walker presses¹⁴. Figure 3.2 shows a schematic view of both presses. The Walker apparatus (Fig.3.2(c)) is a modification of Kawai double-stage apparatus, in which the primary anvils are six removable wedges fitted into a cylindrical system compressed by uniaxial force. The DIA apparatus (Fig.3.2(b)), as already mentioned, has six WC anvils that apply forces perpendicular to the cube's surfaces. Recently, development of deformation-DIA (D-DIA)¹⁵, with independent differential rams for upper and lower anvils, allows to apply axial strain to the material under pressure. The second stage of compression in both the DIA and Walker presses is an octahedral Kawai-cell (Fig.3.2(a)), with eight WC truncated cubic anvils. The truncations are directly in contact with the octahedral pressure medium, and by varying their size and that of the anvils it is possible to attain different pressures. The assemblies are thus defined by the octahedral edge length (OEL) and the truncation edge length (TEL). Typical OEL/TEL assemblies are: 18/11, 14/8, 10/5, 10/4 that can reach 12 mm³ at 4-10 GPa, 5-8 mm³ at 11-16 GPa, 3 mm³ at 17-21 GPa and 1 mm³ at 22-26 GPa respectively¹⁶. The main difference between the DIA and the Walker apparatus stands in the direction of the uniaxial compression exerted on the primary anvils, i.e. the [111] direction of the cube in a Walker modulus, and the [001] in a DIA one. The compression in a DIA apparatus is usually less efficient than in a Walker-type press, but DIA (and D-DIA) modulus are accessible for *in-situ* characterization. In this work, we have used a Walker press for *ex-situ* synthesis at IMPMC, while DIA or D-DIA apparatus were installed on synchrotron beamline.

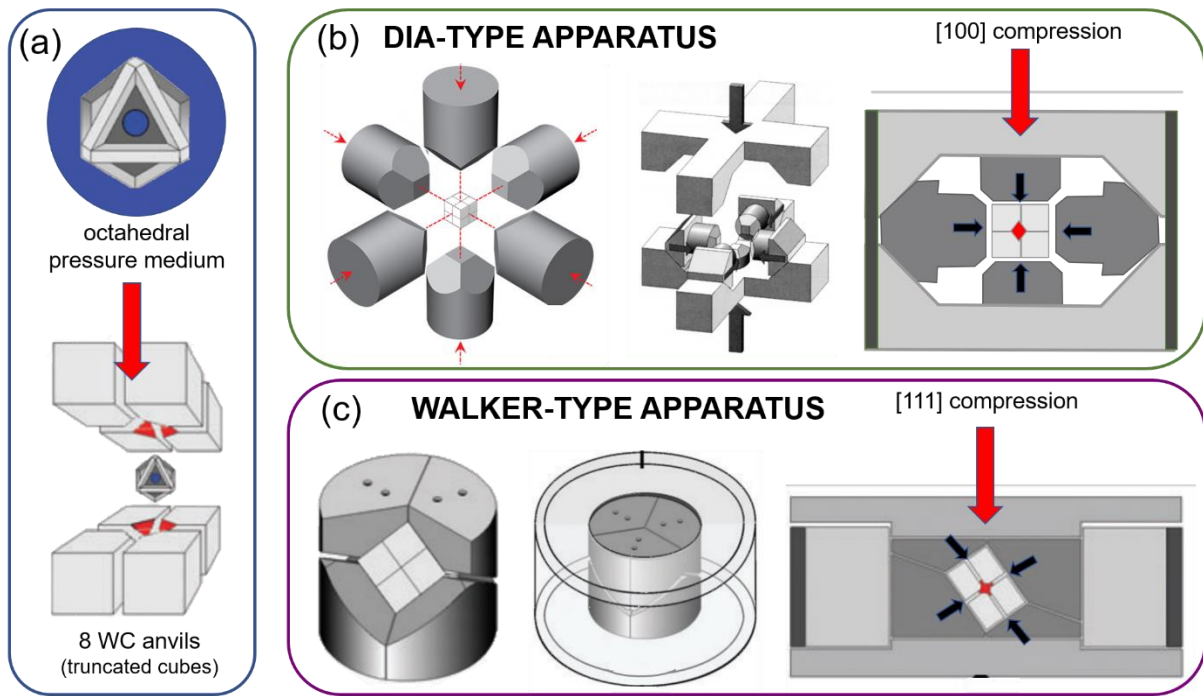


Figure 3.2 : Multi-anvil presses. (a) schematic view of the octahedral pressure medium and how it is inserted in the Kawai-type octahedral cell, made of eight truncated cubical WC anvils. (b) schematic view of the DIA geometry, in which the compression of the anvils takes place along the cube's axis. (c) schematic view of the Walker geometry, in which the anvils are inserted in a cylindrical vessel and the compression happens along the [111] direction of the cube. Figures adapted from ¹⁷ and ¹⁵.

Standard multi-anvil experiments can nowadays reach 25 GPa and 3000K^{6,7}, but with the introduction of sintered-diamond anvils¹⁸ and other technical developments, new records are continuously set. Recently, Yamazaki et al. reported pressures of 71.3 GPa and 120.3 GPa reached at room temperature with tungsten carbide (WC) and sintered diamond cubic anvils, respectively¹⁹. In our work, we needed to maintain the largest possible sample volume for crystal growth and *ex-situ* characterization, thus pressure of at most 17 GPa were applied.

3.2 *In-situ* X-Ray Diffraction at extreme conditions

The synthesis of new materials relies on the possibility of modifying the crystal structure of the starting material. Diffraction, especially from x-rays, is the most suited method to characterize the changes in materials' structure and morphology. X-ray diffraction experiments can be conducted using laboratory sources, such as x-ray tubes, or in large facilities like synchrotrons. In the latter case, x-rays generated by synchrotron source is characterized by very high flux and brilliance, that enable us to perform diffraction in real time during HP-HT experiments. The possibilities offered by *in-situ* characterization of phase transitions at extreme

conditions are countless. Not only we can observe the dynamic of the phase transformations, but *in-situ* experiments allow us to explore multiple P-T state during a single run by tuning pressure and temperature. Compared to *ex-situ* diffraction, *in-situ* experiments allow us to explore the phase diagram more rapidly and efficiently, and the synthesis conditions for new phases can be refined by monitoring the reaction's progress. In this section X-ray diffraction and synchrotron facilities are briefly introduced.

3.2.1 X-Ray Diffraction (XRD)

Diffraction techniques enable us to access information about the symmetry, structure and microstructure of crystalline samples. When a wave propagates through a material, if its wavelength is of the same order of magnitude of the inter-atomic distances (i.e. Å) or smaller, it is scattered by the atoms of the material. In the case of electromagnetic waves, the condition $\lambda \simeq \text{Å}$ ($=10^{-10}$ m) is satisfied by X-Ray with energies of ~ 12.5 keV, and the photons are diffused mainly by the electrons. The electronic clouds act as diffusion centres and can be thus seen as point sources of the diffused spherical waves. If the atoms have a periodic arrangement, i.e. they are part of a crystal, their symmetry modifies the interference pattern of the diffused waves. Indeed, constructive interference (resulting in non-zero intensity of the diffused light) is allowed only along certain directions. The result is a diffraction pattern with bright spots at positions that inform us on the symmetry and the geometry of the diffusion centres²⁰.

For elastic diffusion, the intensity of the diffused waves from the crystal's atoms can be written as: $I \propto \sum_{\{u,v,w\}} e^{-i(ua+vb+wc)\cdot\Delta k}$ where the vectors a, b, c are the basis vector of the translations of the crystal, and thus the sum of all the vectors $r = ua + vb + wc$ identifies the position of the crystalline lattice (the diffusion sources). $\Delta k = k - k'$ is the difference between the momentum of the incident (k) and diffracted (k') waves; for elastic diffusion, $|k| = |k'|$. This formula for I is valid in the far field approximation, for which the source is at a distance R high enough to approximate the diffused waves as planar waves, and $R \gg r$.

The result of the sum is non-zero (constructive interference between the diffused waves) only if every term is of order 1. This poses the condition: $(ua + vb + wc) \cdot \Delta k = 0$, which is satisfied for every vector $\Delta k = G = h a^* + k b^* + l c^*$. Thus, there is diffraction only if Δk is a vector of the crystal's reciprocal lattice. This condition is known as Laue condition, and it is equivalent to the Bragg condition: $2d_{hkl} \sin\theta = n\lambda$ that relates the wavelength of the scattered light with the direction of the propagation vector and the distance of the planes

(individuated by $\{h, k, l\}$, components of the reciprocal space vector perpendicular to the family of planes). Figure 3.3 gives a scheme to clarify the Laue and Bragg diffraction condition.

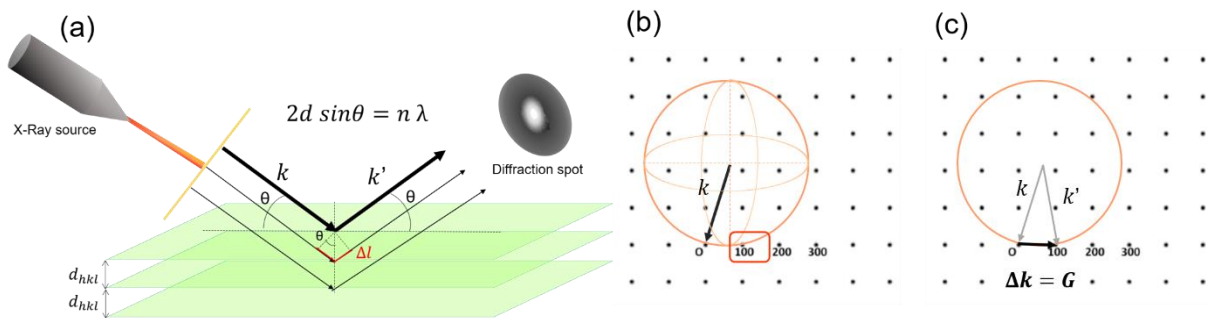


Figure 3.3 : Schematic view of the X-ray diffraction conditions. (a) Bragg condition: constructive interference causes the formation of bright diffraction spots when the difference of the distance travelled by the X-rays ($\Delta l = 2 d \sin \theta$) is an integer multiple of the radiation wavelength ($n\lambda$). (b) construction of the Ewald sphere: the incident wave vector k is drawn so that it points to the origin of the reciprocal lattice. The Ewald sphere is centred at the origin of the vector k and has radius equal to $|k|$. (c) Laue condition: the diffraction condition is satisfied when the Ewald sphere intersects a point in reciprocal space, meaning that another vector k' exists with $|k'|=|k|$ (i.e. the radius of the sphere) such that $\Delta k = k' - k = G$, with G vector of the reciprocal lattice.

Analysis of the diffraction spots' position informs us about the periodicity of the crystal. In a monocrystalline sample, a collection of data covering the solid angle around the sample allows us to visualize the point of the 3D reciprocal lattice that intersect the Ewald sphere (Figure 3.3.(c)). We can thus derive the interplanar distance and the relative orientation of the crystallographic planes. When dealing with polycrystalline samples, the data are usually collected using a 2D detector and integrated as to obtain a unidimensional dataset, i.e. intensity as a function of the angle θ . The Powder XRD signal is the superposition of scattering from crystals with various orientations, and the peaks' position allow to access the interplanar distance and then derive the symmetry system of the crystal under examination.

3.2.2 Synchrotron Radiation and *in-situ* experiments

Synchrotron sources produce very bright radiation exploiting the fact that when charged particles in movement are accelerated, they emit energy in the form of electromagnetic radiation. In the case of electrons moving with ultra-relativistic velocities, i.e. close to the speed of light, the emitted radiation is in the form of x-rays (~ 10 - 150 keV). Figure 3.4 show a scheme of the main elements of a synchrotron.

Electrons are produced by an electron gun in "bunches". The linear accelerator (LINAC) accelerates them up to hundreds of MeV before injection in the booster. The booster is a pre-

accelerator, and it brings the electrons up to energies of the order of GeV before injecting them in the storage ring. The electrons beam is quite stable in time, and the storage ring is kept under vacuum (10^{-9} mbar) to mitigate the decay of the stored-beam²². In this way, the electrons in the storage ring can travel for several hours and only a few refills per day from the LINAC and the booster are needed.

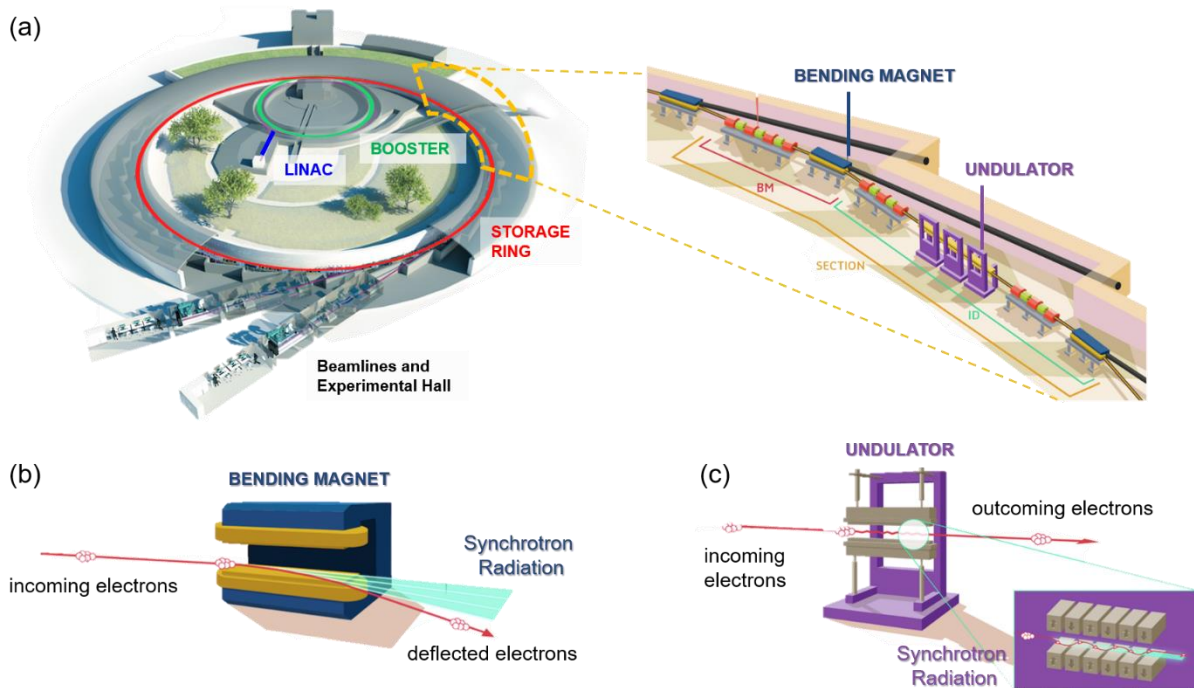


Figure 3.4 : Schematic view of a synchrotron facility. The images represent the European synchrotron in Grenoble (ESRF), and have been adapted from²¹. (a) view of the synchrotron facility and zoom of a portion of the storage ring in which different insertion devices are present. (b) schematic representation of a bending magnet: when placed into a magnetic field, a charged particle (electrons) follows a circular trajectory. (c) schematic representation of an undulator: a series of magnets are placed in series and cause the electron's trajectory to undulate.

Along the electrons' path in the storage ring, different magnetic elements are present. Focusing magnets (i.e. dipole, quadrupoles and hexapoles) maintain the electrons bunches on linear trajectories, while bending magnet and insertion devices deflect the trajectories and induce the emission of synchrotron radiation. Electrons can be deflected by a bending magnet (BM) (Figure 3.4(b)) that, with a uniform magnetic field, keeps them on their orbiting trajectories. The deflected particles emit x-rays along the direction tangential to their trajectory. The beam generated in a BM covers a wide spectral range. Undulators are insertion devices (ID) made of a linear series of magnets that causes the electron to follow a undulatory path (Figure 3.4(c)); at each bend, electrons emit x-rays. For the specific energies at which the

emitted beams interact constructively, the ID generates a more focused and brilliant (10^3 - 10^4 times higher²³) beam with respect to a single BM.

Synchrotron radiation brilliance is several orders of magnitude higher than the beams generated in x-ray tubes (10^{13} times higher in 3rd generation synchrotron than in x-ray tubes²³). The beam brought to the beamlines allows us to collect high-quality data in a short time (~seconds in a multi-anvil press, much shorter than the acquisition time in lab-based XRD experiments). Thanks to the high brilliance, XRD data can be collected in transmission geometry, with the x-rays passing through the HP assemblies and their absorbing components.

3.3 Experimental setup and beamlines for *in-situ* multi-anvil experiments

The *in-situ* experiments reported in this work were performed on two different beamlines equipped for HP-HT XRD in multi-anvil apparatus: ID06-LVP beamline at the European Synchrotron Radiation Facility (ESRF) and PSICHÉ beamline at the SOLEIL Synchrotron. In the following some details on each beamline and the HP cells designed for the experiments are reported.

3.1.1 ID06-LVP beamline at the European Synchrotron Radiation Facility (ESRF), Grenoble (France)

On ID06-LVP beamline at the ESRF, the beam is generated from one of the undulators and its energy is selected by a Si(111) monochromator. The use of an intense monochromatic beam enables users to perform angle-dispersive XRD (AD-XRD) experiments, i.e. collecting x-rays with a defined energy at different angles. Typically, the energy of the beam is set to 33 keV ($\lambda = 0.3757\text{\AA}$) in our experiments. Diffraction data are collected with a DT linear detector. The sample alignment is facilitated by direct visualization via an x-ray camera. The press mounted on the beamline is a D-DIA Voggenreiter modified-cubic apparatus. We use two stages of compression, with WC truncated cubes as second-stage anvils. Typically, we used 10/5 assemblies (i.e. 10 mm octahedra edge length/5 mm truncation length). A schematic view of the typical high-pressure cell is shown in Figure 3.5. The sample pellet (1.95 mm diameter, 2.12 mm height) is made of compacted fine powder and it is prepared in an Ar-filled glovebox. To provide chemical and electrical insulation, the sample is surrounded by a sleeve of *h*BN

(2.75 mm outer diameter (OD), 1.96 mm inner diameter (ID), 2.10 mm height). Resistive heating is performed by a current passing through a Ta foil (25 μm thickness, 2.90 mm OD) that surrounds the *h*BN. The use of a Ta foil heater over a graphite one allows us to increase the sample volume, as the furnace is significantly thinner. The Ta foil is inserted into a 10 mm edge length Cr_2O_3 -doped MgO octahedral pressure medium, along with ZrO_2 plugs. The cross-section of the octahedron that shows the placement of the different components of the assembly is reported in Figure 3.5(a).

MgO octahedron was positioned between eight truncated 25 mm tungsten carbide cubes equipped with pyrophyllite gaskets. Along the beam direction two cylindrical (2 mm OD) amorphous SiBCN X-ray windows and ~ 4 mm wide amorphous boron epoxy rectangles were inserted into the octahedron and gaskets respectively, as shown in Figure 3.5(c). Indeed, when using a monochromatic beam, the flux is reduced because the monochromator selects only a portion of it. It is thus desirable to insert low-absorbing elements along the beam path as to preserve the high quality of the data. The use of this pressure cell and this experimental setup enabled us to easily reach pressures up to 15 GPa and collect high-quality XRD data at a rate of 0.33 acquisition/second (i.e. continuous acquisition, with one XRD pattern every few seconds).

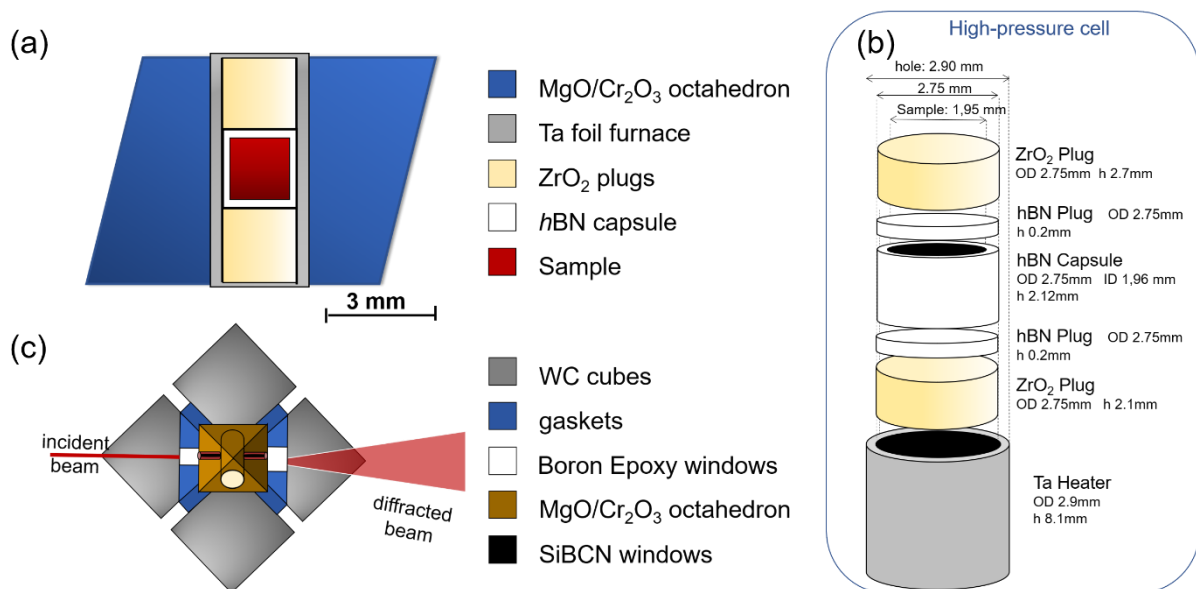


Figure 3.5 : Schematic view of the typical multi-anvil cell used during AD-XRD experiments on ID06 beamline at the ESRF. (a) Cross-section of the octahedral MgO pressure transmitting medium. (b) schematic view of the HP assembly components. (c) Top-view showing the low-absorption elements (i.e. boron epoxy or amorphous powder) inserted along the beam's path to minimize losses due to absorption.

3.1.2 PSICHÉ beamline at the SOLEIL Synchrotron, Saint-Aubin (France)

On the PSICHÉ beamline of the SOLEIL Synchrotron, the x-ray source is multi-pole wiggler which delivers a white beam with a large photon energy range (15-100keV). This allows us to perform experiments in various operating mode, going from AD-XRD to tomography. For our experiments, we performed energy-dispersive XRD (ED-XRD), i.e. the x-rays that pass through the sample are collected at a fixed angle without selecting their energy. The use of the entire energy range of the beam ensures higher flux, thus the use of low-absorption insertion is not necessary once the beam is focused at the center of the assembly. On the other side, the use of ED-XRD hinders quantitative analysis of the XRD profile, because the relative intensities of the XRD peaks are set by the source energy spectrum and by the absorption along the beam path. Indeed, even if the nominal operating energy range goes from 15 to 100 keV, our data showed significant intensity in a more limited range, i.e. 20-80 keV. To overcome this limitation, it is possible to perform Combined Angle and Energy-dispersive Structural Analysis and Refinement (CAESAR)²⁴ by collecting of ED-XRD pattern varying the position of the detector (i.e. varying the angle of the spectra acquisition and keeping a constant volume of sample investigated). The combination of energy-dispersive and angle-dispersive enables to explore a wider region of the reciprocal space. Thus, the collection and the analysis of CAESAR data (via an algorithm that re-normalizes the intensities) allows to perform structural refinement even if performing ED-XRD.

The press mounted on the beamline is a DIA apparatus. We use two stages of compression, with WC truncated cubes as second-stage anvils. Typically, we used 10/4 assemblies (i.e. 10 mm octahedra edge length/4 mm truncation length). A schematic view of the typical high-pressure cell is shown in Figure 3.6. The sample pellet (2.00 mm diameter, 1.00 mm height) is made of a compacted fine powder and is prepared in an Ar-filled glovebox. To provide chemical and electrical insulation, the sample is surrounded by a sleeve of *h*BN (2.50 mm OD, 2.00 mm ID, 2.20 mm height). The *h*BN sleeve is separated in two compartments by a *h*BN plug (OD 2.00 mm). One part hosts the sample, while the other half contains MgO/*h*BN powder used as pressure calibrant and host the thermocouple wires (D-type W/3%Re-W/25%Re). Resistive heating is performed by a current passing through a TiB₂ cylindrical heater (3.00 mm OD, 2.50 mm ID, 5.10 mm height) that surrounds the *h*BN. ZrO₂ plugs are used.

To perform CAESAR analysis, the sample volume probed during the experiment should be the same at every angle. To ensure this, the cylindrical HP assembly should be placed perpendicularly to the direction of propagation of the beam. In this way, the depth of the measured sample is invariant with respect to the azimuthal angle. In order to ensure this geometry, the 10 mm edge length Cr_2O_3 -doped MgO octahedral pressure medium was cut in two parts (~ 4 mm from the top). In this way, the hole hosting the HP assembly was drilled in the cut surface, as shown in the cross-section of the octahedron and WC anvils in Figure 3.6(a). To allow electrical current to flow through the HP cell, Mo contacts were used, either by using a foil and connecting directly the TiB_2 with the anvil's truncation, or by drilling a hole and filling it with Mo powder.

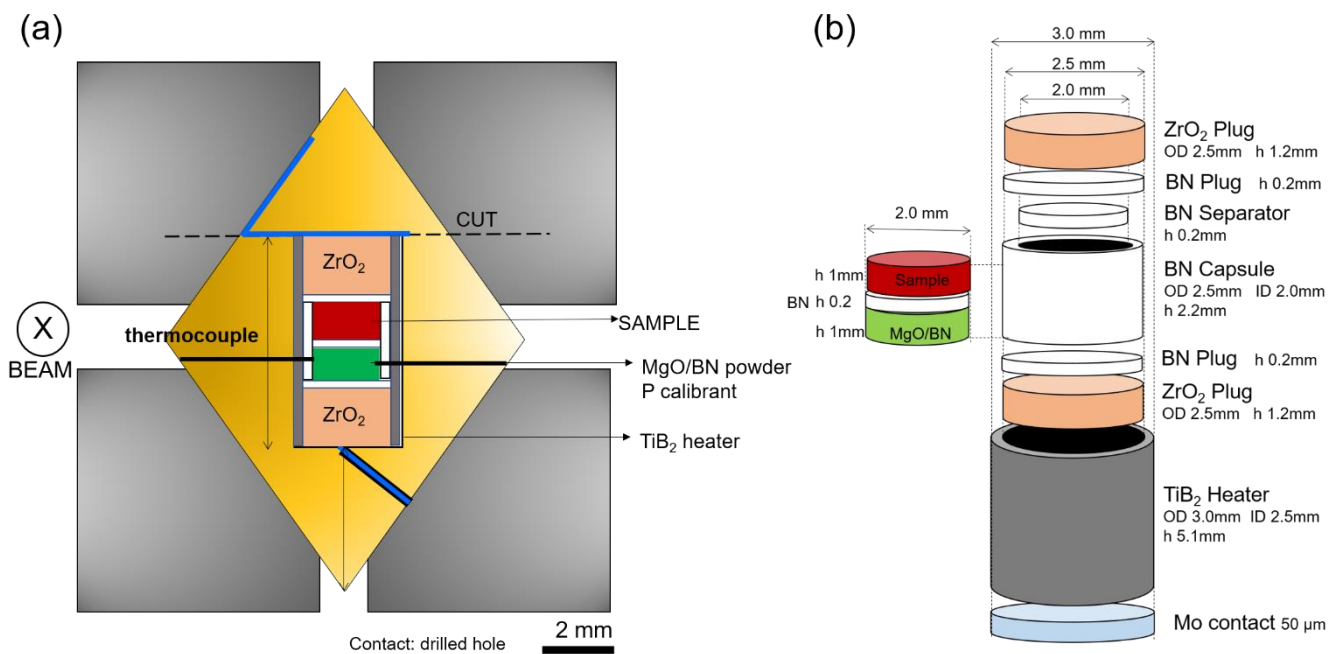


Figure 3.6 : Schematic view of the typical multi-anvil cell used during ED-XRD experiments on PSICHE beamline at the SOLEIL Synchrotron. (a) Cross-section of the WC truncated cubes surrounding the octahedral MgO pressure transmitting medium. As visible in the figure, cutting of the octahedron tip allowed us to drill the hole hosting the HP assembly perpendicularly to the x-ray beam. (b) schematic view of the HP assembly components.

References Chapter 3

- (1) Bridgman, Percy Williams. Bakerian Lecture - Physics above 20,000 Kg./Cm. ². *Proc. R. Soc. Lond. Ser. Math. Phys. Sci.* **1950**, 203 (1072), 1–17. <https://doi.org/10.1098/rspa.1950.0122>.
- (2) Hall, H. T. Ultra-High-Pressure, High-Temperature Apparatus: The ``Belt''. *Rev. Sci. Instrum.* **1960**, 31 (2), 125–131. <https://doi.org/10.1063/1.1716907>.
- (3) Besson, J. M.; Nelmes, R. J.; Hamel, G.; Loveday, J. S.; Weill, G.; Hull, S. Neutron Powder Diffraction above 10 GPa. *Phys. B Condens. Matter* **1992**, 180–181, 907–910. [https://doi.org/10.1016/0921-4526\(92\)90505-M](https://doi.org/10.1016/0921-4526(92)90505-M).
- (4) Crichton, W. A.; Mezouar, M. Methods and Application of the Paris–Edinburgh Press to X-Ray Diffraction Structure Solution with Large-Volume Samples at High Pressures and Temperatures. In *Advances in High-Pressure Technology for Geophysical Applications*; Elsevier, 2005; pp 353–369. <https://doi.org/10.1016/B978-044451979-5.50019-3>.
- (5) Jamieson, J. C.; Lawson, A. W.; Nachtrieb, N. D. New Device for Obtaining X-Ray Diffraction Patterns from Substances Exposed to High Pressure. *Rev. Sci. Instrum.* **1959**, 30 (11), 1016–1019. <https://doi.org/10.1063/1.1716408>.
- (6) Huppertz, H. Multianvil High-Pressure / High-Temperature Synthesis in Solid State Chemistry. *Z. Für Krist. - Cryst. Mater.* **2004**, 219 (6). <https://doi.org/10.1524/zkri.219.6.330.34633>.
- (7) Ito, E. Multi-Anvil Cells and High Pressure Experimental Methods. In *Treatise on Geophysics*; Elsevier, 2015; pp 233–261. <https://doi.org/10.1016/B978-0-444-53802-4.00035-X>.
- (8) Hall, H. T. Some High-Pressure, High-Temperature Apparatus Design Considerations: Equipment for Use at 100 000 Atmospheres and 3000°C. *Rev. Sci. Instrum.* **1958**, 29 (4), 267–275. <https://doi.org/10.1063/1.1716172>.
- (9) Von Platen, Baltazar; Wentorf, R.H. A Multiple Piston, High-Pressure, High-Temperature Apparatus. *Mod. Very High Press. Tech.* **1962**, 118–136.
- (10) Kawai, N. A Static High Pressure Apparatus with Tapering Multi-Pistons Forming a Sphere. I. *Proc. Jpn. Acad.* **1966**, 42 (4), 385–388. <https://doi.org/10.2183/pjab1945.42.385>.
- (11) Kawai, N.; Endo, S. The Generation of Ultrahigh Hydrostatic Pressures by a Split Sphere Apparatus. *Rev. Sci. Instrum.* **1970**, 41 (8), 1178–1181. <https://doi.org/10.1063/1.1684753>.
- (12) Kawai, N.; Togaya, M.; Onodera, A. A New Device for Pressure Vessels. *Proc. Jpn. Acad.* **1973**, 49 (8), 623–626. <https://doi.org/10.2183/pjab1945.49.623>.
- (13) Kato, T.; Ohtani, E.; Morishima, H.; Yamazaki, D.; Suzuki, A.; Suto, M.; Kubo, T.; Kikegawa, T.; Shimomura, O. In Situ X Ray Observation of High-Pressure Phase Transitions of MgSiO₃ and Thermal Expansion of MgSiO₃ Perovskite at 25 GPa by Double-Stage Multianvil System. *J. Geophys. Res. Solid Earth* **1995**, 100 (B10), 20475–20481. <https://doi.org/10.1029/95JB01688>.
- (14) Walker, D.; Carpenter, M. A.; Hitch, C. M. Some Simplifications to Multianvil Devices for High Pressure Experiments. *Am. Mineral.* **1990**, 75 (9–10), 1020–1028.
- (15) Wang, Y.; Durham, W. B.; Getting, I. C.; Weidner, D. J. The Deformation-DIA: A New Apparatus for High Temperature Triaxial Deformation to Pressures up to 15 GPa. *Rev. Sci. Instrum.* **2003**, 74 (6), 3002–3011. <https://doi.org/10.1063/1.1570948>.

- (16) Rubie, D. C. Characterising the Sample Environment in Multianvil High-Pressure Experiments. *Phase Transit.* **1999**, 68 (3), 431–451. <https://doi.org/10.1080/01411599908224526>.
- (17) Huppertz, H. New Synthetic Discoveries via High-Pressure Solid-State Chemistry. *Chem Commun* **2011**, 47 (1), 131–140. <https://doi.org/10.1039/C0CC02715D>.
- (18) Irifune, T.; Naka, H.; Sanehira, T.; Inoue, T.; Funakoshi, K. In Situ X-Ray Observations of Phase Transitions in MgAl₂O₄ Spinel to 40 GPa Using Multianvil Apparatus with Sintered Diamond Anvils. *Phys. Chem. Miner.* **2002**, 29 (10), 645–654. <https://doi.org/10.1007/s00269-002-0275-1>.
- (19) Yamazaki, D.; Ito, E.; Yoshino, T.; Tsujino, N.; Yoneda, A.; Gomi, H.; Vazhakuttiyakam, J.; Sakurai, M.; Zhang, Y.; Higo, Y.; et al. High-Pressure Generation in the Kawai-Type Multianvil Apparatus Equipped with Tungsten-Carbide Anvils and Sintered-Diamond Anvils, and X-Ray Observation on CaSnO₃ and (Mg,Fe)SiO₃. *Comptes Rendus Geosci.* **2019**, 351 (2–3), 253–259. <https://doi.org/10.1016/j.crte.2018.07.004>.
- (20) Bassani, G. F.; Grassano, U. M. *Fisica dello stato solido*; Bollati Boringhieri: Torino, 2000.
- (21) <https://www.esrf.eu/about/synchrotron-science/synchrotron>.
- (22) *Synchrotron Radiation Research*; Winick, H., Doniach, S., Eds.; Springer US: Boston, MA, 1980. <https://doi.org/10.1007/978-1-4615-7998-4>.
- (23) Balerna, A.; Mobilio, S. Introduction to Synchrotron Radiation. In *Synchrotron Radiation*; Mobilio, S., Boscherini, F., Meneghini, C., Eds.; Springer Berlin Heidelberg: Berlin, Heidelberg, 2015; pp 3–28. https://doi.org/10.1007/978-3-642-55315-8_1.
- (24) Wang, Y.; Uchida, T.; Von Dreele, R.; Rivers, M. L.; Nishiyama, N.; Funakoshi, K.; Nozawa, A.; Kaneko, H. A New Technique for Angle-Dispersive Powder Diffraction Using an Energy-Dispersive Setup and Synchrotron Radiation. *J. Appl. Crystallogr.* **2004**, 37 (6), 947–956. <https://doi.org/10.1107/S0021889804022502>.

Chapter 4:

Topology of Si phase diagram: new insights by *in-situ* x-ray diffraction and direct observation of I-II-L triple point

In this chapter, our *in-situ* x-ray diffraction experiments investigating the dynamics of Si transitions at high-pressure and high-temperature are presented. Our results clarify some aspects of Si phase diagram that are still unclear. We provide new insights on the Si-I→Si-II transition, which is fundamental for the synthesis of strategic Si allotropes for optoelectronic applications. We demonstrate that Si-II→Si-XI transition at high T happens via a continuous deformation. We also provide the first direct evidence of the I-II-L triple point, which P-T conditions had been only inferred up to now. With this new understanding, we refine Si phase diagram up to 15 GPa.

Silicon is one of the most abundant elements on Earth, and its behaviour under high-pressure has important implications for fields ranging from material to planetary sciences and high-energy-density physics. Upon increasing pressure, Si-I (cubic diamond-like Si, cd) undergoes several phase transitions¹ that were characterized up to 243 GPa at ambient temperature. Si-I transforms into the metallic β -tin Si-II around 10-12 GPa²⁻⁴, followed by *Imma* Si-XI around 13.5 GPa^{5,6}, sh Si-V at 16 GPa⁷, *Cmca* Si-VI at 37 GPa^{8,9}, hcp Si-VII at 42 GPa¹⁰ and fcc Si-X around 79 GPa^{10,11} (Chapter 2). During decompression, different metastable allotropes have been observed¹²⁻¹⁸. These new phases could potentially be applied in Si-based technology (Chapter 1). Combined high-pressure and high-temperature (HP-HT) conditions were studied to assess Si melting curve using either electrical characterization^{19,20} or differential thermal analysis^{21,22}. More recent *in-situ* HP-HT x-ray diffraction (XRD)^{23,24} experiments enabled researchers to access information on Si phase diagram and its phase transitions at HP-HT conditions. Laser-induced compression experiments, either by shock- or ramp-driven compression, further extended the investigation of Si phase diagram²⁵⁻²⁸. Recently, shock compression in a confined geometry induced a microexplosion that resulted in the formation of at least two new tetragonal allotropes, BT8-Si ($I4_1/a$) and ST12-Si ($P4_32_12$)²⁹. The behaviour of Si at such extreme conditions is of great interest for planetary science³⁰ as well as geophysics³¹ and high-energy-density physics, in which the use of Si as target dopant reduces the growth of instabilities during inertial confinement fusion³².

Despite the abundance of literature and the increasing number of experimental studies that push forward the boundaries of the investigations, some aspects of Si phase diagram remain unclear even at relatively low pressure, i.e. up to 15 GPa. There is not yet a consensus around the Si-I \rightarrow Si-II transformation, which is the first transition encountered upon increasing pressure. The first studies on Si metallization at high-pressure reported transition pressures as high as 16 GPa^{3,4,15}, while later works reduced this estimation down to 12.5 GPa^{33,34} (and even 8 GPa for compression along Si[111] direction³⁵). More recent *in-situ* XRD studies reported coexistence of Si-I and Si-II over a large pressure range, with Si-II that starts forming at \sim 10 GPa but Si-I remains present up to \sim 13 GPa^{5-8,23} (Chapter 2). The disagreement between the observed transition pressures was attributed to the non-hydrostatic stress states in the samples, which could influence the onset of the transition. Recent experiments with helium as pressure-transmitting medium even question the possibility of stabilizing pure Si-II at ambient temperature³⁶. Furthermore, the shortage of reliable melting points over 10 GPa prevents precise determination of the melting curve in the range of the Si-I \rightarrow Si-II transition. Indeed, Kubo et al.²⁴ have stressed the importance of *in-situ* pressure measurement during HP-HT experiments, suggesting that most of the previous studies¹⁹⁻²² may have large uncertainties on the pressure values at high-temperature. The uncertainty is expected to increase with pressure, as over 10 GPa the transition to Si-II affects the sample volume significantly. If the measures affected by the uncertainty on the pressure are discarded, the remaining melting points are very limited. Using *in-situ* x-ray diffraction (XRD), Voronin et al. observed Si-XI melting around 1053 K at 12.7 GPa²³, while Kubo et al. reported melting of Si-XI and Si-V at very close conditions around 14.5 GPa and 1010 K. The current knowledge is thus inadequate for the determination of a reliable melting curve over 10 GPa, as no direct evidence of Si-II melting has been provided, and the currently accepted melting lines rely mostly on interpolation and assumptions.

There is an increasing number of theoretical works investigating the properties of Si under extreme conditions, i.e. subject to a shock wave³⁷⁻⁴⁰ or in a high-energy-density plasma⁴¹. A recent study by Paul et al. used an approach that combined density functional theory (DFT) with evolutionary algorithms and lattice dynamics⁴² to construct Si phase diagram up to 4 TPa and 26000 K. Their results predict two further phase transitions, i.e. fcc(Si-X) \rightarrow bcc at 2.87 TPa and bcc \rightarrow sc at 3.89 GPa. For calculations to be predictive, though, reliable experimental data are needed. In most cases, calculations fail in reproducing correctly all Si phase transitions⁴³⁻⁴⁶ (see also Section 2.2.3). The Si-I \rightarrow Si-II transition is particularly difficult to simulate because

of the ~22% volume change and the modification of the bandstructure⁴⁷ between the two phases. Computational methods have provided inconsistent transition pressures, ranging from 7.8 GPa (DFT with local density approximation⁴⁸) to 16.5 GPa (Quantum Monte Carlo⁴⁹). Clarification of the controversies in Si phase diagram, even at relatively low pressure, is needed in order to test the simulation methods to be used for the extrapolation of Si behaviour at extreme conditions.

In this chapter, we use *in-situ* HP-HT XRD to clarify the topology of Si phase diagram in the vicinity of the semiconductor-metal transition. We report the first direct evidence of the I-II-L triple point of Si and we prove that the Si-II→Si-XI transition happens continuously at high-temperature. Furthermore, we provide new insights on the dynamics of Si-I→Si-II transition. At ambient temperature, the Si-I→Si-II transition is sluggish, and Si-I and Si-II coexist over a large pressure range. These results were previously attributed to the high kinetic barrier⁵⁰ of the transition. The coexistence of Si-I and Si-II may also result from the low plasticity of the phases in contact, i.e. to microscopic stress states induced by the different elastic properties of the two phases⁵¹. We performed experiments without using a pressure-transmitting medium (PTM), which allowed us to investigate the transition mechanism. Furthermore, we determined the synthesis conditions for pure-phase samples, which are fundamental for Si-based materials' synthesis. Our findings give new references for construction of a reliable Si phase diagram.

Table 4.1: *in-situ* HP-HT XRD experiments on Si phase diagram up to 15 GPa.

Experiment	Pressure-transmitting medium (PTM)	Temperature – Pressure determination	Experiment dynamic
Voronin et al. ²³	NaCl+hBN	W/Re26%–W/Re4% and NaCl EOS	Isothermal compression
Kubo et al. ²⁴	hBN	W/Re5%-W/Re26% and Au and MgO EOS	Heating at constant load
This study (ESRF)	none	Power-Temperature calibration curves and Ta EOS	Heating at constant/increasing load
This study (SOLEIL)	none	W/Re25%W/Re3% and MgO EOS	Heating at constant/increasing load

In-situ XRD experiments were performed in multi-anvil apparatus, in which triaxiality of the compression ensures higher hydrostaticity as compared to other large-volume HP apparatus. For the experiments on PSICHE beamline at the SOLEIL Synchrotron, the octahedral pressure-transmitting medium was cut in two and the hole hosting the assembly was drilled perpendicularly to the propagation of the beam. This enabled us to perform both energy-dispersive-XRD (ED-XRD) measurements and x-ray radiography to monitor the position of the sample and the pressure calibrant (see also Appendix 4.2). Temperature was measured with type D (W/Re25%W/Re3%) thermocouple and pressure was estimated from MgO EOS⁵². On ID06-LVP beamline at the European Synchrotron Radiation Facility, angle-dispersive-XRD (AD-XRD) patterns were collected thanks to low-absorption elements inserted along the beam path in the high-pressure assembly. The pressure-temperature conditions were obtained combining temperature calibration curves and the EOS of Si³⁶ and Ta^{53,54}. The sample was a pellet of high-purity Si powder (Alfa Aesar), and no PTM was used (see also Table 4.1). In each experiment, compression was performed at ambient temperature, and resulted in a mixed Si-I/Si-II phase between 11.5 GPa and 13.5 GPa. We performed the initial heating without modifying the primary pressure in the main RAM. In doing so, we gain insight into the dynamics of Si-I→Si-II transition with temperature by observing the evolution of the transformation pathway. The high temporal resolution (a few seconds for the experiments on ID06-LVP beamline) and the good quality of our HP-HT data allow us to obtain a detailed view of the evolution of the system and to analyse aspects that were not accounted for in previous studies.

Figure 4.1(a) shows the P-T evolution during the HP-HT experiments. Pressure was initially increased at ambient temperature. High temperatures can overcome the kinetic barrier (estimated theoretical value: 510 meV/atom⁵⁰) between the two phases, increasing the fraction of Si-II in the sample. Upon increasing temperature, the pressure tends to drop, as the volume decreases during Si-I→Si-II transformation. Indeed, Si-II is ~22% denser than Si-I¹. The contraction of the sample volume ($V_{\text{Si-I}} + V_{\text{Si-II}}$) results in a loss of pressure. During Run3, the presence of residual Si-I above 13 GPa is due to non-hydrostatic stress states in the sample, caused by the compression at ambient temperature and without pressure-transmitting medium. As soon as the stress state become quasi-hydrostatic (~500 K, see also Appendix 4.3), Si-I tends to be replaced by the stable Si-II. During Run3, during the Si-I→Si-II transition the pressure decreases down to 11.2 GPa, and subsequent heating doesn't modify it significantly. During the other experiments, pressure starts decreasing around 810 K when the heating is performed

at 11.5 GPa (Run1) and around 685 K at 12.5 GPa (Run2). Despite the different starting pressures, the P-T conditions of Si-I/Si-II mixture converge towards 800 K at 11.8 GPa. Once the system reaches this state, the Si-I→Si-II transition is interrupted because the pressure is too low.

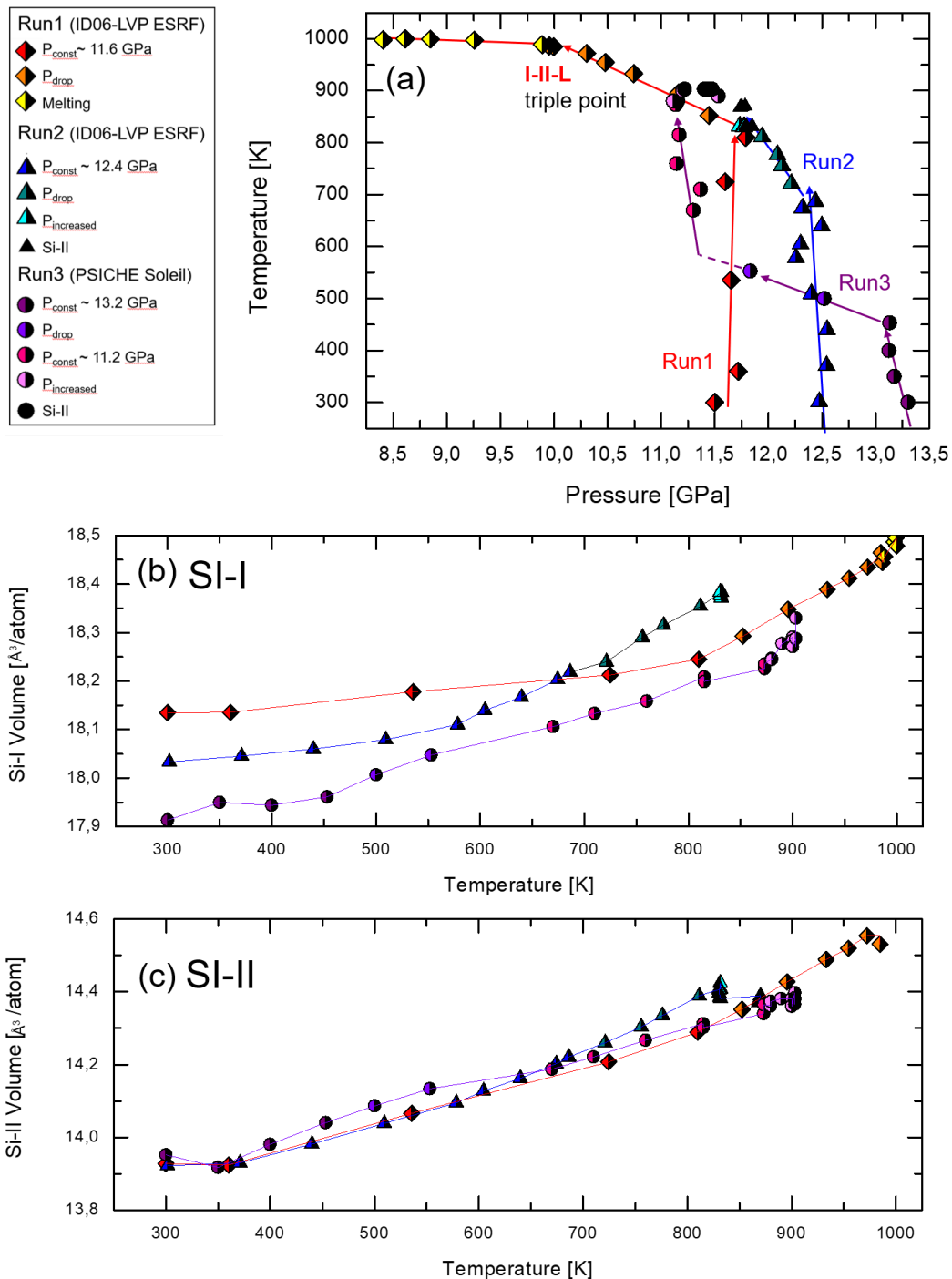


Figure 4.1 : (a) Evolution of the pressure during heating as estimated using Ta EOS (Run1-2) and MgO EOS (Run3). (b)-(c) Atomic volumes of Si-I and Si-II as measured from *in-situ* XRD at HP-HT conditions. In every experiment, the pressure drops upon heating during the Si-I→Si-II transformation. The onset of the pressure loss varies depending on the initial compression state. Data from various experiments are reported using different symbols, while colours are used to show different stages of the heating in terms of pressure stability (i.e. pressure stable or modified during the heating).

The formation of Si-II causes a pressure drop that interrupts the Si-I→Si-II transition in all experiments. After reaching this low-pressure state, we further compressed the system to compensate the pressure loss. In both Run2 and Run3, the main load was increased at high-temperature until completion of the transition was observed. Pure Si-II was obtained at (11.8 GPa; 830 K) and (11.4 GPa; 900 K) respectively. The values obtained are coherent with observation of pure Si-II in previous HP-HT experiments by Voronin et al²³.

Figure 4.1(b),(c) show the atomic volumes of Si-I and Si-II as a function of temperature during the three experimental runs. The volumes measured from XRD patterns are not always coherent with the P-T conditions estimated from the pressure calibrant (P_{PM} , i.e. Ta or MgO pressure marker). Si-I volume is smaller in Run3 with respect to the other experiments despite, above 600 K, the estimated pressure was lower in this run. Also, even if P_{PM} is higher in Run2 than in Run1, Si-I volume is higher in Run2 for temperatures above 700 K. In Appendix 4.1 (Figure 4.5-6) it is also shown that the volume of Si-I increases during the HT-compression performed in Run2 and Run3 to reach the completion of Si-I→Si-II reaction.

We conclude that during Si-I→Si-II transformation at HP-HT conditions the two phases coexist, but they are not in thermodynamic equilibrium. The partial pressures on each phase are different, and their values likely depend on the relative quantity of Si-I and Si-II and on the transition rate. Previous studies have mainly investigated the Si-I→Si-II transition at ambient temperature. The observation of a large (~3 GPa) coexistence region has been attributed to the non-hydrostatic compression states in the sample (which were supposed to lower the transition onset) and to the high kinetic barrier. With our results, we show that there is another factor that influences the transition mechanism, i.e. the microscopic stress due to the different plasticity of the two phases⁵¹. Even after high-temperature reduces the degree of non-hydrostaticity of the system ($T > 500\text{K}$, cf. Appendix 4.3), Si-I and Si-II are subject to microscopic local stress and cannot reach a mechanical equilibrium. Particular care should be taken when defining the thermodynamic state of the mixed Si-I/Si-II phase, as there is not a P value that can describe both phases in the system. For this reason, we include in our updated phase diagram (Figure 4.4) only the P-T conditions at which pure Si-II was observed.

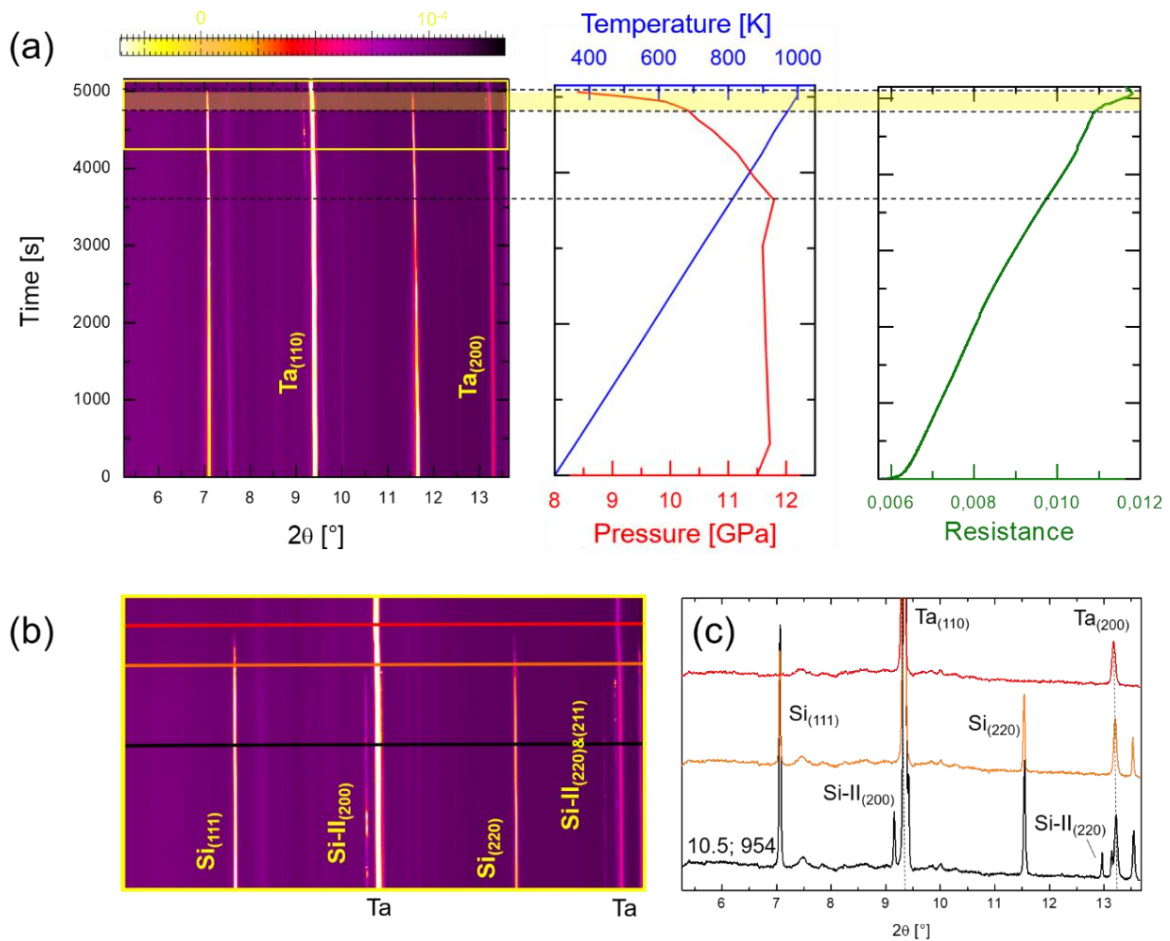


Figure 4.2 : *in-situ* high-pressure data from Run1 (ID06-LVP beamline) showing the simultaneous melting of both Si-I and Si-II. The colormaps show the evolution of the XRD pattern over time (y axis); on the x axis, the 2θ angles at 33 keV ($\lambda=0.3757\text{\AA}$) are reported. In (b) the colormap zooms on the final part of the experiment, shown with a yellow rectangle in (a). While performing the HP-HT experiment, electrical measurements allowed to control in-real-time the power supplied to the assembly (and thus the temperature, central panel in (a)) and the resistance (right panel in (a)). The pressure evolution has been obtained from Ta EOS. We provide evidence of the I-II-L triple point, as concomitant disappearance of XRD peaks and the discontinuity of the sample's resistance are considered proof of melting.

Our experiments prove that, in order to stabilize Si-II at HP-HT condition, it is necessary to compensate the pressure losses caused by negative ΔV of the $Si-I \rightarrow Si-II$ transformation itself. During Run1, instead of compensating pressure, we raised the temperature to promote $Si-I \rightarrow Si-II$ transition; high temperature should overcome the energetic barrier and the stress caused by the plasticity of both phases. We observe that increasing temperature above 850 K triggers further transformation into Si-II, but the pressure drops down to 10 GPa, hindering completion of the transition. In these conditions, both Si-II and Si-I melt upon further increase of the temperature, i.e. we are at the I-II-L triple point. Figure 4.2 shows our experimental

results: the yellow area highlights the disappearance of all Si XRD peaks within a few tens of seconds. Figure 4.2(a) shows that, as the XRD peaks disappear, the pressure drops and the assembly's electrical resistance increases steadily. The concomitant disappearance of the crystalline phases and the resistance increase (Figure 4.2(a), central panel) confirm the melting of the crystalline phases. The onset of melting is 950 K at 10 GPa, which is thus our best estimation of the P-T conditions of the I-II-L triple point. After melting starts, the pressure and temperature estimated from our calibration curves are not reliable because the abrupt change in the resistance may modify the linear power-T relationship. The direct observation of the I-II-L here provided is an important reference for the precise determination of the topology of the Si phase diagram.

Thanks to the temporal resolution of our data acquisition (few seconds/XRD pattern) we observed that at HT, Si-II \rightarrow Si-XI transition happens via a continuous deformation of the cell parameters. Figure 4.3 shows our experimental results, obtained during HP-HT investigation of the K:Si(1:6) system. Simultaneously with the formation of a K-Si phase at \sim 830 K (see also Appendix 4.4), the pressure raises from 10.6 GPa to 12.2 GPa, triggering the transition from Si-II to Si-XI. Si-II and Si-XI crystal structure can both be described in terms of an orthorhombic cell, and Si-XI coincides with the tetragonal Si-II when $a_{Si-XI}=b_{Si-XI}$. Our data show that the splitting of the XRD peaks $(200)_{Si-II} \rightarrow (200)_{Si-XI}$, $(020)_{Si-XI}$ and $(101)_{Si-II} \rightarrow (101)_{Si-XI}$, $(011)_{Si-XI}$ is continuous. Thus, the correspondent deformation $a_{Si-II} = b_{Si-II} \rightarrow a_{Si-XI} \neq b_{Si-XI}$ that breaks the tetragonal symmetry and results in an orthorhombic cell is also continuous. The transition happens without coexistence between the phases. McMahon et al.^{5,6} were the first to discover the existence of the orthorhombic Si-XI, the so-called *Imma* phase, and to characterize its formation upon increasing pressure at ambient temperature. They classified it as a first-order phase transition, even if with a small (0.2%) volume change⁵ and coexistence between the phases was observed. We suppose that the higher degree of hydrostaticity at HT and the higher temporal resolution of our experiments enabled us to appreciate details that were not observed at ambient temperature. Our findings agree with *ab-initio* calculations^{55,56} that suggested that the *Imma* phase is an intermediate phase that deforms continuously from tetragonal Si-II to hexagonal Si-V with increasing pressure. We observe that the splitting of the peaks happens in a relatively short time (\sim s), and during the dwell in temperature there is no further evolution of the unit cell parameters. Additional increase of the temperature brings to Si-XI melting around 990 K at 12.4 GPa.

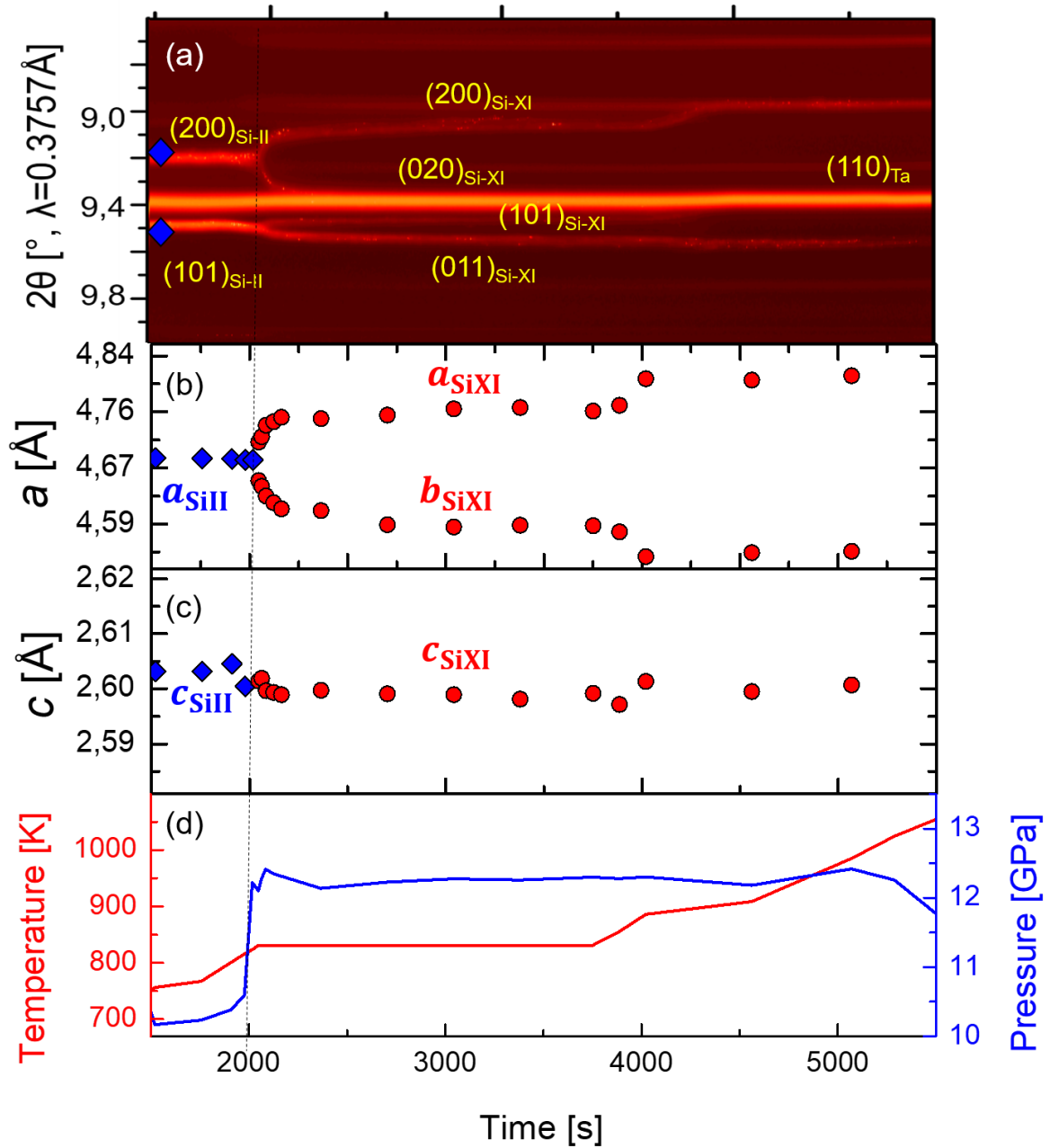


Figure 4.3 : Si-II \rightarrow Si-XI transition studied by *in-situ* high-pressure data from experiments on the ID06-LVP beamline. (a) The colormaps show the evolution of the XRD pattern over time (x axis); on the y axis, the 2θ angles at 33 keV ($\lambda=0.3757\text{\AA}$) are represented. (b),(c) Evolution of the lattice parameters during the transition, the splitting of $a_{\text{Si-II}}$ in $a_{\text{Si-XI}}$ and $b_{\text{Si-XI}}$ happens continuously. While performing the HP-HT experiment, electrical measurements allowed to control in-real-time the power supplied to the assembly (and thus the temperature, central panel in (d)). The pressure evolution has been obtained from Ta EOS (d).

Our results give new insights on the nature Si phase transitions at HP-HT conditions, essential for the determination of a reliable phase diagram. We propose a revised phase diagram (Figure 4.4), which relies exclusively on *in-situ* XRD experiments can measure both P and T in real time. This selection avoids large uncertainties on the pressure values that, as we have shown, are considerable if the Si-I \rightarrow Si-II transition occurs. We included also the low-pressure

melting data by Jayaraman et al. in a piston-cylinder press²¹, for which P can be directly measured. Previous HP-HT multi-anvil studies by Voronin et al.²³ and Kubo et al.²⁴ extrapolated the low-pressure melting curve until it crossed the I-II phase boundary to infer the location of I-II-L triple point. Because of the linear approximation of Si-I melting curve, the pressure of the I-II-L triple point was incorrectly estimated by both groups. The direct observation of the I-II-L triple point enables us to avoid extrapolations and we observe that Si-I melting curve is not linear, as it becomes steeper at high pressure (as already suggested in previous studies²³). We add on the phase diagram the points for which pure Si-II was observed after pressure compensation. The values are consistent with previous studies. By combining our experimental results with those by Kubo et al. and Voronin et al. we see that the II-XI phase boundary has a negative slope dT/dP . For the Si-XI/Si-V phase boundary, we rely on the data from other studies^{8,24} as it was outside the range we probed. We do not define the boundaries of the Si-I/Si-II coexistence region, because, as we have shown, when the two phases coexist, they are not in equilibrium. There is not a single P value that can describes the thermodynamic state of Si-I, Si-II and the pressure markers conventionally used to estimate P. By linking the I-II-L triple point with the Si-XI melting points at 12.4 GPa, we find a positive slope of ~ 16.7 K/GPa for the HP phases. The melting line obtained in this way is consistent with Si-XI and Si-V melting reported by Kubo et al. and Voronin et al. Further studies and systematic investigation of this pressure domain by *in-situ* XRD are still needed for precise determination of Si-II melting curve, as direct melting of pure Si-II has not been reported yet.

In conclusion, we used *in-situ* XRD in a multi-anvil apparatus to investigate the mechanism of Si transitions at HP-HT conditions. The high-quality data obtained at the synchrotron and a high temporal resolution allowed us to gain new insights on the topology of Si phase diagram. We demonstrate that the Si-I \rightarrow Si-II transition causes a loss of pressure that must be compensated to obtain the pure phase; this phase purity is essential to synthesize strategic functional materials. Furthermore, we show that the Si-II \rightarrow SI-XI transition in hydrostatic conditions happens with a continuous deformation of the lattice. We provide the first direct evidence and exact P-T values for the Si I-II-L triple point, which is an important reference to define the reliable phase diagram and melting curves. With this new information, we propose an updated phase diagram of Si in the range up to 14 GPa.

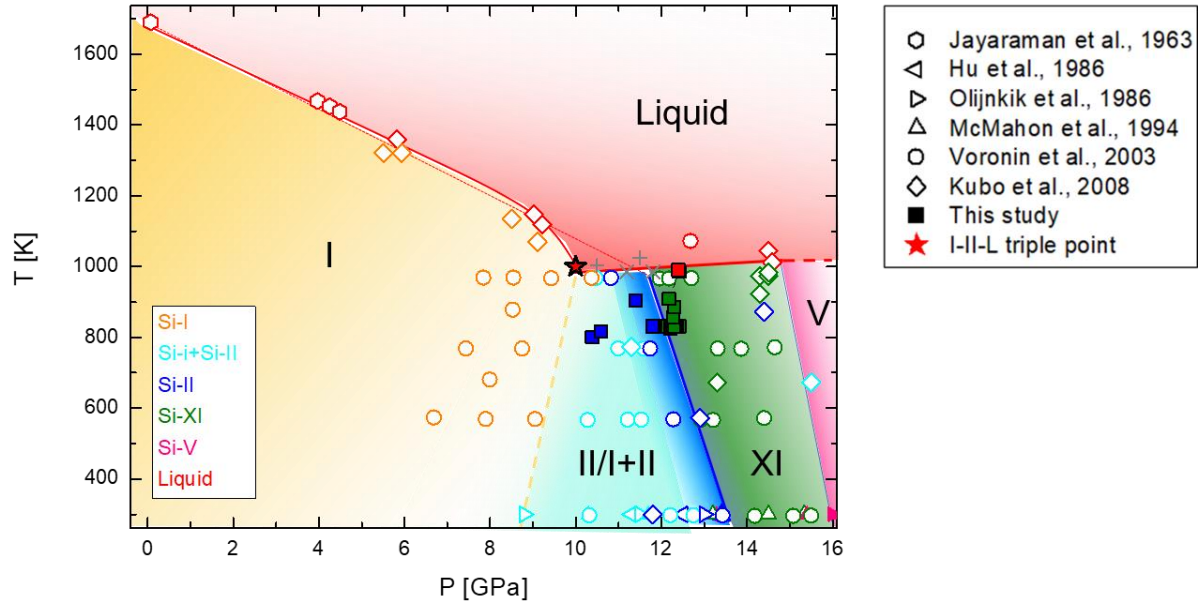


Figure 4.4 : Updated P-T Si phase diagram. We propose a new trend for Si-I melting curve, with a steepening slope at high pressures. This curve meets our measured I-II-L triple point in (10 GPa; 950 K). The phase boundaries and the melting curves are traced by combining XRD data from studies that enabled *in-situ* pressure measurement (apart from the piston-cylinder study of Jayaraman²¹ et al. at low pressures). The filled symbols are data from our study, while the void symbols represent data from previous studies, with each symbol corresponding to different authors. Each phase (included the I-II mixed phase) is represented by a different colour. The stability regions of the different phases are coloured accordingly; because of the sluggish nature of Si-I→Si-II transition and our recent findings that question the possibility of thermodynamic equilibrium between these two phases, we don't indicate a precise phase boundary.

Acknowledgments: the *in-situ* experiments on ID06-LVP (CH-4896/CH-5431 allocated beamtime) were performed with the help of Kristina Spektor (ESRF), Wiston Crichton (ESRF) and Carlos Renero-Lecuna (IDIVAL). The experiments on PSICHE beamline (Proposal 20180190) were performed with the help of Nicolas Guignot (SOLEIL) and Jean-Paul Itie (SOLEIL). A particular thanks goes to Fang Xu (IMPMC) for help all along the beamtime planification, preparation and execution. Also, thanks to Philippe Rosier and Nicolas Dumesnil from the atelier de fabrication mécanique (IMPMC).

References Chapter 4

- (1) Mujica, A.; Rubio, A.; Muñoz, A.; Needs, R. J. High-Pressure Phases of Group-IV, III–V, and II–VI Compounds. *Rev. Mod. Phys.* **2003**, *75* (3), 863–912. <https://doi.org/10.1103/RevModPhys.75.863>.
- (2) Mignot, J. M.; Chouteau, G.; Martinez, G. High Pressure Superconductivity of Silicon. *Phys. BC* **1985**, *135* (1–3), 235–238. [https://doi.org/10.1016/0378-4363\(85\)90473-5](https://doi.org/10.1016/0378-4363(85)90473-5).
- (3) Jamieson, J. C. Crystal Structures at High Pressures of Metallic Modifications of Silicon and Germanium. *Science* **1963**, *139* (3556), 762–764. <https://doi.org/10.1126/science.139.3556.762>.
- (4) Minomura, S.; Drickamer, H. G. Pressure Induced Phase Transitions in Silicon, Germanium and Some III–V Compounds. *J. Phys. Chem. Solids* **1962**, *23* (5), 451–456. [https://doi.org/10.1016/0022-3697\(62\)90085-9](https://doi.org/10.1016/0022-3697(62)90085-9).
- (5) McMahon, M. I.; Nelmes, R. J.; Wright, N. G.; Allan, D. R. Pressure Dependence of the *Imma* Phase of Silicon. *Phys. Rev. B* **1994**, *50* (2), 739–743. <https://doi.org/10.1103/PhysRevB.50.739>.
- (6) McMahon, M. I.; Nelmes, R. J. New High-Pressure Phase of Si. *Phys. Rev. B* **1993**, *47* (13), 8337–8340. <https://doi.org/10.1103/PhysRevB.47.8337>.
- (7) Hu, J. Z.; Merkle, L. D.; Menoni, C. S.; Spain, I. L. Crystal Data for High-Pressure Phases of Silicon. *Phys. Rev. B* **1986**, *34* (7), 4679–4684. <https://doi.org/10.1103/PhysRevB.34.4679>.
- (8) Olijnyk, H.; Sikka, S. K.; Holzappel, W. B. Structural Phase Transitions in Si and Ge under Pressures up to 50 GPa. *Phys. Lett. A* **1984**, *103* (3), 137–140. [https://doi.org/10.1016/0375-9601\(84\)90219-6](https://doi.org/10.1016/0375-9601(84)90219-6).
- (9) Hanfland, M.; Schwarz, U.; Syassen, K.; Takemura, K. Crystal Structure of the High-Pressure Phase Silicon VI. *Phys. Rev. Lett.* **1999**, *82* (6), 1197–1200. <https://doi.org/10.1103/PhysRevLett.82.1197>.
- (10) Duclos, S. J.; Vohra, Y. K.; Ruoff, A. L. Experimental Study of the Crystal Stability and Equation of State of Si to 248 GPa. *Phys. Rev. B* **1990**, *41* (17), 12021–12028. <https://doi.org/10.1103/PhysRevB.41.12021>.
- (11) Duclos, S. J.; Vohra, Y. K.; Ruoff, A. L. Hcp to Fcc Transition in Silicon at 78 GPa and Studies to 100 GPa. *Phys. Rev. Lett.* **1987**, *58* (8), 775–777. <https://doi.org/10.1103/PhysRevLett.58.775>.
- (12) Zhao, Y.-X.; Buehler, F.; Sites, J. R.; Spain, I. L. New Metastable Phases of Silicon. *Solid State Commun.* **1986**, *59* (10), 679–682. [https://doi.org/10.1016/0038-1098\(86\)90372-8](https://doi.org/10.1016/0038-1098(86)90372-8).
- (13) Nelmes, R. J.; McMahon, M. I. Chapter 3 Structural Transitions in the Group IV, III-V, and II-VI Semiconductors under Pressure. In *Semiconductors and Semimetals*; Elsevier, 1998; Vol. 54, pp 145–246. [https://doi.org/10.1016/S0080-8784\(08\)60231-8](https://doi.org/10.1016/S0080-8784(08)60231-8).
- (14) Piltz, R. O.; Maclean, J. R.; Clark, S. J.; Ackland, G. J.; Hatton, P. D.; Crain, J. Structure and Properties of Silicon XII: A Complex Tetrahedrally Bonded Phase. *Phys. Rev. B* **1995**, *52* (6), 4072–4085. <https://doi.org/10.1103/PhysRevB.52.4072>.
- (15) Wentorf, R. H.; Kasper, J. S. Two New Forms of Silicon. *Science* **1963**, *139* (3552), 338–339. <https://doi.org/10.1126/science.139.3552.338-a>.
- (16) Pandolfi, S.; Renero-Lecuna, C.; Le Godec, Y.; Baptiste, B.; Menguy, N.; Lazzeri, M.; Gervais, C.; Spektor, K.; Crichton, W. A.; Kurakevych, O. O. Nature of Hexagonal Silicon Forming via High-Pressure Synthesis: Nanostructured Hexagonal 4H Polytype. *Nano Lett.* **2018**, *18* (9), 5989–5995. <https://doi.org/10.1021/acs.nanolett.8b02816>.

- (17) Kurakevych, O. O.; Le Godec, Y.; Crichton, W. A.; Guignard, J.; Strobel, T. A.; Zhang, H.; Liu, H.; Coelho Diogo, C.; Polian, A.; Menguy, N.; et al. Synthesis of Bulk BC8 Silicon Allotrope by Direct Transformation and Reduced-Pressure Chemical Pathways. *Inorg. Chem.* **2016**, *55* (17), 8943–8950. <https://doi.org/10.1021/acs.inorgchem.6b01443>.
- (18) Zhang, H.; Liu, H.; Wei, K.; Kurakevych, O. O.; Le Godec, Y.; Liu, Z.; Martin, J.; Guerrette, M.; Nolas, G. S.; Strobel, T. A. BC8 Silicon (Si-III) Is a Narrow-Gap Semiconductor. *Phys. Rev. Lett.* **2017**, *118* (14), 146601. <https://doi.org/10.1103/PhysRevLett.118.146601>.
- (19) Bundy, F. P. Phase Diagrams of Silicon and Germanium to 200 Kbar, 1000°C. *J. Chem. Phys.* **1964**, *41* (12), 3809–3814. <https://doi.org/10.1063/1.1725818>.
- (20) Brazhkin, V. V.; Lyapin, A. G.; Popova, S. V.; Voloshin, R. N. Nonequilibrium Phase Transitions and Amorphization in Si, Si/GaAs, Ge, and Ge/GaSb at the Decompression of High-Pressure Phases. *Phys. Rev. B* **1995**, *51* (12), 7549–7554. <https://doi.org/10.1103/PhysRevB.51.7549>.
- (21) Jayaraman, A.; Klement, W.; Kennedy, G. C. Melting and Polymorphism at High Pressures in Some Group IV Elements and III-V Compounds with the Diamond/Zincblende Structure. *Phys. Rev.* **1963**, *130* (2), 540–547. <https://doi.org/10.1103/PhysRev.130.540>.
- (22) Lees, J.; Williams, B. H. J. Combined Very High Pressure/High Temperature Calibration of the Tetrahedral Anvil Apparatus, Fusion Curves of Zinc, Aluminium, Germanium and Silicon to 60 Kilobars. *Nature* **1965**, *208* (5007), 278–279. <https://doi.org/10.1038/208278a0>.
- (23) Voronin, G. A.; Pantea, C.; Zerda, T. W.; Wang, L.; Zhao, Y. *In Situ* x-Ray Diffraction Study of Silicon at Pressures up to 15.5 GPa and Temperatures up to 1073 K. *Phys. Rev. B* **2003**, *68* (2). <https://doi.org/10.1103/PhysRevB.68.020102>.
- (24) Kubo, A.; Wang, Y.; Runge, C. E.; Uchida, T.; Kiefer, B.; Nishiyama, N.; Duffy, T. S. Melting Curve of Silicon to 15GPa Determined by Two-Dimensional Angle-Dispersive Diffraction Using a Kawai-Type Apparatus with X-Ray Transparent Sintered Diamond Anvils. *J. Phys. Chem. Solids* **2008**, *69* (9), 2255–2260. <https://doi.org/10.1016/j.jpcs.2008.04.025>.
- (25) Verburg, P. C.; Smillie, L. A.; Römer, G. R. B. E.; Haberl, B.; Bradby, J. E.; Williams, J. S.; Huis in 't Veld, A. J. Crystal Structure of Laser-Induced Subsurface Modifications in Si. *Appl. Phys. A* **2015**, *120* (2), 683–691. <https://doi.org/10.1007/s00339-015-9238-5>.
- (26) Turneure, S. J.; Sinclair, N.; Gupta, Y. M. Real-Time Examination of Atomistic Mechanisms during Shock-Induced Structural Transformation in Silicon. *Phys. Rev. Lett.* **2016**, *117* (4). <https://doi.org/10.1103/PhysRevLett.117.045502>.
- (27) McBride, E. E.; Krygier, A.; Ehnes, A.; Galtier, E.; Harmand, M.; Konôpková, Z.; Lee, H. J.; Liermann, H.-P.; Nagler, B.; Pelka, A.; et al. Phase Transition Lowering in Dynamically Compressed Silicon. *Nat. Phys.* **2019**, *15* (1), 89–94. <https://doi.org/10.1038/s41567-018-0290-x>.
- (28) Smith, R. F.; Bolme, C. A.; Erskine, D. J.; Celliers, P. M.; Ali, S.; Eggert, J. H.; Brygoo, S. L.; Hammel, B. D.; Wang, J.; Collins, G. W. Heterogeneous Flow and Brittle Failure in Shock-Compressed Silicon. *J. Appl. Phys.* **2013**, *114* (13), 133504. <https://doi.org/10.1063/1.4820927>.
- (29) Rapp, L.; Haberl, B.; Pickard, C. J.; Bradby, J. E.; Gamaly, E. G.; Williams, J. S.; Rode, A. V. Experimental Evidence of New Tetragonal Polymorphs of Silicon Formed through Ultrafast Laser-Induced Confined Microexplosion. *Nat. Commun.* **2015**, *6*, 7555. <https://doi.org/10.1038/ncomms8555>.

- (30) Benuzzi-Mounaix, A.; Mazevet, S.; Ravasio, A.; Vinci, T.; Denoeud, A.; Koenig, M.; Amadou, N.; Brambrink, E.; Festa, F.; Levy, A.; et al. Progress in Warm Dense Matter Study with Applications to Planetology. *Phys. Scr.* **2014**, *T161*, 014060. <https://doi.org/10.1088/0031-8949/2014/T161/014060>.
- (31) Zhang, Y.; Sekine, T.; He, H.; Yu, Y.; Liu, F.; Zhang, M. Shock Compression of Fe-Ni-Si System to 280 GPa: Implications for the Composition of the Earth's Outer Core: Sekine, et al.: Shock Compression of Fe-Ni-Si System. *Geophys. Res. Lett.* **2014**, *41* (13), 4554–4559. <https://doi.org/10.1002/2014GL060670>.
- (32) Hu, S. X.; Fiksel, G.; Goncharov, V. N.; Skupsky, S.; Meyerhofer, D. D.; Smalyuk, V. A. Mitigating Laser Imprint in Direct-Drive Inertial Confinement Fusion Implosions with High-*Z* Dopants. *Phys. Rev. Lett.* **2012**, *108* (19), 195003. <https://doi.org/10.1103/PhysRevLett.108.195003>.
- (33) Weinstein, B. A.; Piermarini, G. J. Raman Scattering and Phonon Dispersion in Si and GaP at Very High Pressure. *Phys. Rev. B* **1975**, *12* (4), 1172–1186. <https://doi.org/10.1103/PhysRevB.12.1172>.
- (34) Welber, B.; Kim, C. K.; Cardona, M.; Rodriguez, S. Dependence of the Indirect Energy Gap of Silicon on Hydrostatic Pressure. *Solid State Commun.* **1975**, *17* (8), 1021–1024. [https://doi.org/10.1016/0038-1098\(75\)90245-8](https://doi.org/10.1016/0038-1098(75)90245-8).
- (35) Gupta, M. C.; Ruoff, A. L. Static Compression of Silicon in the [100] and in the [111] Directions. *J. Appl. Phys.* **1980**, *51* (2), 1072–1075. <https://doi.org/10.1063/1.327714>.
- (36) Anzellini, S.; Wharmby, M. T.; Miozzi, F.; Kleppe, A.; Daisenberger, D.; Wilhelm, H. Quasi-Hydrostatic Equation of State of Silicon up to 1 Megabar at Ambient Temperature. *Sci. Rep.* **2019**, *9* (1), 15537. <https://doi.org/10.1038/s41598-019-51931-1>.
- (37) Militzer, B.; Driver, K. P. Development of Path Integral Monte Carlo Simulations with Localized Nodal Surfaces for Second-Row Elements. *Phys. Rev. Lett.* **2015**, *115* (17), 176403. <https://doi.org/10.1103/PhysRevLett.115.176403>.
- (38) Swift, D. C.; Ackland, G. J.; Hauer, A.; Kyrala, G. A. First-Principles Equations of State for Simulations of Shock Waves in Silicon. *Phys. Rev. B* **2001**, *64* (21), 214107. <https://doi.org/10.1103/PhysRevB.64.214107>.
- (39) Strickson, O.; Artacho, E. Ab Initio Calculation of the Shock Hugoniot of Bulk Silicon. *Phys. Rev. B* **2016**, *93* (9), 094107. <https://doi.org/10.1103/PhysRevB.93.094107>.
- (40) Hu, S. X.; Militzer, B.; Collins, L. A.; Driver, K. P.; Kress, J. D. First-Principles Prediction of the Softening of the Silicon Shock Hugoniot Curve. *Phys. Rev. B* **2016**, *94* (9), 094109. <https://doi.org/10.1103/PhysRevB.94.094109>.
- (41) Hu, S. X.; Gao, R.; Ding, Y.; Collins, L. A.; Kress, J. D. First-Principles Equation-of-State Table of Silicon and Its Effects on High-Energy-Density Plasma Simulations. *Phys. Rev. E* **2017**, *95* (4), 043210. <https://doi.org/10.1103/PhysRevE.95.043210>.
- (42) Paul, R.; Hu, S. X.; Karasiev, V. V. Anharmonic and Anomalous Trends in the High-Pressure Phase Diagram of Silicon. *Phys. Rev. Lett.* **2019**, *122* (12). <https://doi.org/10.1103/PhysRevLett.122.125701>.
- (43) Bartók, A. P.; Kermode, J.; Bernstein, N.; Csányi, G. Machine Learning a General-Purpose Interatomic Potential for Silicon. *Phys. Rev. X* **2018**, *8* (4). <https://doi.org/10.1103/PhysRevX.8.041048>.
- (44) Kaczmariski, M.; Bedoya-Martínez, O. N.; Hernández, E. R. Phase Diagram of Silicon from Atomistic Simulations. *Phys. Rev. Lett.* **2005**, *94* (9). <https://doi.org/10.1103/PhysRevLett.94.095701>.
- (45) Yao, Y.; Klug, D. D. Structural Phase Transitions in Si under Hydrostatic and Uniaxial Compression. *Phys. Rev. B* **2012**, *85* (21). <https://doi.org/10.1103/PhysRevB.85.214122>.

- (46) Yang, C. C.; Li, J. C.; Jiang, Q. Temperature–Pressure Phase Diagram of Silicon Determined by Clapeyron Equation. *Solid State Commun.* **2004**, *129* (7), 437–441. <https://doi.org/10.1016/j.ssc.2003.11.020>.
- (47) Sorella, S.; Casula, M.; Spanu, L.; Dal Corso, A. *Ab Initio* Calculations for the β -Tin Diamond Transition in Silicon: Comparing Theories with Experiments. *Phys. Rev. B* **2011**, *83* (7). <https://doi.org/10.1103/PhysRevB.83.075119>.
- (48) Needs, R. J.; Mujica, A. First-Principles Pseudopotential Study of the Structural Phases of Silicon. *Phys. Rev. B* **1995**, *51* (15), 9652–9660. <https://doi.org/10.1103/PhysRevB.51.9652>.
- (49) Alfè, D.; Gillan, M. J.; Towler, M. D.; Needs, R. J. Diamond and β -Tin Structures of Si Studied with Quantum Monte Carlo Calculations. *Phys. Rev. B* **2004**, *70* (21). <https://doi.org/10.1103/PhysRevB.70.214102>.
- (50) Gaál-Nagy, K.; Strauch, D. Transition Pressures and Enthalpy Barriers for the Cubic Diamond \rightarrow β -Tin Transition in Si and Ge under Nonhydrostatic Conditions. *Phys. Rev. B* **2006**, *73* (13). <https://doi.org/10.1103/PhysRevB.73.134101>.
- (51) Weidner, D. J.; Wang, Y.; Vaughan, M. T. Yield Strength at High Pressure and Temperature. *Geophys. Res. Lett.* **1994**, *21* (9), 753–756. <https://doi.org/10.1029/93GL03549>.
- (52) Dewaele, A.; Fiquet, G.; Andrault, D.; Hausermann, D. P-V-T Equation of State of Periclase from Synchrotron Radiation Measurements. *J. Geophys. Res. Solid Earth* **2000**, *105* (B2), 2869–2877. <https://doi.org/10.1029/1999JB900364>.
- (53) Dewaele, A.; Loubeyre, P.; Mezouar, M. Equations of State of Six Metals above 94 GPa. *Phys. Rev. B* **2004**, *70* (9). <https://doi.org/10.1103/PhysRevB.70.094112>.
- (54) Dorogokupets, P. I.; Oganov, A. R. Ruby, Metals, and MgO as Alternative Pressure Scales: A Semiempirical Description of Shock-Wave, Ultrasonic, x-Ray, and Thermochemical Data at High Temperatures and Pressures. *Phys. Rev. B* **2007**, *75* (2). <https://doi.org/10.1103/PhysRevB.75.024115>.
- (55) Needs, R. J.; Martin, R. M. Transition from β -Tin to Simple Hexagonal Silicon under Pressure. *Phys. Rev. B* **1984**, *30* (9), 5390–5392. <https://doi.org/10.1103/PhysRevB.30.5390>.
- (56) Lewis, S. P.; Cohen, M. L. Theoretical Study of High-Pressure Orthorhombic Silicon. *Phys. Rev. B* **1993**, *48* (21), 16144–16147. <https://doi.org/10.1103/PhysRevB.48.16144>.

Appendix Chapter 4

Appendix 4.1: Pressure, atomic volumes and pressure evolution for each experimental run

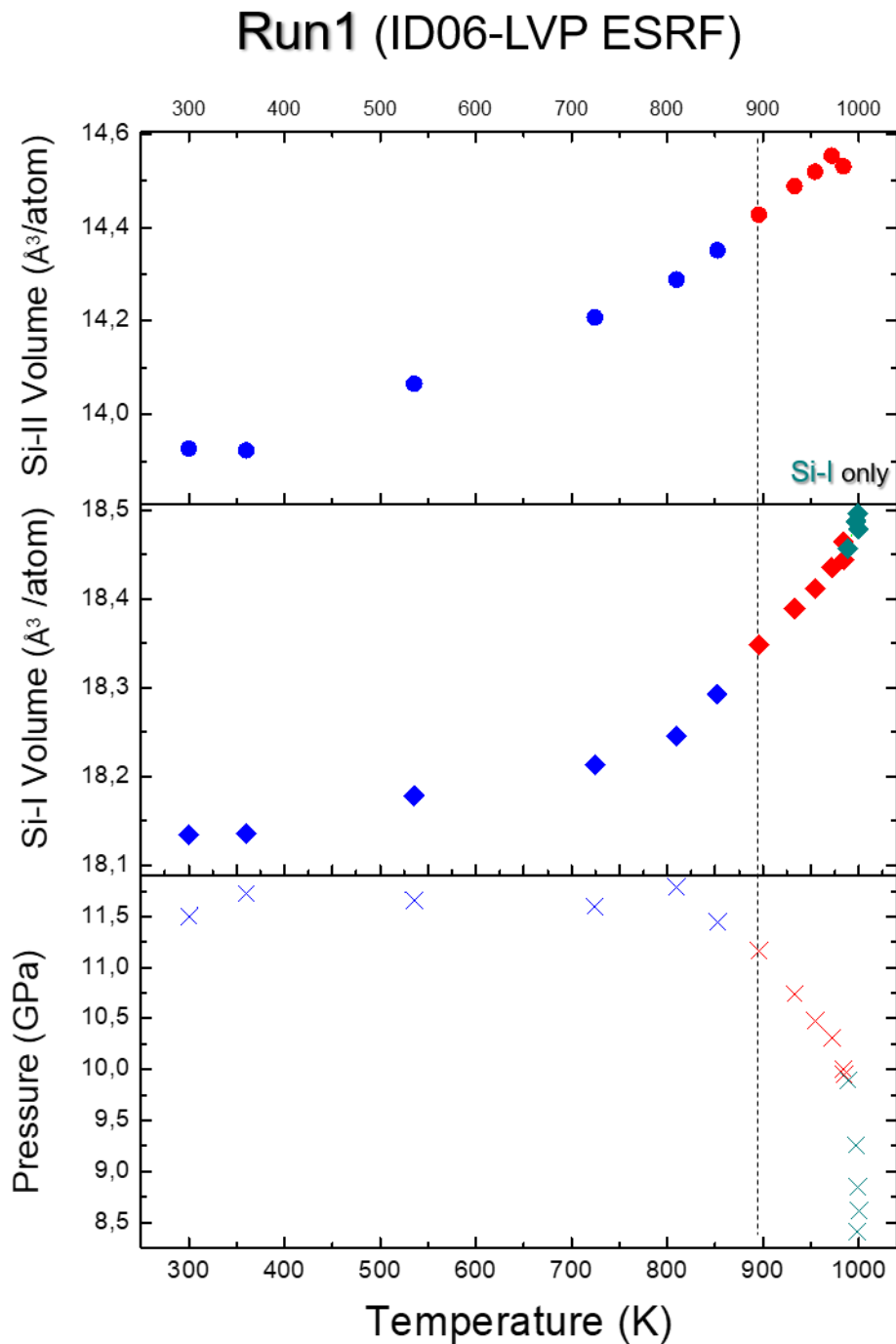


Figure 4.5 : Atomic volumes of Si-I and Si-II and pressure as a function of temperature for Run1 (ID06-LVP beamline at the ESRF synchrotron). Blue symbols stand for measurements at quasi-constant pressure, while red points indicate the pressure drop observed upon heating. Light blue symbols correspond to the point collected after Si-II melting, thus when only Si-I was present.

Run2 (ID06-LVP ESRF)

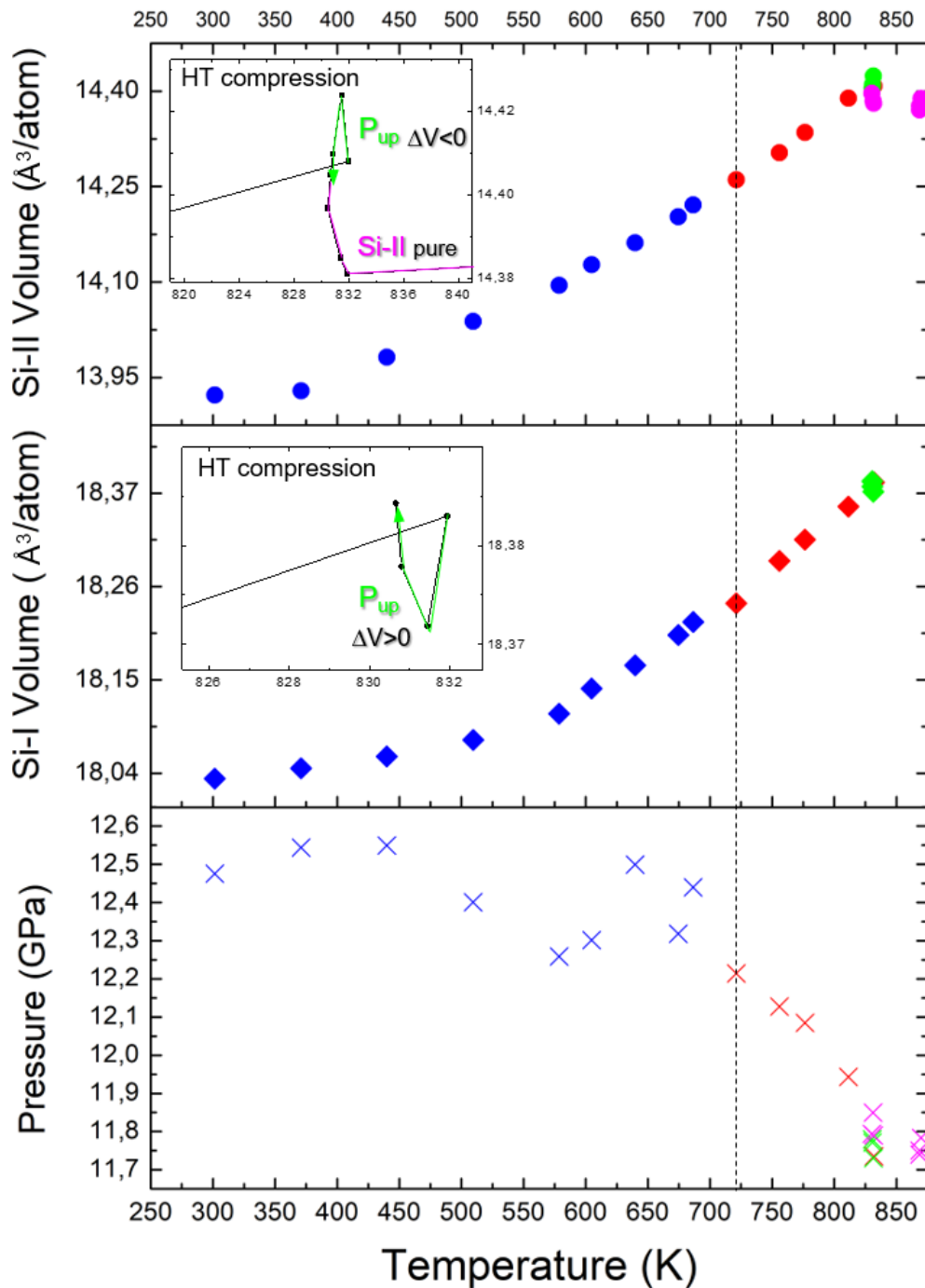


Figure 4.6 : Volumes and pressure as a function of temperature for Run2 (ID06-LVP beamline at the ESRF synchrotron). Blue symbols stand for measurements at quasi-constant pressure, while red points indicate the pressure drop observed upon heating. Light green symbols are used for the measurements during re-compression at high temperature, and pink ones are used when only Si-II is observed, thus at the completion of Si-I \rightarrow Si-II transition. In the inset, a zoom of the volumes of Si-I and Si-II as a function of temperature is reported to evidence their opposite behaviour. While, upon increasing the load, Si-II expands and then starts to shrink. Si-I does exactly the opposite.

Run3 (PSICHE Soleil)

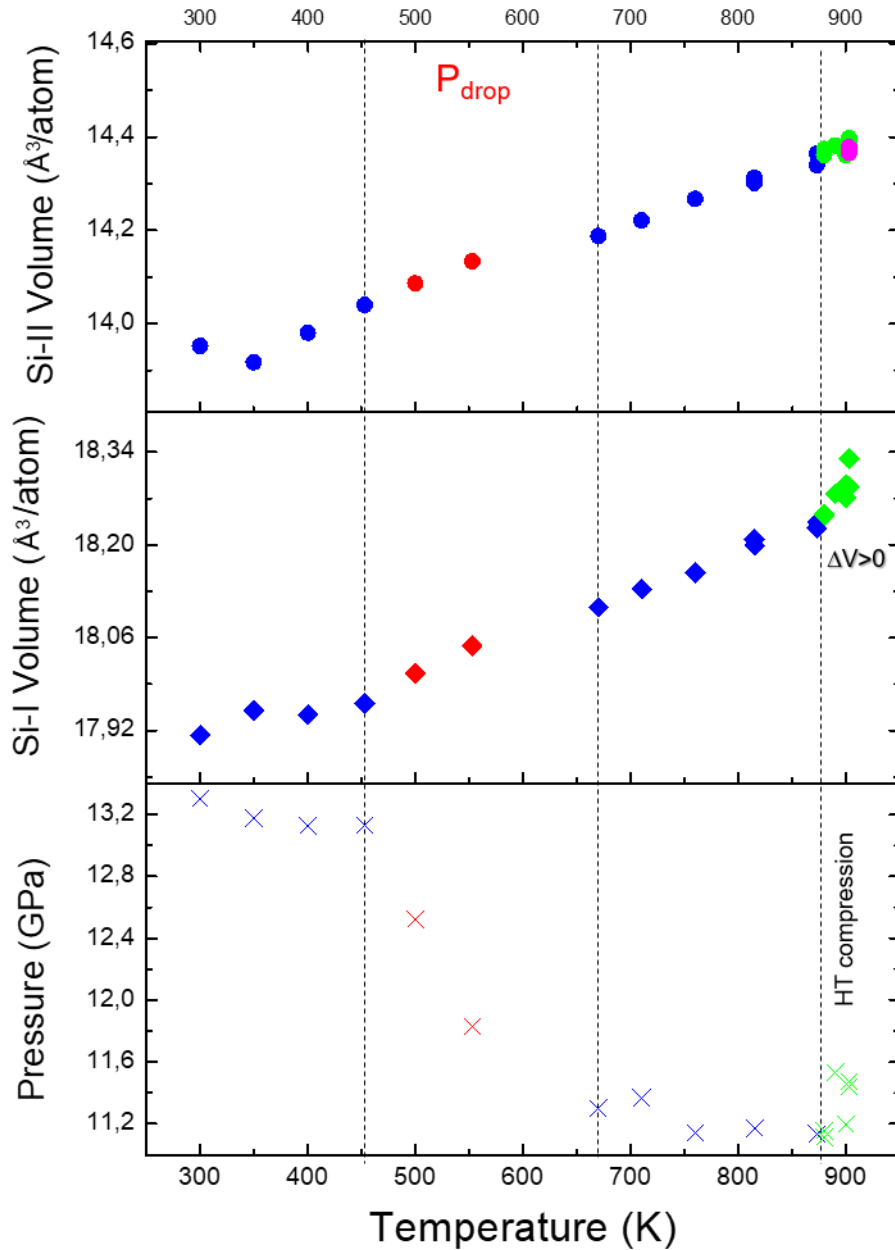
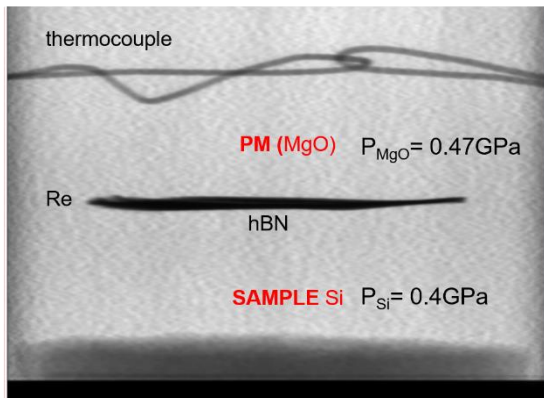


Figure 4.7 : Volumes and pressure as a function of temperature for Run3 (PSICHE beamline at Soleil synchrotron). Blue symbols stand for measurements at quasi-constant pressure, while red points indicate the pressure drop observed upon heating. Light green symbols are used for the measurements during re-compression at high temperature, and pink ones are used when only Si-II is observed, thus at the completion of Si-I→Si-II transition.

Appendix 4.2: x-ray radiography on PSICHE beamline

(a) before compression



(b) after compression

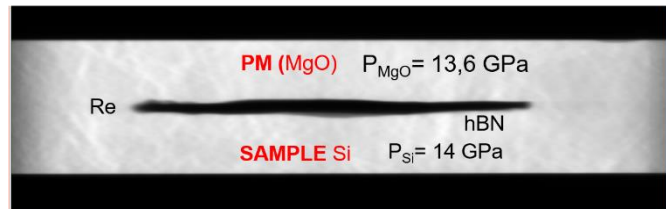


Figure 4.8 : X-Ray imaging *in-situ* on PSICHE beamline allows to determine the position of both the sample and the pressure calibrant during the experiment. A rhenium foil (easily visible for its higher density) and a hBN plug separate the MgO from the Si.

Appendix 4.3: Qualitative evaluation of hydrostaticity during Run3

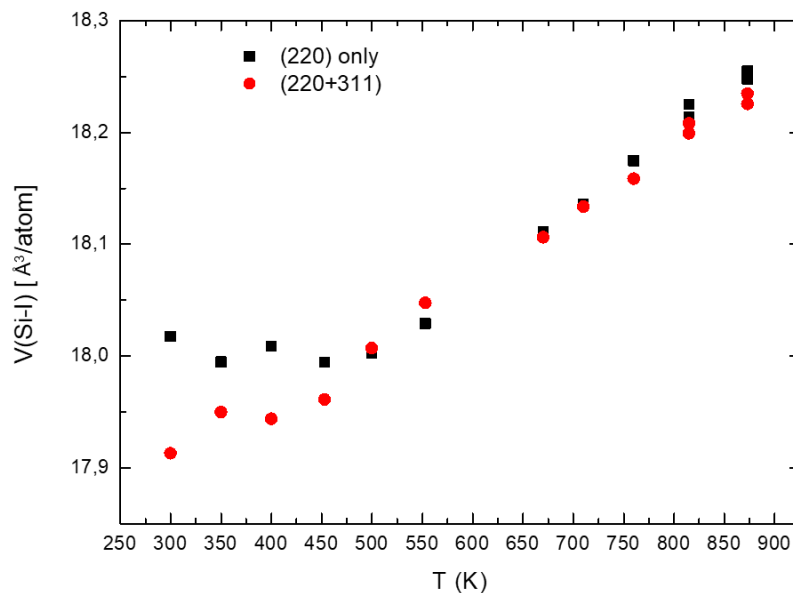


Figure 4.9 : qualitative estimation of the degree of hydrostaticity of the high-pressure cell can be obtained by comparing the volumes obtained via single-peak fitting or whole profile fitting. In hydrostatic condition, the values should coincide

Appendix 4.4: Run4, K:Si(1:6)

The figure shows a larger part of the HP-HT experiment during which we observed the second-order Si-II \rightarrow Si-XI transition. It is visible in the figure that, upon Si-I \rightarrow Si-II transformation, the pressure drops to 10.2 GPa. The value increases subsequently, when there is the simultaneous appearance of the triplet of peaks centred around 7.5 $^\circ$ (i.e. a K-Si compound) and the split of Si-II (i.e. continuous deformation into orthorhombic Si-XI).

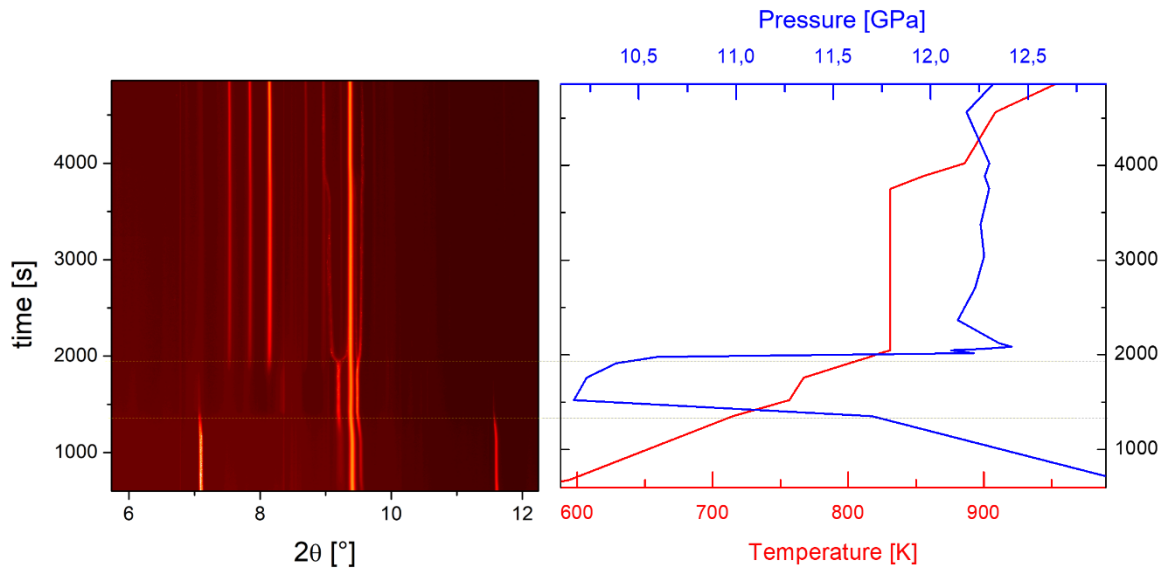


Figure 4.10 : Si-II \rightarrow Si-XI transition studied by *in-situ* high-pressure data from experiments on ID06-LVP beamline. Left: the colormaps show the evolution of the XRD pattern over time (y axis); on the x axis, the 2θ angles at 33 keV ($\lambda=0.3757\text{\AA}$) are represented. Right: pressure and temperature variations during the HP-HT experiment. Pressure was measured from Ta EOS.

Chapter 5:

Nature of hexagonal Si forming via high-pressure synthesis: nanostructured hexagonal 4H polytype.

Hexagonal Si allotropes are expected to enhance light absorption in the visible range as compared to common cubic Si with diamond structure. Therefore, synthesis of these materials is crucial for the development of Si-based optoelectronics. In this chapter our recent results on the synthesis and characterization of hexagonal “Si-IV” are presented. We could quench pure Si-II and transform it into hexagonal Si by combining *in-situ* X-Ray Diffraction during high-pressure high-temperature synthesis and subsequent annealing under vacuum. We provide the first evidence of a polycrystalline bulk sample of hexagonal Si. Exhaustive structural analysis, combining fine-powder X-ray and electron diffraction, afforded resolution of the crystal structure. We demonstrate that hexagonal Si obtained by high-pressure synthesis corresponds to Si-4H polytype (ABCB stacking), in contrast with Si-2H (AB stacking) proposed previously. Further physical characterization, combining experimental data and *ab-initio* calculations, have shown a good agreement with the established structure. The content of this chapter has been published in : *Nano Letters* **189** 5989-5995 (2018).

Silicon (Si) is one of the most widely employed materials in photovoltaic industry¹, a field in which its predominant role has been determined by the favourable combination of huge availability, low-cost and non-toxicity. Still, Si at ambient conditions has a diamond-like structure (d-Si) and is an indirect bandgap semiconductor, which prevents it from efficiently interacting with light². To increase such efficiency, Si allotropes with tunable and/or direct bandgap are highly desirable³⁻⁵. Enhancement of Si absorption in the visible region would indeed open the way for Si-based photovoltaic modules able to reduce both costs and environmental impact^{6,7} taking a further step towards a 100% green energy.

A wide variety of Si allotropes with new crystal structures have been predicted by explorative *ab-initio* algorithms. These allotropes are expected to be metastable at ambient conditions⁸⁻¹⁶ and several among them would have a direct bandgap and strong absorbance in the visible region^{12,13,13-16}, being suitable candidates for photovoltaics. Therefore, a major challenge for both material science and industrial applications consists in the actual synthesis of these new structures. This can be achieved by sophisticated out-of-equilibrium chemical routes¹⁷⁻²¹, as well as by using pressure²²⁻²⁴ as a thermodynamic parameter to stabilize new

structures. Another way to modify the properties of Si is to act on the crystal size. In particular, nanostructure greatly impacts the efficiency of light-matter interaction, with interesting implications for photovoltaics^{25–27}. Confinement on a nanometric scale can indeed modify the optical^{28–30} properties, allowing the design of materials with tunable optoelectronic properties.

Looking towards future applications, the synthesis of high-purity nanoparticles is required to ensure high charge-carrier lifetime^{34,35} and to improve device performance. For this purpose, pressure-induced nanostructuration has been proven the method of choice, as the solid-to-solid transformation ensures that the synthesized ingot maintains the purity of the starting material^{36,37} and it is thus preferable to chemical methods³⁸. Moreover, high-pressure (HP) synthesized samples can range from well crystallized to strained nanostructures; crystal morphology can modify the optoelectronic properties dramatically, to the point of obtaining strain-induced direct bandgaps^{39,40}.

HP research on Si started more than 50 years ago and since then several allotropes⁴¹, displaying a wide variety of physical properties, have been reported. The narrow-bandgap semiconductor Si-III⁴² with BC8 structure (originally believed to be semimetal⁴³) was obtained from the high-pressure tetragonal metallic phase, Si-II⁴⁴, which becomes superconductor below 6.3 K⁴⁵. Such transformation during decompression can be either direct, Si-II→Si-III⁴⁶, or with an intermediate step Si-II→Si-XII→Si-III^{47,48}. Upon heating Si-III at ambient pressure a hexagonal structure, named Si-IV, was observed⁴⁶.

This allotrope was believed to be a structural analogue of the hexagonal diamond found in meteorites (called also *lonsdaleite*⁴⁹) with the 2H polytype structure. Polytypes are allotropes that differ for the stacking sequence along one direction: in the case of Si, hexagonal (H) polytypes can be obtained by modifying the ABC stacking of the hexagonal buckled planes along the [111] direction. Calculations have predicted several hexagonal polytypes of Si and of other Group-IV elements to be metastable, such as 2H (AB), 4H (ABCB) and 6H (ABCACB)^{50–52}. Over the last decades, Si-IV obtained from both HP^{43,46,53–55} and chemical synthesis⁵⁶ has been identified in literature as Si-2H polytype despite compelling evidence is still missing, as no structural refinement has been reported. It is worth stressing that alternative polytypes, namely Si-4H and Si-6H, are energetically more favourable⁵². These allotropes have been observed^{57–59} in polycrystalline Si nanostructures^{57–59}, but no pure microcrystalline phase has ever been reported. Until now, a hexagonal 2H-like arrangement of Si atoms (as suggested for Si-IV) was demonstrated only by epitaxial growth during chemical-vapor deposition on a GaP

nanowire (NW) core⁶⁰. The structure of the hexagonal Si shells has been unambiguously proven by Transmission Electron Microscopy and X-Ray Diffraction, and the process has been successfully applied to obtain GaP/Si/SiGe NWs⁶¹.

Lonsdaleite-like Si-2H should exhibit an enhanced absorption in the visible region with respect to d-Si, as predicted by Empirical or Model Pseudopotentials^{62,63}, as well as many-body perturbation theory^{39,64}. These predictions should apply also for other hexagonal polytypes of Si, as they are expected to have similar optoelectronic properties⁶⁵. Moreover, the bandgap should become direct in the presence of strain³⁹ or in low-dimensional systems, such as hexagonal Si NWs⁶⁶; in this field, intriguing possibilities are also offered by the synthesis of Ge and SiGe hexagonal NWs^{57,67}. Briefly, hexagonal polytypes of Si, both bulk and nanostructures, could have a key role in the future of Si-based optoelectronics and photovoltaics.

In this Chapter we provide the first evidence and physical characterization of a bulk Si sample with purely hexagonal crystal symmetry. The sample is obtained in a multi-anvil press, in which triaxiality of compression and decompression ensures higher hydrostaticity compared to previous experiments (Diamond Anvil Cell^{43,54} and opposed-anvil toroid geometry⁵⁵). First, we detail the synthesis route that combines *in-situ* high-pressure high-temperature (HP-HT) synthesis of Si-III (probed by diffraction of synchrotron radiation) and subsequent primary-vacuum heating at moderate temperature. In the second part, a detailed characterization of the crystal structure and physical properties of this new allotrope is presented. An accurate analysis of the structure, combining Rietveld analysis of X-Ray Diffraction (XRD) pattern, Selected-Area Electron Diffraction (SAED) and Transmission Electron Microscopy (TEM) measurements, has allowed us to unambiguously determine the crystal structure of the sample. “Si-IV” phase obtained through HP is Si-4H polytype, in contrast with the previously suggested structure for Si-IV, i.e. *lonsdaleite*-like Si-2H polytype⁴⁶. Raman spectroscopy and Nuclear Magnetic Resonance (NMR) data, combined with computer simulations based on Density Functional Theory (DFT), give results compatible with the proposed structural model. Si-4H

shows also a strong Photoluminescence (PL) emission in a range of interest for future photovoltaic devices.

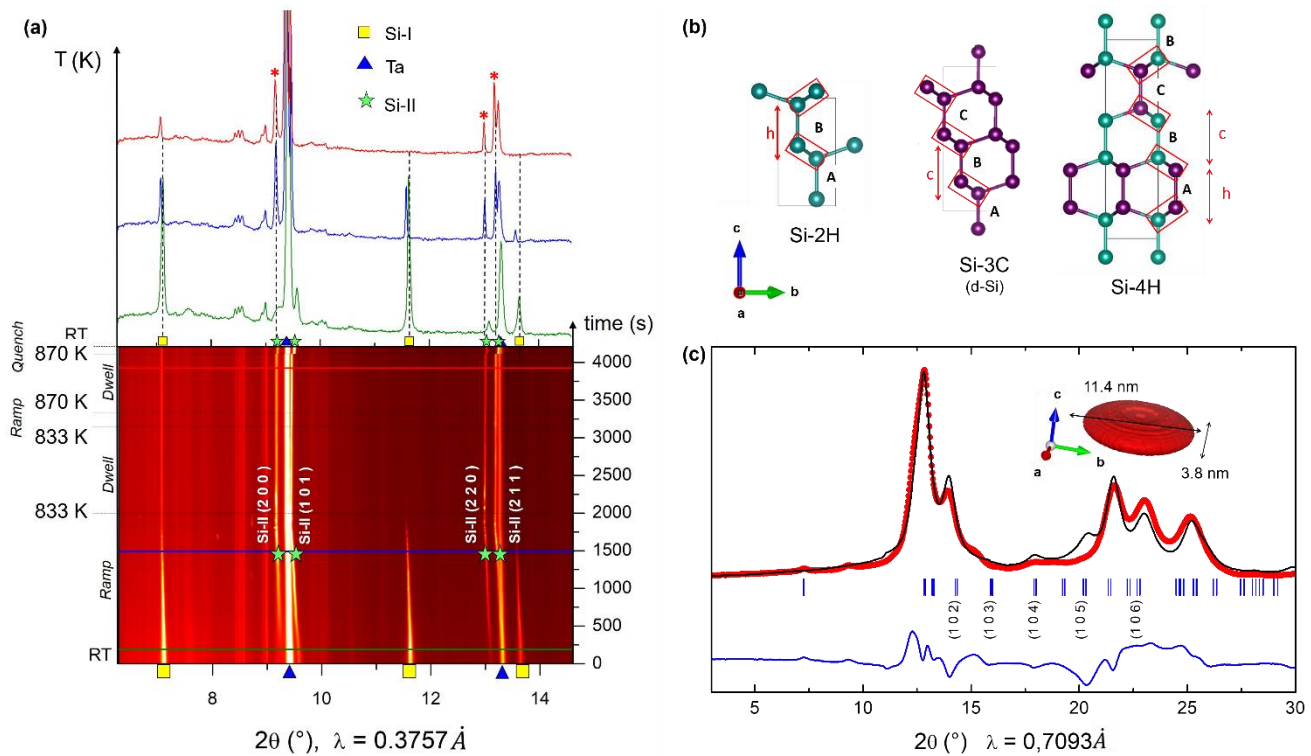


Figure 5.1 : (a) HP-HT synthesis. Colormap showing the evolution of XRD patterns at 13 GPa; time goes upward along the y axis. In the upper panel, the patterns corresponding to the coloured lines traced on the 2D colormap are reported; Si-II peaks are highlighted by the red symbol * in the final (red) pattern. (b) Schematic view of different Si polytypes. The red rectangles evidence Si dumbbells forming the hexagonal planes. In Si-2H and Si-3C (i.e. d-Si) planes are all in the hexagonal (twisted consecutive dumbbells) or in the cubic configuration respectively, while in Si-4H these two configurations alternate. The presence of both cubic and hexagonal dumbbells give rise to two inequivalent atomic position, evidenced by atoms of different colours. (c) Structure investigation through Powder-XRD. Experimental data collected with a Mo anode are represented by red dots; the black line corresponds to the best Rietveld fit; the blue line represents the difference between experimental and calculated pattern. In addition, Bragg reflections of Si-4H are represented with the blue symbols. A schematic view of the crystallites shape and size is reported.

Synthesis of the Si-III (BC8) precursor was performed at the European Synchrotron Radiation Facility (ESRF) in Grenoble (France), employing the large-volume multi-anvil press on ID06 beamline⁶⁸. Si-I powder (Alfa Aesar, 99.999% purity) has been used as starting material. The sample was placed into a 10/5 multi-anvil assembly in an argon inert atmosphere; an hexagonal boron nitride capsule was employed to avoid chemical reactions with the tantalum foil heater. Synchrotron radiation allowed to collect XRD patterns in real time during the whole HP-HT treatment (see also Appendix 5.1). The sample was heated at 833 K and subsequently at 870 K for a total of 45 minutes under a quasi-constant pressure of ~13 GPa (according to Si-

I equation of state). The evolution of the XRD patterns over time indicates the structural changes during the heating, as reported in Figure 5.1(a). Our *in-situ* observations allowed us to ensure the complete transformation Si-I→Si-II at HP-HT and to recover pure Si-III upon releasing pressure. Finally, heating of the Si-III sample was performed in a vacuum oven at 500 K for 2 hours in order to obtain the hexagonal phase. The recovered sample has shown to be metastable at ambient condition, but it does not transform back into Si-III precursor or any other Si form even after several months in air.

The structure of the recovered sample has been analysed by Powder-XRD (PXRD) data and Rietveld^{69,70} refinement using the FullProf Suite software^{71,72}. As starting point for structural refinement, a number of polytypes among the most probable ones (2H, 3C, 4H, 6H) have been tested both as individual phases and in mixtures. The only Rietveld fit compatible with experimental data, presented in Figure 5.1(c), was obtained using Si-4H polytype, *viz.* a cell made of 4 buckled hexagonal planes with ABCB stacking along the *c* axis. The ideal structure of hexagonal polytypes can be constructed from d-Si by modifying the sequence of the {111} hexagonal planes, maintaining the hexagonal lattice parameter $a_{hex} = a_{d-Si}/\sqrt{2}$.

The *n*H polytypes differ along the [001] axis so that the hexagonal lattice parameter, c_{hex} , can be estimated as $n \times d(111)$, or $n \times a_{d-Si}/\sqrt{3}$. With $a_{d-Si} = 5.4303 \text{ \AA}$, both the 2H and 4H polytypes share an approximate $a_{hex} = 3.8398 \text{ \AA}$, while $c_{2H} = 6.270 \text{ \AA}$ and 4H is twice this, at $c_{4H} = 12.540 \text{ \AA}$ (see also Figure 5.1(b)). The refined structure of the sample shows a contraction of around 1.18% of the in-plane parameter a_{4H} with respect to the ideal case, while the average interplanar distance c_{4H}/n is 1.33% larger than that of d-Si, $d(111)$. Previous DFT calculations^{50,52} had already reported shrinking of a_{hex} , but the computed contractions were below 1%. We observe in our Si-4H sample a further distortion of the tetrahedral bond angles with respect to d-Si, which results in a more pronounced buckling of Si-4H hexagonal planes. The additional corrugation causes a reduction of interatomic distances in the hexagonal planes and a subsequent increase of their thickness, which is coherent with our values for both a_{hex} and c_{4H}/n . This result, along with the incorrect evaluation of (10 l) reflections intensity in the fit (Figure 5.1(c)) led us to further investigate the Si-4H structure.

The crystallites shape has been determined by refinement of spherical harmonic coefficients Y00 and Y20 as implemented in FullProf⁷¹. The Rietveld fit suggests a flake-like configuration. There is thus a strong anisotropy in the crystallites morphology, with the average

flakes height (3.8 nm) markedly smaller than the estimated diameter (11.4 nm), as shows the sketch in Figure 5.1(c). This can explain the non-uniform broadening of PXRD peaks.

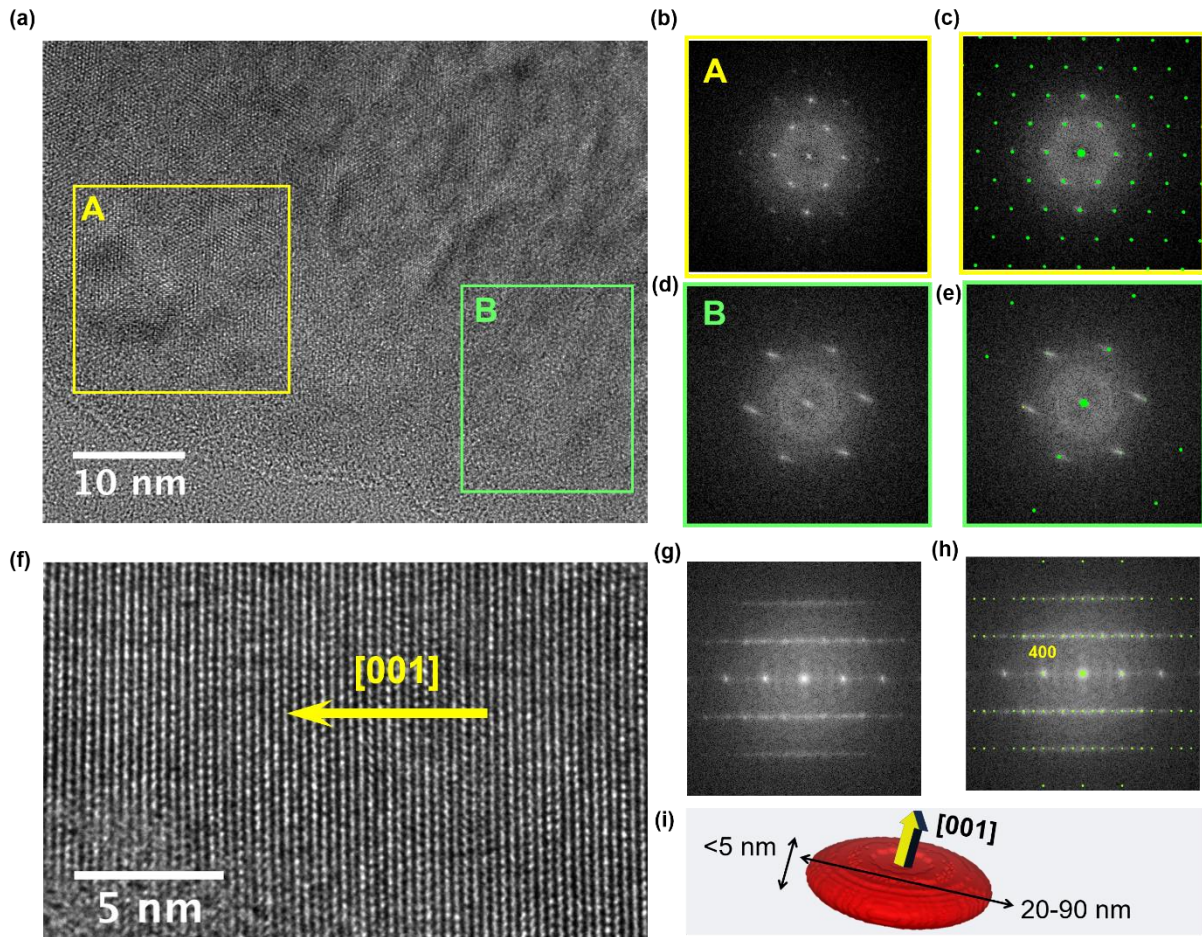


Figure 5.2 : (a) High-Resolution TEM image; two different domains, A and B, are evidenced. FFT-TEM of the A and B are reported in (b) and (d). Both domains have Si-4H structure, as shown in (c) and (e) where the simulation of Si-4H reciprocal space along [001] and $[2\bar{2}3]$ directions respectively has been superposed to the pattern. (f) HR-TEM image of the hexagonal planes stacking; the corresponding FFT-TEM pattern and the simulated Si-4H [010] are shown in (g) and (h). (i) A schematic view of the crystallites shape and size as determined by TEM.

A local analysis of the grains' structure has been conducted at nanometric scale by TEM. Combining TEM direct-space images and Fast-Fourier Transform TEM (FFT-TEM) has enabled us to verify the flake-like configuration by determining the size of the coherent scattering domains. Figure 5.2(f) shows the stacking of the hexagonal planes along the c axis, i.e. [001] direction. The resolution does not allow the observer to distinguish the arrangement of the Si dumbbells, but thanks to FFT-TEM we can confirm the flake size to be just a few nm along the c axis. Indeed, it was not possible to isolate FFT-TEM single-crystal domains along

this direction; since the coherence length of the instrument is 5 nm, this sets 5nm as the upper limit for flakes' height. The typical FFT-TEM collected patterns (Figure 5.2(g-h)) are compatible with Si-4H theoretical one along [010], the unidirectional broadening of the spots along [001] indicating the presence of stacking faults (SFs). We therefore conclude that the flake configuration is induced by the SFs, which separates crystallites limiting dimensions along the *c* axis. The in-plane hexagonal pattern instead presents well defined spots, as shown in Figure 5.2(b-c). All the examined regions have been identified using the Si-4H structural model and they are coherent over relatively large domains, ranging from 20 nm up to 90 nm. It is worth stressing that all the FFT-TEM patterns here reported are not compatible with Si-2H nor Si-6H polytypes (see Figure 5.2(a-e) and Appendix 5.2 for further discussion regarding Si-4H and SFs identification through FFT-TEM).

The flake-like structure of the crystallites delimited by stacking faults and the sizes measured by TEM can explain the inconsistency between experimental and calculated PXRD patterns in Figure 5.1(c). A simplified model was employed in the Rietveld refinement to simulate the anisotropic shape. The effective anisotropy, as seen in TEM images, is more pronounced: 20 – 90 nm \times < 5 nm, compared to 11.4 nm \times 3.8 nm of Rietveld fit. We would thus expect further attenuation and widening of the (1 0 *l*) reflections, which is compatible with the experimental data (Figure 5.1(c)). It is worth noting that, despite the different accuracies, XRD and TEM measurements unambiguously confirm the same polytypic structure and crystallite shape of the sample.

Obtaining a large-volume sample has enabled us to measure ^{29}Si NMR of the recovered sample, providing a first reference for hexagonal Si. DFT^{73,74} was used to compute the expected NMR spectra for different polytypes (see also Appendix 5.3-5.4). According to the number of independent crystallographic positions per unit cell, we expect two NMR signals to appear for Si-4H, at -127.7 ppm and -96.9 ppm, corresponding to the 4e and 4f Wyckoff positions of space group $P6_3/mmc$ respectively. From the experimental data reported in Figure 5.3 together with the computed signals for Si polytypes, we see two peaks, shifted of ~ 10 ppm with respect to the DFT prediction for Si-4H. The identification of a doublet demonstrates the presence of more than one crystallographic position, confirming that the hexagonal Si recovered from HP does not correspond to a Si-2H polytype. The signal at around -50 ppm, already observed in the HP-HT synthesis of Si-III⁷⁵, can be explained by the presence of stacking faults. The results of ^{29}Si NMR measurements are thus coherent with previous structural investigations. It is also

important to stress that no signal corresponding to Si-III is observed, confirming the completion of Si-III \rightarrow Si-4H transformation. In future, the use of ^{29}Si as starting material could help to improve the quality of the data for a clearer interpretation of ^{29}Si NMR spectra.

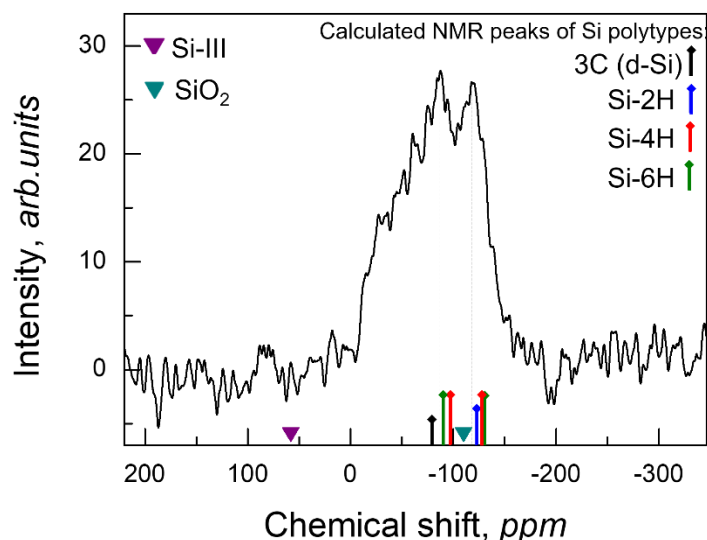


Figure 5.3 : ^{29}Si NMR measurements of Si-4H; vertical lines show evidence of a doublet. On the x axis, experimental chemical shifts of Si-III and SiO₂ (triangles) together with the DFT results for Si polytypes are reported for comparison.

A Raman spectrum is reported in Figure 5.4(a). We observe a smooth increase of intensity from 410 cm^{-1} , in contrast with the steep decrease of the high-energy side of the spectrum from 510 cm^{-1} . A straightforward identification of Raman peaks is not possible. Several theoretical studies have already addressed the vibrational and optical properties of Si-2H^{65,76–78}, but an investigation of different hexagonal polytypes is still missing (with the exception of a study concerning Si NWs⁷⁹). We have thus performed DFT^{73,74} simulations of Raman spectra for 2H, 4H and 6H bulk crystals (see also Appendix 5.3-5.4), reported in Figure 5.4(b). In agreement with previous literature^{76,80}, we predict two Raman peaks in the Si-2H spectrum, corresponding to E_{2g} mode and to the quasi degenerate E_{1g} and A_{1g} modes, respectively (see also Appendix 5.3). This degeneracy is no longer present in Si-4H and Si-6H, hence a minimum of three distinct Raman peaks appears in the spectra. The computed Si-4H spectrum is compatible with measurements and it is the only one showing a Raman active mode below 420 cm^{-1} , in the range of the observed low-energy tail. Reduced size of crystallites can induce broadening and asymmetry of the Raman active peaks in d-Si^{81,82}, while residual stress can cause shift of the Raman modes⁸³. These effects are however too small to quantitatively explain the extension of the presently measured low-energy tail.

This feature is not uncommon^{53,84,85} and we attribute it to the specific shape of the present crystallites (few nm thin flakes, highly ordered in the directions parallel to the hexagonal plane) or, equivalently, to the presence of stacking faults in the sequence of the hexagonal planes.

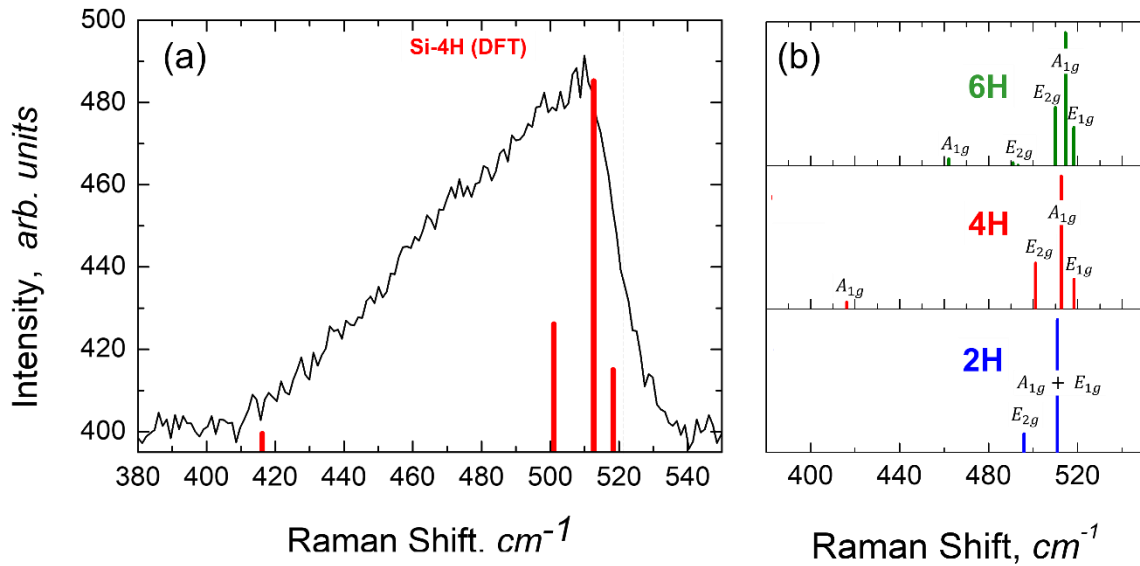


Figure 5.4 : Raman measurements and DFT calculations. Upper panels: Raman spectra as predicted by DFT calculations for three different polytypes. Lower panel: experimental data obtained with a green laser ($\lambda = 514.5 \text{ nm}$) as exciting radiation in back-scattering geometry, compared to the Si-4H Raman spectrum from DFT. The vertical dashed line corresponds to the Raman shift of the d-Si optical phonon at 52 cm^{-1} .

PL measurements, performed at ambient temperature with a blue laser ($\lambda = 460 \text{ nm}$) as exciting radiation, evidence a strong emission in the NIR-Visible region, as reported in Figure 5.5: the emission peak is centred around 750 nm , i.e. 1.65 eV and exhibits a large superposition with solar spectrum in the visible region. The origin of the emission has still to be verified, as similar results have already been reported in cubic Si nanostructures (NWs⁸⁶, porous Si^{87,88} and nano-particles⁸⁹) and thus cannot be directly ascribed to hexagonal Si. Generally, visible emission in Si nanostructures has been explained as a consequence of confinement^{28,29,88,89}. Confinement is expected to cause a blue-shift of the electronic states, raising the value of the band-gap³⁰ while increasing the efficiency of radiative recombination thanks to carrier concentration and indirect space delocalization⁹⁰. It is unlikely that the Si-4H PL emission is caused by the presence of SFs, as the effects of Si dislocations and defects were observed at lower energies^{86,91}. Si-4H PL emission could be instead compatible with a direct transition at the Γ point, as already reported in B-doped wurtzite (thus 2H structure) Si NWs⁹². Indeed, *ab initio* calculations predict that the strain of Si-Si bonds should induce a direct

bandgap in Γ in both cubic⁴⁰ and hexagonal³⁹ Si, as well as in Si NWs with diameters up to 9-11 nm²⁹.

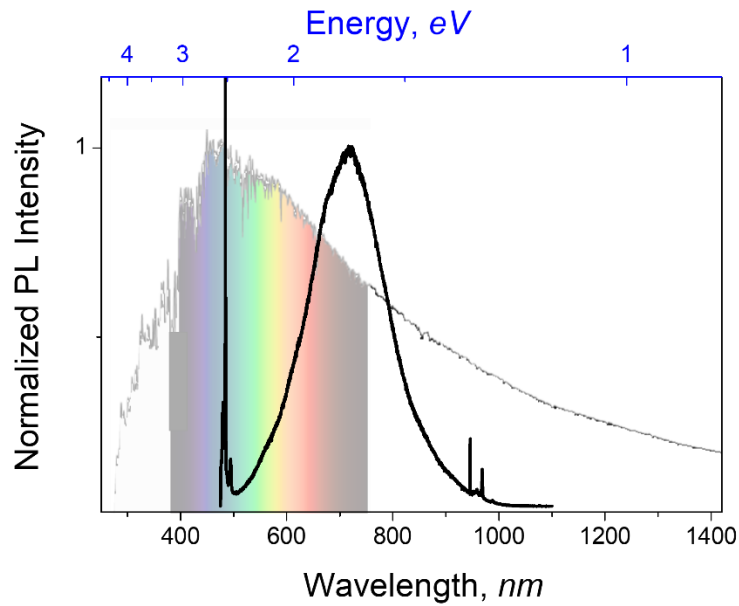


Figure 5.5 : Photoluminescence spectrum of Si-4H at ambient condition, using a blue laser ($\lambda = 460 \text{ nm}$). Solar spectrum irradiance is reported on the background to evidence the large superposition of the sample emission with the visible region.

At the present moment our measurements do not allow us to distinguish whether the bandgap of this newly synthesized material is direct, nor whether its value is determined by the flakes' size or by the hexagonal crystal symmetry (see further discussion on Appendix 5.3). In the future, systematic studies should be conducted with varying Si-4H crystallite sizes and by comparing the results with cubic d-Si nanostructures. If possible, synthesis of different polytypes, such as Si-2H and Si-6H, would complete the picture, investigating separately the influence of crystal structure and size on the optoelectronic properties of hexagonal Si nanostructures. Despite the uncertainty regarding its origin, visible PL emission is of great interest for future employ in photovoltaic applications. Indeed, assuming that absorption band of Si-4H and emission spectra of the sun overlaps as for the PL spectra, we can conclude that nanostructured hexagonal Si-4H polytype is more efficient than commonly used cubic d-Si in absorbing visible light. This feature could play an important role in the development of Si-based solar panels, as employ of Si-4H as absorber would allow to reduce thickness of the absorbing layer while increasing efficiency.

Our synthesis route has demonstrated to be an efficient way to obtain hexagonal Si crystals. This peculiar approach results in high-purity ingots, suitable for future

characterizations able to shed light on the physical properties of hexagonal Si polytypes. Use of HP-HT synthesis for precursor Si-III constitutes a twofold advantage. On one side it allows us to obtain large-volume samples while, on the other hand, the nanostructured morphology could confer new and exotic properties. The challenge for the future is to deeply understand the growth mechanism of hexagonal Si polytype, with the aim of bandgap engineering through a combined polytype/size control.

Acknowledgments: the synthesis has been performed on ID-06-LVP beamline at the ESRF with the help from Carlos Renero-Lecuna (IDIVAL), Kristina Spektor (ESRF) and Wilson Crichton (ESRF). Benoit Baptiste (IMPMC) and Nicolas Menguy (IMPMC) helped collecting and analysing the XRD and TEM data respectively. Michele Lazzeri (IMPMC) helped and supervised the Raman spectra DFT simulations. Christel Gervais (LCMCP) performed the ^{29}Si NMR measurements and simulations. Kevin Beneut (IMPMC) and Kirill Cherednichenko (LSPM) helped in Raman and PL measurements respectively.

References Chapter 5

- (1) Glunz, S. W.; Preu, R.; Biro, D. Crystalline Silicon Solar Cells. In *Comprehensive Renewable Energy*; Elsevier, 2012; pp 353–387. <https://doi.org/10.1016/B978-0-08-087872-0.00117-7>.
- (2) *Properties of Crystalline Silicon*; Hull, R., Institution of Electrical Engineers, Eds.; EMIS datareviews series; INSPEC: London, 1999.
- (3) Shockley, W.; Queisser, H. J. Detailed Balance Limit of Efficiency of *P-n* Junction Solar Cells. *J. Appl. Phys.* **1961**, *32* (3), 510–519. <https://doi.org/10.1063/1.1736034>.
- (4) Archer, M. D.; Bolton, J. R. Requirements for Ideal Performance of Photochemical and Photovoltaic Solar Energy Converters. *J. Phys. Chem.* **1990**, *94* (21), 8028–8036. <https://doi.org/10.1021/j100384a011>.
- (5) Vos, A. D. Detailed Balance Limit of the Efficiency of Tandem Solar Cells. *J. Phys. Appl. Phys.* **1980**, *13* (5), 839–846. <https://doi.org/10.1088/0022-3727/13/5/018>.
- (6) Kazmerski, L. L. Solar Photovoltaics R&D at the Tipping Point: A 2005 Technology Overview. *J. Electron Spectrosc. Relat. Phenom.* **2006**, *150* (2–3), 105–135. <https://doi.org/10.1016/j.elspec.2005.09.004>.
- (7) Braga, A. F. B.; Moreira, S. P.; Zampieri, P. R.; Bacchin, J. M. G.; Mei, P. R. New Processes for the Production of Solar-Grade Polycrystalline Silicon: A Review. *Sol. Energy Mater. Sol. Cells* **2008**, *92* (4), 418–424. <https://doi.org/10.1016/j.solmat.2007.10.003>.
- (8) Demkov, A. A.; Windl, W.; Sankey, O. F. Expanded-Volume Phases of Silicon: Zeolites without Oxygen. *Phys. Rev. B* **1996**, *53* (17), 11288–11291. <https://doi.org/10.1103/PhysRevB.53.11288>.
- (9) Gryko, J.; McMillan, P. F.; Marzke, R. F.; Ramachandran, G. K.; Patton, D.; Deb, S. K.; Sankey, O. F. Low-Density Framework Form of Crystalline Silicon with a Wide Optical Band Gap. *Phys. Rev. B* **2000**, *62* (12), R7707–R7710. <https://doi.org/10.1103/PhysRevB.62.R7707>.
- (10) Zhao, H.-Y.; Wang, J.; Ma, Q.-M.; Liu, Y. Sp³-Bonded Silicon Allotropes Based on the Kelvin Problem. *Phys. Chem. Chem. Phys.* **2013**, *15* (40), 17619–17625. <https://doi.org/10.1039/c3cp50946j>.
- (11) Zhang, P.; Crespi, V. H.; Chang, E.; Louie, S. G.; Cohen, M. L. Computational Design of Direct-Bandgap Semiconductors That Lattice-Match Silicon. *Nature* **2001**, *409* (6816), 69–71. <https://doi.org/10.1038/35051054>.
- (12) Wang, Q.; Xu, B.; Sun, J.; Liu, H.; Zhao, Z.; Yu, D.; Fan, C.; He, J. Direct Band Gap Silicon Allotropes. *J. Am. Chem. Soc.* **2014**, *136* (28), 9826–9829. <https://doi.org/10.1021/ja5035792>.
- (13) Amsler, M.; Botti, S.; Marques, M. A. L.; Lenosky, T. J.; Goedecker, S. Low-Density Silicon Allotropes for Photovoltaic Applications. *Phys. Rev. B* **2015**, *92* (1). <https://doi.org/10.1103/PhysRevB.92.014101>.
- (14) Xiang, H. J.; Huang, B.; Kan, E.; Wei, S.-H.; Gong, X. G. Towards Direct-Gap Silicon Phases by the Inverse Band Structure Design Approach. *Phys. Rev. Lett.* **2013**, *110* (11), 118702. <https://doi.org/10.1103/PhysRevLett.110.118702>.
- (15) Botti, S.; Flores-Livas, J. A.; Amsler, M.; Goedecker, S.; Marques, M. A. L. Low-Energy Silicon Allotropes with Strong Absorption in the Visible for Photovoltaic Applications. *Phys. Rev. B* **2012**, *86* (12), 121204. <https://doi.org/10.1103/PhysRevB.86.121204>.

- (16) Lee, I.-H.; Lee, J.; Oh, Y. J.; Kim, S.; Chang, K. J. Computational Search for Direct Band Gap Silicon Crystals. *Phys. Rev. B* **2014**, *90* (11), 115209. <https://doi.org/10.1103/PhysRevB.90.115209>.
- (17) Blom, B.; Said, A.; Szilvási, T.; Menezes, P. W.; Tan, G.; Baumgartner, J.; Driess, M. Alkaline-Earth-Metal-Induced Liberation of Rare Allotropes of Elemental Silicon and Germanium from N-Heterocyclic Metallylenes. *Inorg. Chem.* **2015**, *54* (17), 8840–8848. <https://doi.org/10.1021/acs.inorgchem.5b01643>.
- (18) Von Schnering, H.-G.; Schwarz, M.; Nesper, R. The Lithium Sodium Silicide Li_3NaSi_6 and the Formation of Allo-Silicon. *J. Common Met.* **1988**, *137* (1–2), 297–310. [https://doi.org/10.1016/0022-5088\(88\)90095-1](https://doi.org/10.1016/0022-5088(88)90095-1).
- (19) Zeilinger, M.; Jantke, L.-A.; Scherf, L. M.; Kiefer, F. J.; Neubüser, G.; Kienle, L.; Karttunen, A. J.; Konar, S.; Häussermann, U.; Fässler, T. F. Alkali Metals Extraction Reactions with the Silicides $\text{Li}_{15}\text{Si}_4$ and Li_3NaSi_6 : Amorphous Si versus Allo-Si. *Chem. Mater.* **2014**, *26* (22), 6603–6612. <https://doi.org/10.1021/cm503371e>.
- (20) Okamoto, H.; Sugiyama, Y.; Nakano, H. Synthesis and Modification of Silicon Nanosheets and Other Silicon Nanomaterials. *Chem. - Eur. J.* **2011**, *17* (36), 9864–9887. <https://doi.org/10.1002/chem.201100641>.
- (21) McMillan, P. F.; Gryko, J.; Bull, C.; Arledge, R.; Kenyon, A. J.; Cressey, B. A. Amorphous and Nanocrystalline Luminescent Si and Ge Obtained via a Solid-State Chemical Metathesis Synthesis Route. *J. Solid State Chem.* **2005**, *178* (3), 937–949. <https://doi.org/10.1016/j.jssc.2004.12.040>.
- (22) Haberl, B.; Strobel, T. A.; Bradby, J. E. Pathways to Exotic Metastable Silicon Allotropes. *Appl. Phys. Rev.* **2016**, *3* (4), 040808. <https://doi.org/10.1063/1.4962984>.
- (23) Kurakevych, O. O.; Strobel, T. A.; Kim, D. Y.; Muramatsu, T.; Struzhkin, V. V. Na-Si Clathrates Are High-Pressure Phases: A Melt-Based Route to Control Stoichiometry and Properties. *Cryst. Growth Des.* **2013**, *13* (1), 303–307. <https://doi.org/10.1021/cg3017084>.
- (24) McMillan, P. F. New Materials from High-Pressure Experiments. *Nat. Mater.* **2002**, *1* (1), 19–25. <https://doi.org/10.1038/nmat716>.
- (25) Dutta, M.; Thirugnanam, L.; Fukata, N. Si Nanowire Solar Cells: Principles, Device Types, Future Aspects, and Challenges. In *Advances in Silicon Solar Cells*; Ikhmayies, S., Ed.; Springer International Publishing: Cham, 2018; pp 299–329. https://doi.org/10.1007/978-3-319-69703-1_11.
- (26) Dutta, M.; Thirugnanam, L.; Trinh, P. V.; Fukata, N. High Efficiency Hybrid Solar Cells Using Nanocrystalline Si Quantum Dots and Si Nanowires. *ACS Nano* **2015**, *9* (7), 6891–6899. <https://doi.org/10.1021/acs.nano.5b03268>.
- (27) Ferry, V. E.; Sweatlock, L. A.; Pacifici, D.; Atwater, H. A. Plasmonic Nanostructure Design for Efficient Light Coupling into Solar Cells. *Nano Lett.* **2008**, *8* (12), 4391–4397. <https://doi.org/10.1021/nl8022548>.
- (28) Delerue, C.; Allan, G.; Lannoo, M. Optical Band Gap of Si Nanoclusters. *J. Lumin.* **1998**, *80* (1–4), 65–73. [https://doi.org/10.1016/S0022-2313\(98\)00071-4](https://doi.org/10.1016/S0022-2313(98)00071-4).
- (29) Jensen, I. J. T.; Ulyashin, A. G.; Løvvik, O. M. Direct-to-Indirect Bandgap Transitions in $\langle 110 \rangle$ Silicon Nanowires. *J. Appl. Phys.* **2016**, *119* (1), 015702. <https://doi.org/10.1063/1.4938063>.
- (30) Kovalev, D.; Heckler, H.; Polisski, G.; Koch, F. Optical Properties of Si Nanocrystals. *Phys. Status Solidi B* **1999**, *215* (2), 871–932. [https://doi.org/10.1002/\(SICI\)1521-3951\(199910\)215:2<871::AID-PSSB871>3.0.CO;2-9](https://doi.org/10.1002/(SICI)1521-3951(199910)215:2<871::AID-PSSB871>3.0.CO;2-9).
- (31) He, Y.; Li, X.; Li, H.; Jiang, Y.; Bian, X. Layering Transition in Confined Silicon. *Nanoscale* **2014**, *6* (8), 4217–4224. <https://doi.org/10.1039/c3nr06174d>.

- (32) Wu, W.; Zhang, L.; Liu, S.; Ren, H.; Zhou, X.; Li, H. Liquid–Liquid Phase Transition in Nanoconfined Silicon Carbide. *J. Am. Chem. Soc.* **2016**, *138* (8), 2815–2822. <https://doi.org/10.1021/jacs.5b13467>.
- (33) Sastry, S.; Austen Angell, C. Liquid–Liquid Phase Transition in Supercooled Silicon. *Nat. Mater.* **2003**, *2* (11), 739–743. <https://doi.org/10.1038/nmat994>.
- (34) Graff, K.; Pieper, H. Degradation of Carrier Lifetime in Silicon Crystals at Room Temperature. *Phys. Status Solidi A* **1978**, *49* (1), 137–144. <https://doi.org/10.1002/pssa.2210490116>.
- (35) Wang, T. H.; Ciszek, T. F.; Schuyler, T. Micro-Defect Effects on Minority Carrier Lifetime in High Purity Dislocation-Free Silicon Single Crystals. *Sol. Cells* **1988**, *24* (1–2), 135–145. [https://doi.org/10.1016/0379-6787\(88\)90043-9](https://doi.org/10.1016/0379-6787(88)90043-9).
- (36) Solozhenko, V. L.; Kurakevych, O. O.; Le Godec, Y. Creation of Nanostructures by Extreme Conditions: High-Pressure Synthesis of Ultrahard Nanocrystalline Cubic Boron Nitride. *Adv. Mater.* **2012**, *24* (12), 1540–1544. <https://doi.org/10.1002/adma.201104361>.
- (37) Irifune, T.; Kurio, A.; Sakamoto, S.; Inoue, T.; Sumiya, H. Ultrahard Polycrystalline Diamond from Graphite: Materials. *Nature* **2003**, *421* (6923), 599–600. <https://doi.org/10.1038/421599b>.
- (38) Ganguly, S.; Kazem, N.; Carter, D.; Kauzlarich, S. M. Colloidal Synthesis of an Exotic Phase of Silicon: The BC8 Structure. *J. Am. Chem. Soc.* **2014**, *136* (4), 1296–1299. <https://doi.org/10.1021/ja412213q>.
- (39) Rödl, C.; Sander, T.; Bechstedt, F.; Vidal, J.; Olsson, P.; Laribi, S.; Guillemoles, J.-F. Wurtzite Silicon as a Potential Absorber in Photovoltaics: Tailoring the Optical Absorption by Applying Strain. *Phys. Rev. B* **2015**, *92* (4), 045207. <https://doi.org/10.1103/PhysRevB.92.045207>.
- (40) Karazhanov, S. Zh.; Davletova, A.; Ulyashin, A. Strain-Induced Modulation of Band Structure of Silicon. *J. Appl. Phys.* **2008**, *104* (2), 024501. <https://doi.org/10.1063/1.2940135>.
- (41) Mujica, A.; Rubio, A.; Muñoz, A.; Needs, R. J. High-Pressure Phases of Group-IV, III–V, and II–VI Compounds. *Rev. Mod. Phys.* **2003**, *75* (3), 863–912. <https://doi.org/10.1103/RevModPhys.75.863>.
- (42) Zhang, H.; Liu, H.; Wei, K.; Kurakevych, O. O.; Le Godec, Y.; Liu, Z.; Martin, J.; Guerrette, M.; Nolas, G. S.; Strobel, T. A. BC8 Silicon (Si-III) Is a Narrow-Gap Semiconductor. *Phys. Rev. Lett.* **2017**, *118* (14), 146601. <https://doi.org/10.1103/PhysRevLett.118.146601>.
- (43) Besson, J. M.; Mokhtari, E. H.; Gonzalez, J.; Weill, G. Electrical Properties of Semimetallic Silicon III and Semiconductive Silicon IV at Ambient Pressure. *Phys. Rev. Lett.* **1987**, *59* (4), 473–476. <https://doi.org/10.1103/PhysRevLett.59.473>.
- (44) McMahon, M. I.; Nelmes, R. J.; Wright, N. G.; Allan, D. R. Pressure Dependence of the *Imma* Phase of Silicon. *Phys. Rev. B* **1994**, *50* (2), 739–743. <https://doi.org/10.1103/PhysRevB.50.739>.
- (45) Mignot, J. M.; Chouteau, G.; Martinez, G. High Pressure Superconductivity of Silicon. *Phys. BC* **1985**, *135* (1–3), 235–238. [https://doi.org/10.1016/0378-4363\(85\)90473-5](https://doi.org/10.1016/0378-4363(85)90473-5).
- (46) Wentorf, R. H.; Kasper, J. S. Two New Forms of Silicon. *Science* **1963**, *139* (3552), 338–339. <https://doi.org/10.1126/science.139.3552.338-a>.
- (47) Nelmes, R. J.; McMahon, M. I. Chapter 3 Structural Transitions in the Group IV, III–V, and II–VI Semiconductors under Pressure. In *Semiconductors and Semimetals*; Elsevier, 1998; Vol. 54, pp 145–246. [https://doi.org/10.1016/S0080-8784\(08\)60231-8](https://doi.org/10.1016/S0080-8784(08)60231-8).

- (48) Piltz, R. O.; Maclean, J. R.; Clark, S. J.; Ackland, G. J.; Hatton, P. D.; Crain, J. Structure and Properties of Silicon XII: A Complex Tetrahedrally Bonded Phase. *Phys. Rev. B* **1995**, *52* (6), 4072–4085. <https://doi.org/10.1103/PhysRevB.52.4072>.
- (49) Frondel, C.; Marvin, U. B. Lonsdaleite, a Hexagonal Polymorph of Diamond. *Nature* **1967**, *214* (5088), 587–589. <https://doi.org/10.1038/214587a0>.
- (50) Joannopoulos, J. D.; Cohen, M. L. Electronic Properties of Complex Crystalline and Amorphous Phases of Ge and Si. II. Band Structure and Optical Properties. *Phys. Rev. B* **1973**, *8* (6), 2733–2755. <https://doi.org/10.1103/PhysRevB.8.2733>.
- (51) Persson, C.; Janzén, E. Electronic Band Structure in Hexagonal Close-Packed Si Polytypes. *J. Phys. Condens. Matter* **1998**, *10* (47), 10549–10555. <https://doi.org/10.1088/0953-8984/10/47/006>.
- (52) Raffy, C.; Furthmüller, J.; Bechstedt, F. Properties of Hexagonal Polytypes of Group-IV Elements from First-Principles Calculations. *Phys. Rev. B* **2002**, *66* (7), 075201. <https://doi.org/10.1103/PhysRevB.66.075201>.
- (53) Kobliska, R. J.; Solin, S. A. Raman Spectrum of Wurtzite Silicon. *Phys. Rev. B* **1973**, *8* (8), 3799–3802. <https://doi.org/10.1103/PhysRevB.8.3799>.
- (54) Weill, G.; Mansot, J. L.; Sagon, G.; Carlone, C.; Besson, J. M. Characterisation of Si III and Si IV, Metastable Forms of Silicon at Ambient Pressure. *Semicond. Sci. Technol.* **1989**, *4* (4), 280–282. <https://doi.org/10.1088/0268-1242/4/4/029>.
- (55) Demishev, S. V.; Lunts, D. G.; Nekhaev, D. V.; Sluchanko, N. E.; Smarin, N. A.; Brazhkin, V. V.; Lyapin, A. G.; Popova, S. V.; Mel'nik, N. N. Structural Relaxation of the Metastable Kasper Phase of Silicon. *J. Exp. Theor. Phys.* **1996**, *82* (6), 1159–1167.
- (56) Jennings, H. M.; Richman, M. H. A Hexagonal (Wurtzite) Form of Silicon. *Science* **1976**, *193* (4259), 1242–1243. <https://doi.org/10.1126/science.193.4259.1242>.
- (57) Vincent, L.; Patriarche, G.; Hallais, G.; Renard, C.; Gardès, C.; Troadec, D.; Bouchier, D. Novel Heterostructured Ge Nanowires Based on Polytype Transformation. *Nano Lett.* **2014**, *14* (8), 4828–4836. <https://doi.org/10.1021/nl502049a>.
- (58) Cerva, H. High-Resolution Electron Microscopy of Diamond Hexagonal Silicon in Low Pressure Chemical Vapor Deposited Polycrystalline Silicon. *J. Mater. Res.* **1991**, *6* (11), 2324–2336. <https://doi.org/10.1557/JMR.1991.2324>.
- (59) Tang, J.; Maurice, J.-L.; Fossard, F.; Florea, I.; Chen, W.; Johnson, E. V.; Foldyna, M.; Yu, L.; Roca i Cabarrocas, P. Natural Occurrence of the Diamond Hexagonal Structure in Silicon Nanowires Grown by a Plasma-Assisted Vapour–Liquid–Solid Method. *Nanoscale* **2017**, *9* (24), 8113–8118. <https://doi.org/10.1039/C7NR01299C>.
- (60) Hauge, H. I. T.; Verheijen, M. A.; Conesa-Boj, S.; Etzelstorfer, T.; Watzinger, M.; Kriegner, D.; Zardo, I.; Fasolato, C.; Capitani, F.; Postorino, P.; et al. Hexagonal Silicon Realized. *Nano Lett.* **2015**, *15* (9), 5855–5860. <https://doi.org/10.1021/acs.nanolett.5b01939>.
- (61) Hauge, H. I. T.; Conesa-Boj, S.; Verheijen, M. A.; Koelling, S.; Bakkers, E. P. A. M. Single-Crystalline Hexagonal Silicon–Germanium. *Nano Lett.* **2017**, *17* (1), 85–90. <https://doi.org/10.1021/acs.nanolett.6b03488>.
- (62) De, A.; Pryor, C. E. Electronic Structure and Optical Properties of Si, Ge and Diamond in the Lonsdaleite Phase. *J. Phys. Condens. Matter* **2014**, *26* (4), 045801. <https://doi.org/10.1088/0953-8984/26/4/045801>.
- (63) Chelikowsky, J. R.; Cohen, M. L. Nonlocal Pseudopotential Calculations for the Electronic Structure of Eleven Diamond and Zinc-Blende Semiconductors. *Phys. Rev. B* **1976**, *14* (2), 556–582. <https://doi.org/10.1103/PhysRevB.14.556>.
- (64) Hedin, L. New Method for Calculating the One-Particle Green's Function with Application to the Electron-Gas Problem. *Phys. Rev.* **1965**, *139* (3A), A796–A823. <https://doi.org/10.1103/PhysRev.139.A796>.

- (65) Ortenburger, I. B.; Rudge, W. E.; Herman, F. Electronic Density of States and Optical Properties of Polytypes of Germanium and Silicon. *J. Non-Cryst. Solids* **1972**, *8–10*, 653–658. [https://doi.org/10.1016/0022-3093\(72\)90206-2](https://doi.org/10.1016/0022-3093(72)90206-2).
- (66) Amato, M.; Kaewmaraya, T.; Zobelli, A.; Palummo, M.; Rurali, R. Crystal Phase Effects in Si Nanowire Polytypes and Their Homojunctions. *Nano Lett.* **2016**, *16* (9), 5694–5700. <https://doi.org/10.1021/acs.nanolett.6b02362>.
- (67) Cartoixà, X.; Palummo, M.; Hauge, H. I. T.; Bakkers, E. P. A. M.; Rurali, R. Optical Emission in Hexagonal SiGe Nanowires. *Nano Lett.* **2017**, *17* (8), 4753–4758. <https://doi.org/10.1021/acs.nanolett.7b01441>.
- (68) Guignard, J.; Crichton, W. A. The Large Volume Press Facility at ID06 Beamline of the European Synchrotron Radiation Facility as a High Pressure-High Temperature Deformation Apparatus. *Rev. Sci. Instrum.* **2015**, *86* (8), 085112. <https://doi.org/10.1063/1.4928151>.
- (69) Young, R. A. *The Rietveld Method*; IUCr Monographs in Crystallography; Oxford University Press: New York, 1993; Vol. 5.
- (70) Rietveld, H. M. A Profile Refinement Method for Nuclear and Magnetic Structures. *J. Appl. Crystallogr.* **1969**, *2* (2), 65–71. <https://doi.org/10.1107/S0021889869006558>.
- (71) Rodríguez-Carvajal, J. FULLPROF: A Program for Rietveld Refinement and Pattern Matching Analysis, Abstracts of the Satellite Meeting on Powder Diffraction of the XV Congress of the IUCr, p. 127, Toulouse, France (1990). *XV Congr. IUCr Toulouse Fr.* **1990**, 127.
- (72) Rodríguez-Carvajal, J. Recent Advances in Magnetic Structure Determination by Neutron Powder Diffraction. *Phys. B Condens. Matter* **1993**, *192* (1–2), 55–69. [https://doi.org/10.1016/0921-4526\(93\)90108-I](https://doi.org/10.1016/0921-4526(93)90108-I).
- (73) Giannozzi, P.; Baroni, S.; Bonini, N.; Calandra, M.; Car, R.; Cavazzoni, C.; Ceresoli, D.; Chiarotti, G. L.; Cococcioni, M.; Dabo, I.; et al. QUANTUM ESPRESSO: A Modular and Open-Source Software Project for Quantum Simulations of Materials. *J. Phys. Condens. Matter* **2009**, *21* (39), 395502. <https://doi.org/10.1088/0953-8984/21/39/395502>.
- (74) Perdew, J. P.; Zunger, A. Self-Interaction Correction to Density-Functional Approximations for Many-Electron Systems. *Phys. Rev. B* **1981**, *23* (10), 5048–5079. <https://doi.org/10.1103/PhysRevB.23.5048>.
- (75) Kurakevych, O. O.; Le Godec, Y.; Crichton, W. A.; Guignard, J.; Strobel, T. A.; Zhang, H.; Liu, H.; Coelho Diogo, C.; Polian, A.; Menguy, N.; et al. Synthesis of Bulk BC8 Silicon Allotrope by Direct Transformation and Reduced-Pressure Chemical Pathways. *Inorg. Chem.* **2016**, *55* (17), 8943–8950. <https://doi.org/10.1021/acs.inorgchem.6b01443>.
- (76) Bandet, J.; Despax, B.; Caumont, M. Vibrational and Electronic Properties of Stabilized Wurtzite-like Silicon. *J. Phys. Appl. Phys.* **2002**, *35* (3), 234–239. <https://doi.org/10.1088/0022-3727/35/3/311>.
- (77) Prades, J. D.; Arbiol, J.; Cirera, A.; Morante, J. R.; Fontcuberta i Morral, A. Concerning the 506cm⁻¹ Band in the Raman Spectrum of Silicon Nanowires. *Appl. Phys. Lett.* **2007**, *91* (12), 123107. <https://doi.org/10.1063/1.2786606>.
- (78) Wu, B. R. First-Principles Study on the High-Pressure Behavior of the Zone-Center Modes of Lonsdaleite Silicon. *Phys. Rev. B* **2000**, *61* (1), 5–8. <https://doi.org/10.1103/PhysRevB.61.5>.
- (79) Lopez, F. J.; Givan, U.; Connell, J. G.; Lauhon, L. J. Silicon Nanowire Polytypes: Identification by Raman Spectroscopy, Generation Mechanism, and Misfit Strain in Homostructures. *ACS Nano* **2011**, *5* (11), 8958–8966. <https://doi.org/10.1021/nn2031337>.

- (80) Raya-Moreno, M.; Aramberri, H.; Seijas-Bellido, J. A.; Cartoixà, X.; Rurali, R. Thermal Conductivity of Hexagonal Si and Hexagonal Si Nanowires from First-Principles. *Appl. Phys. Lett.* **2017**, *111* (3), 032107. <https://doi.org/10.1063/1.4985278>.
- (81) Richter, H.; Wang, Z. P.; Ley, L. The One Phonon Raman Spectrum in Microcrystalline Silicon. *Solid State Commun.* **1981**, *39* (5), 625–629. [https://doi.org/10.1016/0038-1098\(81\)90337-9](https://doi.org/10.1016/0038-1098(81)90337-9).
- (82) Campbell, I. H.; Fauchet, P. M. The Effects of Microcrystal Size and Shape on the One Phonon Raman Spectra of Crystalline Semiconductors. *Solid State Commun.* **1986**, *58* (10), 739–741. [https://doi.org/10.1016/0038-1098\(86\)90513-2](https://doi.org/10.1016/0038-1098(86)90513-2).
- (83) Murphy, D. V.; Brueck, S. R. J. Optical Microanalysis of Small Semiconductor Structures. *MRS Proc.* **1982**, *17*, 81. <https://doi.org/10.1557/PROC-17-81>.
- (84) De Padova, P.; Generosi, A.; Paci, B.; Ottaviani, C.; Quaresima, C.; Olivieri, B.; Salomon, E.; Angot, T.; Le Lay, G. Multilayer Silicene: Clear Evidence. *2D Mater.* **2016**, *3* (3), 031011. <https://doi.org/10.1088/2053-1583/3/3/031011>.
- (85) Knight, D. S.; White, W. B. Characterization of Diamond Films by Raman Spectroscopy. *J. Mater. Res.* **1989**, *4* (02), 385–393. <https://doi.org/10.1557/JMR.1989.0385>.
- (86) Li, Y.; Liu, Z.; Lu, X.; Su, Z.; Wang, Y.; Liu, R.; Wang, D.; Jian, J.; Lee, J. H.; Wang, H.; et al. Broadband Infrared Photoluminescence in Silicon Nanowires with High Density Stacking Faults. *Nanoscale* **2015**, *7* (5), 1601–1605. <https://doi.org/10.1039/C4NR05410E>.
- (87) Lockwood, D. J. Optical Properties of Porous Silicon. *Solid State Commun.* **1994**, *92* (1–2), 101–112. [https://doi.org/10.1016/0038-1098\(94\)90863-X](https://doi.org/10.1016/0038-1098(94)90863-X).
- (88) Lockwood, D. J.; Wang, A. G. Quantum Confinement Induced Photoluminescence in Porous Silicon. *Solid State Commun.* **1995**, *94* (11), 905–909. [https://doi.org/10.1016/0038-1098\(95\)00186-7](https://doi.org/10.1016/0038-1098(95)00186-7).
- (89) Hannah, D. C.; Yang, J.; Podsiadlo, P.; Chan, M. K. Y.; Demortière, A.; Gosztola, D. J.; Prakapenka, V. B.; Schatz, G. C.; Kortshagen, U.; Schaller, R. D. On the Origin of Photoluminescence in Silicon Nanocrystals: Pressure-Dependent Structural and Optical Studies. *Nano Lett.* **2012**, *12* (8), 4200–4205. <https://doi.org/10.1021/nl301787g>.
- (90) Hybertsen, M. S. Absorption and Emission of Light in Nanoscale Silicon Structures. *Phys. Rev. Lett.* **1994**, *72* (10), 1514–1517. <https://doi.org/10.1103/PhysRevLett.72.1514>.
- (91) Binetti, S.; Le Donne, A.; Sassella, A. Photoluminescence and Infrared Spectroscopy for the Study of Defects in Silicon for Photovoltaic Applications. *Sol. Energy Mater. Sol. Cells* **2014**, *130*, 696–703. <https://doi.org/10.1016/j.solmat.2014.02.004>.
- (92) Fabbri, F.; Rotunno, E.; Lazzarini, L.; Fukata, N.; Salviati, G. Visible and Infra-Red Light Emission in Boron-Doped Wurtzite Silicon Nanowires. *Sci. Rep.* **2015**, *4* (1), 3603. <https://doi.org/10.1038/srep03603>.

Appendix Chapter 5

Appendix 5.1: Temperature profile during HP-HT synthesis

The assembly was compressed at a rate of 0.04 GPa/min up to 13 GPa and heated in a Voggenreiter modified-cubic press located at the beamline ID06-LVP, ESRF [2]. During compression pressure was estimated using d-Si equation of state (EOS) [3] before starting the heating and was then assumed quasi-constant during the heating.

Temperature evolution during the heating is reported in Figure 5.6 Heating was performed at a rate of 26 K/min up to 604 K and then rate was decreased to 13 K/min up to 833 K. The temperature was then dwelled for 20 minutes to check the transformation Si-I→Si-II. To observe the complete disappearance of Si-I peaks, temperature was raised up to 870 K (rate 16 K/min) and then dwelled for other 20 minutes. During the dwell, pressure loading was increased of 20 bar to compensate the pressure loss during Si-I→Si-II transformation and maintain the sample pressure 13 GPa. As soon as the reaction was complete, the system has been quenched to ambient temperature. Temperature was evaluated using Si melting temperature to calibrate the Power-Temperature curve.

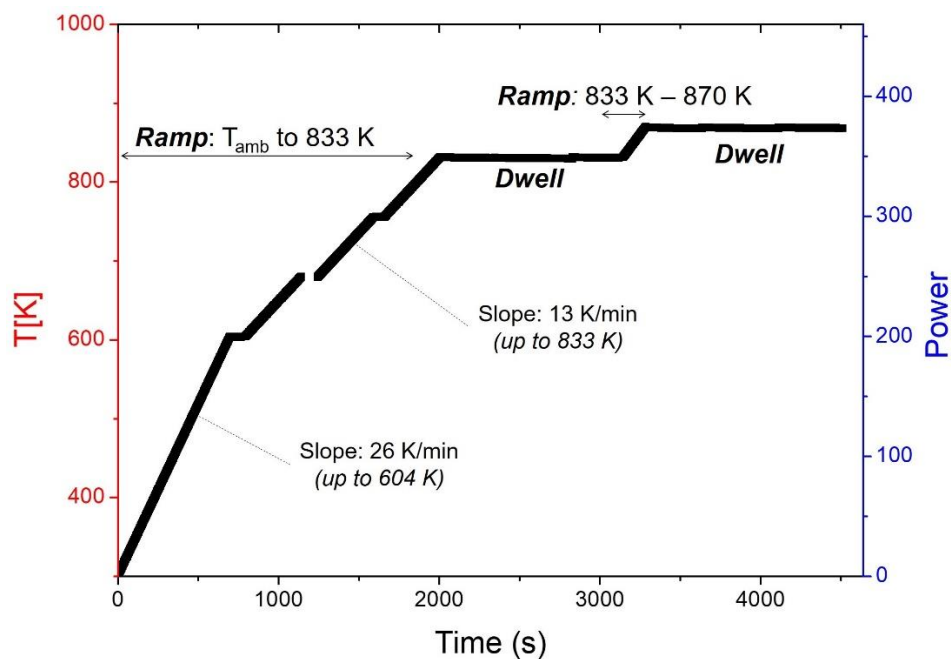


Figure 5.6 Profile of Temperature and Power during the heating at 13 GPa.

Appendix 5.2: Electron Diffraction Patterns and FFT-TEM proof of Si-4H stacking faults

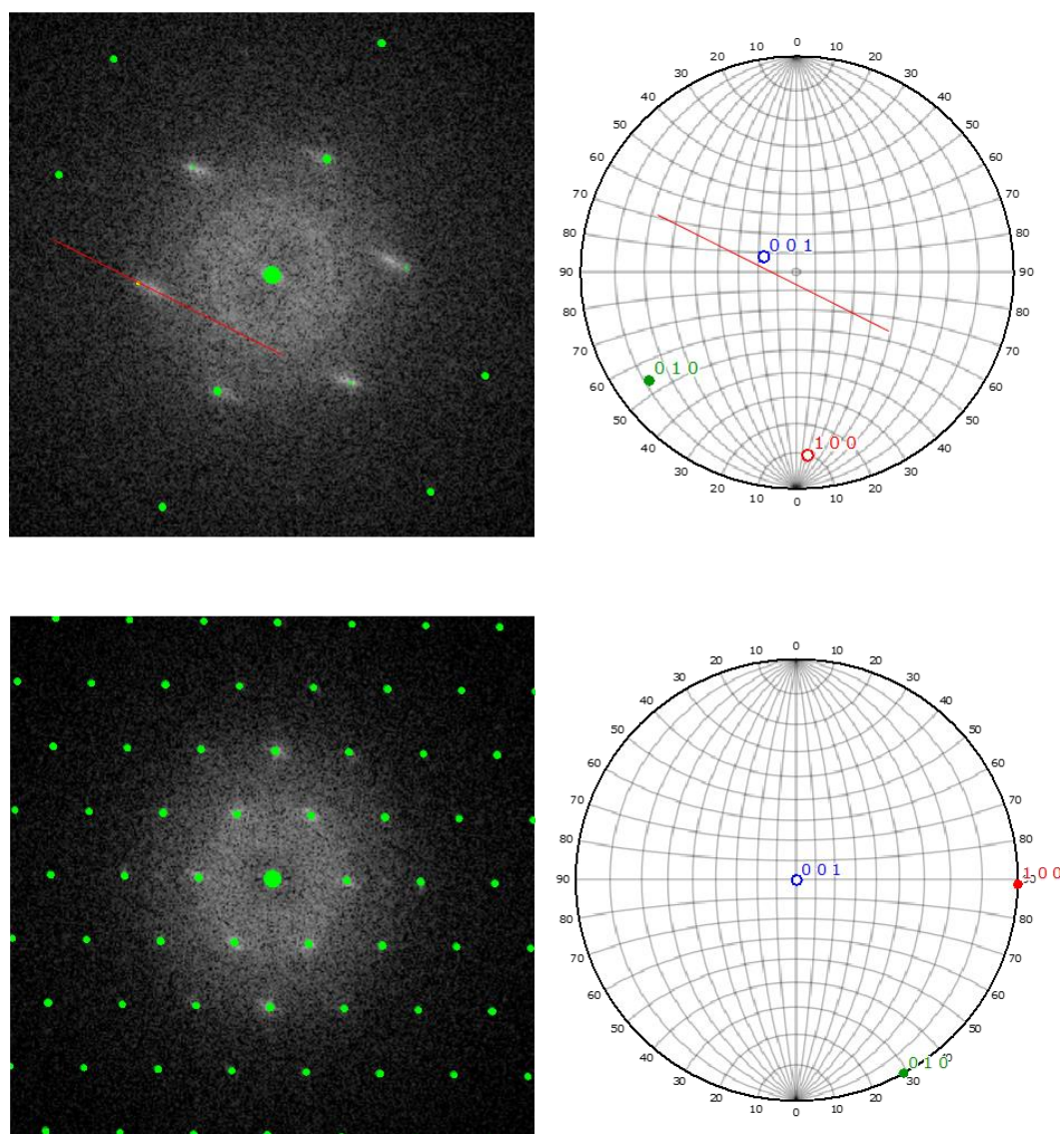


Figure 5.7 FFT-TEM patterns of zone 3 of the sample, shown also in the main text. Green dots are simulated Si-4H diffraction pattern along $[2 -2 3]$ and $[0 0 1]$ direction respectively.

As visible in the upper panel of Figure 5.7, the spots of $[2 -2 3]$ pattern are deformed along one precise direction; looking at the projection on the right, we see that this direction corresponds to the $[0 0 1]$, i.e. the c axis. The deformation of the spots can thus be interpreted as due to stacking faults, that cause the superposition of several domains along the $[0 0 1]$ direction. On the contrary, looking at the $[1 0 0]$ pattern, that is perpendicular to the c axis, no deformation of the spots is observed.

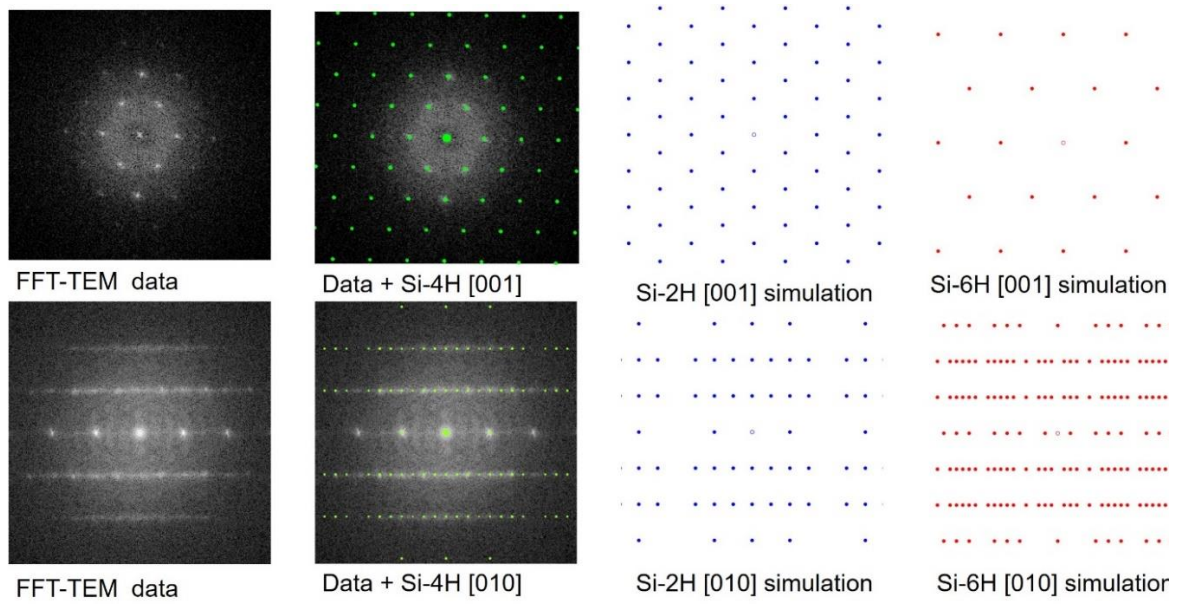


Figure 5.8 FFT-TEM patterns are compared with simulated electron diffraction patterns for Si-2H, Si-4H and Si-6H polytypes. From left to right, for two different patterns are reported: FFT-TEM data; Si-4H simulation superimposed to the data to underline the good agreement between data and simulation; Si-2H and Si-6H simulation of the electron diffraction pattern along the same direction. Comparison evidences that the experimental data are compatible with Si-4H structural model and could not be explained with other hexagonal polytypes.

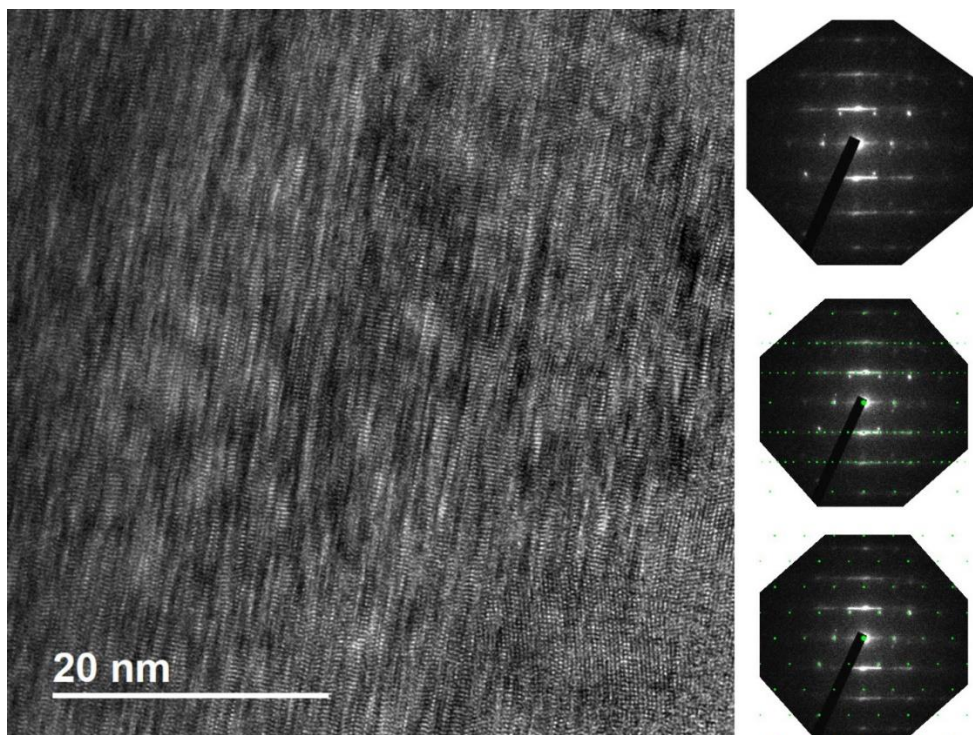


Figure 5.9 TEM image and Electron Diffraction pattern of the sample (zone 14). Green dots are simulated Si-4H diffraction pattern along [010] and [100] direction respectively.

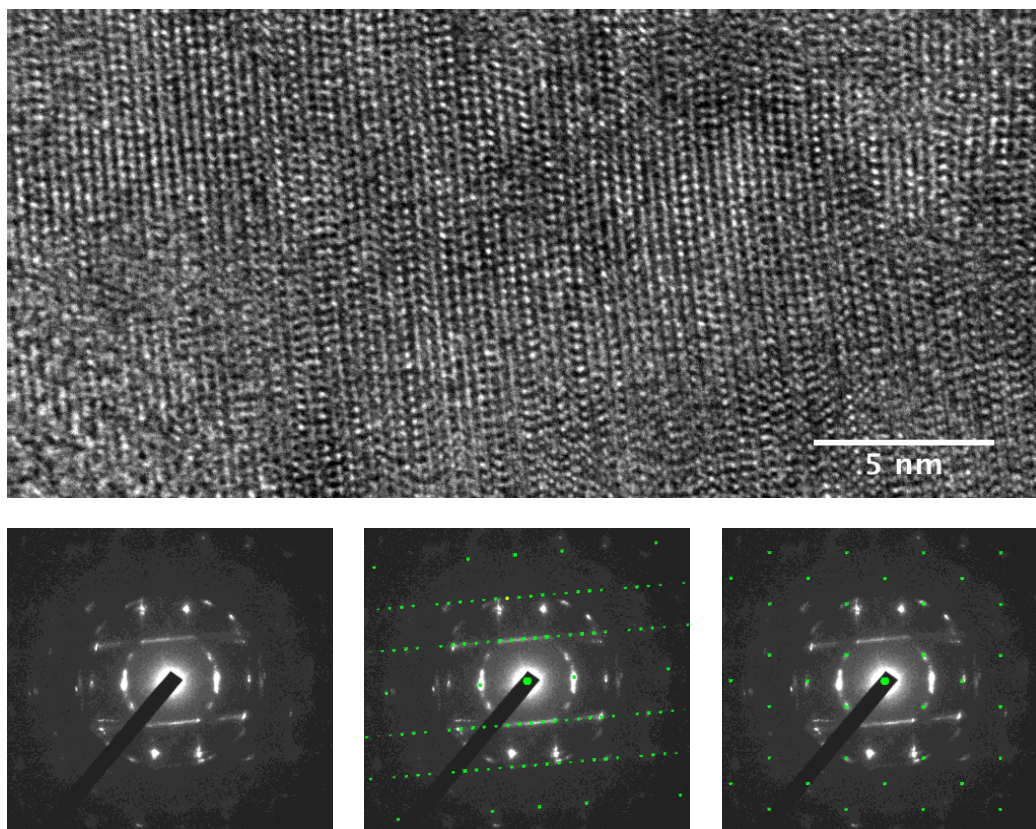


Figure 5.10 TEM image and Electron Diffraction pattern of the sample (zone 15). Green dots are simulated Si-4H diffraction pattern along [010] and [100] direction respectively.

Appendix 5.3: DFT Calculations Results

Calculations for the NMR chemical shift and for Raman spectra were done using density functional theory (DFT) using periodic boundary conditions, plane-waves and pseudopotential approaches as implemented in the Quantum ESPRESSO package [4-5] (see Appendix 4 for computational details).

The difference between the applied external magnetic field and the effective magnetic field at the nucleus positions is at the origin of the NMR chemical shift. It can be obtained by calculating, for a given crystalline structure, the shielding of the nuclei relative to the electronic current induced by the external magnetic field. This induced current can be calculated by using the GIPAW (Gauge Including Projector Augmented Wave) approach, which allows reconstructing the all-electron magnetic response from the pseudo-wave-functions. In Table 5.1 calculated ^{29}Si NMR chemical shifts are reported for Si-2H, Si-4H and Si-4H polytype; d-Si is reported for comparison.

Table 5.1 ^{29}Si NMR Chemical Shifts of Hexagonal Si Polytypes

	<i>Crystallographic position</i>	δ_{iso} (^{29}Si) [ppm]
Si-I (d-Si), O^7_h	Si	-79
Si-2H, D^4_{6h} 4	Si	-122.7
Si-4H, D^4_{6h}	Si1	-127.7
	Si2	-96.9
Si-6H, D^4_{6h}	Si1	-90.0
	Si2	-90.4
	Si3	-128.8

The simulated Raman spectra are obtained within the non-resonant (Plackzek) approximation: the position (Stokes Raman shift) of the peaks is equal to the zero-wavevector phonon vibrations ω_ν (ν is the branch index) and the corresponding intensity I_ν is given by

$$I_\nu \propto |\mathbf{e}_i \cdot \vec{\mathbf{A}}^\nu \cdot \mathbf{e}_s|^2 \frac{1}{\omega_\nu} (n_\nu + 1),$$

where \mathbf{e}_i (\mathbf{e}_s) is the polarization of the incident (scattered) radiation, n_ν is the phonon occupation given by the Bose-Einstein statistics (calculated for room temperature), and $\vec{\mathbf{A}}^\nu$ is the Raman tensor. The Raman tensor can be calculated as the derivative of the dielectric tensor $\vec{\epsilon}_\infty$ with respect to the atomic displacement pattern corresponding to the phonon mode ν . In the present work the phonon frequencies were calculated using standard first-order density functional perturbation theory [6] and the Raman tensor was calculated using the second-order approach of Ref. [7]. Both approaches are exact within DFT and the computational details are given in Appendix 4.

Table 5.2 Frequency of the Raman active modes of Hexagonal Si Polytypes

<i>Mode</i>	<i>Degeneration</i>	<i>Raman Shift [cm⁻¹]</i>	<i>Relative Intensity</i>
Si-2H, D_{6h}^4 4 atoms/unit cell			
$A_{1g}(\text{LO})$	1	511	1
$E_{1g}(\text{TO})$	2	511	0.11
$E_{2g}(\text{TO})$	2	496	0.14
Si-4H, D_{6h}^4 8 atoms/unit cell			
$E_{1g}(\text{TO})$	2	518	0.22
$A_{1g}(\text{LO})$	1	513	1
$E_{2g}(\text{TO})$	2	501	0.34
$A_{1g}(\text{LO})$	1	416	0.05
Si-6H, D_{6h}^4 12 atoms/unit cell			
$E_{1g}(\text{TO})$	2	518	0.29
$A_{1g}(\text{LO})$	1	515	1
$E_{2g}(\text{TO})$	2	510	0.44
$E_{2g}(\text{TO})$	2	491	0.02
$A_{1g}(\text{LO})$	1	462	0.05

It is known that LDA-DFT slightly underestimates the phonon frequencies of the considered Si polymorphs. In order to simplify the discussion of Figure 5.4 in the main text, we have upshifted the calculated frequencies by $+2.6 \text{ cm}^{-1}$ so that the frequency of diamond Si (d-Si) coincides with the experimental value of 521 cm^{-1} . Results are reported in Table 5.2.A. Note that, in [8] the Raman active A_{1g} and the E_{1g} modes of Si-2H are split by 9 cm^{-1} . A similar splitting is not observable in the calculations reported by [9] and also according to the present calculation (Table 5.2.A) the two modes have the same frequency. We remark that all the present calculations are done by relaxing, through energy minimization, the two cell parameters of the hexagonal cell and the atomic positions. If we compute the Raman spectra of the ideal configuration for the wurtzite structure (with ideal c/a ratio and no relaxation of the internal degrees of freedom), we obtain that the A_{1g} and the E_{1g} modes of Si-2H are split by $\sim 10 \text{ cm}^{-1}$, similar to the value reported by [8]; this split is reduced to $\sim 8 \text{ cm}^{-1}$ if we relax only the atomic

position but we keep the ideal cell parameters, and it disappears once we let both relax. We argue that this is the origin of the mentioned discrepancy.

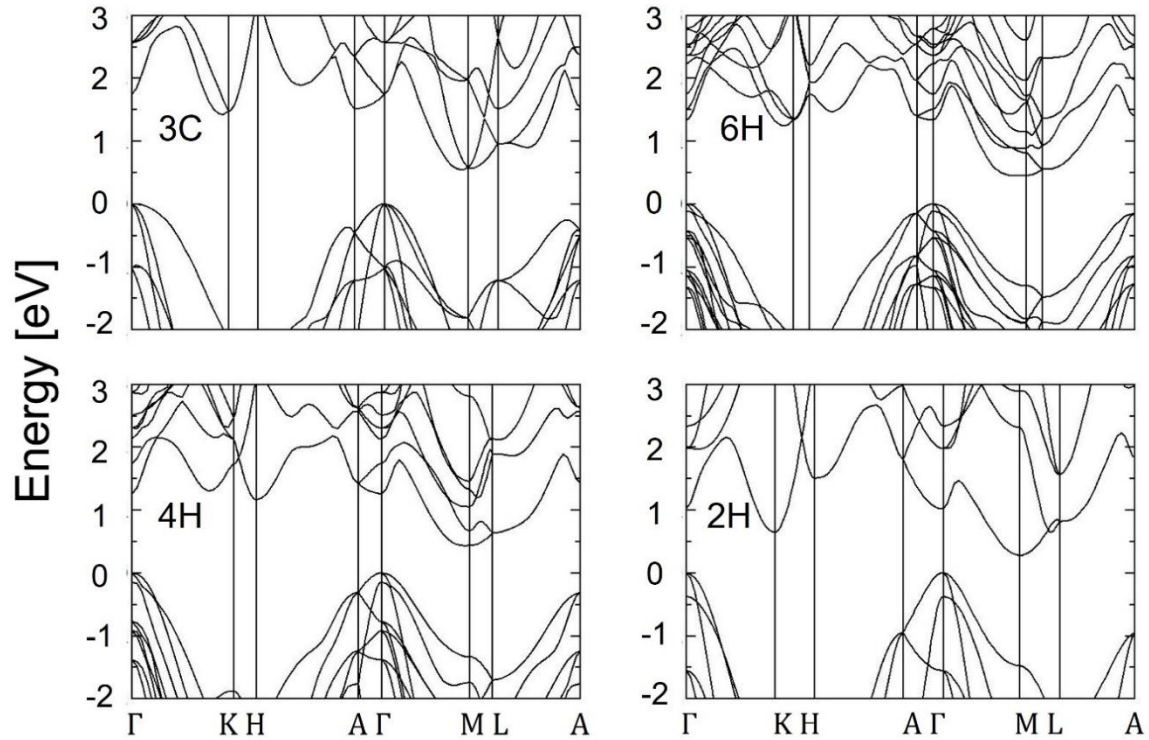


Figure 5.11 Electronic band structures of different polytypes as calculated by LDA-DFT. 3C polytype (i.e. cubic d-Si) is reported for comparison. Our results are in good agreement with previous calculations [10-11].

In order to compare with previous literature [10-11] in Figure 5.11 we show the electronic band structures of the polytypes described in the text. There is a good agreement with the LDA-DFT results previously published. All hexagonal polytypes of Si are indirect bandgap semiconductor, with the maximum of the valence band at the Γ point and the minimum of the conduction band at the M point for Si-2H and moving along the M- Γ line for Si-4H and Si-6H. Indirect bandgap values are smaller than that of d-Si [10-11], with a clear trend of approaching d-Si value with decreasing “hexagonality” (i.e. from Si-2H, 100% hexagonal, to Si-4H, 50%, and Si-6H, 33%). Since LDA-DFT systematically underestimates the bandgap value, another useful reference for understanding hexagonal Si optoelectronic properties is given by [12]. In this study, many-body perturbation theory was used to compute quasiparticle band gaps and optical absorption spectra for Si-2H. With this approach, more reliable value for the electronic bandgaps can be obtained. While the computed value of the indirect bandgap (0.95 eV) is not substantially smaller than d-Si one (1.14 eV), a larger difference is found for the direct transition

at the Γ point, i.e. 1.63 eV for Si-2H compared to 3.20 eV for d-Si. This reduction of the transition energy is due to the backfolding of d-Si electronic bands when the symmetry changes from cubic to hexagonal in Si-2H and has the effect on increasing the absorption in the whole visible spectral range compared to d-Si [12]. Even though this study addresses Si-2H and this approach has not yet been applied to Si-4H, it seems reasonable to expect that all hexagonal polytypes would exceed d-Si absorption in the visible range. Indeed, this absorption increase is primarily caused by the change in the symmetry and by the reduction of the transition energy at the Γ point, which has been reported by LDA-DFT calculations for both Si-4H and Si-6H [10]. Another factor that could play a fundamental role for increasing hexagonal Si polytypes absorption is crystal size. Indeed, the transition at the Γ point is optically forbidden in Si-2H [12], but we could expect a relaxation of dipole transition selection rules in strongly confined system which could tremendously raise the absorption around the direct bandgap energy.

Appendix 5.4: Experimental and Calculation Procedures

***In-situ* X-Ray Diffraction** During HP-HT synthesis at the ESRF, angle-dispersive PXRD patterns were collected continuously. The data write-rate was typically maintained at 32s/pattern during compression and decompression, while during the heating rate was increased up to 0.1s/pattern and 32X re-bin. A constant wavelength ($\lambda = 0.3757 \text{ \AA}$) was selected by a Si111 double-crystal monochromator from the emission of a U18 cryogenic insertion device at $\sim 6 \text{ mm}$ magnetic gap. Data acquisition was performed in the 2θ range of $6.27\text{--}14.64^\circ$ using a Detection Technology X-Scan series1 linear pixelated detector. Sample-to-detector distance and the detector offset were calibrated using LaB6-SRM660a (NIST). Data were integrated and manipulated using Fit2D software [13-14].

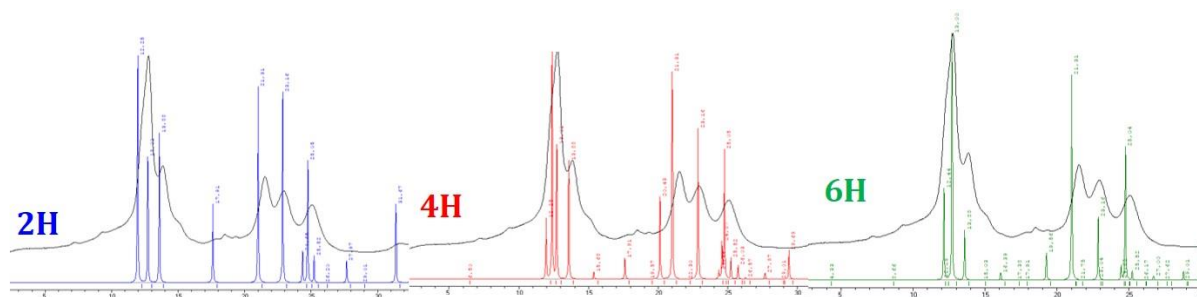


Figure 5.12 Comparison of XRD diffraction measured pattern and computed profiles for different hexagonal polytypes. Data are reported with a black line and were collected using a Mo radiation source ($\lambda_{K\alpha 1} = 0.709319 \text{ \AA}$, $\lambda_{K\alpha 2} = 0.713609 \text{ \AA}$). Structural models for hexagonal polytypes are taken from [10] and thus do not correspond with the ideal polytypic structure, but with a relaxed one obtained by DFT calculations.

X-Ray Diffraction at IMPMC X-Ray powder diffraction measurements were carried out at the XRD platform of the IMPMC on a Rigaku MM007HF diffractometer equipped with a Mo rotating anode source ($\lambda_{K\alpha1} = 0.709319 \text{ \AA}$, $\lambda_{K\alpha2} = 0.713609 \text{ \AA}$), Varimax focusing optics and a RAXIS4++ image plate detector. X-ray data were collected at 25°C between 0° and 30° 2 θ with a 0.028° 2 θ step. Cell parameters, crystallite sizes and microstrain were refined using Rietveld method as implemented in the Fullprof [15-16].

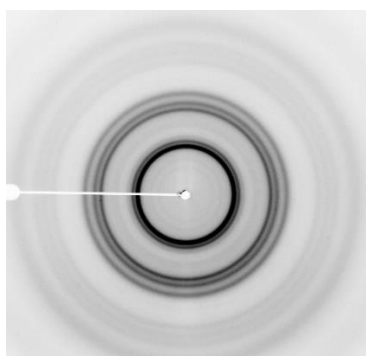


Figure 5.13 2D diffractogram of Si-4H sample. Since there is no evidence of texture in the sample, such effects have not been taken into account when performing Rietveld refinement.

A Rietveld refinement was performed starting from the known model for Si-4H [10]. The unit cell and Si atomic positions were refined first. Then, since the peak width was larger than the instrumental one, isotropic size (Y) and isotropic strain (X) parameters were refined. The two effects can be decoupled on the diagram because the first induces a peak broadening as $Y/\cos\theta$ whereas the second as $X\tan\theta$. Then, anisotropic refinements of size parameters allowed to improve the fit and the corresponding spherical harmonic coefficients are given in the following tables. To perform anisotropic size refinement, Y (isotropic Lorentzian size parameter) was reset to zero. Fractional atomic coordinates along the *c* axis were then refined independently for both Si atoms (4e and 4f), while a constrain maintained the isotropic displacement B equal for both atomic site. The result of Rietveld refinement are reported, together with the corresponding errors, in the following tables.

Table 5.3 Fractional atomic coordinates and equivalent isotropic displacement parameters

Atom	<i>x</i>	<i>y</i>	<i>z</i>	B(eq)
Si1 (4e)	0	0	0.0906(5)	1.94(6)
Si2 (4f)	1/3	2/3	0.1646(8)	1.94(6)

Table 5.4 Results of the Rietveld refinement on the X-Ray powder pattern of Si₄H

Si ₄ H, X-ray Diffractometer, λ_{Mo}		
<i>P</i> 6 ₃ / <i>mmc</i>		R _{Bragg} = 18.1 %
<i>a</i> = 3.7948(7) Å	<i>b</i> = 3.7948(7) Å	<i>c</i> = 12.7099(60) Å
<i>V</i> = 158.51(8) Å ³		
Size Parameters		
<i>Y</i> ₀₀ = 14.5(1.3), <i>Y</i> ₂₀ = 11.6(1.3)		
Strain Parameters		
<i>X</i> = 2.2(2)		

Photoluminescence PL measurements have been performed at ambient temperature using the blue excitation laser beam ($\lambda = 460$ nm, 10 μ m beam spot) of an Ar laser. The PL & Raman spectra were collected using a high-resolution confocal Horiba Jobin Yvon HR800 μ Raman system with Peltier-chilled Si detector. The spectrometer was calibrated at room temperature using Ne lines for absolute energy values (for PL spectra) and a single crystal of cubic Si for relative inverse wavenumber (for Raman spectra). A laser power at the sample was estimated to be less than 30 mW. No effect due to laser heating of the sample was observed. Raman spectra have been performed prior to PL in order to assure the good signal from the sample.

Nuclear Magnetic Resonance + DFT Calculations ²⁹Si magic angle spinning nuclear magnetic resonance (MAS NMR) experiments were performed at LCMCP on a 700 MHz AVANCE III Bruker spectrometer operating at 139.15 MHz, using a 2.5 mm Bruker probe spinning at 20 kHz. A single-pulse excitation with a flip angle of 90° and a recycle delay of 200 s were used. ²⁹Si chemical shifts were referenced to TMS.

The theoretical ²⁹Si NMR properties of various Si polytypes were investigated within the DFT framework, using periodic boundary conditions and the generalized gradient approximation (GGA) to the exchange-correlation functional as proposed by Perdew, Burke and Ernzerhof [17]. The NMR chemical shift describes the difference between the applied external magnetic field and the magnetic field at the nucleus positions. It can be obtained on the structural model by calculating the shielding of the nuclei relative to the electronic current

induced by the external magnetic field. This current was calculated by using the GIPAW approach, which allows reconstructing the all-electron magnetic response from the pseudo-wave-functions [18-19]. The calculations were performed using the PWscf and GIPAW codes of the Quantum ESPRESSO package [4-5]. Norm-conserving pseudo-potentials were used and the wave functions kinetic energy cutoff was increased to 80 Ry. The integral over the Brillouin zone was done using Monkhorst-Pack $13 \times 13 \times 8$, $16 \times 16 \times 5$, $15 \times 15 \times 3$, k -point grids for Si-2H, Si-4H and Si-6H structures respectively. A $10 \times 10 \times 10$ k -point grid was used for Si-I, calculated as a reference. The isotropic chemical shift δ_{iso} is defined as $\delta_{\text{iso}} = -(\sigma - \sigma^{\text{ref}})$, where σ is the isotropic shielding (one-third of the trace of the NMR shielding tensor) and σ^{ref} is the isotropic shielding of the same nucleus in a reference system. In our calculations, absolute shielding tensors are obtained. To fix the scales, σ^{ref} was chosen by comparing experimental (79 ppm) and calculated δ_{iso} values of Si-I.

Raman Spectroscopy + DFT Calculations The Raman spectra were recorded at the IMPMC spectroscopy platform on a HR460 (Jobin-Yvon/Horiba) spectrometer using as excitation source an Ar^+ laser under 514.5 nm excitation wavelength. The light was dispersed in a grating of 1500 lines and centered in 532 nm. The power of the laser was kept lower than 15 mW over the sample to avoid overheating and the typical recording parameters for the spectra were 5 accumulations of 30s each.

Density functional theory calculations were done with the quantum-espresso package [4-5], by using the local density approximation [20-21], norm-conserving pseudopotential and plane-waves (80 Ry energy cut-off) approaches. The Brillouin zone integration is performed by using k -points sampling with a grid equivalent to the $10 \times 10 \times 4$ for the Si bulk in the hexagonal 3C structure (6 atoms per cell). Atomic positions and cell parameters were always relaxed by energy minimization. Phonon modes and Raman tensor were calculated with the approaches of [6] and [7]. The Raman spectra shown in the text simulate a non-polarized experiment done on powder and are obtained by averaging over different polarizations and orientations. The 521 cm^{-1} mode of d-Si has been taken as a reference to evaluate systematic errors. Therefore, in order to make DFT and experimental d-Si phonon coincide at 521 cm^{-1} , all computed Raman frequencies have been shifted of $+2.6 \text{ cm}^{-1}$.

Transmission Electron Microscopy and Diffraction TEM observations (High Resolution TEM and Selecting Area Electron Diffraction) were carried out at IMPMC on a Jeol

2100F TEM operating at 200 kV, equipped with a high-resolution UHR pole piece and a Gatan US4000 CCD camera.

Appendixes References:

- [1] Kurakevych, O. O.; Le Godec, Y.; Crichton, W. A.; Guignard, J.; Strobel, T. A.; Zhang, H.; Liu, H.; Coelho Diogo, C.; Polian, A.; Menguy, N.; Juhl, S. J.; Gervais, C. *Inorg. Chem.* 2016, *55*, 8943-8950.
- [2] Guignard, J.; Crichton, W. A. *Rev. Sci. Instrum.* 2015, *86*, 085112.
- [3] Landolt,; Börnstein, *Crystal and Solid State Physics ; Numerical Data and Functional Relationships in Science and Technology*, Springer-Verlag: Amsterdam, 1966; Vol. I.
- [4] Giannozzi, P.; Baroni, S.; Bonini, N.; Calandra, M.; Car, R.; Cavazzoni, C.; Ceresoli, D.; Chiarotti, G. L.; Cococcioni, M.; Dabo, I.; Dal Corso, A.; de Gironcoli, S.; Fabris, S.; Fratesi, G.; Gebauer, R.; Gerstmann, U.; Gougoussi, C.; Kokalj, A.; Lazzeri, M.; Martin-Samos, L.; Marzari, N.; Mauri, F.; Mazzarello, R.; Paolini, S.; Pasquarello, A.; Paulatto, L.; Sbraccia, C.; Scandolo, S.; Sclauzero, G.; Seitsonen, A. P.; Smogunov, A.; Umari, P.; Wentzcovitch, R. M. *J. Phys.: Condens.Matter* 2009, *21*, 395502.
- [5] Quantum Espresso is available at the URL www.quantum-espresso.org
- [6] Baroni, S.; de Gironcoli, S.; Dal Corso, A.; Giannozzi, P. *Rev. Mod. Phys.* 2001, *73*, 515-562.
- [7] Lazzeri, M.; Mauri, F. *Phys. Rev. Lett.* 2003, *90*, 036401.
- [8] Wu, B. R. *Phys. Rev. B* 2000, *61*, 5-8.
- [9] Raya-Moreno, M.; Aramberri, H.; Seijas-Bellido, J. A.; Cartoixa, X.; Rurali, R. *Appl. Phys. Lett.* 2017, *111*, 032107.
- [10] Raffy, C.; Furthmüller, J.; Bechstedt, F. *Phys. Rev. B* 2002, *66*, 075201.
- [11] Persson, C.; Janzén, E. *J. Phys.: Condens. Matter* 1998, *10*, 10549-10555.
- [12] Rödl, C.; Sander, T.; Bechstedt, F.; Vidal, J.; Olsson, P.; Laribi, S.; Guillemoles, J.-F. *Phys. Rev. B* 2015, *92*, 045207.
- [13] Hammersley, A.; Svensson, S.; Thompson, A. *Nucl. Instrum. Methods Phys. Res., Sect. A* 1994, *346*, 312-321.
- [14] Hammersley, A. P.; Svensson, S. O.; Hanfland, M.; Fitch, A. N.; Hausermann, D. *High Pressure Res.* 1996, *14*, 235-248.
- [15]vRodriguez-Carvajal, J. *XV Congress of the IUCr, Toulouse (France)* 1990, 127.
- [16] Rodriguez-Carvajal, J. *Phys. B* 1993, *192*, 55-69.
- [17] Perdew, J. P.; Burke, K.; Ernzerhof, M. *Phys. Rev. Lett.* 1996, *77*, 3865-3868.
- [18] Pickard, C. J.; Mauri, F. *Phys. Rev. B* 2001, *63*, 245101.
- [19] Bonhomme, C.; Gervais, C.; Babonneau, F.; Coelho, C.; Pourpoint, F.; Azaïs, T.; Ashbrook, S. E.; Griffin, J. M.; Yates, J. R.; Mauri, F.; Pickard, C. *J. Chem. Rev.* 2012, *112*, 5733-5779.
- [20] Ceperley, D. M.; Alder, B. J. *Phys. Rev. Lett.* 1980, *45*, 566-569.
- [21] Perdew, J. P.; Zunger, A. *Phys. Rev. B* 1981, *23*, 5048-507

Chapter 6:

Multi-scale Structure of Hexagonal Si-4H from high-pressure

In this chapter the results of a more detailed structural characterization of hexagonal Si-4H are presented. Our multi-scale approach has revealed a hierarchical structure in the native morphology of hexagonal Si-4H obtained from high-pressure synthesis. We provide direct evidence of nanostructure on a different length-scale from the inferred crystallites' size (i.e. ~ 5 nm-high coherent crystalline domains, called *nano-flakes*, see Chapter 5). Structural characterization combining optical and electron microscopy has enabled discovery of a new structural unit, that we named *platelets*. The dimensions of the platelets, i.e. hundreds of nanometres in the lateral dimensions and tens of nanometres thickness, suggest that they might have an impact on Si-4H applications, as size effects may modify the bandstructure and determine the bandgap value. We developed an experimental procedure to separate and disperse quasi-single platelets without evident damages to their crystallinity nor carbon contamination. Our procedure to access and manipulate the platelets, i.e. quasi-2D nanoparticles of hexagonal Si, opens the way to devices design and engineering through micromanipulation.

6.1 Introduction

Hexagonal silicon (Si) is expected to pack into a range of different polytypes comprised of quasi-2D hexagonal sheets and differing for the stacking sequence along the third dimension. Si hexagonal (H) polytypes can be obtained by modifying the sequence of Si {111} planes, i.e. ABC in the case of cubic Si-I (3C polytype). Calculations have predicted several metastable polytypes, such as 2H (AB), 4H (ABCB) and 6H (ABCACB)¹⁻³. Theoretical studies have addressed the optoelectronic properties of hexagonal Si polytypes, especially the *lonsdaleite*⁴-like Si-2H. These studies suggest that, when arranged in a hexagonal symmetry, Si should present considerable advantages for optoelectronic applications compared to the cubic counterpart. Hexagonal Si is expected to exhibit enhanced absorption efficiency in the range of interest for solar applications⁵⁻⁸, with a bandgap that is predicted to shift and to become direct with strain and pressure^{3,7,9} or in low-dimensional systems¹⁰. Enhancement of Si absorption in the visible region would open the way for a new generation of solar devices able to combine high-efficiency with moderate costs and environmental impact^{11,12}. Thus, synthesis of hexagonal Si could be a major step forward in the field of Si-based technology, and it would contribute to resolve the longstanding challenge of obtaining optimized yet Si-based materials.

Because of the promising optoelectronic properties predicted for hexagonal Si, researchers have used different synthetic approaches in the attempt of stabilizing it. Synthesis of Si-2H has been reported from chemical methods¹³, as an inclusion in polycrystalline Si nanostructures^{14–16}, and as the result of high-pressure treatment^{17–21} (the so-called Si-IV phase, obtained by annealing of the cubic Si-III^{17,22,23} recovered upon decompression). A hexagonal 2H-like arrangement of Si atoms (as the one suggested for Si-IV) was demonstrated by epitaxial growth of Si on a GaP nanowire (NW) core²⁴. The process has been successfully applied to obtain GaP/Si/SiGe NWs²⁵. Despite this extended experimental effort, characterization of hexagonal Si's properties has remained elusive, as synthesis of a pure-phase material was still missing. We recently established the first synthesis of pure hexagonal Si from high-pressure and demonstrated its Si-4H structure²⁶, paving the way for the exploration of its physical properties (for more details, see Chapter 5). The advantage of our high-pressure synthesis approach is that the solid-to-solid transformations ensure that the purity of the product matches that of the starting material^{27,28}, making it preferable to chemical methods²⁹.

Preliminary investigation of the pure Si-4H samples, as reported in Chapter 5, revealed a substantial nanostructure. Structural characterization combining x-ray diffraction (XRD) and transmission electron microscopy (TEM) has shown that Si-4H obtained from high-pressure is comprised of flake-like crystallites, as set by the high density of stacking faults²⁶. These highly textured nanostructure present significant questions as to its influence on Si-4H optoelectronic properties. Indeed, quantum confinement on the nanometric scale could have a significant impact on the bandgap of this material^{10,30}. We measured a strong photoluminescence showing a good overlap with the visible range of solar spectrum. The origin of this emission has not yet been assessed, and further investigation is needed to determine the main factors that set the bandgap of nanostructured Si-4H.

Hexagonal polytypes of Si are expected to play a fundamental role in the development of high-efficiency Si-based photovoltaics, and several theoretical studies have addressed their optoelectronic properties in both the bulk and the NWs form. We have provided the first synthesis of pure hexagonal Si from high-pressure treatment in the form of a bulk yet nanostructured material. High-pressure synthesis enables thus to combine the advantage of large-volume synthesis with those of confinement-enhanced optoelectronic properties. Our preliminary characterization has revealed flake-like nano-crystallites, i.e. quasi-2D nanoparticles which properties have not yet been addressed by theoretical nor experimental

studies. Through characterization and full understanding of the complex nanostructure of hexagonal Si-4H is a fundamental step to assess its feasibility for solar applications and the possibility of tuning its optical properties by acting on the crystallites' size or by applying strain. In this work we use high-purity samples to investigate the native nanostructure of Si-4H and we report characterization of its multi-scale morphology.

6.2 Experimental Results

We use a multi-scale approach to characterize the structure and the morphology of Si-4H, and we observe a hierarchical structure in the samples as obtained from high-pressure. We report discovery of discrete disks at the nanoscale, which we refer to as *platelets* to distinguish them from the previously inferred flake-like crystallites.

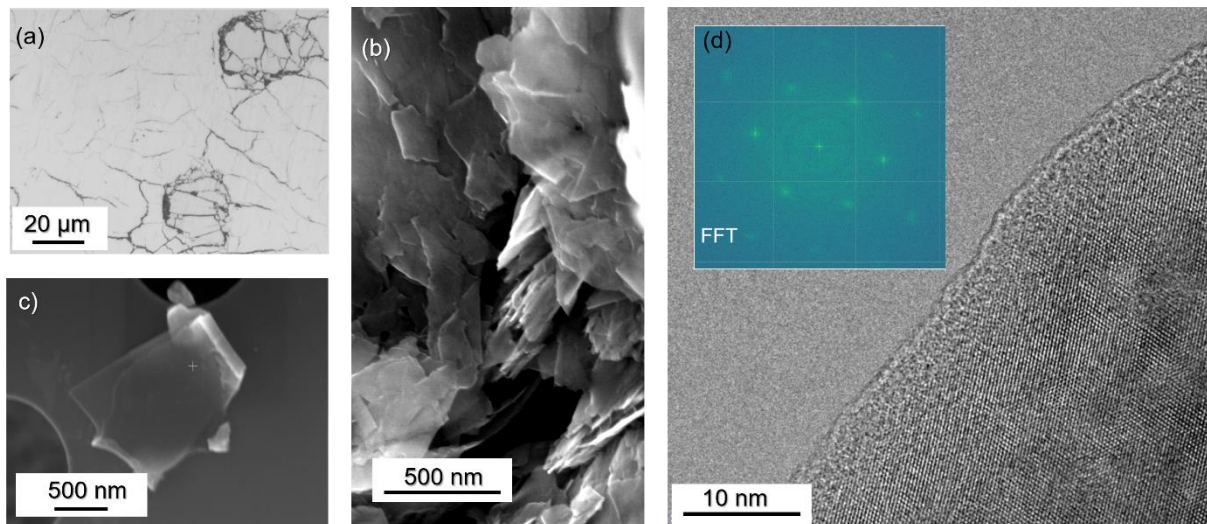


Figure 6.1 : Multi-scale analysis of the hierarchical structure of Si-4H. A combination of optical and electron microscopy techniques was used to access the different length-scales. (a) Cracks observed at the sample surface upon polishing. Observation of the finely patterned cracks led us to further investigate the grains' size in our material. (b) Image revealing the substantial nanostructure of the pristine Si-4H morphology. We observe quasi-2D discrete structural units, that we refer to as *platelets*. (c) Image of quasi-single platelets dispersed on a TEM grid. (d) Image of a single platelet. The crystal planes are well visible, and the crystalline quality is also confirmed by the FFT pattern (i.e. the reciprocal lattice corresponding to the image).

From our previous characterization we had inferred that Si-4H is a nanostructured material, comprised of flake-like crystallites stacked along the c axis and separated by stacking faults (Chapter 5). Thus, on the nanoscale the material is highly textured, as the flakes have a preferential orientation. Figure 6.2(c) shows typical XRD data from Si-4H samples, and the presence of continuous Debye-Scherrer rings demonstrates that the sample, when the entire sample volume is probed, appears like a perfect powder. The well-ordered behavior at the

nanoscale is in contrast with the random orientation of the crystals at the biggest length-scale. The substantial differences between these two length-scales led us to suppose the existence of (at least) an intermediate length-scale, at which the preferential orientation is lost. To verify this supposition, we performed Electron Backscatter Diffraction (EBSD) to characterize the mosaicity of the sample at the μm scale. To prepare the sample and to obtain a clean and flat surface, we mechanically polished the as-synthesized pellet of Si-4H (see also Appendix 6.1). The images in Figure 6.2(a-b) were collected with an optical microscope and they show the surface cracks that we observed after polishing. These cracks could be caused either by material sensitivity or because of the native structure. We performed EBSD, but no detectable signal was measured. The absence of signal from EBSD could be caused either by the amorphization of the sample's surface upon polishing or by the presence of sub-micron crystalline domains, not detectable by EBSD.

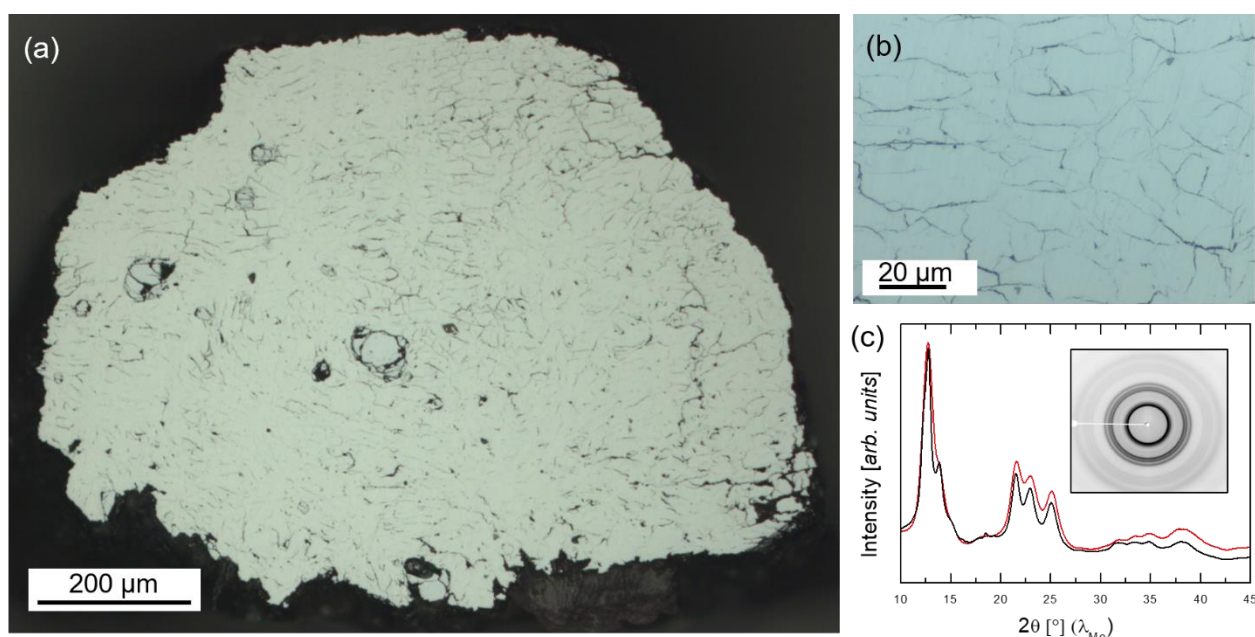


Figure 6.2 : (a)-(b) Images of the pellet's surface after fine polishing. Cracks are visible at the sample's surface. (c) XRD pattern of the Si-4H sample from the original batch (black, Chapter 5) and from the sample analysed in this study (red). The inset shows the 2D image plate, displaying continuous Debye-Scherrer rings.

Both the absence of EBSD signal and the presence of fine cracks at the sample's surface could be caused by mosaicity on a length-scale not detectable by optical microscope. To verify the presence of sub-micron grains, we performed Scanning Electron Microscopy (SEM) imaging on the sides of the as-synthesized sample investigating Si-4H's pristine morphology. The images in Figure 6.3 reveal a complex morphology, with voids and cracks observable already on the pristine sample (see inset in Figure 6.3(a)). Ultra-High-Resolution (UHR)

imaging using the so-called *immersion mode* (i.e. the sample is immersed in the lenses' magnetic field) enabled us to finely observe the morphology of Si-4H. These results (Figure 6.3) demonstrate that the material is comprised of discrete structural units that entirely cover the surface, as shown in Figure 6.3(b-c).

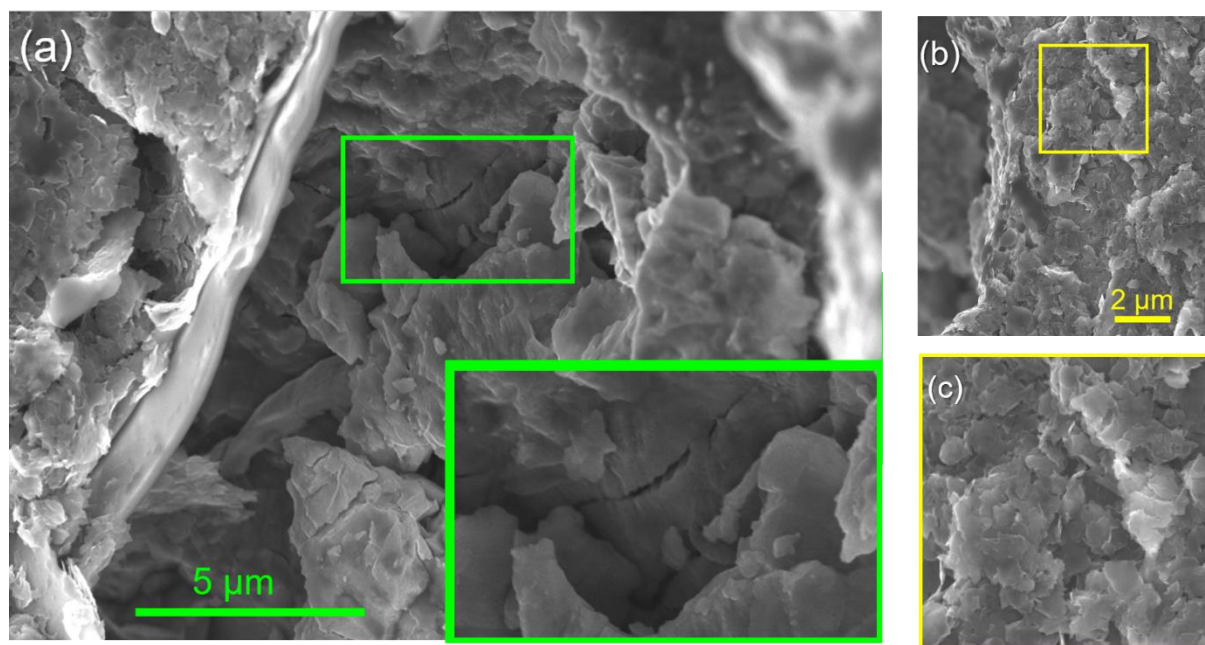


Figure 6.3 : Images investigating the pristine morphology of Si-4H. The complex conformation of the sample, that comprises voids, cracks and discrete flat units, is here demonstrated by SEM imaging. (a) Evidence of voids and cracks on the as-synthesized Si-4H sample; the inset dimensions are 5 μm and 2.4 μm . (b) Image of the sample's surface that evidences the presence of the platelets. (c) Magnification of the region framed in yellow in (b); dimensions are 3.8 μm x 3.8 μm .

Further analysis of these structural units revealed a disk-like shape, that resembles that of the previously reported nano-flakes²⁶, (see also Figure 6.4). With respect to the flake-like crystallites ($\sim 5\text{nm}$ high), the units that emerged from SEM imaging are on a larger length-scale, and we referred them as *platelets*, in analogy with SiC-4H crystals obtained via Acheson process³¹⁻³³. Figure 6.4(b) shows a group of platelets that are loosely packed together and have no evident preferential orientation. By analysing the magnifications in Figure 6.4(b-c), we observed that the platelets are electron-transparent. Indeed, the figure shows three distinct platelets that are superposed. The edges of all three platelets are visible, which is only possible if at least one of them is partially transparent to the electron beam. This observation sets an upper limit for their height at around 100 nm and gives direct evidence of the nanostructured morphology of as-synthesized Si-4H.

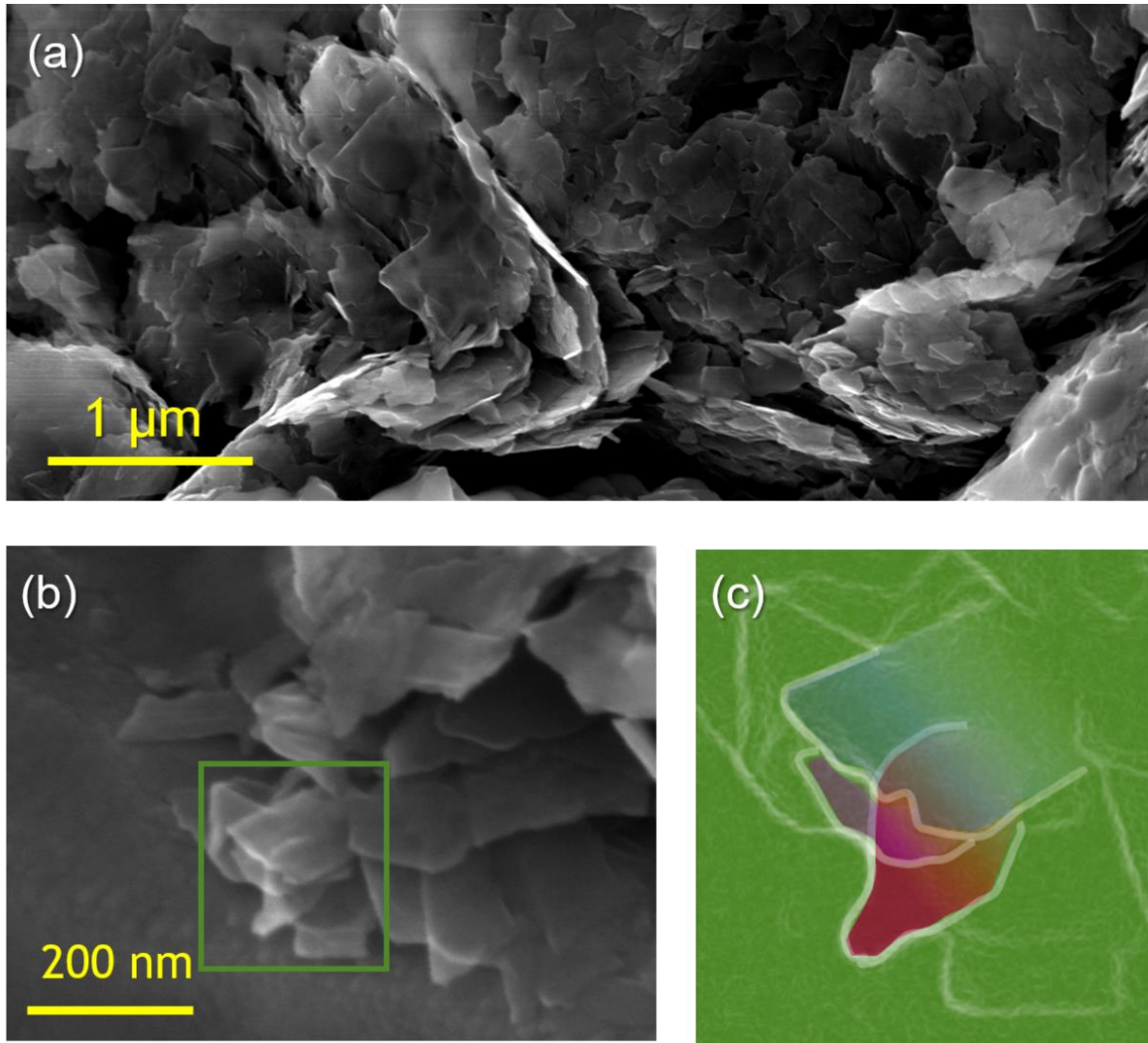


Figure 6.4 : Images showing a representative collection of platelets. The platelets are disordered and show no sign of preferential orientation. (a), (b) UHR-SEM images of the pristine morphology of Si-4H. (c) Magnification of the region evidenced in (b). The edges of the platelets as obtained from edge-finding methods are evidenced.

The electron-transparency of the platelets enabled us to study single platelets and collections of very few platelets by TEM without additional processing. We developed a procedure to separate and disperse the platelets on a TEM grid (Figure 6.5); the weak binding between the platelets facilitated the preparation procedure (for more details on the dispersion procedure see Appendix 6.1). We used TEM grid covered with a thin Grafoil® supporting film, and we studied only the platelets that were suspended over the holes in the substrate.

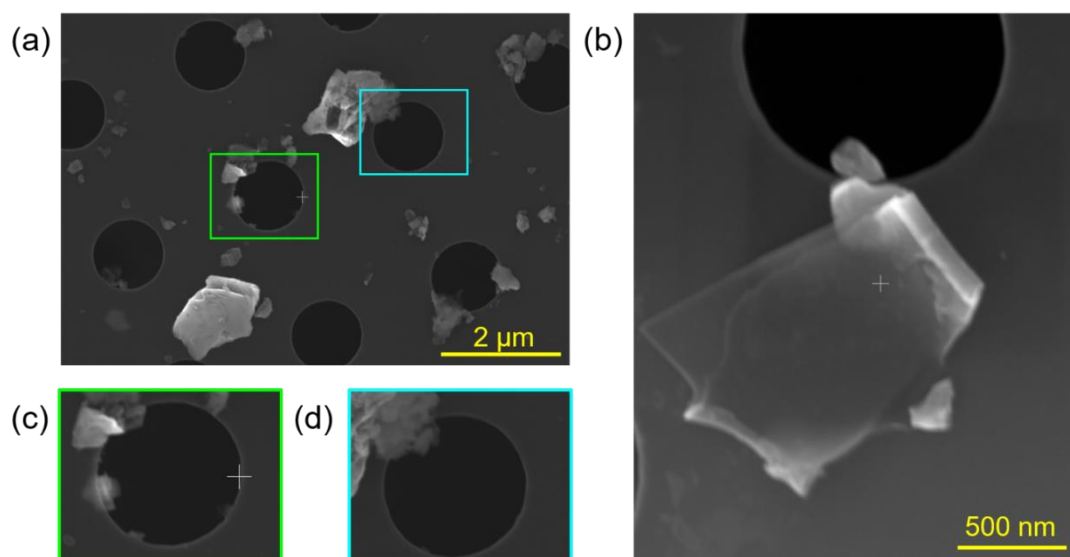


Figure 6.5 : (a-d) UHR-SEM images of the TEM grid prepared following the methodology detailed in the text. The magnified images in (c-d) ($1.80\ \mu\text{m} \times 1.40\ \mu\text{m}$) evidence the suspended electron-transparent units at the border of the holes of the Quantifoil support film.

Figure 6.6 shows a typical high-resolution (HR) TEM image of the sample after the dispersion processing. We studied a region in which a few platelets are superposed. Using EELS, we confirmed no carbon contamination from the substrate nor from the dispersion procedure. Most of the platelets present good crystalline quality after TEM sample preparation, i.e. the crystalline planes are clearly visible in the HR-TEM images. Some of the thinnest platelets (e.g. right edge of Figure 6.6), and the edges of larger platelets appear amorphous, i.e. there is no evidence of crystalline planes. In such thin samples, we would expect the crystalline domains to be visible in transmission geometry regardless the orientation of the platelet. We interpret thus the absence of ordered features in the HR-TEM images as the signature of amorphous zones.

We used Electron Energy Loss Spectroscopy (EELS) to verify whether the structural differences we observed in the TEM images are coupled to chemical differences. The black line in Figure 6.6(a) shows the line along which EELS scans rastered through the sample. Figure 6.6(b) shows representative EELS spectra from regions that appear crystalline and amorphous, as discussed previously. The spectra in Figure 6.6(b) were acquired in the points marked in the zoomed panel (top-right of Figure 6.6). While data collected far from the platelet's edge (black curve) is consistent with the $L_{2,3}$ edge of crystalline Si, at the sample's boundary (red curve) a mixture of Si and SiO_2 ^{34,35} is present.

Figure 6.6(c) shows the intensity of the EELS peaks along the scanned line. Si and SiO₂ peaks' intensities have been calculated by integrating the regions of the EELS spectra delimited by the dashed vertical lines in Figure 6.6(b). The intensities were then normalized by the value at the first position of the scan and the data are reported in Figure 6.6(c) in purple (Si) and green (SiO₂). The ratio between the SiO₂ and Si peaks' intensities is represented by the red symbols. The relative intensity of SiO₂/Si increases at 5 nm from the edge of the sample, i.e. from the point at which both intensities go to zero. The quantity of SiO₂ is thus higher at the platelets' edges than in other thicker zones. Combination of high-resolution imaging and electron spectroscopy enabled us to correlate the amorphous appearance of the thinnest regions of the sample to the oxidization.

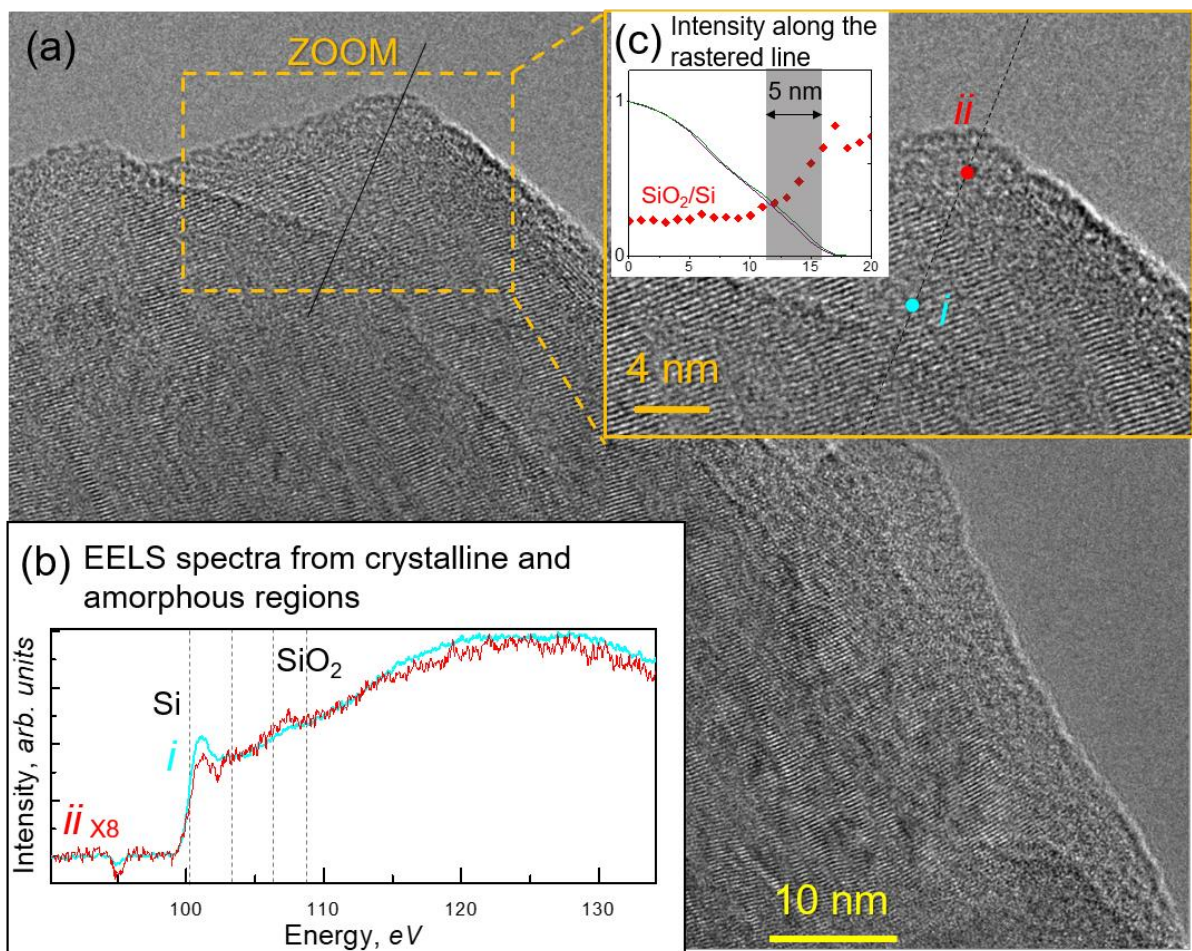


Figure 6.6 : Images of the dispersed platelets and EELS data. (a) HR-TEM image of Si-4H platelets dispersion. EELS data have been collected along the black line (b) Spectra from the points marked in the top-right zoom panel. (c) Normalized intensities of Si and SiO₂ EELS peaks in purple and green respectively (the dashed vertical lines in (b) show the integration interval around the peaks). The red points show the SiO₂/Si ratio along the profile.

6.3 Discussion

At the largest length-scale investigated, our results from optical microscopy suggest that the high-pressure synthesis route had an impact on the material's structure. During the preparation of a clean surface we observe a fine network of cracks at the sample's surface. The presence of the cracks suggests the existence of grains on an intermediate length-scale between the powder-like bulk sample (as emerged from XRD) and the highly ordered nano-flakes (Chapter 5).

By analysis of the μm scale with SEM, we demonstrate that Si-4H sample has a varied native morphology, with voids and cracks that could be the origin of those observed using optical microscopy on a larger length-scale. The origin of the observed voids is probably linked with the phase transformations at high-pressure during the synthesis procedure. Indeed, during Si-I \rightarrow Si-II transition, we have observed a pressure drop caused by a volume contraction of more than 20%^{36,37} (Chapter 4). The high-pressure conditions are generated by a solid $\text{Cr}_2\text{O}_3\text{:MgO}$ pressure transmitting medium and a *h*BN capsule (which becomes more rigid around 10 GPa at high-temperature³⁸) is used. Since the maximum temperature attained during the synthesis is 870 K and Si remains in the solid state during the transformations. It is thus possible that the nucleation and growth of denser Si-II crystals causes the formation of low-density and/or voids regions in the assembly, as there is no redistribution of matter during the solid-to-solid phase transition.

SEM imaging has enabled us to discover and characterize discrete and strongly planar structural units, Si-4H platelets. In our previous studies, we had inferred the crystallites' size from XRD Rietveld fitting and FFT-TEM analysis (Chapter 5). The inferred *nano-flakes* were only a few (~ 5) nanometres high, suggesting that their dimensions were limited by the high density of stacking fault along the *c* axis²⁶. From our SEM images reported in this Chapter, we see that the platelets are hundreds of nanometres long in their lateral dimensions, while the inferred size of the flakes was smaller. Discovery of the platelets adds thus another relevant length-scale to the study of hexagonal Si-4H structure and provides the first direct evidence of the nanostructured morphology of Si-4H. As was shown in Figure 6.4 and described in Section 6.2, the platelets appear as solid units that have well defined edges.

The platelets are loosely packed, suggesting relatively weak interaction between them. As direct lattice bonds would hold together the nano-flakes via stacking faults, the loosely

packed platelets and the nano-flakes differ substantially. Exploiting their weak interactions, we developed a procedure to disperse single and quasi-single platelets. TEM combined with EELS spectroscopy showed that, after dispersion, each platelet showed both crystalline and amorphous regions. We remark that the lone platelets at the thinnest parts of the samples' edges appeared amorphous with higher concentrations of SiO₂. Despite the presence of these amorphous regions, the majority of platelets are well-crystallized.

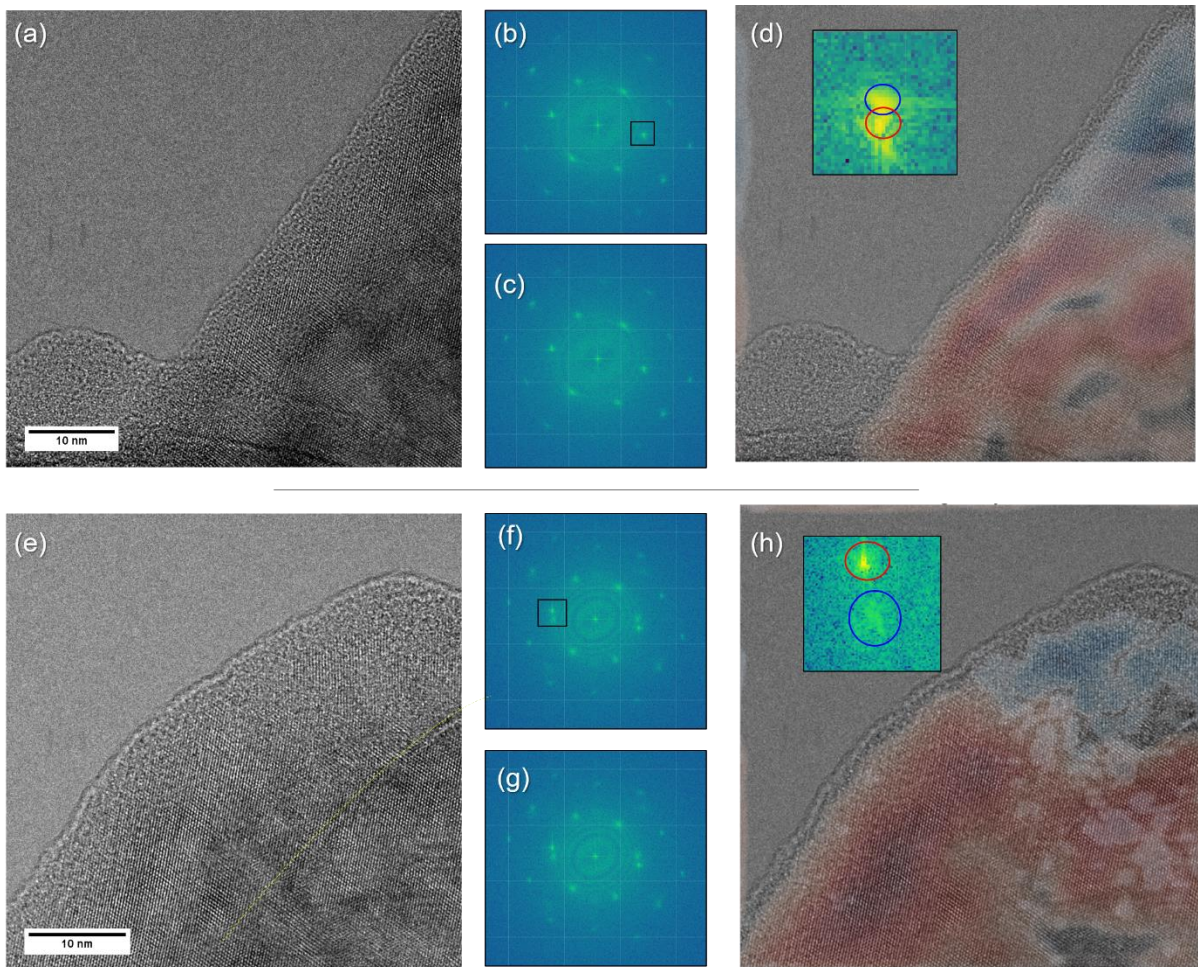


Figure 6.7 : Images showing some representative Si-4H platelets and FFT-TEM analysis of the crystalline domains. The direct-space HR-TEM image, the FFT-TEM pattern alone and superposed with the calculated one from Si-4H structural model are shown in (a),(b),(c) and (e),(f),(g) respectively. (d) and (h) show the FFT-filtered images, in which coloured overlays are superposed to the original TEM image to evidence the crystalline domains. The inset shows the peaks used for Fourier filtering; the colours used to evidence each peak are the same of the correspondent overlays' ones.

To compare the crystalline structures that we measured by TEM, we performed Fast Fourier Transform (FFT) and Fourier filtering on our images. This analysis allowed us to assess the extent and relative orientation of crystalline domains. Figure 6.7 shows the results of this Fourier analysis on some representative TEM images of Si-4H platelets. The interplanar distances obtained by FFT-TEM analysis are consistent with our previous reports and with the

Si-4H structural model^{3,26}. Figure 6.7 (a-b) shows a TEM image and its corresponding FFT-TEM pattern (superposed with the calculated one in Figure 6.7(c)) and the filtered image in Figure 6.7(d). We were able to index all FFT peaks to the Si-4H [021] reflections, individuating thus the orientation of the platelet. While the planes appear well ordered in the direct-space images, the FFT peaks are broad, which would, on the contrary, suggest the presence of a disordered region. The inset of Figure 6.7(d) shows that each spot corresponds to two $(0\bar{1}2)$ reflections, tilted of around 2.5° and not completely resolvable. FFT filtering of these spots reveals two domains, highlighted in red and blue respectively. The presence of two well crystallized Si-4H [021] domains oriented in slightly different directions causes thus the presence of broad FFT peaks.

Domains formed by families of planes tilted with respect to each other are found also in other regions (Figure 6.7(e-h)). In Figure 6.7(e) the edge of a second superposed platelet is visible and highlighted in yellow. The spots on the FFT-TEM pattern show Si-4H [021] reflections, with two distinct $(0\bar{1}2)$ spots tilted $\sim 12^\circ$ with respect to each other. The result from FFT filtering shows that the tilted crystalline domains cover the lower and the upper portion of the platelets, as opposed to each platelet having a different orientation. Both Figure 6.7(a-d) and Figure 6.7(e-h) show reflections that index by FFT-TEM to [021]. In both regions, a second crystalline domain tilted with respect to the most extended [021] one is present. The platelets thus don't correspond strictly to one crystalline domain. The domains evidenced in Figure 6.7 have one family of planes in common, i.e. the one corresponding to the $(0\bar{1}2)$ reflection. The presence of these domains tilted with respect to each other could be linked with the crystallization of Si-4H and it could be a signature of the crystalline growth process.

The edges of the sample, as well as some platelets in the lower part of Figure 6.7(a) don't belong to any of the crystalline domains highlighted via Fourier filtering. These regions are thus amorphous. Previously, in Section 6.2 and in Figure 6.6, the amorphous nature of the edges was only inferred by qualitative considerations looking at the direct space HR-TEM images. FFT-TEM and Fourier filtering confirm thus our qualitative identification of the amorphous regions.

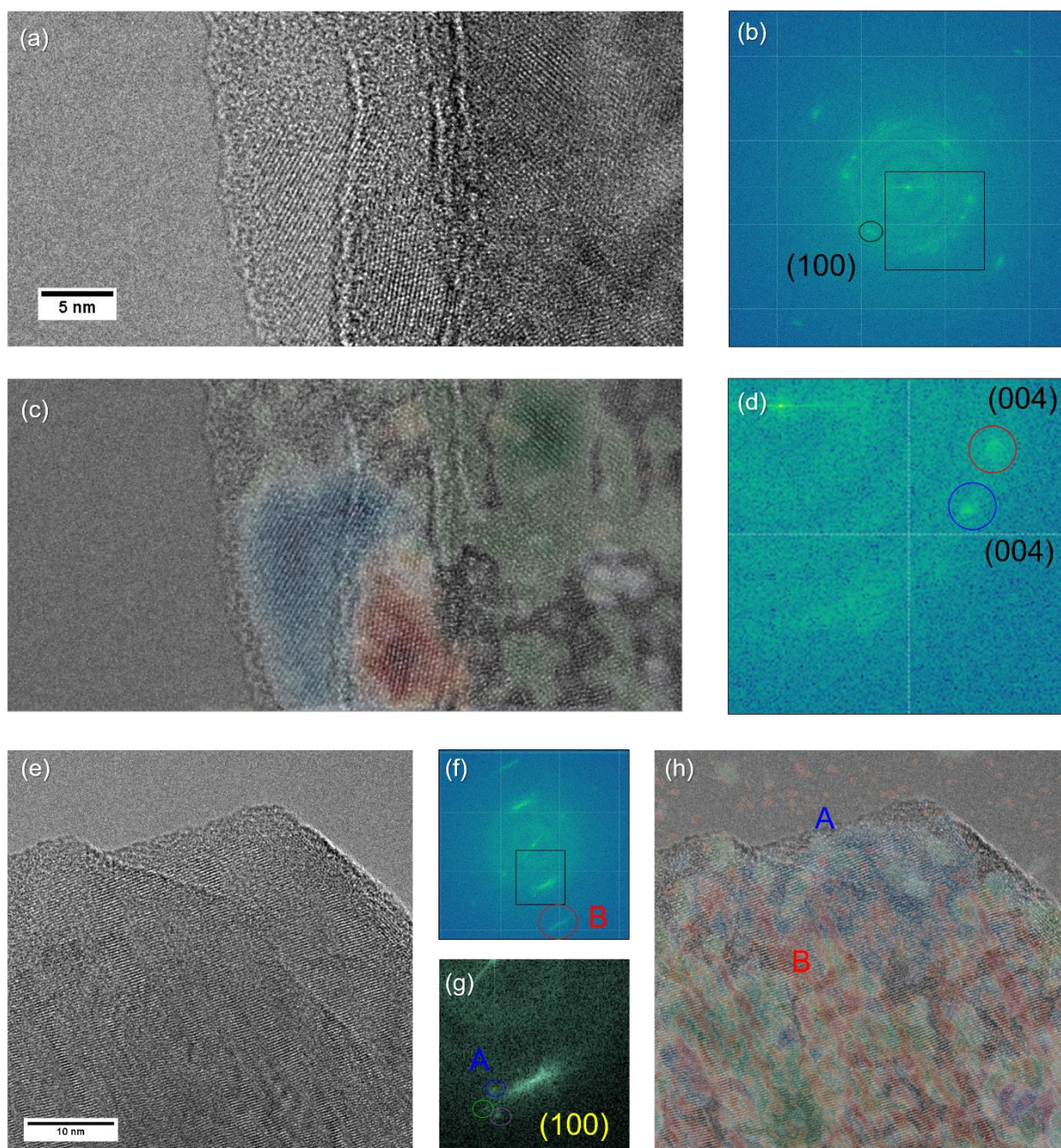


Figure 6.8 : Analysis of the crystalline domains by FFT-TEM filtering. For two different zones of the sample the direct-space HR-TEM image, the FFT-TEM pattern and the FFT filtered images are shown in (a),(b),(c) and (e),(f),(h) respectively. (d),(h): Zoom of the FFT-TEM pattern corresponding to the black squares in (b) and (f) to evidence the peaks used for FFT filtering. The filtered peaks are highlighted by coloured circles respectively; the same colours have been used to evidence the correspondent crystalline domains with the overlay in (c) and (h).

Figure 6.8 shows analysis of Si-4H platelets exhibiting different structural features within the crystalline domains. In Figure 6.8(a-d) the FFT-filtering procedure was applied to a region in which the edges of three superposed platelets are visible. Different crystallographic planes have been identified based on comparison to the predicted diffraction patterns. The peaks highlighted in red and blue in Figure 6.8(d) correspond to (004) reflections and are tilted $\sim 16.5^\circ$ with respect to each other. The peak highlighted in green (Figure 6.8(b)) corresponds to (100)

reflections. The FFT-filtered image in Figure 6.8(c) demonstrates that each of the highlighted peaks correspond to a distinct platelet.

A very different picture is given by Figure 6.8(e-h), in which the small peaks shown in Figure 6.8(g) correspond to extended areas of the sample, but not to a single platelet. The (100) reflection correspond to domains formed by {100} planes, i.e. the planes perpendicular to the *a* axis, or, equivalently by symmetry, the *b* axis. Two {100} domains that are twisted with respect to each other and differ for the peaks' width are highlighted in blue and red (A and B). The peaks of the B {100} domain (red) are very broad and appear as linear streaks in reciprocal space that cover continuous spreads of 2θ . The broadened streak-like peaks suggest presence of disorder along one specific direction. The corresponding crystalline domain is comprised of very narrow (a few nanometers) crystalline-crystalline bands oriented perpendicularly to the {100} planes. The orientation of the FFT peak's broadening and the configuration of the narrow crystalline domains suggest structures analogous to the previously observed nano-flakes²⁶.

Figure 6.8 presents thus two opposite situations: in the first one each of the superposed platelets corresponds to a single crystalline domain, while in the second region streak-like domains alternate on a surface that covers more than a single platelet. Our data suggest thus a relation between the flake-like crystallites and the platelets more complex than a simple stacking along the *c* axis. The current FFT-TEM data cannot identify the precise orientation of the crystalline bands in Figure 6.8(h) because only one reflection per crystalline domain is visible in the FFT-TEM pattern. This prevents us from directly corroborating our previously observed flake-like crystallites at this time. Further studies using dark-field TEM and investigating the short dimension of the platelets are needed for a complete understanding of the relation between the length-scale of the crystallites and that of the platelets.

Our data suggest also that the platelets might play an important role in the crystal growth, as the Si-III \rightarrow Si-IV(Si-4H) transformation is expected to happen by twisting of bonds³⁹. Most of the examined platelets correspond to one crystallographic orientation (eventually with some twisting of the planes) and could be thus the fundamental units in the Si-4H growth process from Si-III precursor. Our results will contribute to the understanding of Si-4H nanostructure's origin and its growth mode, but its full understanding is beyond the scope of this work and the reach of our current experimental data.

6.4 Conclusion

We performed a detailed structural characterization, combining different microscopy techniques as to cover different length-scales. We give direct proof of a substantial nanostructure in Si-4H and we indicate an additional length-scale of interest for the future applications of hexagonal Si-4H. We discovered and characterized quasi-2D Si-4H nanostructures, that we named *platelets*. The newly discovered platelets are different from the inferred flake-like crystallites previously reported, and they could play a key role in the design of devices. Indeed, Si-4H platelets can be separated and dispersed without affecting their crystal quality, which makes them ideal candidates for devices engineering. Our multi-scale approach has thus revealed a hierarchical nanostructure in hexagonal Si-4H obtained through high-pressure, which is expected to strongly affect and improve its potential for optoelectronic applications. We have used a bulk synthetic approach through high-pressure, obtaining large quantities of hexagonal Si nanoparticles for optoelectronic and solar devices.

Acknowledgments: the work presented in this chapter was partially financed by Lawrence Livermore National Laboratory (Livermore, CA) during my Summer Internship under the supervision of Leora Dresselhaus-Cooper and Jon Eggert. A special thanks to Leora Dresselhaus-Copper for the mentoring and the fruitful collaboration during the development and the realization of the whole project. The microscopy experiments were performed at the National Center for Electron Microscopy at Lawrence Berkeley National Laboratory (Berkeley, CA) with the collaboration of Andrew Minor, Shitengo Zhao, John Turner, Peter Ercius, Chengyu Song and Rohan Dhall. Synthesis of Si-4H samples was performed both at the European Synchrotron Radiation Facility (Grenoble, France) with the help of Kristina Spektor and Wilson Crichton and at the IMPMC with the help of Paraskevas Parisiadis and Louis Amand. Initial XRD characterization were performed in collaboration with Benoit Baptiste, Ludovic Delbes (IMPMC) and Jon Lee (LLNL).

References Chapter 6

- (1) Joannopoulos, J. D.; Cohen, M. L. Electronic Properties of Complex Crystalline and Amorphous Phases of Ge and Si. II. Band Structure and Optical Properties. *Phys. Rev. B* **1973**, *8* (6), 2733–2755. <https://doi.org/10.1103/PhysRevB.8.2733>.
- (2) Persson, C.; Janzén, E. Electronic Band Structure in Hexagonal Close-Packed Si Polytypes. *J. Phys. Condens. Matter* **1998**, *10* (47), 10549–10555. <https://doi.org/10.1088/0953-8984/10/47/006>.
- (3) Raffy, C.; Furthmüller, J.; Bechstedt, F. Properties of Hexagonal Polytypes of Group-IV Elements from First-Principles Calculations. *Phys. Rev. B* **2002**, *66* (7), 075201. <https://doi.org/10.1103/PhysRevB.66.075201>.
- (4) Frondel, C.; Marvin, U. B. Lonsdaleite, a Hexagonal Polymorph of Diamond. *Nature* **1967**, *214* (5088), 587–589. <https://doi.org/10.1038/214587a0>.
- (5) De, A.; Pryor, C. E. Electronic Structure and Optical Properties of Si, Ge and Diamond in the Lonsdaleite Phase. *J. Phys. Condens. Matter* **2014**, *26* (4), 045801. <https://doi.org/10.1088/0953-8984/26/4/045801>.
- (6) Chelikowsky, J. R.; Cohen, M. L. Nonlocal Pseudopotential Calculations for the Electronic Structure of Eleven Diamond and Zinc-Blende Semiconductors. *Phys. Rev. B* **1976**, *14* (2), 556–582. <https://doi.org/10.1103/PhysRevB.14.556>.
- (7) Rödl, C.; Sander, T.; Bechstedt, F.; Vidal, J.; Olsson, P.; Laribi, S.; Guillemoles, J.-F. Wurtzite Silicon as a Potential Absorber in Photovoltaics: Tailoring the Optical Absorption by Applying Strain. *Phys. Rev. B* **2015**, *92* (4), 045207. <https://doi.org/10.1103/PhysRevB.92.045207>.
- (8) Hedin, L. New Method for Calculating the One-Particle Green's Function with Application to the Electron-Gas Problem. *Phys. Rev.* **1965**, *139* (3A), A796–A823. <https://doi.org/10.1103/PhysRev.139.A796>.
- (9) Jensen, I. J. T.; Ulyashin, A. G.; Løvvik, O. M. Direct-to-Indirect Bandgap Transitions in ⟨110⟩ Silicon Nanowires. *J. Appl. Phys.* **2016**, *119* (1), 015702. <https://doi.org/10.1063/1.4938063>.
- (10) Amato, M.; Kaewmaraya, T.; Zobelli, A.; Palumbo, M.; Rurali, R. Crystal Phase Effects in Si Nanowire Polytypes and Their Homojunctions. *Nano Lett.* **2016**, *16* (9), 5694–5700. <https://doi.org/10.1021/acs.nanolett.6b02362>.
- (11) Kazmerski, L. L. Solar Photovoltaics R&D at the Tipping Point: A 2005 Technology Overview. *J. Electron Spectrosc. Relat. Phenom.* **2006**, *150* (2–3), 105–135. <https://doi.org/10.1016/j.elspec.2005.09.004>.
- (12) Braga, A. F. B.; Moreira, S. P.; Zampieri, P. R.; Bacchin, J. M. G.; Mei, P. R. New Processes for the Production of Solar-Grade Polycrystalline Silicon: A Review. *Sol. Energy Mater. Sol. Cells* **2008**, *92* (4), 418–424. <https://doi.org/10.1016/j.solmat.2007.10.003>.
- (13) Jennings, H. M.; Richman, M. H. A Hexagonal (Wurtzite) Form of Silicon. *Science* **1976**, *193* (4259), 1242–1243. <https://doi.org/10.1126/science.193.4259.1242>.
- (14) Vincent, L.; Patriarche, G.; Hallais, G.; Renard, C.; Gardès, C.; Troadec, D.; Bouchier, D. Novel Heterostructured Ge Nanowires Based on Polytype Transformation. *Nano Lett.* **2014**, *14* (8), 4828–4836. <https://doi.org/10.1021/nl502049a>.
- (15) Cerva, H. High-Resolution Electron Microscopy of Diamond Hexagonal Silicon in Low Pressure Chemical Vapor Deposited Polycrystalline Silicon. *J. Mater. Res.* **1991**, *6* (11), 2324–2336. <https://doi.org/10.1557/JMR.1991.2324>.
- (16) Tang, J.; Maurice, J.-L.; Fossard, F.; Florea, I.; Chen, W.; Johnson, E. V.; Foldyna, M.; Yu, L.; Roca i Cabarrocas, P. Natural Occurrence of the Diamond Hexagonal Structure

- in Silicon Nanowires Grown by a Plasma-Assisted Vapour–Liquid–Solid Method. *Nanoscale* **2017**, *9* (24), 8113–8118. <https://doi.org/10.1039/C7NR01299C>.
- (17) Besson, J. M.; Mokhtari, E. H.; Gonzalez, J.; Weill, G. Electrical Properties of Semimetallic Silicon III and Semiconductive Silicon IV at Ambient Pressure. *Phys. Rev. Lett.* **1987**, *59* (4), 473–476. <https://doi.org/10.1103/PhysRevLett.59.473>.
- (18) Wentorf, R. H.; Kasper, J. S. Two New Forms of Silicon. *Science* **1963**, *139* (3552), 338–339. <https://doi.org/10.1126/science.139.3552.338-a>.
- (19) Kobliska, R. J.; Solin, S. A. Raman Spectrum of Wurtzite Silicon. *Phys. Rev. B* **1973**, *8* (8), 3799–3802. <https://doi.org/10.1103/PhysRevB.8.3799>.
- (20) Weill, G.; Mansot, J. L.; Sagon, G.; Carlone, C.; Besson, J. M. Characterisation of Si III and Si IV, Metastable Forms of Silicon at Ambient Pressure. *Semicond. Sci. Technol.* **1989**, *4* (4), 280–282. <https://doi.org/10.1088/0268-1242/4/4/029>.
- (21) Demishev, S. V.; Lunts, D. G.; Nekhaev, D. V.; Sluchanko, N. E.; Smarin, N. A.; Brazhkin, V. V.; Lyapin, A. G.; Popova, S. V.; Mel'nik, N. N. Structural Relaxation of the Metastable Kasper Phase of Silicon. *J. Exp. Theor. Phys.* **1996**, *82* (6), 1159–1167.
- (22) Zhang, H.; Liu, H.; Wei, K.; Kurakevych, O. O.; Le Godec, Y.; Liu, Z.; Martin, J.; Guerrette, M.; Nolas, G. S.; Strobel, T. A. BC8 Silicon (Si-III) Is a Narrow-Gap Semiconductor. *Phys. Rev. Lett.* **2017**, *118* (14), 146601. <https://doi.org/10.1103/PhysRevLett.118.146601>.
- (23) Kurakevych, O. O.; Le Godec, Y.; Crichton, W. A.; Guignard, J.; Strobel, T. A.; Zhang, H.; Liu, H.; Coelho Diogo, C.; Polian, A.; Menguy, N.; et al. Synthesis of Bulk BC8 Silicon Allotrope by Direct Transformation and Reduced-Pressure Chemical Pathways. *Inorg. Chem.* **2016**, *55* (17), 8943–8950. <https://doi.org/10.1021/acs.inorgchem.6b01443>.
- (24) Hauge, H. I. T.; Verheijen, M. A.; Conesa-Boj, S.; Etzelstorfer, T.; Watzinger, M.; Kriegner, D.; Zardo, I.; Fasolato, C.; Capitani, F.; Postorino, P.; et al. Hexagonal Silicon Realized. *Nano Lett.* **2015**, *15* (9), 5855–5860. <https://doi.org/10.1021/acs.nanolett.5b01939>.
- (25) Hauge, H. I. T.; Conesa-Boj, S.; Verheijen, M. A.; Koelling, S.; Bakkers, E. P. A. M. Single-Crystalline Hexagonal Silicon–Germanium. *Nano Lett.* **2017**, *17* (1), 85–90. <https://doi.org/10.1021/acs.nanolett.6b03488>.
- (26) Pandolfi, S.; Renero-Lecuna, C.; Le Godec, Y.; Baptiste, B.; Menguy, N.; Lazzeri, M.; Gervais, C.; Spektor, K.; Crichton, W. A.; Kurakevych, O. O. Nature of Hexagonal Silicon Forming via High-Pressure Synthesis: Nanostructured Hexagonal 4H Polytype. *Nano Lett.* **2018**, *18* (9), 5989–5995. <https://doi.org/10.1021/acs.nanolett.8b02816>.
- (27) Solozhenko, V. L.; Kurakevych, O. O.; Le Godec, Y. Creation of Nanostructures by Extreme Conditions: High-Pressure Synthesis of Ultrahard Nanocrystalline Cubic Boron Nitride. *Adv. Mater.* **2012**, *24* (12), 1540–1544. <https://doi.org/10.1002/adma.201104361>.
- (28) Irifune, T.; Kurio, A.; Sakamoto, S.; Inoue, T.; Sumiya, H. Ultrahard Polycrystalline Diamond from Graphite: Materials. *Nature* **2003**, *421* (6923), 599–600. <https://doi.org/10.1038/421599b>.
- (29) Ganguly, S.; Kazem, N.; Carter, D.; Kauzlarich, S. M. Colloidal Synthesis of an Exotic Phase of Silicon: The BC8 Structure. *J. Am. Chem. Soc.* **2014**, *136* (4), 1296–1299. <https://doi.org/10.1021/ja412213q>.
- (30) Delerue, C.; Allan, G.; Lannoo, M. Optical Band Gap of Si Nanoclusters. *J. Lumin.* **1998**, *80* (1–4), 65–73. [https://doi.org/10.1016/S0022-2313\(98\)00071-4](https://doi.org/10.1016/S0022-2313(98)00071-4).
- (31) Powders, Fibers, Platelets, and Composites. In *Ceramic Materials*; Springer New York: New York, NY, 2007; pp 359–378. https://doi.org/10.1007/978-0-387-46271-4_20.

- (32) Mitchell, T.; Jonghe, L. C.; MoberlyChan, W. J.; Ritchie, R. O. Silicon Carbide Platelet/Silicon Carbide Composites. *J. Am. Ceram. Soc.* **1995**, *78* (1), 97–103. <https://doi.org/10.1111/j.1151-2916.1995.tb08366.x>.
- (33) Sadow, S. E.; Agarwal, A. *Advances in Silicon Carbide Processing and Applications*; Artech House: Boston, 2004.
- (34) Garvie, L. A.; Craven, A. J.; Brydson, R. Use of Electron-Energy Loss near-Edge Fine Structure in the Study of Minerals. *Am. Mineral.* **1994**, *79* (5–6), 411–425.
- (35) Worch, M.; Engelmann, H. J.; Blum, W.; Zschech, E. Cross-Sectional Thin Film Characterization of Si Compounds in Semiconductor Device Structures Using Both Elemental and ELNES Mapping by EFTEM. *Thin Solid Films* **2002**, *405* (1–2), 198–204. [https://doi.org/10.1016/S0040-6090\(01\)01680-7](https://doi.org/10.1016/S0040-6090(01)01680-7).
- (36) Gaál-Nagy, K.; Strauch, D. Transition Pressures and Enthalpy Barriers for the Cubic Diamond \rightarrow β -Tin Transition in Si and Ge under Nonhydrostatic Conditions. *Phys. Rev. B* **2006**, *73* (13). <https://doi.org/10.1103/PhysRevB.73.134101>.
- (37) Mujica, A.; Rubio, A.; Muñoz, A.; Needs, R. J. High-Pressure Phases of Group-IV, III–V, and II–VI Compounds. *Rev. Mod. Phys.* **2003**, *75* (3), 863–912. <https://doi.org/10.1103/RevModPhys.75.863>.
- (38) Bundy, F. P.; Wentorf, R. H. Direct Transformation of Hexagonal Boron Nitride to Denser Forms. *J. Chem. Phys.* **1963**, *38* (5), 1144–1149. <https://doi.org/10.1063/1.1733815>.
- (39) Zhu, L.; Cohen, R. E.; Strobel, T. A. Phase Transition Pathway Sampling via Swarm Intelligence and Graph Theory. *J. Phys. Chem. Lett.* **2019**, *10* (17), 5019–5026. <https://doi.org/10.1021/acs.jpcclett.9b01715>.
- (40) Guignard, J.; Crichton, W. A. The Large Volume Press Facility at ID06 Beamline of the European Synchrotron Radiation Facility as a High Pressure-High Temperature Deformation Apparatus. *Rev. Sci. Instrum.* **2015**, *86* (8), 085112. <https://doi.org/10.1063/1.4928151>.

Appendix Chapter 6

Appendix 6.1: Detailed Experimental Procedure

Surface Polishing: Mechanical polishing was used to minimize the roughness and the strain at the sample surface. Cycles of polishing using lapping diamond discs with 1 μm and 0.1 μm particle size were performed. At the end of the polishing procedure, the surface is flattened and the streaks on the surface are reduced, but at every stage cracks and holes appear at the surface, as shown in Figure 6.6. The presence of the fractures at every length-scale and their high-density didn't allow preparation of a flat area extended enough to perform mosaicity analysis with backscattered electron diffraction.

TEM Sample Preparation: Scotch tape cleavage has been tested as a way to obtain dispersed platelets for TEM sample preparation. Carbon tape has given good results, with the possibility of cleaving groups of platelets, that could be imaged by SEM as shown in Figure 6.9. Despite that, the method couldn't be used for the preparation of TEM samples, as the density of cleaved platelets was too low. Furthermore, the use of carbon tape was a source of C contamination.

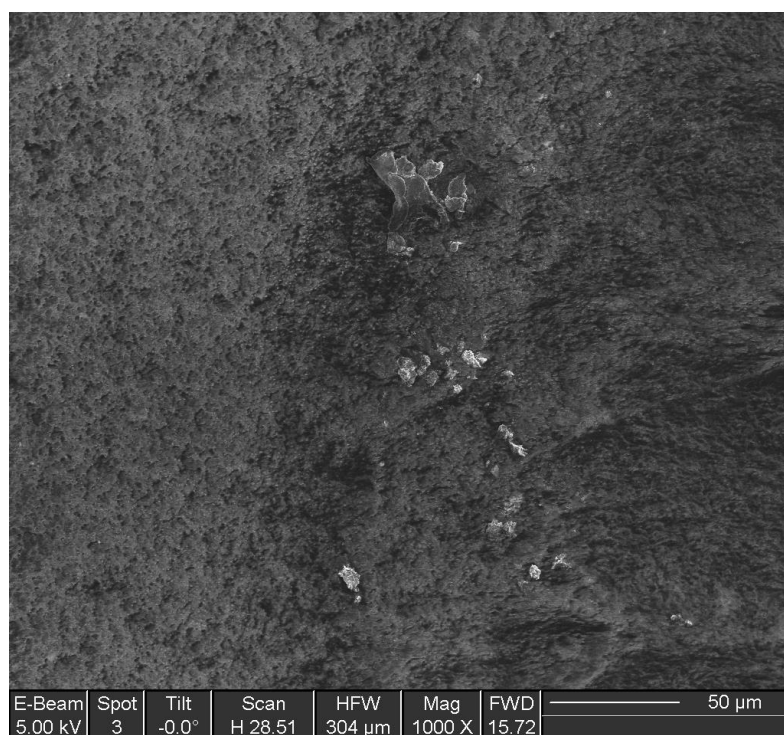


Figure 6.9: SEM image of the carbon scotch-tape after cleavage of the polished Si-4H surface.

TEM samples were prepared using diamond lapping disc (1 μ m particles) to scratch the polished surface of Si-4H bulk sample. A drop of ethanol was used to disperse the portions of the samples transferred to the lapping disc and to transfer them onto the TEM grid. To study small sized particles, TEM copper grid (300 mesh) with Quantifoil support film (orthogonal array of 1.2 μ m holes on a 20 nm thick film) were used. Figure 6.4 in the main text shows SEM images of a TEM grid prepared in this way and demonstrates that the procedure allows to disperse and deposit small agglomerates of platelets, maintaining the morphology observed on the pristine sample.

Si-4H Synthesis Procedure: The sample was synthesized at the European Synchrotron Radiation Facility (ESRF) on the ID06-LVP beamline⁴⁰. We used a 10/5 multianvil assembly to recover Si-III precursor from high pressure with a Deformation-DIA apparatus. The sample pellet (1.95 mm diameter, 2.12 mm height and prepared in an Ar-filled glovebox) was surrounded by an *h*BN sleeve (2.75 mm outer diameter (OD), 1.96 mm inner diameter (ID), 2.12 mm height) and a Ta foil (25 μ m thickness, 2.90 mm OD) resistance furnace. The Ta foil was inserted into a 10 mm octahedron edge length (OEL) Cr₂O₃-doped MgO octahedral pressure medium, along with ZrO₂ plugs. The sample was compressed up to \sim 13 GPa and then heated up to \sim 870 K while maintaining the pressure quasi-constant. After quenching, a pure Si-II (i.e. the metallic HP phase) was stabilized. We then released the pressure, transforming the HP Si-II into BC8 cubic Si-III. We then formed hexagonal Si-4H by heating the recovered Si-III pellet to \sim 200°C under vacuum (\sim 10⁻³ mbar).

Structural characterization: structural characterization via microscopy was performed at the National Center for Electron Microscopy (NCEM) at Lawrence Berkeley National Laboratory (LBNL), Berkeley (CA). Optical microscopy characterization was performed with a Leica DFC295 and objectives with magnifications up to a factor 100X. SEM was performed using the SEM integrated in the FEI Helios G4 UX Focused Ion Beam system. UHR was achieved in the so-called *immersion mode*, with the sample immersed in the lenses' field. HR-TEM and EELS were performed with a 200kV FEI monochromated F20 UT Tecnai; for imaging, the high-tension was kept at a constant value of 200 kV.

Conclusions and Perspectives

In this work, we have addressed the question of synthesizing new functional materials for high-efficiency solar applications. Silicon is currently the cornerstone of the photovoltaic industry, but its absorption is severely limited by its indirect bandgap. Our scope is thus the synthesis of new forms of silicon, able to combine high efficiency with all the practical advantages that have determined silicon's success, such as its huge availability, the moderate cost and the efficient processing procedures. We have opted for a high-pressure synthetic approach. Careful design of high-pressure synthetic pathways can lead to the synthesis of new materials with exotic structures and properties. While high-pressure synthesis has been mainly applied for large-scale production of diamonds and ultra-hard materials, recent experimental studies, as well as theoretical calculations, show that this approach can be successfully applied also for silicon-based materials.

We used synchrotron-based *in-situ* x-ray diffraction to study and optimize high-pressure synthetic pathways. This experimental method is timesaving, because it allows us to explore several pressure-temperature conditions at once and to determine the precise pathway for the stabilization of new phases. We designed and adapted high-pressure cells to run *in-situ* experiments on different beamlines.

We investigated silicon (Si) phase transition mechanisms at high-pressure high-temperature conditions. We focused on the Si-I→Si-II transformation, which is an important step in the synthesis of functional Si-based materials. Previous studies had reported different transition onsets, as well as different extents of Si-I/Si-II coexistence pressure range. The diversity of these results was attributed to the high kinetic barrier of the transition and to the presence of non-hydrostatic stress. We characterized the evolution of pure Si samples under high-pressure and high-temperature. Our results show that the transformation from semiconducting Si-I to metallic Si-II, which involves a 20% volume change, causes a substantial loss of pressure that hinders complete transformation into Si-II. Thus, over-pressurization is always needed to complete the Si-I→Si-II phase transition. We also reported that Si-I and Si-II are not in mechanical equilibrium even at high-temperature, where the compression is quasi-hydrostatic. The additional microscopic stress is most likely due to the difference in plasticity between the two phases, and it could influence the dynamics of the transformation. We demonstrated also that, at high temperature, Si-II→Si-XI transition happens

with a continuous deformation of the Si-II's cell parameters. The high temporal resolution of our data enabled us to confirm that the *Imma* Si-XI phase defines a deformation pathway between tetragonal Si-II and hexagonal Si-V.

Our data provided also the first direct evidence of the I-II-L triple point of Si, at 10 GPa-1000 K. Previous experimental studies had proposed various phase diagrams that relied mostly on extrapolation and assumptions. Exact location of Si triple point gives now a reliable reference for the determination of Si phase diagram and its melting curve. The new insights from our *in-situ* data clarify some aspects of Si phase diagram up to 15 GPa. This range of pressures is interesting for material science and high-pressure synthesis. More generally, a reliable phase diagram is the foundation for prediction, via theoretical calculations, of Si behaviour at extreme conditions like those at the interior of the planets or in plasmas. There is still a lack of Si melting data above 13 GPa, as most of the previous high-pressure studies were conducted at ambient temperature. In future, systematic analysis and investigation of Si melting curve will allow to refine our knowledge of Si phase diagram.

Characterization of Si behaviour under high-pressure and high-temperature was essential in the synthesis of hexagonal Si. Upon decompression, Si-II transforms into a cubic BC8 phase (Si-III) and further heating under vacuum forms hexagonal Si (Si-IV). Thanks to our *in-situ* study, we could provide the first synthesis of a pure bulk sample of hexagonal Si, a longstanding challenge in material science. The interest for this allotrope stands in the predicted absorption properties, suitable for solar applications and tunable by an applied strain. With the first synthesis of a pure-phase sample, we opened the way for the characterization of its properties. We performed a thorough physical characterization, mainly focusing on its structure. Indeed, given the strict intercorrelation between the morphology and the bandstructure, complete characterization of the sample structure is essential to understand the origin and eventually tune its optoelectronic properties.

We demonstrated that hexagonal Si obtained via high-pressure synthesis is a different polytype, and thus has a different stacking sequence than the one previously reported. We combined x-ray diffraction, transmission electron microscopy and nuclear magnetic resonance to confirm our proposed structural model: 4H polytype with ABCB stacking, i.e. Si-4H. From our preliminary characterization, we inferred confinement effects in the sample set by the high density of stacking faults. Further structural characterization, using different microscopy techniques has investigated different length-scale, revealing a hierarchical nanostructure in Si-

4H. Besides the flake-like crystallites separated by stacking faults, other planar structural units were observed by electron microscopy on the nanoscale: Si-4H platelets. We developed and tested a procedure to separate and disperse the platelets, opening the way to manipulate these planar nanoparticles of hexagonal silicon.

Our results provide new opportunities for the design of Si-based solar devices. There are still some aspects of Si-4H's complex structure that need to be clarified, such as the relationship between the nano-flake crystallites and the platelets. Furthermore, the optoelectronic properties of the planar Si-4H platelets should be tested both theoretically and experimentally. Indeed, direct measurement of Si-4H absorption and emission spectra, together with the characterization of its photoconductivity, would help assess its feasibility for photovoltaic applications. Theoretical investigation of the relationship between the structure and the optoelectronic properties, i.e. size effects and quantum confinement, would shed light on the possibility of engineering Si-4H absorption properties by acting on the crystals' size. Further *in-situ* characterization of the synthesis procedure could enable the development of synthetic pathways with different output microstructures. Our results open the way for the study of a new promising material that could play a fundamental role in the future development of Si-based devices.

Acknowledgements

There are many people that have contributed to this work, but I would like to start by thanking my supervisors, Yann Le Godec and Alexandre Courac. Thank you for giving me the opportunity to work on this project and for introducing me to the world of high-pressure. Yann, thank you for your constant support and for your ability to smile and joke with me even under a lot (a lot!) of stress.

And thank you to Fernando Rodriguez and Romain Viennois for agreeing to read and evaluate my work; to Chrystèle Sanloup, Pascale Roy and Leora Dresselhaus-Cooper for being part of my commission.

A special thanks to Leora, who was stubborn and courageous enough to bet on me after meeting me in front of a poster, not much more than one year ago. You have helped me and taught me in so many ways that I can barely believe it. Thank you for the incredible opportunities you have given me, I hope not to let you down.

Thanks to all my colleagues at IMPMC, because every person I have crossed in this laboratory has helped me in some way. Looking back at these three years, if I have learned so much is thanks to all the people who took their time to share with me and teach me something. A special thanks to Benoit Baptiste, Paola Giura, Nicolas Menguy, Guillaume Morard, Daniele Antonangeli, Philippe Rosier and Ludovic Delbes. To my officemates, for their support and their friendship. To Carlos, for walking me into this PhD, always smiling. To Fang, for the serious work combined with hysterical laughing at 5am on the beamline. To G. and M., for being mean. To my lunch-mates, coffee-mates, pause-mates, beer-mates who have made everything more fun.

Thanks to all the people who have welcomed me at LLNL and LBNL during my summer internship. To Jon Eggert and Andrew Minor for their support. To the team at NCEM, to John and Peter for participating with such great enthusiasm. To the teams at ESRF and SOLEIL who supported us during long hours and days of experiments. To Kristina, for her patience, to Wilson, for the *fantastic* time on ID06.

A special mention to gbb aka Giovanni Battista Bachelet, who I will always look up for guidance, and that I can now call a friend (I hope). Thank you for being the best mix possible between Yoda and the Fairy Godmother.

Thanks to the MaisCan, to Titta, Fil and Fra for becoming family. For being serious (sometimes), but especially for being always supportive and ready to make me laugh at the end of a bad day. I wouldn't have made it without you, the guanciaie and, of course, the couch. Butter, thank you for being you. And thanks to Alberto, because despite all you know that you had a big part in all this, and I have a lot to be thankful for.

At last, I would really like to thank my family. You guys have supported me all along this journey. Over the years, you got passionate of foxes, rabbits, and gravitational waves, and then you didn't hesitate to become the first and the biggest fans of my tiny silicon chunk. You always have a good word for greeting me or motivating me. Without you, things would be much harder, and also less fun. I know I am lucky.

Thanks to the people who are reading this thesis, I hope you enjoyed. I surely enjoyed working on it. I hope that you didn't suffer too much this last page of sweetness; after three years under pressure, I had a lot to make up for, with a lot of people!

Appendix A:

High-pressure clathrate(s) in the K-Si system

In this Appendix, our preliminary results on the high-pressure behaviour of the potassium-silicon (K-Si) system are presented. The study of Si clathrates is of great interest for material science, as some of these binary compounds can be freed of their guest atoms, allowing the stabilization of new and exotic framework forms of Si¹. The synthesis of these low-density framework is expected to lead to materials with optimal optoelectronic properties for photovoltaics^{2,3}. Na-Si clathrates have been studied for decades, and chemical synthesis routes have been developed since the 1960s⁴. Recent studies, though, have proven that Na-Si clathrates are high-pressure phases⁵, and that high-pressure synthesis enables to obtain a new structure, like NaSi₆. When the Na atoms are expelled from this channel-like structure via degas at 400K, Si₂₄, a quasi-direct bandgap material⁶, is obtained (Section 1.1.2). These promising results reported for the Na-Si system have motivated further investigations of the chemistry and the phase diagram of Si clathrates. The scope of this project is to investigate the behaviour of the K-Si system. The use of K instead of Na is expected to give higher stability and higher control on the stoichiometry. We have performed *in-situ* XRD experiments starting from both the elemental mixture and the crystalline clathrate with structure I.

Chemical synthetic routes have been successfully applied to K-Si clathrates, allowing us to stabilize both structure I (K₈Si₄₆⁷) and structure II (K₁₈Si₁₃₆⁸) with good control of the stoichiometry and the crystal quality of the produced crystals. The behaviour of K₈Si₄₆ at high pressure has been investigated at ambient temperature in diamond-anvil cell⁹. No transition from K₈Si₄₆ to Si-II has been reported, demonstrating higher stability with respect to Na-Si clathrates¹⁰. Our experiments will complement K-Si clathrates HP characterization by performing HP-HT studies that, so far, have not been tested for the K-Si system.

We performed *in-situ* synthesis in a multi-anvil apparatus on ID06-LVP beamline at the ESRF. Compression and subsequent heating of a K-Si mixture (K:Si=1:6) led to the formation of clathrate I (i.e. K₈Si₄₆^j) at two different pressures, 10 GPa (Figure A.1) and 12.5 GPa (Appendix 4.4). Our results demonstrate that, as already demonstrated in the Na-Si system, K-Si clathrate I is a high-pressure phase. K₈Si₄₆ remains stable upon increasing temperature up to the melting temperature without further phase transitions. To explore the K-Si phase diagram,

^j The exact stoichiometry of our synthesized compound has not been verified yet. Thus, in the following, we will refer to it using the stoichiometric formula for simplification.

we also performed *in-situ* HP-HT experiments using K_8Si_{46} as the starting material trying to limit any pressure losses during the K-Si reaction. The use of K_8Si_{46} as a metastable starting material could indeed allow us to explore a wider region of the free-energy landscape, eventually reaching the stability domain of (a possible) KSi_6 . The experiments were performed on both ID06-LVP (ESRF) and PSICHE (SOLEIL) beamlines.

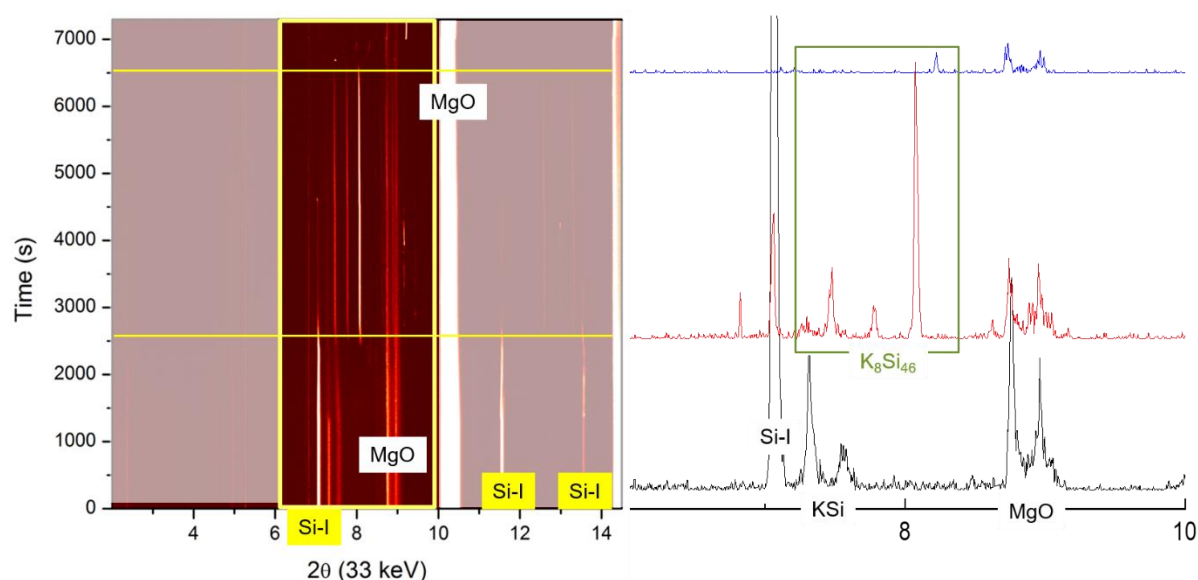


Figure A.1 : XRD data collected upon heating at 10 GPa. The formation of the K_8Si_{46} clathrate, starting from an elemental mixture, is confirmed by the concomitant disappearance of Si-I peaks and appearance of the clathrate's characteristic triplet (right panel).

Figure A.2 summarizes our results. We investigated K_8Si_{46} 's formation and its melting at HP-HT conditions in the pressure range 6-16 GPa. We could observe direct melting of K_8Si_{46} for pressures higher than 7 GPa. K_8Si_{46} melting line has negative slope (-48 K/GPa), indicating thus that the liquid phase is denser than the solid one. At lower pressure, heating caused decomposition of the clathrate, preventing direct melting. Partial dissociation into K and Si was observed also at higher pressures, but it interested only a small fraction of the sample. Besides the partial dissociation, we have also observed the appearance of new peaks at temperatures close to melting. These peaks have not yet been identified and further analysis are needed to clarify whether a different clathrate can be formed at HT. Previous studies have reported an isostructural transition at 15 GPa, but in that case there was a change of compressibility rather than a structural modification.

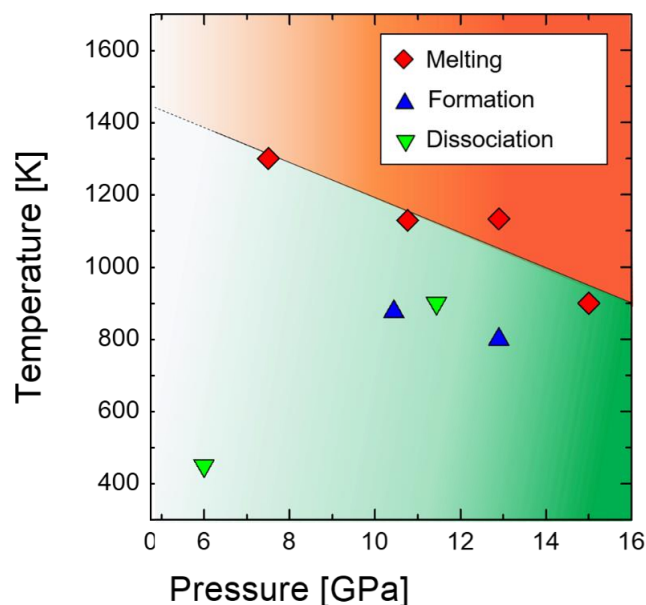


Figure A.2 : K_8Si_{46} from our *in-situ* HP-HT experiments. When the starting material was an elemental mixture K:Si=1:6, formation of K_8Si_{46} was observed upon increasing temperature (blue triangles). When the starting material was K_8Si_{46} , partial dissociation (i.e. the appearance of the HP Si phases) was observed upon heating (green triangles).

By *ex-situ* tests, we discovered a low-pressure (3.5 GPa) synthesis route that enabled us to obtain large volumes of K_8Si_{46} . This result will allow for further physical characterization to assess any differences between the high-pressure synthesized material and the chemical synthesized one.

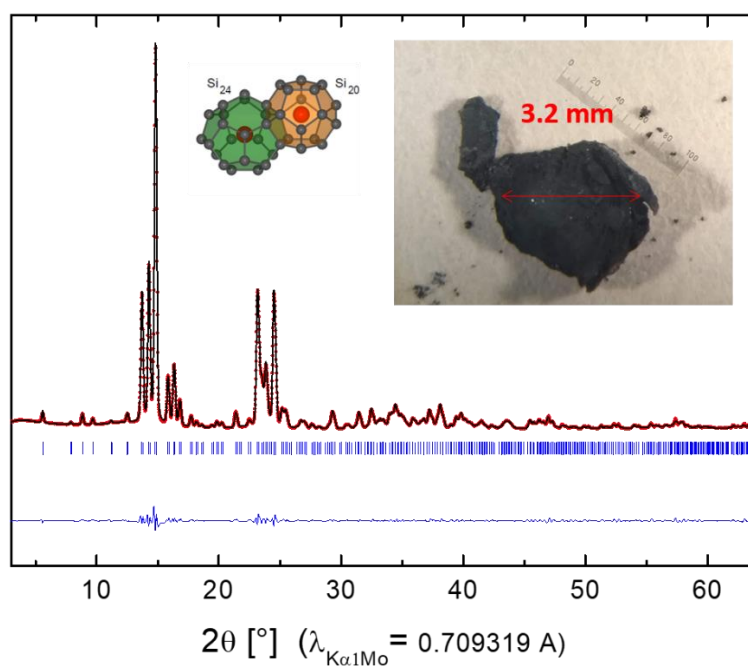


Figure A.3 : XRD data and Le Bail fit of a pure sample of K_8Si_{46} as obtained from our low-pressure synthesis route.

References Appendix A

- (1) Gryko, J.; McMillan, P. F.; Marzke, R. F.; Ramachandran, G. K.; Patton, D.; Deb, S. K.; Sankey, O. F. Low-Density Framework Form of Crystalline Silicon with a Wide Optical Band Gap. *Phys. Rev. B* **2000**, *62* (12), R7707–R7710. <https://doi.org/10.1103/PhysRevB.62.R7707>.
- (2) Amsler, M.; Botti, S.; Marques, M. A. L.; Lenosky, T. J.; Goedecker, S. Low-Density Silicon Allotropes for Photovoltaic Applications. *Phys. Rev. B* **2015**, *92* (1). <https://doi.org/10.1103/PhysRevB.92.014101>.
- (3) Botti, S.; Flores-Livas, J. A.; Amsler, M.; Goedecker, S.; Marques, M. A. L. Low-Energy Silicon Allotropes with Strong Absorption in the Visible for Photovoltaic Applications. *Phys. Rev. B* **2012**, *86* (12), 121204. <https://doi.org/10.1103/PhysRevB.86.121204>.
- (4) Kasper, J. S.; Hagemuller, P.; Pouchard, M.; Cros, C. Clathrate Structure of Silicon Na₈Si₄₆ and Na_xSi₁₃₆ ($x < 11$). *Science* **1965**, *150* (3704), 1713–1714. <https://doi.org/10.1126/science.150.3704.1713>.
- (5) Kurakevych, O. O.; Strobel, T. A.; Kim, D. Y.; Muramatsu, T.; Struzhkin, V. V. Na-Si Clathrates Are High-Pressure Phases: A Melt-Based Route to Control Stoichiometry and Properties. *Cryst. Growth Des.* **2013**, *13* (1), 303–307. <https://doi.org/10.1021/cg3017084>.
- (6) Kim, D. Y.; Stefanoski, S.; Kurakevych, O. O.; Strobel, T. A. Synthesis of an Open-Framework Allotrope of Silicon. *Nat. Mater.* **2014**, *14* (2), 169–173. <https://doi.org/10.1038/nmat4140>.
- (7) Ramachandran, G. K.; McMillan, P. F.; Dong, J.; Sankey, O. F. K₇Si₄₆ and Rb₆Si₄₆: Two Structure I Clathrates with Fully Occupied Framework Sites. *J. Solid State Chem.* **2000**, *154* (2), 626–634. <https://doi.org/10.1006/jssc.2000.8906>.
- (8) Nolas, G. S.; Kendziora, C. A.; Gryko, J.; Dong, J.; Myles, C. W.; Poddar, A.; Sankey, O. F. Raman Scattering Study of Stoichiometric Si and Ge Type II Clathrates. *J. Appl. Phys.* **2002**, *92* (12), 7225–7230. <https://doi.org/10.1063/1.1523146>.
- (9) Tse, J. S.; Desgreniers, S.; Li, Z.; Ferguson, M. R.; Kawazoe, Y. Structural Stability and Phase Transitions in K₈Si₄₆ Clathrate under High Pressure. *Phys. Rev. Lett.* **2002**, *89* (19), 195507. <https://doi.org/10.1103/PhysRevLett.89.195507>.
- (10) San-Miguel, A.; Kéghélian, P.; Blase, X.; Mélinon, P.; Perez, A.; Itié, J. P.; Polian, A.; Reny, E.; Cros, C.; Pouchard, M. High Pressure Behavior of Silicon Clathrates: A New Class of Low Compressibility Materials. *Phys. Rev. Lett.* **1999**, *83* (25), 5290–5293. <https://doi.org/10.1103/PhysRevLett.83.5290>.
- (11) Glunz, S. W.; Preu, R.; Biro, D. Crystalline Silicon Solar Cells. In *Comprehensive Renewable Energy*; Elsevier, 2012; pp 353–387. <https://doi.org/10.1016/B978-0-08-087872-0.00117-7>.

List of Figures

- Figure 1.1** : Maximum achievable absorption and efficiency of photovoltaic materials. (a) for an ideal material with the optimal bandgap, the orange portion shows the maximum energy that can be absorbed, while the grey areas are the portion of the solar spectrum that cannot be absorbed. Figure adapted from Glunz et al¹¹. (b) absorption efficiency as a function of the bandgap energy, as calculated by Shockley and Queisser, showing that the maximum conversion efficiency is obtained for energy gaps around 1.1-1.3 eV. The solar spectrum irradiance is also shown in the lower part of the figure. 12
- Figure 1.2** : Optoelectronic properties are determined by the crystal structure. (a) diamond Si-I and its bandstructure; (b) hexagonal Si-IV (i.e. 2H-Si polytype) and its bandstructure as calculated by Rodl et al²⁵. (c) comparison of Si-I (cubic) and Si-IV (hexagonal) absorption in the region of interest (the yellow area represents the solar spectrum). Figure adapted from Amato et al²³ 14
- Figure 1.3** : Calculated enthalpy at T=0 K for Si-I, Si-II and Si-III. The figure shows that, by tuning the pressure, the enthalpy changes may induce a phase transition. At pressures higher than 8 GPa, Si-II becomes the lowest-enthalpy phase, while Si-III is not the energetically favourable phase at any P. Data are taken from ³² and ΔH are calculated with respect to the one of the cubic (bcc) high-pressure phase. 15
- Figure 1.4** : Calculated enthalpy variations at 8 GPa along different transformation pathways starting from Si-II. In black, direct transition back to the cubic Si-I is shown to have a higher kinetic barrier than the transition Si-II (β -tin) \rightarrow Si-XII (r8) \rightarrow Si-III (bc8). This favours the formation the transition to Si-III rather than Si-I upon decompression, even though the final state (Si-III) is not the globally stable phase. Data for Si-II \rightarrow Si-I pathway are taken from ⁴⁴ and have been recently reproduced by ⁴², from which the Si-II \rightarrow Si-III data shown in purple have been taken. 17
- Figure 1.5** : Schematic view of the recoverable metastable phases that have been reported from HP-HT treatment of cubic Si-I. On the left, Si-VIII and Si-IX are reported; these phases can be obtained by fast (~ 10 GPa/ms) decompression, their structures have not been refined. On the right, the phase transformations upon slow decompression at ambient temperature (Si-II \rightarrow Si-XII \rightarrow Si-III) and subsequent annealing (Si-III \rightarrow Si-IV) are shown..... 18
- Figure 1.6** : Summary of the Na-Si clathrates synthesized via HP. Clathrate II and the open-framework NaSi₆ phases can be transformed into guest-free allotropes with bandgap energies as shown. No evidence of the guest-free clathrate I framework has been reported so far. 19
- Figure 2.1** : High-pressure phases of Si. For each phase name, space group and pressure formation at ambient temperature (as determined by experiments) are reported. 29
- Figure 2.2** : Experimental results showing the Si phase transitions at high-pressure, presented in chronological order. Each colour corresponds to the stable phase observed for each pressure. When coexistence was observed, two colours are shown for that pressure. The only exception is the indentation study by Gupta et al.¹⁴, for which the horizontal division corresponds to the different orientation of the Si indented surfaces. The advent of high-pressure *in-situ* XRD allowed to characterize not only the structure of different high-pressure allotropes, but also the extension of coexistence domains. For each work, the high-pressure apparatus as well as the *in-situ* characterization used to detect phase transition are indicated. The vertical bars (|) indicate whether in the study Si-I \rightarrow Si-II transition has been observed also at pressures lower than the reported onset. 33
- Figure 2.3** : Comparison between electrical and structural x-rays characterization under pressure. (a) Minomura's *in-situ* resistance measurements of *n*-doped Si under pressure. The

transition was detected as a drop of several order of magnitude of the resistance. (b) <i>in-situ</i> XRD pattern showing the coexistence region, with Si-I peaks (\square) and Si-II ones (\triangle) present. Figures adapted from ²⁵ and ¹⁷	34
Figure 2.4 : T vs P plot showing Si melt. (a) Melting of Si with T vs P data up to 16 GPa. Black full symbols a show the experiments with <i>in-situ</i> XRD. (b) Melting points from electrical or thermal analysis only. The linear fit of the melting curve of both Si-I and high-pressure phases is shown. Crossing of the two melting lines gives the position of the extrapolated I-II-L triple points.....	36
Figure 2.5 : Si P-T phase diagram from <i>in-situ</i> XRD studies. Each phase and each study are represented by a colour and a symbol respectively. Fit of the Si-I and Si-II melting curves from ¹⁷ and ³³ are also included. The extrapolated triple points are annotated with unfilled markers, while filled red markers indicate experimental observation of melting.....	37
Figure 2.6 : Pressure-temperature phase diagram of Si, as determined by combination of DFT, evolutionary algorithms and lattice dynamics. This new approach gives results coherent with available experimental data at ambient temperature and at melting, and it predicts two transitions above 250 GPa (fcc \rightarrow bcc \rightarrow sc). Figure adapted from ²⁴	40
Figure 3.1 : Pressure scale, starting from the atmospheric pressure. In the lower part of the figure, natural phenomena are shown at their corresponding pressure. On the upper part of the figure, experimental capabilities for static high-pressure experiments are shown. Three different static high-pressure apparatus are represented, and the surface of the correspondent triangles shows the range of pressure attainable with each technique (along the <i>x</i> axis) and the sample volumes that is possible to study (along the <i>y</i> axis). The sample volume necessarily diminishes when we increase the pressure we want to attain.	49
Figure 3.2 : Multi-anvil presses. (a) schematic view of the octahedral pressure medium and how it is inserted in the Kawai-type octahedral cell, made of eight truncated cubical WC anvils. (b) schematic view of the DIA geometry, in which the compression of the anvils takes place along the cube's axis. (c) schematic view of the Walker geometry, in which the anvils are inserted in a cylindrical vessel and the compression happens along the [111] direction of the cube. Figures adapted from ¹⁷ and ¹⁵	52
Figure 3.3 : Schematic view of the X-ray diffraction conditions. (a) Bragg condition: constructive interference causes the formation of bright diffraction spots when the difference of the distance travelled by the X-rays ($\Delta l = 2 d \sin \theta$) is an integer multiple of the radiation wavelength ($n\lambda$). (b) construction of the Ewald sphere: the incident wave vector k is drawn so that it points to the origin of the reciprocal lattice. The Ewald sphere is centred at the origin of the vector k and has radius equal to $ k $. (c) Laue condition: the diffraction condition is satisfied when the Ewald sphere intersects a point in reciprocal space, meaning that another vector k' exists with $ k' = k $ (i.e. the radius of the sphere) such that $\Delta k = k' - k = G$, with G vector of the reciprocal lattice.....	54
Figure 3.4 : Schematic view of a synchrotron facility. The images represent the European synchrotron in Grenoble (ESRF), and have been adapted from ²¹ . (a) view of the synchrotron facility and zoom of a portion of the storage ring in which different insertion devices are present. (b) schematic representation of a bending magnet: when placed into a magnetic field, a charged particle (electrons) follows a circular trajectory. (c) schematic representation of an undulator: a series of magnets are placed in series and cause the electron's trajectory to undulate.	55
Figure 3.5 : Schematic view of the typical multi-anvil cell used during AD-XRD experiments on ID06 beamline at the ESRF. (a) Cross-section of the octahedral MgO pressure transmitting medium. (b) schematic view of the HP assembly components. (c) Top-view showing the low-absorption elements (i.e. boron epoxy or amorphous powder) inserted along the beam's path to minimize losses due to absorption.	57

Figure 3.6 : Schematic view of the typical multi-anvil cell used during ED-XRD experiments on PSICHE beamline at the SOLEIL Synchrotron. (a) Cross-section of the WC truncated cubes surrounding the octahedral MgO pressure transmitting medium. As visible in the figure, cutting of the octahedron tip allowed us to drill the hole hosting the HP assembly perpendicularly to the x-ray beam. (b) schematic view of the HP assembly components..... 59

Figure 4.1 : (a) Evolution of the pressure during heating as estimated using Ta EOS (Run1-2) and MgO EOS (Run3). (b)-(c) Atomic volumes of Si-I and Si-II as measured from *in-situ* XRD at HP-HT conditions. In every experiment, the pressure drops upon heating during the Si-I→Si-II transformation. The onset of the pressure loss varies depending on the initial compression state. Data from various experiments are reported using different symbols, while colours are used to show different stages of the heating in terms of pressure stability (i.e. pressure stable or modified during the heating). 67

Figure 4.2 : *in-situ* high-pressure data from Run1 (ID06-LVP beamline) showing the simultaneous melting of both Si-I and Si-II. The colormaps show the evolution of the XRD pattern over time (y axis); on the x axis, the 2θ angles at 33 keV ($\lambda=0.3757\text{\AA}$) are reported. In (b) the colormap zooms on the final part of the experiment, shown with a yellow rectangle in (a). While performing the HP-HT experiment, electrical measurements allowed to control in-real-time the power supplied to the assembly (and thus the temperature, central panel in (a)) and the resistance (right panel in (a)). The pressure evolution has been obtained from Ta EOS. We provide evidence of the I-II-L triple point, as concomitant disappearance of XRD peaks and the discontinuity of the sample's resistance are considered proof of melting..... 69

Figure 4.3 : Si-II→Si-XI transition studied by *in-situ* high-pressure data from experiments on the ID06-LVP beamline. (a) The colormaps show the evolution of the XRD pattern over time (x axis); on the y axis, the 2θ angles at 33 keV ($\lambda=0.3757\text{\AA}$) are represented. (b),(c) Evolution of the lattice parameters during the transition, the splitting of $a_{\text{Si-II}}$ in $a_{\text{Si-XI}}$ and $b_{\text{Si-XI}}$ happens continuously. While performing the HP-HT experiment, electrical measurements allowed to control in-real-time the power supplied to the assembly (and thus the temperature, central panel in (d)). The pressure evolution has been obtained from Ta EOS (d)..... 71

Figure 4.4 : Updated P-T Si phase diagram. We propose a new trend for Si-I melting curve, with a steepening slope at high pressures. This curve meets our measured I-II-L triple point in (10 GPa; 950 K). The phase boundaries and the melting curves are traced by combining XRD data from studies that enabled *in-situ* pressure measurement (apart from the piston-cylinder study of Jayaraman²¹ et al. at low pressures). The filled symbols are data from our study, while the void symbols represent data from previous studies, with each symbol corresponding to different authors. Each phase (included the I-II mixed phase) is represented by a different colour. The stability regions of the different phases are coloured accordingly; because of the sluggish nature of Si-I→Si-II transition and our recent findings that question the possibility of thermodynamic equilibrium between these two phases, we don't indicate a precise phase boundary..... 73

Figure 4.5 : Atomic volumes of Si-I and Si-II and pressure as a function of temperature for Run1 (ID06-LVP beamline at the ESRF synchrotron). Blue symbols stand for measurements at quasi-constant pressure, while red points indicate the pressure drop observed upon heating. Light blue symbols correspond to the point collected after Si-II melting, thus when only Si-I was present. 79

Figure 4.6 : Volumes and pressure as a function of temperature for Run2 (ID06-LVP beamline at the ESRF synchrotron). Blue symbols stand for measurements at quasi-constant pressure, while red points indicate the pressure drop observed upon heating. Light green symbols are used for the measurements during re-compression at high temperature, and pink ones are used when only Si-II is observed, thus at the completion of Si-I→Si-II transition. In the inset, a zoom of the volumes of Si-I and Si-II as a function of temperature is reported to

evidence their opposite behaviour. While, upon increasing the load, Si-II expands and then starts to shrink. Si-I does exactly the opposite. 80

Figure 4.7 : Volumes and pressure as a function of temperature for Run3 (PSICHE beamline at Soleil synchrotron). Blue symbols stand for measurements at quasi-constant pressure, while red points indicate the pressure drop observed upon heating. Light green symbols are used for the measurements during re-compression at high temperature, and pink ones are used when only Si-II is observed, thus at the completion of Si-I→Si-II transition. 81

Figure 4.8 : X-Ray imaging *in-situ* on PSICHE beamline allows to determine the position of both the sample and the pressure calibrant during the experiment. A rhenium foil (easily visible for its higher density) and a hBN plug separate the MgO from the Si. 82

Figure 4.9 : qualitative estimation of the degree of hydrostaticity of the high-pressure cell can be obtained by comparing the volumes obtained via single-peak fitting or whole profile fitting. In hydrostatic condition, the values should coincide..... 82

Figure 4.10 : Si-II→Si-XI transition studied by *in-situ* high-pressure data from experiments on ID06-LVP beamline. Left: the colormaps show the evolution of the XRD pattern over time (y axis); on the x axis, the 2θ angles at 33 keV ($\lambda=0.3757\text{\AA}$) are represented. Right: pressure and temperature variations during the HP-HT experiment. Pressure was measured from Ta EOS. 83

Figure 5.1 : (a) HP-HT synthesis. Colormap showing the evolution of XRD patterns at 13 GPa; time goes upward along the y axis. In the upper panel, the patterns corresponding to the coloured lines traced on the 2D colormap are reported; Si-II peaks are highlighted by the red symbol * in the final (red) pattern. (b) Schematic view of different Si polytypes. The red rectangles evidence Si dumbbells forming the hexagonal planes. In Si-2H and Si-3C (i.e. d-Si) planes are all in the hexagonal (twisted consecutive dumbbells) or in the cubic configuration respectively, while in Si-4H these two configurations alternate. The presence of both cubic and hexagonal dumbbells give rise to two inequivalent atomic position, evidenced by atoms of different colours. (c) Structure investigation through Powder-XRD. Experimental data collected with a Mo anode are represented by red dots; the black line corresponds to the best Rietveld fit; the blue line represents the difference between experimental and calculated pattern. In addition, Bragg reflections of Si-4H are represented with the blue symbols. A schematic view of the crystallites shape and size is reported. 88

Figure 5.2 : (a) High-Resolution TEM image; two different domains, A and B, are evidenced. FFT- TEM of the A and B are reported in (b) and (d). Both domains have Si-4H structure, as shown in (c) and (e) where the simulation of Si-4H reciprocal space along [001] and [223] directions respectively has been superposed to the pattern. (f) HR-TEM image of the hexagonal planes stacking; the corresponding FFT-TEM pattern and the simulated Si-4H [010] are shown in (g) and (h). (i) A schematic view of the crystallites shape and size as determined by TEM. 90

Figure 5.3 : ^{29}NMR measurements of Si-4H; vertical lines show evidence of a doublet. On the x axis, experimental chemical shifts of Si-III and SiO₂ (triangles) together with the DFT results for Si polytypes are reported for comparison. 92

Figure 5.4 : Raman measurements and DFT calculations. Upper panels: Raman spectra as predicted by DFT calculations for three different polytypes. Lower panel: experimental data obtained with a green laser ($\lambda = 514.5\text{ nm}$) as exciting radiation in back-scattering geometry, compared to the Si-4H Raman spectrum from DFT. The vertical dashed line corresponds to the Raman shift of the d-Si optical phonon at 52 cm^{-1} 93

Figure 5.5 : Photoluminescence spectrum of Si-4H at ambient condition, using a blue laser($\lambda = 460\text{ nm}$). Solar spectrum irradiance is reported on the background to evidence the large superposition of the sample emission with the visible region..... 94

Figure 5.6 Profile of Temperature and Power during the heating at 13 GPa..... 103

Figure 5.7 FFT-TEM patterns of zone 3 of the sample, shown also in the main text. Green dots are simulated Si-4H diffraction pattern along [2 -2 3] and [0 0 1] direction respectively.	104
Figure 5.8 FFT-TEM patterns are compared with simulated electron diffraction patterns for Si-2H, Si-4H and Si-6H polytypes. From left to right, for two different patterns are reported: FFT-TEM data; Si-4H simulation superimposed to the data to underline the good agreement between data and simulation; Si-2H and Si-6H simulation of the electron diffraction pattern along the same direction. Comparison evidences that the experimental data are compatible with Si-4H structural model and could not be explained with other hexagonal polytypes....	105
Figure 5.9 TEM image and Electron Diffraction pattern of the sample (zone 14). Green dots are simulated Si-4H diffraction pattern along [010] and [100] direction respectively.	105
Figure 5.10 TEM image and Electron Diffraction pattern of the sample (zone 15). Green dots are simulated Si-4H diffraction pattern along [010] and [100] direction respectively.	106
Figure 5.11 Electronic band structures of different polytypes as calculated by LDA-DFT. 3C polytype (i.e. cubic d-Si) is reported for comparison. Our results are in good agreement with previous calculations [10-11].	109
Figure 5.12 Comparison of XRD diffraction measured pattern and computed profiles for different hexagonal polytypes. Data are reported with a black line and were collected using a Mo radiation source ($\lambda_{K\alpha 1} = 0.709319 \text{ \AA}$, $\lambda_{K\alpha 2} = 0.713609 \text{ \AA}$). Structural models for hexagonal polytypes are taken from [10] and thus do not correspond with the ideal polytypic structure, but with a relaxed one obtained by DFT calculations.	110
Figure 5.13 2D diffractogram of Si-4H sample. Since there is no evidence of texture in the sample, such effects have not been taken into account when performing Rietveld refinement.	111
Figure 6.1 : Multi-scale analysis of the hierarchical structure of Si-4H. A combination of optical and electron microscopy techniques was used to access the different length-scales. (a) Cracks observed at the sample surface upon polishing. Observation of the finely patterned cracks led us to further investigate the grains' size in our material. (b) Image revealing the substantial nanostructure of the pristine Si-4H morphology. We observe quasi-2D discrete structural units, that we refer to as <i>platelets</i> . (c) Image of quasi-single platelets dispersed on a TEM grid. (d) Image of a single platelet. The crystal planes are well visible, and the crystalline quality is also confirmed by the FFT pattern (i.e. the reciprocal lattice corresponding to the image).	117
Figure 6.2 : (a)-(b) Images of the pellet's surface after fine polishing. Cracks are visible at the sample's surface. (c) XRD pattern of the Si-4H sample from the original batch (black, Chapter 5) and from the sample analysed in this study (red). The inlay shows the 2D image plate, displaying continuous Debye-Scherrer rings.	118
Figure 6.3 : Images investigating the pristine morphology of Si-4H. The complex conformation of the sample, that comprises voids, cracks and discrete flat units, is here demonstrated by SEM imaging. (a) Evidence of voids and cracks on the as-synthesized Si-4H sample; the inset dimensions are 5 μm and 2.4 μm . (b) Image of the sample's surface that evidences the presence of the platelets. (c) Magnification of the region framed in yellow in (b); dimensions are 3.8 μm x 3.8 μm	119
Figure 6.4 : Images showing a representative collection of platelets. The platelets are disordered and show no sign of preferential orientation. (a), (b) UHR-SEM images of the pristine morphology of Si-4H. (c) Magnification of the region evidenced in (b). The edges of the platelets as obtained from edge-finding methods are evidenced.	120
Figure 6.5 : : (a-d) UHR-SEM images of the TEM grid prepared following the methodology detailed in the text. The magnified images in (c-d) (1.80 μm x 1.40 μm) evidence the	

suspended electron-transparent units at the border of the holes of the Quantifoil support film. 121

Figure 6.6 : Images of the dispersed platelets and EELS data. (a) HR-TEM image of Si-4H platelets dispersion. EELS data have been collected along the black line (b) Spectra from the points marked in the top-right zoom panel. (c) Normalized intensities of Si and SiO₂ EELS peaks in purple and green respectively (the dashed vertical lines in (b) show the integration interval around the peaks). The red points show the SiO₂/Si ratio along the profile. 122

Figure 6.7 : Images showing some representative Si-4H platelets and FFT-TEM analysis of the crystalline domains. The direct-space HR-TEM image, the FFT-TEM pattern alone and superposed with the calculated one from Si-4H structural model are shown in (a),(b),(c) and (e),(f),(g) respectively. (d) and (h) show the FFT-filtered images, in which coloured overlays are superposed to the original TEM image to evidence the crystalline domains. The inset shows the peaks used for Fourier filtering; the colours used to evidence each peak are the same of the correspondent overlays' ones..... 124

Figure 6.8 : Analysis of the crystalline domains by FFT-TEM filtering. For two different zones of the sample the direct-space HR-TEM image, the FFT-TEM pattern and the FFT filtered images are shown in (a),(b),(c) and (e),(f),(h) respectively. (d),(h): Zoom of the FFT-TEM pattern corresponding to the black squares in (b) and (f) to evidence the peaks used for FFT filtering. The filtered peaks are highlighted by coloured circles respectively; the same colours have been used to evidence the correspondent crystalline domains with the overlayer in (c) and (h). 126

Figure 6.9: SEM image of the carbon scotch-tape after cleavage of the polished Si-4H surface. 133

Figure A.1 : XRD data collected upon heating at 10 GPa. The formation of the K₈Si₄₆ clathrate, starting from an elemental mixture, is confirmed by the concomitant disappearance of Si-I peaks and appearance of the clathrate's characteristic triplet (right panel).....142

Figure A.2 : K₈Si₄₆ from our *in-situ* HP-HT experiments. When the starting material was an elemental mixture K:Si=1:6, formation of K₈Si₄₆ was observed upon increasing temperature (blue triangles). When the starting material was K₈Si₄₆, partial dissociation (i.e. the appearance of the HP Si phases) was observed upon heating (green triangles).....143

Figure A.3 : XRD data and Le Bail fit of a pure sample of K₈Si₄₆ as obtained from our low-pressure synthesis route.....143

List of Tables

Table 2.1: Selected high-pressure high-temperature experiments on Si.	35
Table 2.2: Experimental results on the melting curve of Si at high pressures and proposed triple points for I-II-L, II-XI-L and XI-V-L.	38
Table 2.2: Results of high-pressure studies on Si at room temperature. All transition pressures are expressed in GPa. Si-I→Si-II (onset) column indicates the lower bound of the transition region, or the lowest pressure at which Si-II has been detected.	47
Table 4.1 <i>in-situ</i> HP-HT XRD experiments on Si phase diagram up to 15 GPa.	65
Table 5.1 ²⁹ Si NMR Chemical Shifts of Hexagonal Si Polytypes.	107
Table 5.2 Frequency of the Raman active modes of Hexagonal Si Polytypes.	108
Table 5.3 Fractional atomic coordinates and equivalent isotropic displacement parameters	111
Table 5.4 Results of the Rietveld refinement on the X-Ray powder pattern of Si-4H.	111

[Méthodes de synthèse à haute-pression pour des nouveaux matériaux à base de Si avec propriétés optoélectroniques remarquables et leur caractérisation]

Résumé :

Dans cet ouvrage, le traitement à haute température et haute pression est utilisé pour développer et optimiser la synthèse de nouvelles formes exotiques du silicium. La synthèse de nouvelles phases de silicium est un point clé dans le développement de technologies à base de Si, en particulier l'énergie solaire. Le développement de nouveaux matériaux à base de silicium à haut rendement pourrait faire face à la fois à l'optimisation des performances et à la réduction des coûts. Au niveau industriel, la haute pression a été principalement utilisée pour la synthèse des diamants et des matériaux super-durs, mais des études récentes ont prouvé qu'elle est également efficace pour la synthèse de nouveaux matériaux à base de silicium à propriétés remarquables pour les applications. Nous abordons ce défi sous tous ses aspects, à partir de l'étude des mécanismes de transition à haute pression jusqu'à la synthèse et à la caractérisation d'un nouveau matériau de silicium. Nous utilisons la diffraction *in situ* de rayons X à haute-pression haute-température pour observer et caractériser des transitions de phase du silicium et leur dynamique. Grâce à nos résultats, nous donnons de nouvelles perspectives capables de clarifier certains aspects du diagramme de phase du silicium qui étaient encore en discussion. Nous obtenons la première synthèse de silicium hexagonal pur, un défi de longue date dans le domaine. Grâce à notre échantillon de phase pure, nous caractérisons ses propriétés physiques et structurales. Nous prouvons que le silicium hexagonal obtenu à partir du traitement haute pression est sous forme du polytype 4H (séquence d'empilement ABCB). D'autres caractérisations structurales révèlent une nanostructure hiérarchique dans la morphologie de l'échantillon. La découverte et la caractérisation de nanoparticules quasi-2D accessibles à la manipulation ouvrent de nouvelles perspectives pour le développement de nouveaux dispositifs optoélectroniques.

Mots clés : [silicium, synthèse haute-pression, DRX, Si hexagonale]

[High-pressure pathways towards new functional Si-based materials with tailored optoelectronic properties and their characterization]

Abstract :

In this work, high-pressure high-temperature treatment is used to develop and optimize synthetic pathways to new and exotic forms of silicon. The synthesis of new phases of silicon is a key point in the future development of Si-based technology, especially for solar energy. Development of new Si-based materials with high-efficiency could both optimise the performances and reduce the costs. At an industrial level, high-pressure has been mainly used for the synthesis of diamonds and super-hard materials, but recent studies have proven it also efficient in the synthesis of new silicon-based materials with enhanced properties for applications. We tackle this challenge in all its aspects, starting from the study of transition mechanisms at high-pressure and arriving to the synthesis and characterization of a new silicon material. We use *in-situ* x-ray diffraction at high-pressure high-temperature conditions to monitor and characterize silicon phase transitions and their dynamics. Our results give new insights that clarify some aspects of the silicon phase diagram that were still a matter of debate. We obtain the first synthesis of pure hexagonal silicon, a longstanding challenge in the field. Thanks to our pure-phase sample, we characterize its physical and structural properties. We prove that hexagonal silicon obtained from high-pressure is in the form of 4H polytype (ABCB stacking sequence). Further structural characterizations reveal a hierarchical nanostructure in the pristine morphology of the sample. Discovery and characterization of discrete quasi-2D nanoparticles accessible for manipulation opens new perspectives for the design of new optoelectronic devices.

Keywords : [silicon, high-pressure synthesis, XRD, hexagonal Si]